


Spring 2007

Assessment of Preliminary Design Approaches for Metallic Stiffened Cylindrical Shell Instability Problems

Vicki Owen Britt
Old Dominion University

Follow this and additional works at: https://digitalcommons.odu.edu/mae_etds

 Part of the [Navigation, Guidance, Control and Dynamics Commons](#), [Structures and Materials Commons](#), and the [Systems Engineering and Multidisciplinary Design Optimization Commons](#)

Recommended Citation

Britt, Vicki O.. "Assessment of Preliminary Design Approaches for Metallic Stiffened Cylindrical Shell Instability Problems" (2007). Doctor of Philosophy (PhD), dissertation, Aerospace Engineering, Old Dominion University, DOI: 10.25777/3mdz-jw26 https://digitalcommons.odu.edu/mae_etds/48

This Dissertation is brought to you for free and open access by the Mechanical & Aerospace Engineering at ODU Digital Commons. It has been accepted for inclusion in Mechanical & Aerospace Engineering Theses & Dissertations by an authorized administrator of ODU Digital Commons. For more information, please contact digitalcommons@odu.edu.

**ASSESSMENT OF PRELIMINARY DESIGN APPROACHES
FOR METALLIC STIFFENED CYLINDRICAL SHELL
INSTABILITY PROBLEMS**

by

Vicki Owen Britt
B.S. December 1987, North Carolina State University
M.S. May 1990, North Carolina State University

A Dissertation Submitted to the Faculty of
Old Dominion University in Partial Fulfillment of the
Requirement for the Degree of

DOCTOR OF PHILOSOPHY

AEROSPACE ENGINEERING

OLD DOMINION UNIVERSITY
May 2007

Approved by:

Chuh Mei (Co-Director)

Norman F. Knight, Jr. (Co-Director)

Robert L. Ash (Member)

ABSTRACT

ASSESSMENT OF PRELIMINARY DESIGN APPROACHES FOR METALLIC STIFFENED CYLINDRICAL SHELL INSTABILITY PROBLEMS

Vicki Owen Britt

Old Dominion University, 2007

Co-Directors: Dr. Chuh Mei and Dr. Norman F. Knight, Jr.

A preliminary design tool for metallic stiffened fuselage cylindrical panels subjected to longitudinal compression has been developed and validated by comparison to test results. Several methodologies for stiffened panel buckling and failure predictions were examined and evaluated. An appropriate level of analysis fidelity was determined for different failure modes and design details. Results from panel tests conducted to verify analytical methods used to design the Gulfstream V aircraft were presented. The panels were representative of four general skin/stringer configurations on the aircraft. Finite Element analyses and standard analytical methods were used to predict panel failure loads. The accuracy of the finite element analysis predictions was dependent upon the level of detail included in the model. The inclusion of such details as fasteners had a significant effect on the predicted failure load. The omission of such complexities from the finite element model led to unconservative failure predictions. Standard analytical methods were found to be more efficient than finite element methods and produced conservative panel failure loads. Improvements for a preliminary design tool were identified to reduce conservatism in failure predictions and thereby reduce structural weight.

This thesis is dedicated to the memory of
Dr. James H. Starnes, Jr.
(1939-2003)

ACKNOWLEDGMENTS

Several people have contributed to the successful completion of this work. I would first like to thank my advisor Dr. Norman Knight, Jr. for his patience and perseverance in directing and reviewing my research for the entire 13 years that I worked on my doctorate. His continued dedication to helping me reach this goal was invaluable. I would also like to thank my other committee members, Dr. Chuh Mei and Dr. Robert Ash, for their guidance in the editing of this manuscript and for their support of my research work over an extended period of time. I also would like to thank Dr. Frank Simmons, III for his assistance in selecting a topic relative to my work at Gulfstream Aerospace. Finally, I would like to thank my family for all of their support in this endeavor. My parents, Joyce and Glenn Owen, have always provided unending encouragement for my academic endeavors and have instilled in me the tenacity and confidence to attain whatever goals I set out to achieve. My husband, Wade Britt, has cheered me on tirelessly for many years and cared for our daughters, Amelia, Claire, and Kate, on countless Saturdays and late nights during this lengthy endeavor. I appreciate with all of my heart the assistance of these people in my quest to become 'Dr. Mom'.

TABLE OF CONTENTS

	Page
LIST OF TABLES	vii
LIST OF FIGURES	ix
 Section	
1. INTRODUCTION	1
1.1 Background and Motivation	1
1.2 Literature Review.....	2
1.3 Objectives	6
1.4 Scope.....	7
1.5 Roadmap	7
2. METHODOLOGY FOR STIFFENED FUSELAGE PANEL DESIGN.....	9
2.1 Stiffened Panel Geometry and Loading.....	9
2.2 Design Requirements for Stiffened Panels	11
2.3 Global and Local Failure Modes for Stiffened Fuselage Panels.....	13
2.4 Levels of Analysis.....	18
2.4.1 Closed-Form and Rayleigh-Ritz Solution Methods	19
2.4.2 Finite Strip Analysis Methods.....	20
2.4.3 Finite Element and Finite Difference Analysis Methods	21
2.5 Representative Analysis Tools.....	22
2.6 Current Analysis Effort.....	24
3. EXPERIMENTAL STUDIES	25
3.1 Geometry and Materials.....	25
3.2 Test Boundary Conditions and Generalized Imperfections	29
3.3 Instrumentation and Data Acquisition	33
3.4 Test Results.....	39
3.4.1 General	39
3.4.2 Panels 614-1 and 614-2	39
3.4.3 Panels 615-1 and 615-2	46
3.4.4 Panels 616-1 and 616-2	52
3.4.5 Panels 617-1 and 617-2	58
3.5 Test Results Summary	65
4. BASELINE NUMERICAL STUDIES.....	68
4.1 Geometry, Boundary Conditions, and Loads.....	69
4.2 PAGE Results	71
4.3 PANDA2 Results	72
4.4 STAGS Results for Single-Stiffener Repeating Section.....	75
4.4.1 Smearred Stiffener Properties	77

Section	Page
4.4.2 Discrete Stiffener.....	86
4.4.3 Branched-Shell Bonded-Stiffener	92
4.4.4 Branched-Shell Riveted-Stiffener	97
4.5 STAGS Results for Three Repeating Elements.....	101
4.5.1 Smearred Stiffener Properties.....	102
4.5.2 Discrete Stiffeners	106
4.5.3 Branched-Shell Bonded-Stiffeners.....	109
4.5.4 Branched-Shell Riveted-Stiffeners.....	113
4.6 Summary	117
5. NUMERICAL ANALYSIS OF TEST PANELS	124
5.1 PAGE Analysis Results	125
5.2 STAGS Analysis Results	127
5.2.1 STAGS Predictions for Panel 614.....	129
5.2.2 STAGS Predictions for Panel 615.....	140
5.2.3 STAGS Predictions for Panel 616.....	144
5.2.4 STAGS Predictions for Panel 617.....	148
5.2.5 STAGS Analysis Summary.....	152
5.3 Proposed PAGE Analysis/Design Improvements.....	158
5.3.1 Euler-Column Failure Mode	158
5.3.2 Skin Wrinkling Failure Mode.....	165
5.4 Analysis Summary	167
6. CONCLUSIONS AND RECOMMENDATIONS	169
6.1 Conclusions.....	169
6.2 Recommendations.....	170
REFERENCES	172
APPENDICES	
A. REVIEW OF SELECTED STIFFENED FUSELAGE PANEL ANALYSIS TOOLS.....	177
B. STRAIN GAGE DATA FOR FUSELAGE PANEL TESTS	206
VITA.....	231

LIST OF TABLES

Table	Page
1. Representative panel analysis codes	23
2. Test panel configuration definition	27
3. Frame and stringer property values	29
4. Dial gage measurements	32
5. Test panel material properties	33
6. Buckling loads of skin bays for panels 614-1 and 614-2 based on visual observations	43
7. Buckling loads of skin bays for panels 615-1 and 615-2 based on visual observations	49
8. Buckling loads of skin bays for panels 616-1 and 616-2 based on visual observations	55
9. Buckling loads of skin bays for panels 617-1 and 617-2 based on visual observations	61
10. Test panel failure summary	65
11. PANDA2 buckling predictions for a single-stiffener panel section	74
12. PANDA2 buckling predictions for a three-stiffener panel section	74
13. STAGS baseline panel model results summary	119
14. Test panel configuration summary	124
15. Test and PAGE-predicted panel maximum loads	125
16. Test and STAGS buckling and failure loads	153

17. Results for gusseted-stringer models	161
18. Second order polynomial coefficients	162
19. Comparison of failure loads calculated by finite element analysis and derived polynomial equations	164
20. Panel 614, 615, and 616 study model results.....	166
21. Summary of STAGS and PAGE failure predictions.....	168

LIST OF FIGURES

Figure	Page
1. Stiffened panel geometry	9
2. Typical stiffener cross-sections.....	10
3. In-plane forces and moments applied to panel	11
4. Local skin buckling mode for hat-stiffened panel	14
5. Typical buckling modes for stiffened panels – cross-sectional view	15
6. Stiffener torsional buckling modes	15
7. Stiffener buckling failure modes.....	16
8. Euler-column skin/stringer failure mode for tee-stiffened panel	18
9. General test panel configuration	26
10. Frame and stringer geometries for the test panels	28
11. Compression test fixture	30
12. Dial-gage measurement locations	31
13. Strain gage locations for panel configurations 614 and 615.....	35
14. Strain gage locations for panel configuration 616	36
15. Strain gage locations for panel configuration 617	37
16. Out-of-plane displacement gage locations viewed from exterior side of panel.....	38
17. Test panel reference numbering system for identifying panel locations	39
18. Load end-shortening response curve for panel 614-1.....	41
19. Back-to-back strain-gage data for panel 614-1 skin bays.....	42
20. Panel 614-1 failure mode	45

21. Exterior view of failed section of panel 614-2.....45

22. Interior view of failed section of panel 614-2.....46

23. Load end-shortening response curve for panel 615-2.....47

24. Strain-gage data for 615-2 panel skin bays.....48

25. Exterior view of failed section of panel 615-1.....50

26. Interior view of failed section of panel 615-1.....50

27. Stringer strain-gage data for panel 615-2.....51

28. Load end-shortening response curve for panel 616-2.....53

29. Strain-gage data for 616-2 panel skin bays.....54

30. Exterior view of failed section of panel 616-1.....56

31. Interior view of failed section of panel 616-1.....57

32. Stringer 3 strain-gage data for panel 616-2.....58

33. Load end-shortening response curve for panel 617-1.....59

34. Strain-gage data for 617-1 panel skin bays.....60

35. Stringer attach flange strain-gage data for panel 617-162

36. Exterior view of failed section of panel 617-1.....63

37. Interior view of failed section of panel 617-1.....64

38. Interior view of failed section of panel 617-2.....64

39. Load-end shortening response curves for all test panels66

40. Analysis panel configurations.....70

41. Stiffener configurations for PANDA2 analysis73

42. Smearred-stiffener finite element model.....78

43. Linear eigenmodes and buckling loads for smearred-stiffener model79

44. Load-shortening curve for perfect single-stiffener repeating section model with smeared-stiffener properties.....	80
45. Failure shapes from nonlinear analyses for smeared-stiffener section model with and without geometric imperfection	81
46. Load-shortening curves for single-stiffener repeating section model with globally-smeared stiffener properties.....	82
47. Linear eigenmodes and buckling loads for smeared-stiffener model where stiffener properties are smeared locally over stiffener region.....	83
48. First four eigenmodes and buckling loads for the locally smeared-stiffener section calculated from a nonlinear equilibrium state.....	84
49. Load-shortening curves for single-stiffener repeating section model with locally smeared-stiffener properties.....	85
50. Discrete stiffener finite element model	87
51. STAGS rectangular subelement stiffener definition	87
52. First four eigenmodes and buckling loads for the discrete beam model calculated from a nonlinear equilibrium state	88
53. Load-shortening curve for single-stiffener repeating section model with discrete beam stiffener	90
54. Load-shortening curve for single-stiffener repeating section model with discrete beam stiffener for elastic and elasto-plastic materials.....	91
55. Plastic deformation of section with discrete beam stiffener.....	92
56. STAGS branched-shell bonded stiffener model.....	93
57. First four eigenmodes and buckling loads for the bonded-stiffener model calculated from a nonlinear equilibrium state	94
58. Deformed shapes at the failure load for the bonded-stiffener model	96
59. Load-shortening curve for single-stiffener repeating section of branched-shell bonded-stiffener model.....	97
60. First four eigenmodes and buckling loads for the riveted-stiffener model calculated from a nonlinear equilibrium state	99

61. Deformed shapes at failure loads for the riveted-stiffener model	100
62. Load-shortening curve for single-stiffener repeating section of branched-shell riveted-stiffener model	101
63. Elastic three-stiffener repeating section model failure shape for globally smeared-stiffener approach	103
64. Load-shortening curves for elastic single- and three-stiffener repeating section models with locally and globally smeared stiffener properties	105
65. Elastic three-stiffener repeating section model failure shape for locally smeared-stiffener approach	106
66. Load-shortening curves for single- and three-stiffener repeating section models with discrete stiffeners and initial imperfections	107
67. Elastic three-stiffener repeating section buckling and failure shapes for discrete-stiffener approach	108
68. Elasto-plastic three-stiffener repeating section model failure shape for discrete-stiffener approach	109
69. Load-shortening curves for single- and three-stiffener repeating section models (bonded-stiffener branched-shell) with initial imperfections	110
70. Elastic three-stiffener repeating section model failure shape for bonded-stiffener branched-shell approach	111
71. Center hat-stiffener deformed shapes for elastic bonded-stiffener branched-shell modeling approach	112
72. Elasto-plastic three-stiffener repeating section model failure shape for bonded-stiffener branched-shell approach	113
73. Load-shortening curves for single- and three-stiffener repeating section models (riveted-stiffener branched-shell) with initial imperfections	114
74. Elastic three-stiffener repeating section model failure shape for riveted-stiffener branched-shell approach	115
75. Elasto-plastic three-stiffener repeating section model failure shape for riveted-stiffener branched-shell approach	116
76. Load-shortening curves for single-stiffener repeating section model with elastic material properties	121

77. Load-shortening curves for three-stiffener repeating section model with elastic material properties.....	121
78. Load-shortening curves for single-stiffener repeating section model with elasto-plastic material properties.....	122
79. Load-shortening curves for three-stiffener repeating section model with elasto-plastic material properties.....	123
80. Finite element models for 614 panel configuration.....	130
81. Panel 614 first buckling mode shape.....	131
82. Nonlinear buckling mode shape for 614 panel.....	132
83. Load vs. end-shortening response for perfect and imperfect 614 panel.....	134
84. Skin buckling sequence for panel 614 configuration	136
85. Deformed shape of 614 panel configuration at failure.....	137
86. Single-bay model failures for 614 panel configuration.....	139
87. Deformed shape of 615 panel configuration at predicted failure load of 45,621 lb.....	141
88. Single-bay model failures for 615 panel configuration.....	143
89. Deformed shape of 616 panel configuration at failure.....	145
90. Single bay model failures for 616 panel configuration	147
91. Panel 617 configuration finite element model	149
92. Deformed shape of 617 panel configuration at failure.....	150
93. Single bay model failures for 617 panel configuration	151
94. Stringer imperfection shape for 614 panel configuration.....	155
95. Load-shortening curves for the 614 panel configuration with imperfections	156
96. Baseline and adjusted failure loads for the 614 panel configuration	157
97. Finite element model of stringer with attached gusset	159

98. Effective stringer length for Euler-column failure calculations as a function of stringer and gusset geometry162

SECTION 1

INTRODUCTION

1.1 Background and Motivation

The majority of all conventional aircraft structures are made using stiffened panel construction. For some aircraft components, such as frame webs, buckling is not allowed and is therefore considered the failure load of the structure. However, for most stiffened panel sections of an aircraft, there is an acceptable level of buckling that is allowed to occur at some load level prior to ultimate load. Therefore, analysis methods are required not only to predict the buckling load of a metallic stiffened panel, but also to predict the ultimate failure load of the panel. Because weight is a primary consideration in aircraft design, the accuracy of structural analysis tools is important so that unnecessary weight is not added to the aircraft structure. Having a robust predictive capability also provides a better understanding of damage tolerance design issues which affect inspection intervals which affect operation cost. In order to assess the accuracy of its primary stiffened panel analysis code, PAGE, Gulfstream Aerospace Corporation conducted a series of compression tests on metallic curved stiffened panels. These panels are representative of four general structural configurations on the Gulfstream V business jet fuselage. The tests were conducted at the National Aerospace Laboratory in Amsterdam, the Netherlands. Results of the panel tests showed that the PAGE analysis tool predicted the failure loads of all the test panels conservatively. However, for certain failure modes, the conservatism in the prediction led to the design of a panel that was unnecessarily heavy.

Journal model used for dissertation format is *International Journal of Solids and Structures*.

An investigation was undertaken to identify the source of the conservatism and recommend a way to improve the analysis method so that the next generation of Gulfstream aircraft could be designed in the most efficient and lightweight manner possible. The results of this investigation are presented herein.

1.2 Literature Review

Early work in shell stability considered the elastic behavior of unstiffened isotropic cylindrical shells. Donnell (1934) proposed a method based on the classical theory of elasticity to predict the buckling loads of thin cylinders with large radii under axial compression and bending. Von Karman and Tsien (1941) studied the effects on initial geometric imperfections on the buckling loads of thin cylindrical shells subject to axial compression. In his Ph. D. thesis, Koiter (1946), developed the theory of elastic buckling and post-buckling behavior, studied the effect of initial geometric imperfections on buckling, and applied this theory to columns, plates and shells. Leggett (1937) first tackled the problem of shear buckling of cylindrical shells. His study was limited to cases when the shell curvature was small. Later, Kromm (1939) investigated cylindrical panels with larger curvature subject to combined axial compression and shear loads using the energy approach and the Ritz method. However these solutions are for the unstiffened elastic shell only. Batdorf, Schildcrout, and Stein (1947b) provided initial buckling solutions for long curved panels subject to shear and either axial or transverse loads using the Galerkin method to solve the differential equations of equilibrium. Schildcrout and Stein (1949) later proposed a buckling solution for finite curved panels subjected to shear loading using a semi-empirical method. The design curves derived

from their work are used extensively in the fuselage design guidebooks by Gerard and Becker (1957) and Bruhn (1973).

Melcon and Ensrud (1953) used empirically based equations to create a mathematical model for determining the buckling load of isotropic curved panels with longitudinal stiffeners and subject to shear and compression loading. Baruch and Singer (1963) investigated the effects of the eccentricity of stiffeners on the instability of isotropic cylindrical shells subject to hydrostatic pressure. They examined a full cylindrical shell with stringers and rings on both the shell exterior and interior surfaces. They concluded that cylinders with internally-attached rings usually showed a significant increase in buckling load over cylinders with the same ring arrangement attached externally. However, the effect was opposite for stringers in that cylinders with externally-attached stringers showed an increase in buckling load over cylinders with internally-attached stringers. Weller and Singer (1971) conducted an experimental study of integrally stiffened cylindrical shells subject to axial compression to determine the applicability of linear shell theory. They concluded that the level of agreement between experimental results and linear shell theory was based on the ratio of stringer cross-sectional area to the product of stringer spacing and skin thickness. They found that linear theory was most applicable to thin shells with hefty closely-spaced stringers. Yang and Kunoo (1977) did an extensive analytical study of the buckling loads of orthogonally stiffened cylindrical shells subject to axial compression and external pressure. They used a total potential energy approach based on the Ritz iteration method combined with the Chebyshev procedure for their analysis. Their analysis proved to be more efficient at calculating

buckling loads than the Ritz method used alone. The results obtained from their analysis were compared with experimental results and showed good agreement for external pressure loading; however for the case of axial compression, the agreement between their analysis and experimental results was poor.

Early in the 1970's, research began on the buckling of composite panels. Loendorf, Sobieszczanski, and Stroud (1973) presented a design study of fuselage structure with metallic skins and either metallic or composite frames and stringers. Loads were obtained from a finite element program and a nonlinear mathematical programming technique was used for sizing. The structure was analyzed for general buckling, local buckling, and material yield. Viswanathan, Tamekuni, and Baker (1974) analyzed unstiffened long curved anisotropic panels subjected to combined inplane loads. Zhang and Matthews (1984) and Whitney (1984) used different methods to analyze unstiffened curved anisotropic panels under combined compression and shear. More recently Jaunky and Knight (1999) conducted an assessment of shell theories for the buckling of cylindrical laminated composite shells loaded in compression. The theories examined were those of Sanders-Koiter, Love, and Donnell. The accuracy of the theories was assessed using finite element models. It was shown that the Sanders-Koiter and Love theories showed good agreement with finite element results. The comparison also indicated that Donnell's theory could be in error for some geometrical parameters and degrees of anisotropy. It was theorized that inaccuracies in Donnell's theory were a result of neglecting the transverse shearing force in the equilibrium equations in the circumferential direction. Starnes, Hilburger, and Nemeth (2000) conducted an analytical

and experimental study on the effects of imperfections on the compression buckling of composite cylindrical shells with and without a cutout. They concluded that generalized imperfections (variations in surface shape, thickness, end conditions, and eccentricities) can have significant influences on achieving test and analysis correlation. Domb (2002) presented similar results for the buckling of curved anisotropic panels with imperfections and subjected to both shear and compression loading.

Over the past twenty years significant work has been done in the area of postbuckling and failure analyses of curved panels. In 1987 Arnold and Parekh (1987) presented results for the buckling, postbuckling, and failure of edge-stiffened composite shallow-curved panels subject to axial compression and shear loading. Failure modes included stiffener disbonding and panel crippling due to exceeding fiber strain allowables. Minnetyan, Rivers, Murthy, and Chamis (1992) predicted ply damage leading to failure of stiffened composite shells subject to axial loads, shear, and internal pressure. Collier, Yarrington, and Van West (2002) presented a postbuckling analysis for grid-stiffened curved panels subject to axial loads, shear, and bending moments. The analysis was performed using the Hypersizer design tool discussed in Appendix A. Several failure modes were analyzed such as stiffener local buckling and crippling, web buckling, and exceedence of maximum strain allowables. The analysis was verified through comparisons to finite element models and experimental data. Similar optimization results were presented by Lamberti, Venkataraman, Haftka, and Johnson (2003) using the PANDA2 code also described in Appendix A. The propellant tank of a reusable launch vehicle was optimized, and several design configurations were considered including metallic and

composite materials, honeycomb sandwich construction, stringer-ring configurations, orthogrid and isogrid-stiffened, and corrugated panels. Internal and external stringers and rings were considered, and the effects of imperfections were included.

1.3 Objectives

The first part of this work is to investigate several available methodologies for predicting the buckling, postbuckling, and ultimate failure loads of stiffened fuselage panel structures and to determine the most accurate and efficient methods for predicting each type of failure mode observed in aircraft fuselage structures. This evaluation will identify the closed-form solutions that provide high-fidelity failure predictions and can therefore be included in a preliminary design tool to be used with confidence. Certain failure modes may be determined that can only be predicted through more computationally demanding analysis methods. This research work will distinguish those failure modes that can be incorporated into an efficient preliminary design code from those failure modes that can only be predicted through a detailed analysis tool such as finite element analyses.

The results of the evaluation will be used to propose improvements to the preliminary design and analysis tools for stiffened fuselage panels accounting for local failure. Current analysis tools predict Euler-column buckling with great accuracy but are conservative by as much as 50% when predicting skin wrinkling and local stringer buckling failures. This conservatism translates into a significant weight penalty. Methods for less conservative failure prediction for some failure modes will be

recommended as updates to current methods, and those failure modes that have been identified as needing more detailed analysis will be investigated using finite element analysis. Using the preliminary design tool in conjunction with finite element analyses only where necessary will lead to the ultimate goal of having a hybrid preliminary design and analysis process that predicts failure modes accurately and is computationally efficient.

1.4 Scope

This investigation will focus on metallic structures. Composite materials will not be addressed. While the use of composites in aircraft design is increasing, the majority of today's business jet fuselage structure designs are metallic. The stiffened panels will include both axial and circumferential stiffeners that are either bonded or mechanically fastened to the panel skin. The circumferential stiffeners (frames) will be Z-shaped, and the axial stiffeners (stringers) will be either open- or closed-hat sections. Doublers bonded to the skin will be included and are located either under frames, under stringers, or over the entire skin panel. The only loading condition considered for this study will be compression loading.

1.5 Roadmap

The remainder of the document is organized as follows. Section 2 gives an overview of the standard methodology used in the aircraft industry for the fuselage stiffened panel design cycle. Section 3 presents the results of the experimental study undertaken by Gulfstream to validate its internal methodology for analyzing the Gulfstream V stiffened

fuselage panels. Section 4 presents an extensive assessment of three stiffened panel analytical tools with varying levels of efficiency and accuracy and compares the analytical results with experimental results for one of the test panels described in Section 3. Section 5 presents a comparison of the failure prediction capability of the closed-form analysis code PAGE and the nonlinear finite element code STAGS, both described in Section 4. The comparison is accomplished by using both analytical tools to predict the buckling and failure loads for all four of the stiffened fuselage panels tested by Gulfstream and described in Section 3. Conclusions and recommendations for future aircraft design methodology are given in Section 6. Appendix A presents a review of several selected stiffened panel analysis tools, and Appendix B presents all of the strain gage data for the Gulfstream test panels.

SECTION 2

METHODOLOGY FOR STIFFENED FUSELAGE PANEL DESIGN

2.1 Stiffened Panel Geometry and Loading

Stiffened panels are utilized in aircraft structural design to maximize stiffness and strength while minimizing the amount of material required to meet design requirements and thereby minimizing structural weight. A simple representation of a stiffened fuselage panel is shown in Figure 1. It is essentially an orthogonally stiffened cylindrical panel that exhibits skin-thickness variations over the panel surface.

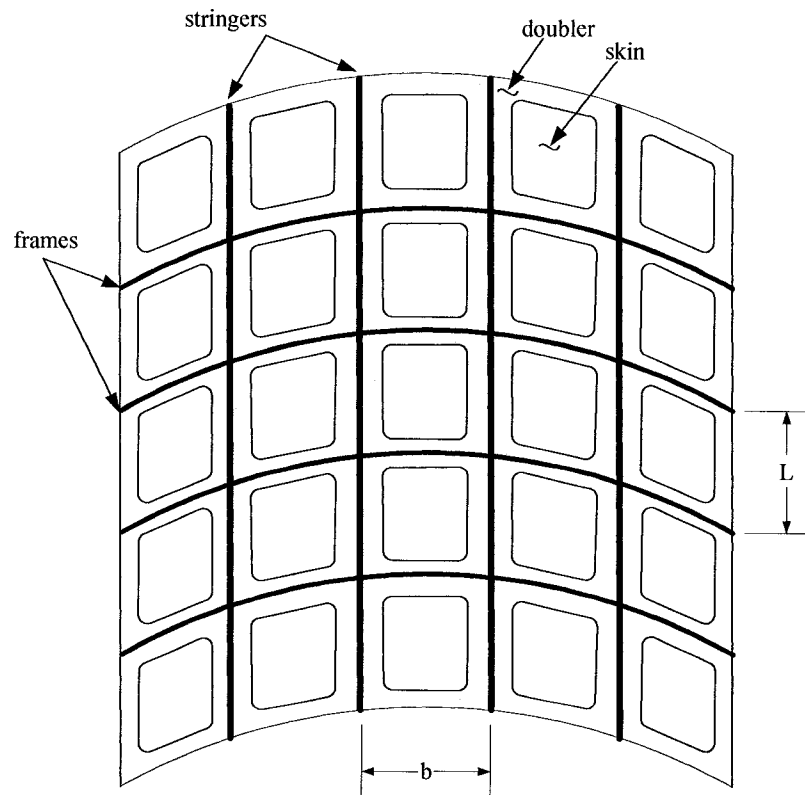


Figure 1. Stiffened panel geometry

The stiffened panel consists of a relatively thin skin supported in the longitudinal and/or transverse directions by equally spaced stiffeners. In the context of fuselage design, the stiffeners in the longitudinal direction are referred to as stringers, and stiffeners in the transverse or hoop direction are called frames. Stringer spacing will be denoted with a 'b', and frame spacing will be denoted with an 'L' as shown on Figure 1. Stiffeners can be either fastened to the skin panel mechanically using rivets or bolts, bonded to the panel, or integrally machined into the panel during fabrication. Typical stiffener cross-sections are shown in Figure 2.

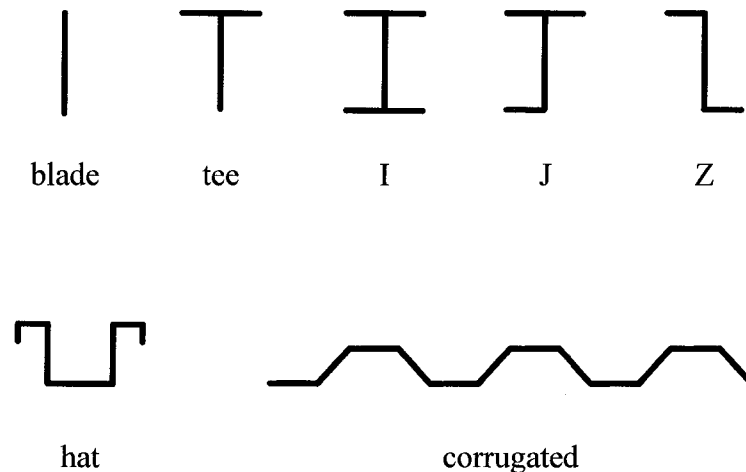


Figure 2. Typical stiffener cross-sections

Doublers can be integrally machined into the skin or attached to the skin to provide extra strength and/or to provide protection against growing cracks when the doubler is mechanically fastened to the skin. Doublers are thin sheets of material that can extend over the entire skin or can be limited to an area directly underneath the stiffeners. The doubler regions, shown in Figure 1, are limited to the areas underneath the frames and

stringers. This doubler configuration is referred to as a “waffle” doubler because of its appearance.

The loads most commonly associated with stiffened fuselage panels are in-plane forces and moments, pressure load applied normal to the panel skin, temperature loading, and enforced displacements. The in-plane forces and moments representing the positive sign convention are shown in Figure 3. Enforced displacements are applied in the same direction as the in-plane forces.

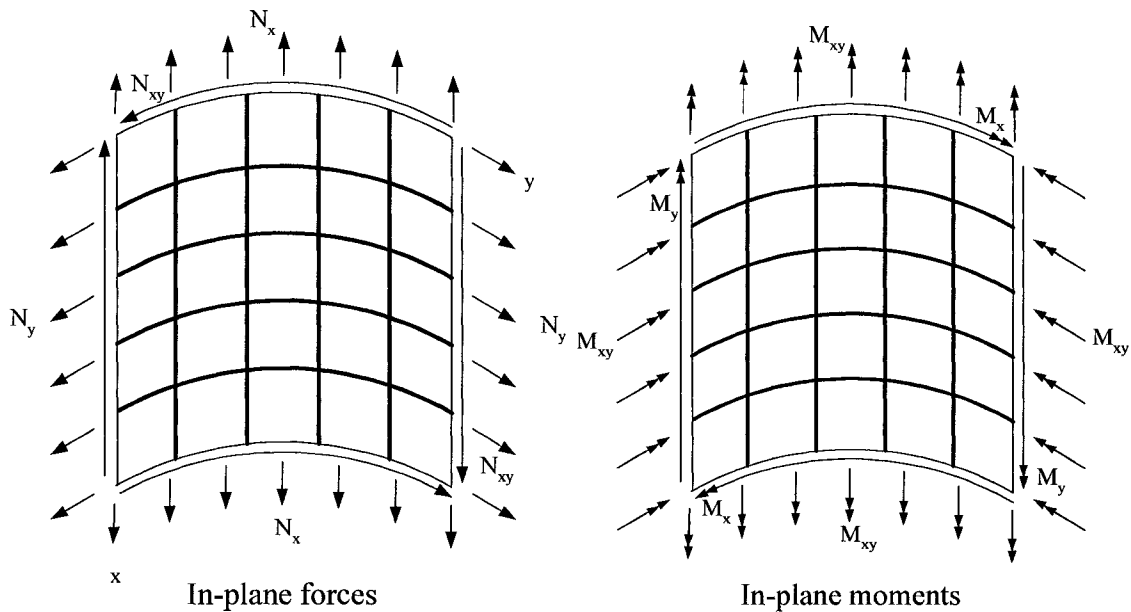


Figure 3. In-plane forces and moments applied to panel

2.2 Design Requirements for Stiffened Panels

The main goal in fuselage stiffened panel design is to create a structure that satisfies the strength criteria at a given load level and does so at the minimum weight possible.

Strength requirements are usually applied at two load levels: limit load and ultimate load.

Limit load is defined as the maximum load an aircraft will experience in its lifetime. Ultimate load is some factor of limit load that provides a comfortable safety factor to account for uncertainties in load and strength calculations. Currently in the commercial side of the aerospace industry, this factor is typically taken to be 1.5 times limit load. At limit load, no structural components must experience any permanent deformation caused by material yielding. The skin panels are allowed to buckle prior to limit load, and the load redistribution is taken into account for adjacent structure. Permanent deformation is allowed to occur at ultimate load, but the overall structure must be able to sustain ultimate load without catastrophic failure. Catastrophic failure is defined as the loss of all load carrying capability.

Characteristics other than strength and weight are considered in fuselage stiffened panel design. Fatigue and crack-growth analyses must be performed to insure that the panel will remain intact over the life of the airplane, or that any cracks present in the panel will grow slowly enough to be detected at regular inspection intervals. The results of these damage tolerance analyses directly determine the inspection interval. Should damage occur, repairs need to be easily designed and applied to the structure. Material considerations include cost, fracture toughness, compatibility with other materials, availability of a statistical material properties database, susceptibility to corrosion, and for some applications, high-temperature material properties are required. Ease of assembly of the panel is important to reduce manufacturing cost. For example, bonded stiffeners are sometimes preferred over mechanically fastened stiffeners due to the amount of labor required for fastener installation. All of these diverse issues must be

considered when designing fuselage structure; therefore, it is important to have rapid structural analysis tools for preliminary design as well as more advanced structural analysis tools for final design evaluation.

2.3 Global and Local Failure Modes for Stiffened Fuselage Panels

Stiffened fuselage panels exhibit several modes of failure including global panel failures, local stiffener failures, and local skin-panel failures. The load at which a global panel failure occurs always constitutes the maximum load-carrying capability of the panel. However, the buckling load associated with a local failure mode may or may not be considered the maximum allowable panel load, depending on the design criteria for that structural element. For example, local skin buckling in the elastic range of a material is not considered to be a failure load for most fuselage applications; however, local skin buckling of wing covers is not usually allowed due to aerodynamic constraints. In this section, both global and local failure modes are discussed. Whether or not local failures are used to define the ultimate failure load of the panel is left up to the aircraft designer. Three failure modes are considered for the skin between stiffeners: local skin buckling, skin crippling, and skin wrinkling.

Local skin buckling occurs when the skin between stiffeners buckles elastically, and the stiffeners are not affected by the skin deformation as shown in Figures 4 and 5(a).



Figure 4. Local skin buckling mode for hat-stiffened panel

Typically these local-skin buckling modes exhibit buckle halfwaves on the order of the stiffener spacing and are often referred to as short-wavelength buckles. Local skin buckling usually does not lead to the overall failure of the panel, but it does reduce the stiffness of the panel as load is redistributed to the stiffeners. Analysis methods that extend into the postbuckling range must account for the redistribution of load resulting from the locally buckled skin panels. When the local buckling of the skin becomes severe enough to cause plastic deformation of the skin, it is referred to as skin crippling. The load at which crippling occurs is usually considered to be the overall failure load of the panel. When the local buckles in the skin run across the stiffeners and extend into adjacent skin bays, it is referred to as skin wrinkling. Skin wrinkling can distort the attachment flanges of the stiffeners and lead to an overall strength failure of the panel. Typically these buckling modes exhibit buckle halfwaves on the order of the overall panel dimensions or long-wavelength buckles.

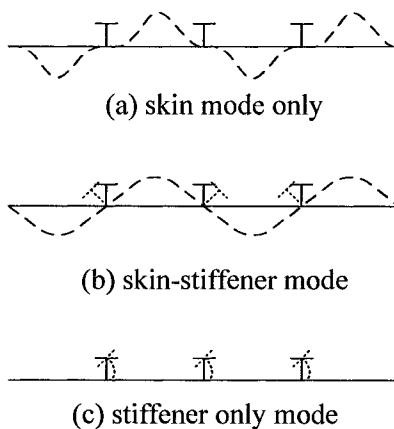


Figure 5. Typical buckling modes for stiffened panels – cross-sectional view (solid line is original geometry; dashed line represents buckling mode shape)

Skin-stiffener failure modes occur when the stiffeners roll with the skin as it buckles, as shown in Figure 5(b). Stiffener rolling can contribute to stiffener torsional buckling resulting from the twisting of the stiffener along its length while the cross-section remains rigid. Flexural-torsional buckling is a combination of stiffener twisting and bending out of plane. Possible distorted stiffener cross-sections are shown in Figure 6 for the torsional buckling modes.

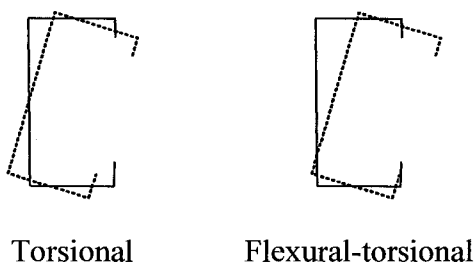


Figure 6. Stiffener torsional buckling modes (Lamberti et al., 2003)

Another skin-stiffener failure mode occurs if the forces imposed on the stiffener flange by the skin cause the allowable bending stress of the flange to be exceeded, resulting in

the overall failure of the stiffener. This failure mode is known as forced crippling of the stiffener.

Stiffener-only local failure modes are possible as shown in Figure 5(c). Stiffener local buckling occurs when the buckling stress of a single element (flange or web) of the stiffener is exceeded. Each element of the stiffener cross-section is considered individually with boundary conditions imposed according to whether a side is free or attached to an adjacent element. The failure extends across the entire element of the stiffener, but the stiffener element edges remain in the same position. Local buckling of the stiffener results in a waviness of the web or flange as shown in Figure 7 for different stiffener local buckling failure modes.

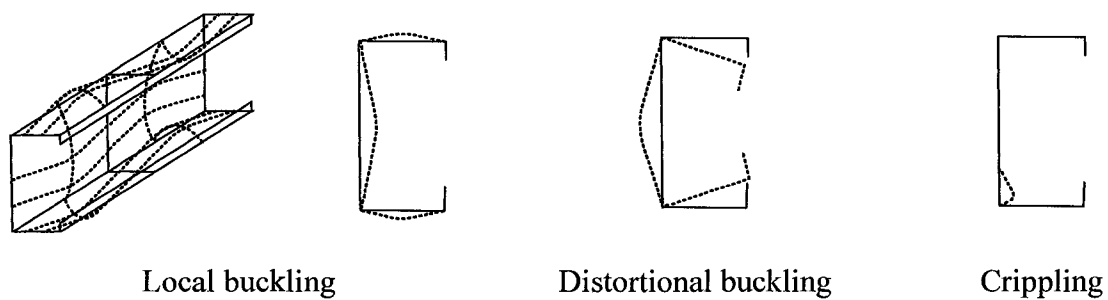


Figure 7. Stiffener buckling failure modes (Lamberti et al., 2003)

Distortional buckling of the stiffener cross-section is defined as a rotation of the flange at the flange/web junction as shown in the middle of Figure 7. In this case, some stiffener element edges move from their original position. The localized buckling of a stiffener

element immediately adjacent to a loaded flange is referred to as stiffener crippling and is shown on the right side of Figure 7.

The overall buckling of a skin-stiffener section is referred to as Euler-column buckling. The Euler-column buckling mode is an overall failure mode for the panel. The Euler-column buckling load is a theoretical critical compressive load that causes infinite deflection of the stiffener. This load is the ultimate strength of a column in compression. The equation derived by Euler is:

$$P_{cr} = \frac{k\pi^2 EI}{L^2}$$

where:

- P_{cr} is the critical Euler buckling load
- E is the modulus of elasticity
- I is the moment of inertia of the column
- L is the column length
- k is a constant that depends on column end conditions

Before P_{cr} is reached, some yielding in the material will often occur and the actual maximum panel load will be less than the critical Euler buckling load, P_{cr} . If the column is not perfectly straight, the failure load will be less than the Euler load; however, for design purposes, the Euler-buckling load can be considered the maximum axial load that can be carried by the stiffener. A Euler-buckling failure mode shape is shown in Figure 8.

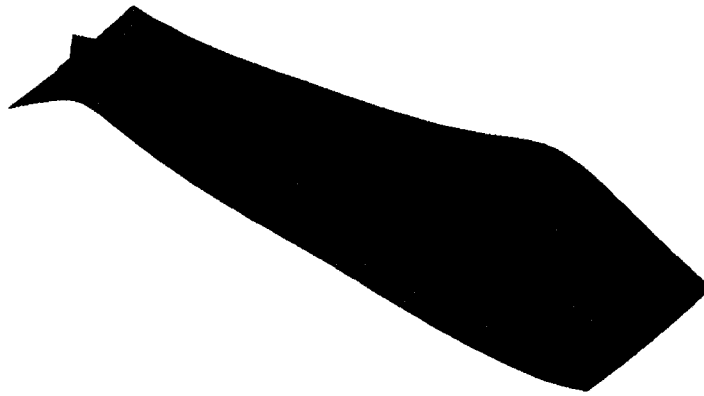


Figure 8. Euler-column skin/stringer failure mode for tee-stiffened panel

Other stiffened panel failure modes include material yielding, fastener failure for mechanically fastened stiffened panels, and skin/stiffener separation in bonded panels. As each failure model is understood and the design process accounts for them, new modes of failure are often discovered as the loading level increases. As a result, the analysis tools must be continually sharpened and updated.

2.4 Levels of Analysis

Different levels of analysis are required to accomplish the varied tasks in the aircraft stiffened panel design cycle. In the preliminary design phase, stiffened panel design optimizations are performed based on initial load and weight estimates. Simple, efficient structural analysis methods such as closed-form and Rayleigh-Ritz solutions are desired at this stage of design so that a large number of panel configurations can be analyzed and optimized in a short period of time. These low-fidelity methods do not capture localized stiffener failures or skin/stiffener interaction effects well and are often limited in their range of application. However, these methods are useful for trade studies and conceptual

studies. Once aircraft loads are refined and the number of stiffened panel design configurations has narrowed in scope, structural analysis methods with increased fidelity such as finite strip, finite element, or finite difference analyses are performed to provide more detailed results and ensure a safer, more robust structure. A summary of three levels of stiffened fuselage panel analysis used in aircraft structural design follows.

2.4.1 Closed-Form and Rayleigh-Ritz Solution Methods

Simple analytical models are used to predict individual failure modes such as column buckling, local stiffener buckling, skin-panel buckling, stiffener crippling, and skin crippling. Often closed-form solutions from handbooks such as Young (1989) are used. These models approximate the response of the stiffened panels and often are empirical in nature. Smearing stiffener analyses are sometimes incorporated into the closed-form solution category. For this approach, the stiffened structure is replaced by an unstiffened shell with an equivalent orthotropic stiffness. The closed-form solutions are good for preliminary design because the predicted results are generally conservative, the computational cost is minimal, and the analyses are readily amenable to optimization procedures. The hat-stiffened panel analysis code PAGE (Piurkowski, 1992) is an example of a preliminary design tool that uses closed-form solutions exclusively to predict stiffened panel behavior. Strict limitations are put on panel geometry, boundary conditions, and loading conditions to fit within the scope of the closed-form solutions. Multi-fidelity codes such as PANDA2 (Bushnell, 1987a & b) and Hypersizer (Collier et al., 1999) use closed-form solutions to perform initial calculations for optimization purposes, and then use higher fidelity methods to predict more accurately the response of

a narrowed field of stiffened panel designs. Such approaches are examples of hybrid design methodologies that exploit the features of different methods to achieve a robust design.

Rayleigh-Ritz solutions are often used in conjunction with closed-form solutions for preliminary design tools because they provide reasonable results at a low computational cost. These solutions represent the buckling mode displacements u , v , and w as Rayleigh-Ritz expansions. The potential energy is minimized to determine the critical load factor for a range of feasible wavelengths. Smearred-stiffener analyses can also be performed using Rayleigh-Ritz methods to simplify the analyses. POSTOP (Batdorf et al., 1947a & b), PANDA2, and Hypersizer all employ Rayleigh-Ritz solutions to predict some of their failure modes.

2.4.2 Finite Strip Analysis Methods

Finite strip analysis methods bridge the gap between low-fidelity closed-form analysis and the higher fidelity finite element and finite difference analyses. Finite strip analyses model a stiffened panel as an assembly of plates or shells. Equations are formulated and solved for each strip and interfaces between strips are matched. The equations for each strip can be solved exactly or approximated with assumed displacement functions depending on the boundary conditions. The assumed displacement functions allow for a continuous buckle pattern along plate junctures. This type of analysis provides more detailed information about stiffener/skin interaction than the closed-form solutions. PASCO (Stroud and Anderson, 1980), PAGE, VICON (Loendorf et al., 1973), and

PANDA2 all employ finite strip analyses for some of their buckling and/or failure calculations. PASCO and VICON are limited to elastic buckling predictions.

2.4.3 Finite Element and Finite Difference Analysis Methods

Finite element and finite difference analysis methods are necessary to model the local details of a stiffened panel and its nonlinear response. The fidelity and computational efficiency of finite element and finite difference methods are determined by the amount of detail the analyst includes in the discrete model. Simple, efficient models using smeared stiffener properties or a coarse mesh can be created for a limited range of applicability. Finite element and finite difference methods are often used to generate high-fidelity models of the stiffened fuselage panel to interrogate possible local failure modes and complex nonlinear behavior. These high-fidelity models may offer the most accurate results; however, they are also generally computationally intensive problems.

A variety of loading conditions including in-plane loads, normal pressures, temperature, and enforced displacements can be included. Loads can be defined to vary across an edge or surface. Boundary conditions can be defined individually for each degree of freedom and are not locked into simple support, clamped, or free conditions along entire edges as with many closed-form solutions. Many finite element codes have the ability to model fastener connections and contact between surfaces. Measured or approximated initial geometric imperfections (i.e., surface imperfections and/or thickness variations) can also be included, as well as material plasticity. Nonlinear material and geometric modeling capabilities allow the postbuckled path to be predicted more accurately than

with closed-form or finite strip methods. STAGS (Brogan et al., 1994), MSC NASTRAN (Anonymous, 1970), and HKS/ABAQUS (Anonymous, 1994) are representative finite element analysis codes often applied to this class of problems. However, while general-purpose finite element codes like NASTRAN and ABAQUS provide extensive features and capabilities, STAGS has been developed for aerospace structural applications, especially stiffened panel buckling and postbuckling response predictions.

2.5 Representative Analysis Tools

Several computational tools are available to predict the structural response of stiffened fuselage panels found in aircraft structures. These analysis methods vary in capabilities and computational efficiency. Many of these analysis tools are tied to structural sizing computer codes. These methods range from simple elastic buckling codes to extensive finite element codes which include both geometric and material nonlinearity. A hierarchical overview of a representative group of stiffened panel analysis tools is presented in Appendix A. The selected set of structural analysis tools for the present study includes PASCO, POSTOP, PAGE, PANDA2, STAGS, and Hypersizer. The overview presented in Appendix A describes geometric and material limitations, loading capability, available failure modes, theoretical approach, analysis fidelity, and computational effort. A general summary of the codes discussed in Appendix A is shown in Table 1.

		Analysis Codes					
		PASCO	POSTOP	PAGE	PANDA2	STAGS	Hypersizer
Theory	closed-form	✓	✓	✓	✓		✓
	Rayleigh-Ritz		✓		✓		✓
	finite strip	✓		✓	✓		
	finite difference				✓		
	finite element				✓ (1)	✓	✓ (2)
Geometry	flat	✓	✓	✓	✓	✓	✓
	curved	✓ (3)		✓	✓	✓ (3)	✓
	longitudinal	✓	✓	✓	✓	✓	✓
	transverse			✓	✓	✓	✓
	skewed					✓	✓
	imperfections	✓	✓		✓	✓	✓
	fasteners			✓		✓	
	contact					✓	
Boundary Conditions	free	✓				✓	✓
	simple support	✓	✓	✓	✓	✓	✓
	clamped	✓		✓		✓	✓
	symmetry	✓				✓	✓
Longitudinal Edges	free					✓	✓
	simple support	✓	✓	✓	✓	✓	✓
	clamped			✓	✓	✓	✓
	symmetry					✓	✓
Transverse Edges	free					✓	✓
	simple support	✓	✓	✓	✓	✓	✓
	clamped			✓	✓	✓	✓
	symmetry					✓	✓
Loading Conditions	Nx (longitudinal)	✓	✓	✓	✓	✓	✓
	Ny	✓	✓		✓	✓	✓
	Nxy	✓	✓	✓	✓	✓	✓
	Mx	✓			✓	✓	✓
	My				✓	✓	✓
	Mxy					✓	✓
	temperature	✓	✓		✓	✓	✓
	pressure	✓	✓		✓	✓	✓
	enforced displacement					✓	✓
Material	isotropic	✓	✓	✓	✓	✓	✓
	specially orthotropic		✓		✓	✓	✓
	orthotropic	✓			✓	✓	✓
	anisotropic				✓	✓	✓
	sandwich construction				✓	✓	✓
	linear elastic	✓	✓	✓	✓	✓	✓
	nonlinear elastic				✓	✓	✓
Failure	plastic				✓ (4)	✓	✓
	skin buckling	✓	✓	✓	✓	✓	✓
	material yield	✓	✓	✓	✓	✓	✓
	cripling			✓	✓	✓	✓
	Euler-column buckling		✓	✓	✓	✓	✓
	stiffener local buckling	✓	✓	✓		✓	✓
	stiffener rolling		✓		✓	✓	
	stiffener torsional buckling		✓			✓	
	skin/stiffener separation		✓			✓	✓
	fastener failure			✓		✓	✓
sandwich failures				✓	✓	✓	
Model Fidelity		low	low	low	low→med	high	low→high
Computational Cost		low	low	low	low→med	low→high	low→high

(1) Program creates STAGS input deck

(4) Plasticity is only allowed for isotropic materials

(2) Program creates STAGS input and imports loads from STAGS output

(3) Curved panel can be approximated by an assembly of flat plates

Table 1. Representative panel analysis codes

2.6 Current Analysis Effort

The current analysis effort consists of an evaluation of different types of solutions for the failure prediction of stiffened fuselage panels. Three structural analysis tools are chosen to perform the failure analyses of four fuselage panels that are tested under compression loading. The tools used to predict the failure of the panels are PAGE, PANDA2, and STAGS. PAGE uses closed-form equations and finite strip analyses to predict failure. This structural design tool is limited to certain types of panel geometries and is designed to give conservative failure estimates. PANDA2 is a higher fidelity structural design tool than PAGE and includes closed-form equations, Rayleigh-Ritz approximations, finite strip, and finite difference methods in its solution strategy. STAGS is a finite element analysis tool and has the capability to model the panels in the greatest detail, and has the potential to predict the most accurate failure loads, provided the finite element models include sufficient detail. The level of detail required to predict failure accurately with STAGS will also be explored. Finite element models ranging from a single skin-stringer bay to a complete or full-size test panel will be developed and analyzed. The effects of model fidelity for the stiffener, method of stiffener attachment, and inclusion of material nonlinearity or failure load prediction will be examined.

SECTION 3

EXPERIMENTAL STUDIES

In order to demonstrate proof of structure for the Gulfstream V business jet fuselage, a series of tests were performed at the National Aerospace Laboratory in Amsterdam, the Netherlands (Simmons, 2000). Tests were conducted on metallic curved stiffened panels representative of four general structural configurations on the Gulfstream V business jet fuselage. The panels were designed and fabricated at Gulfstream Aerospace Corporation in Savannah, Georgia. A total of eight panels, two of each configuration, were tested in compression. A detailed description of the test panels, test set up, and the test results follows.

3.1 Geometry and Materials

The general test panel configuration is shown in Figure 9. All of the test panels have four frames and five hat-section stringers. They have an overall length of 43 inches, an arclength of 38 inches (46-degrees of arc), and a radius of 47 inches. The frame spacing, L , is 12 inches, and the center-to-center stringer spacing, b , is 7.55 inches. The frames and stringers are riveted together at each frame/stringer intersection. The rivets have a 0.125-in. diameter and are spaced 0.625 in. apart. On each side of the panel, there is an 0.032-inch-thick 2024-T3 aluminum skin doubler extending from the edge of the panel underneath the first stringer in the axial direction and underneath the first frame in the circumferential direction. The doubler stops at the inside edge of the stringer or frame shear tie. The height of the two outside stringers is reduced by the thickness of the

doubler. Gussets are located at each frame/stringer intersection along the axial edges of the test panel giving a total of eight gussets as indicated in Figure 9.

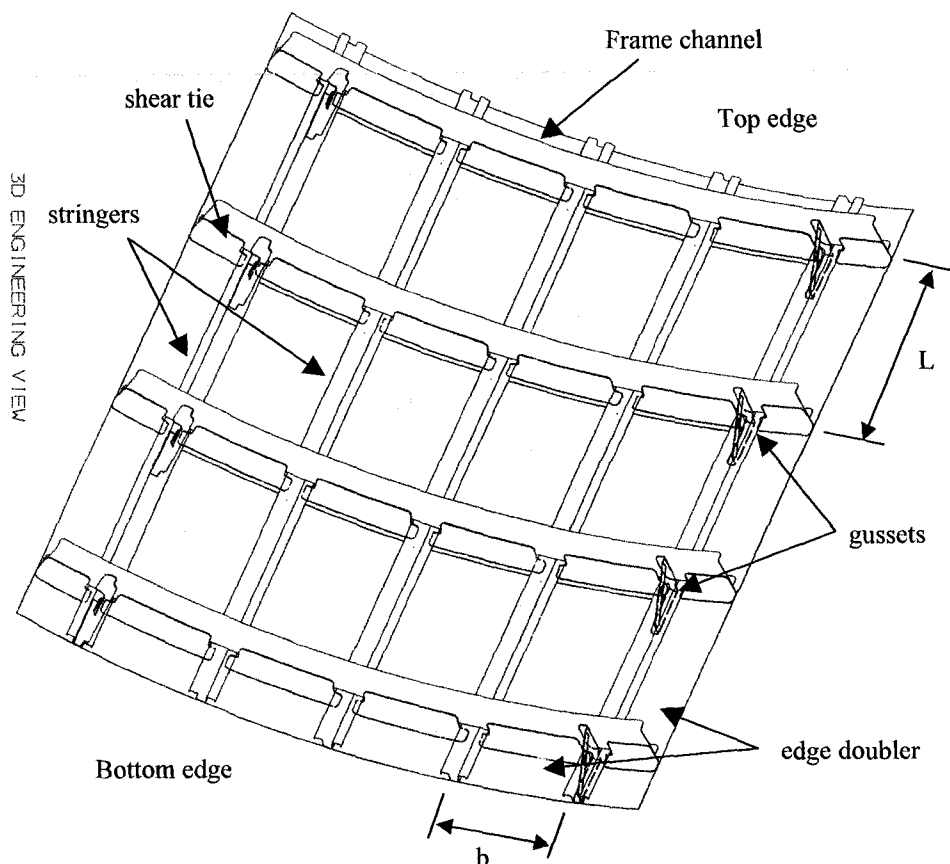


Figure 9. General test panel configuration

A summary of the four test panel configurations is shown in Table 2. The four test panel configurations, numbered 614, 615, 616, and 617, differ in their skin and stiffener material thicknesses, skin-doubler configuration, and orientation and attachment of the hat-section stringers. Panel 614 has a skin thickness of 0.04 inches, includes a doubler under the frames only, and has open hat stringers. Panel 615 has a skin thickness of 0.04 inches, has a waffle doubler that lies beneath the frames and stringers, and has open hat

stringers. Panel 616 has a skin thickness of 0.04 inches, includes a doubler over the entire skin, and has open hat stringers. Panel 617 has a skin thickness of 0.063 inches, does not have a doubler on the skin except at the panel edges, has inverted hat stringers, and has gussets at each frame/stringer intersection for a total of 20 gussets. All structural components (skins, doublers, frames, stringers, shear clips, and gussets) are fastened together with rivets. The relative weights of the panels, with respect to the lightest-weight baseline panel, 614, is also shown in Table 2.

	Test Panel Configuration			
	614	615	616	617
Skin thickness (in.)	0.04	0.04	0.04	0.063
Stringer thickness (in.)	0.025	0.025	0.063	0.025
Stringer orientation	open hat	open hat	open hat	inverted hat
Doubler location	under frames	under frames and stringers	over entire skin	none
Gussets	edges only	edges only	edges only	all frame/stringer intersections
Weight relative to baseline 614 panel	1.00	1.16	1.85	1.45

Table 2. Test panel configuration definition

The frame geometry, as shown in Figure 10, is the same for each panel. The frame consists of a channel connected to the panel skin by an angle shear tie. The values of the geometric properties for the frame, stringer, and doubler cross-sectional shapes that are held constant are shown in Figure 10 for each panel configuration along with labels for cross-sectional dimensions that vary (i.e., df , ds , s_1 , s_2 , s_3 , s_4 , and t_s). Specific values of these variables are tabulated in Table 3. The doubler widths, df for the frames and ds for the stringers, are also given in Table 3. For the case where the width of the doubler is equal to the frame or stringer spacing, the doubler is over the entire skin. For each panel, the skin and doublers are made from 2024-T3 clad aluminum. The stringers, frames, and

shear ties connecting the frame to the skin are made from 7075-T62 clad aluminum. The cross-section of the hat stiffeners is defined using the five geometric parameters (s_1 , s_2 , s_3 , s_4 , and t_s) shown in Figure 10. The doubler widths for the frames and stringers are defined by d_f and d_s , respectively, as indicated in Figure 10. All values are given in Table 3 and have values of inches.

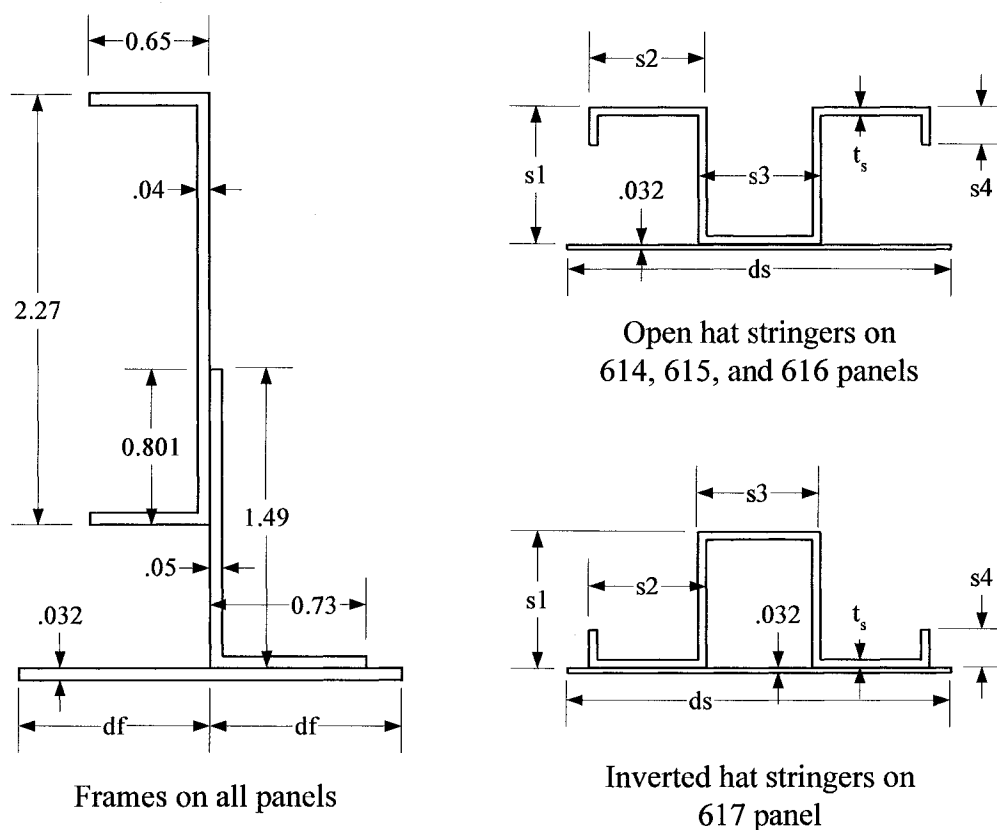


Figure 10. Frame and stringer geometries for the test panels (all units are in inches)

Panel	df*	ds ^ψ	s1	s2	s3	s4	t _s
614	1.0	0.0	0.689	0.52	0.58	0.188	0.025
615	1.0	2.0	0.657	0.52	0.58	0.188	0.025
616	12.0	7.55	0.657	0.51	0.67	0.0	0.063
617	0.0	0.0	0.689	0.52	0.58	0.188	0.025

*value of 12.0 indicates doubler over entire panel

^ψvalue of 7.55 indicates doubler over entire panel

all units are in inches

Table 3. Frame and stringer property values

3.2 Test Boundary Conditions and Generalized Imperfections

The top and bottom edges of the test panels were molded in resin and then milled flat and parallel to each other to provide an even surface for load introduction. The panels were supported along the straight edges with a clamping device to approximate simple support boundary conditions. To prevent the simple support clamping device from carrying axial load, teflon tape was bonded on the test panel at the location where the clamping device contacted the panel thus creating a sliding connection. Each of the four frames were supported at their right and left edges to prevent frame translation without restraining frame rotation. A rod was attached to the end of the frame utilizing a clevis and pin arrangement. The test set up is shown in Figure 11.

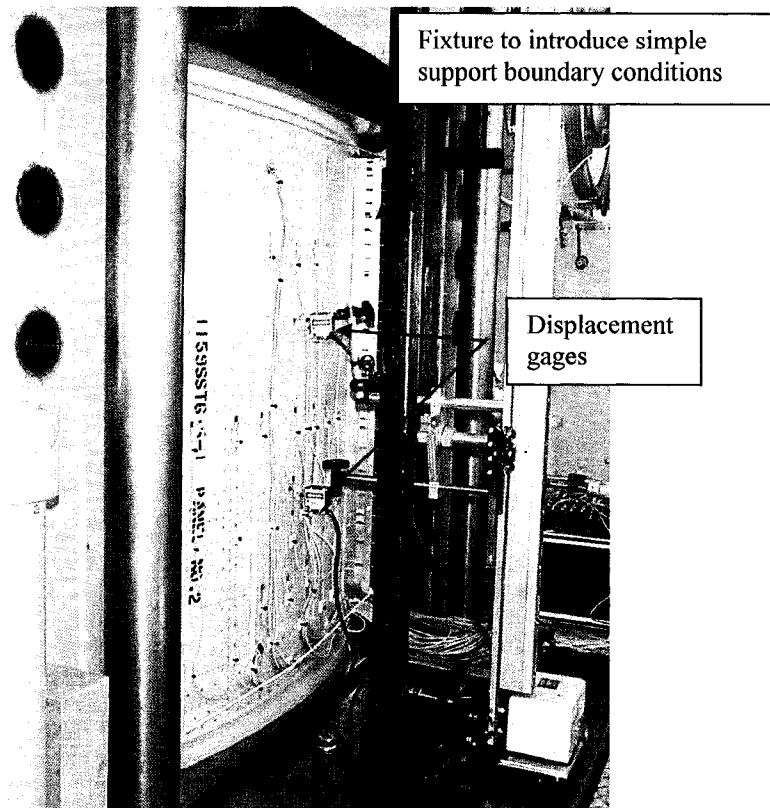


Figure 11. Compression test fixture

While the panels were clamped to the milling table, the wave shape was measured with a dial gage. The wave shape is a measure of the deviation of the actual radius of the panel skin from a perfectly circular radius. This information will be used to approximate the initial geometric surface imperfection shape for the nonlinear analysis models. On one side of the panel, the dial gage was set to zero at the centerline of the skin in the first bay (i.e., at measurement point b1a). This point is assumed to serve as a reference point for a nominal radius. Note that panel 614-1 was placed in the measurement fixture with its top edge down, therefore its zero-measurement point was actually measurement point b12d. Measurements were recorded at four locations in each skin bay of the panel in the axial direction as indicated in Figure 12. Negative values indicate that the measurement point has a larger radius than point b1a, and positive values indicate that the measurement point

Gage location	Panel number							
	614-1	614-2	615-1	615-2	616-1	616-2	617-1	617-2
b1a	-0.0264	0.0000	0.0000	0.0000	0.0000	0.0000	0.0000	0.0000
b1b	-0.0185	-0.0024	0.0114	0.0094	0.0067	0.0043	0.0028	0.0043
b1c	-0.0157	0.0138	0.0157	0.0106	0.0067	0.0083	0.0091	0.0047
b1d	-0.0142	0.0157	0.0224	0.0118	0.0004	0.0087	0.0130	0.0063
b2a	0.0315	0.0000	0.0000	0.0000	0.0000	0.0000	0.0000	0.0000
b2b	0.0236	-0.0016	0.0055	0.0098	0.0118	0.0051	0.0016	-0.0043
b2c	0.0150	-0.0047	0.0059	0.0173	0.0071	0.0094	0.0031	-0.0118
b2d	0.0079	-0.0079	0.0079	-0.0244	0.0020	0.0098	0.0055	-0.0165
b3a	0.0374	0.0000	0.0000	0.0000	0.0000	0.0000	0.0000	0.0000
b3b	0.0315	0.0020	0.0020	-0.0039	0.0047	0.0087	0.0098	-0.0035
b3c	0.0236	-0.0008	-0.0020	-0.0039	-0.0004	0.0091	0.0098	-0.0106
b3d	0.0185	-0.0047	-0.0004	0.0012	-0.0075	0.0063	0.0039	-0.0181
b4a	-0.0161	0.0000	0.0000	0.0000	0.0000	0.0000	0.0000	0.0000
b4b	-0.0087	0.0138	0.0083	0.0020	0.0067	0.0094	0.0110	0.0063
b4c	-0.0028	-0.0118	0.0130	0.0047	0.0043	0.0134	0.0189	0.0087
b4d	0.0094	0.0024	0.0165	0.0122	0.0087	0.0157	0.0256	0.0071
b5a	-0.0094	0.0067	0.0193	0.0142	0.0012	0.0126	0.0189	0.0087
b5b	-0.0063	-0.0098	0.0358	0.0339	0.0067	0.0213	0.0189	0.0012
b5c	-0.0059	0.0043	0.0110	0.0382	0.0075	0.0272	0.0197	0.0024
b5d	0.0024	-0.0020	0.0504	0.0350	0.0087	0.0244	0.0189	0.0047
b6a	0.0031	-0.0079	0.0138	0.0236	-0.0047	0.0185	0.0091	-0.0205
b6b	-0.0059	-0.0031	0.0197	0.0370	-0.0043	0.0071	0.0051	-0.0268
b6c	-0.0110	-0.0055	-0.0236	0.0472	-0.0114	0.0177	0.0067	-0.0323
b6d	0.0075	-0.0051	0.0276	0.0516	-0.0236	0.0173	0.0067	-0.0366
b7a	0.0067	-0.0055	0.0118	0.0067	-0.0118	0.0028	0.0055	-0.0169
b7b	-0.0016	-0.0071	0.0098	0.0091	-0.0165	0.0091	0.0122	-0.0201
b7c	-0.0063	-0.0055	0.0098	0.0161	-0.0181	0.0138	0.0134	-0.0244
b7d	-0.0039	-0.0051	0.0106	0.0201	-0.0169	0.0142	0.0110	-0.0299
b8a	0.0122	-0.0157	0.0118	0.0224	-0.0134	0.0220	0.0323	0.0161
b8b	0.0063	-0.0146	0.0118	0.0283	-0.0059	0.0394	0.0354	0.0154
b8c	0.0071	-0.0197	0.0087	0.0409	-0.0087	0.0472	0.0394	0.0169
b8d	0.0161	-0.0157	0.0059	0.0559	-0.0138	0.0472	0.0402	0.0177
b9a	-0.0051	-0.0157	0.0587	0.0413	0.0102	0.0350	0.0193	0.0059
b9b	-0.0024	-0.0079	0.0862	0.0709	0.0126	0.0417	0.0193	0.0177
b9c	-0.0020	-0.0071	0.0972	0.0906	0.0094	0.0465	0.0181	0.0295
b9d	0.0000	-0.0118	0.0949	0.1024	0.0075	0.0472	0.0189	0.0386
b10a	-0.0055	-0.0020	0.0295	0.0543	-0.0354	0.0193	0.0118	-0.0429
b10b	-0.0079	0.0047	0.0492	0.0709	-0.0283	0.0276	0.0091	-0.0461
b10c	-0.0059	0.0063	0.0579	0.0768	-0.0323	0.0331	0.0094	-0.0500
b10d	0.0000	0.0039	0.0606	0.0850	-0.0378	0.0370	0.0098	-0.0567
b11a	-0.0094	-0.0071	0.0189	0.0315	-0.0189	0.0114	0.0146	-0.0248
b11b	-0.0091	0.0016	0.0197	0.0469	-0.0181	0.0201	0.0157	-0.0268
b11c	-0.0087	0.0059	0.0220	0.0618	-0.0165	0.0240	0.0201	-0.0287
b11d	0.0000	0.0028	0.0236	0.0732	-0.0130	0.0280	0.0240	-0.0346
b12a	0.0106	-0.0157	0.0012	0.0602	-0.0157	0.0453	0.0543	0.0260
b12b	0.0067	-0.0177	0.0079	0.0717	-0.0051	0.0591	0.0602	0.0240
b12c	0.0028	-0.0138	0.0051	0.0846	-0.0047	0.0630	0.0665	0.0209
b12d	0.0000	-0.0189	-0.0012	0.0866	-0.0075	0.0591	0.0689	0.0157

Table 4. Dial-gage measurements (inches)

Coupon material testing was conducted by Westmoreland Mechanical Testing and Research, Inc. (ref. Simmons, 2000, Appendix B) to verify the test panel material mechanical properties. From this testing, no significant variation in material properties was found between the test specimens and the baseline allowables in the Metallic Materials Properties Development and Standardization Manual (Rice, et al., 2003), abbreviated MMPDS. A comparison of the material properties derived from test and those given in MMPDS are shown in Table 5.

Property	Source	Materials				
		.01”-.062” 2024-T3 Clad Aluminum	.063”-.128” 2024-T3 Clad Aluminum	.012”-.039” 7075-T6 Clad Aluminum	.040”-.062” 7075-T6 Clad Aluminum	.063”-.187” 7075-T6 Clad Aluminum
F _{tu}	MMPDS ‘A-basis’	60 ksi	62 ksi	70 ksi	71 ksi	73 ksi
	MMPDS ‘B-basis’	61 ksi	63 ksi	74 ksi	75 ksi	77 ksi
	Test average	63 ksi	66 ksi	76 ksi	74 ksi	77 ksi
F _{ty}	MMPDS ‘A-basis’	44 ksi	45 ksi	62 ksi	63 ksi	65 ksi
	MMPDS ‘B-basis’	45 ksi	47 ksi	65 ksi	66 ksi	69 ksi
	Test average	45 ksi	51 ksi	64 ksi	64 ksi	67 ksi
F _{cy}	MMPDS ‘A-basis’	36 ksi	37 ksi	61 ksi	62 ksi	64 ksi
	MMPDS ‘B-basis’	37 ksi	39 ksi	64 ksi	65 ksi	68 ksi
	Test average	50 ksi	47 ksi	72 ksi	73 ksi	73 ksi
E _t	MMPDS	10500 ksi	10500 ksi	10300 ksi	10300 ksi	10300 ksi
	Test average	10260 ksi	10260 ksi	10130 ksi	10130 ksi	10130 ksi
E _c	MMPDS	10700 ksi	10700 ksi	10500 ksi	10500 ksi	10500 ksi
	Test average	9970 ksi	9970 ksi	9810 ksi	9810 ksi	9810 ksi

A-basis: 95% confidence that 99% of the samples will exceed the allowable

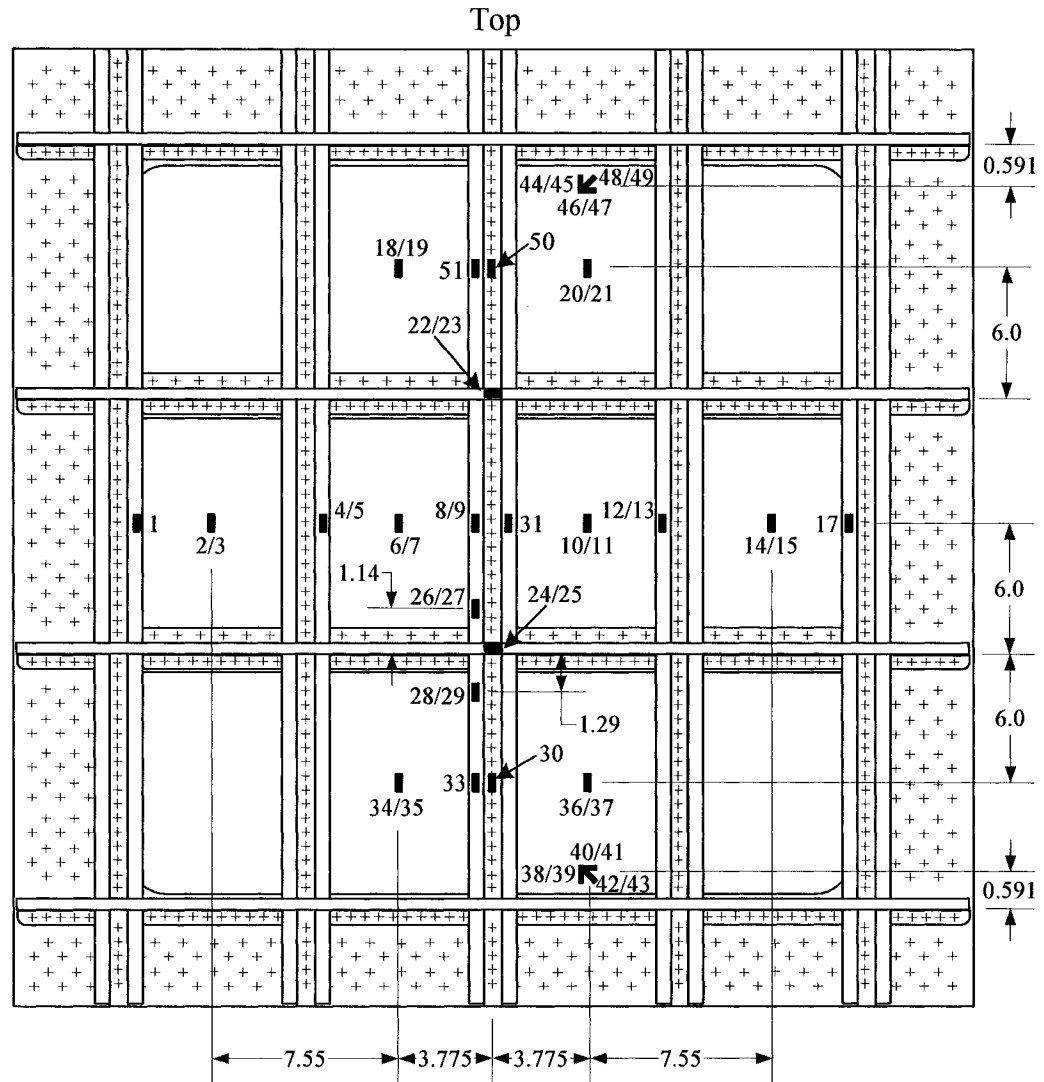
B-basis: 95% confidence that 90% of the samples will exceed the allowable

Table 5. Test panel material properties

3.3 Instrumentation and Data Acquisition

All of the panels have strain gages mounted on the interior (stiffened side) and exterior (unstiffened side) of the panel. The strain gage locations and numbering for the different panel configurations are shown in Figures 13-15. The gage patterns for configurations

614 and 615 are the same. Odd-numbered strain gages are located on the interior of the panel, and even-numbered strain gages are located on the exterior of the panel. Strain gages located on the panel skin are back-to-back strain-gage pairs. Back-to-back strain-gage pairs provide a way to determine when buckling within a bay occurs. The locations of the strain gages on the frames and stringers are also shown in Figures 13-15. All single strain gages are bonded on the panel in the longitudinal direction except for gages 22, 23, 24, and 25 which were bonded on in the transverse direction. Two pairs of strain-gage rosettes are oriented exactly as shown in Figures 13-15. The test was load-controlled, and strain-gage measurements were taken and recorded at 5 to 20 pound load increments during the test, depending on the magnitude of the predicted panel failure load.



strain gage numbers:
 odd numbers = interior surface (stringer side)
 even numbers = exterior surface

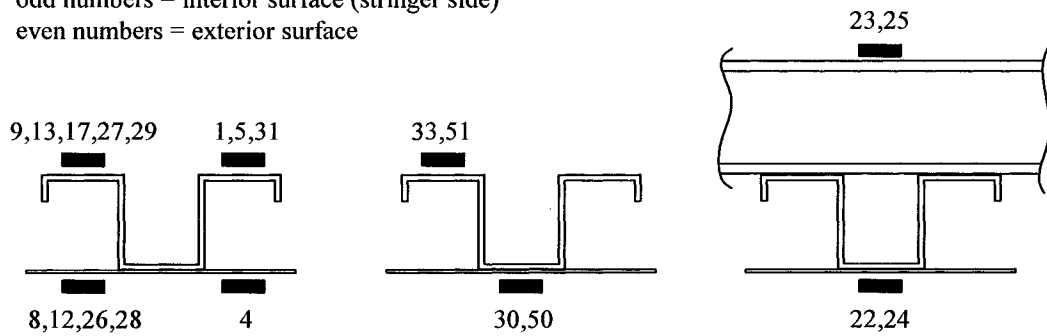
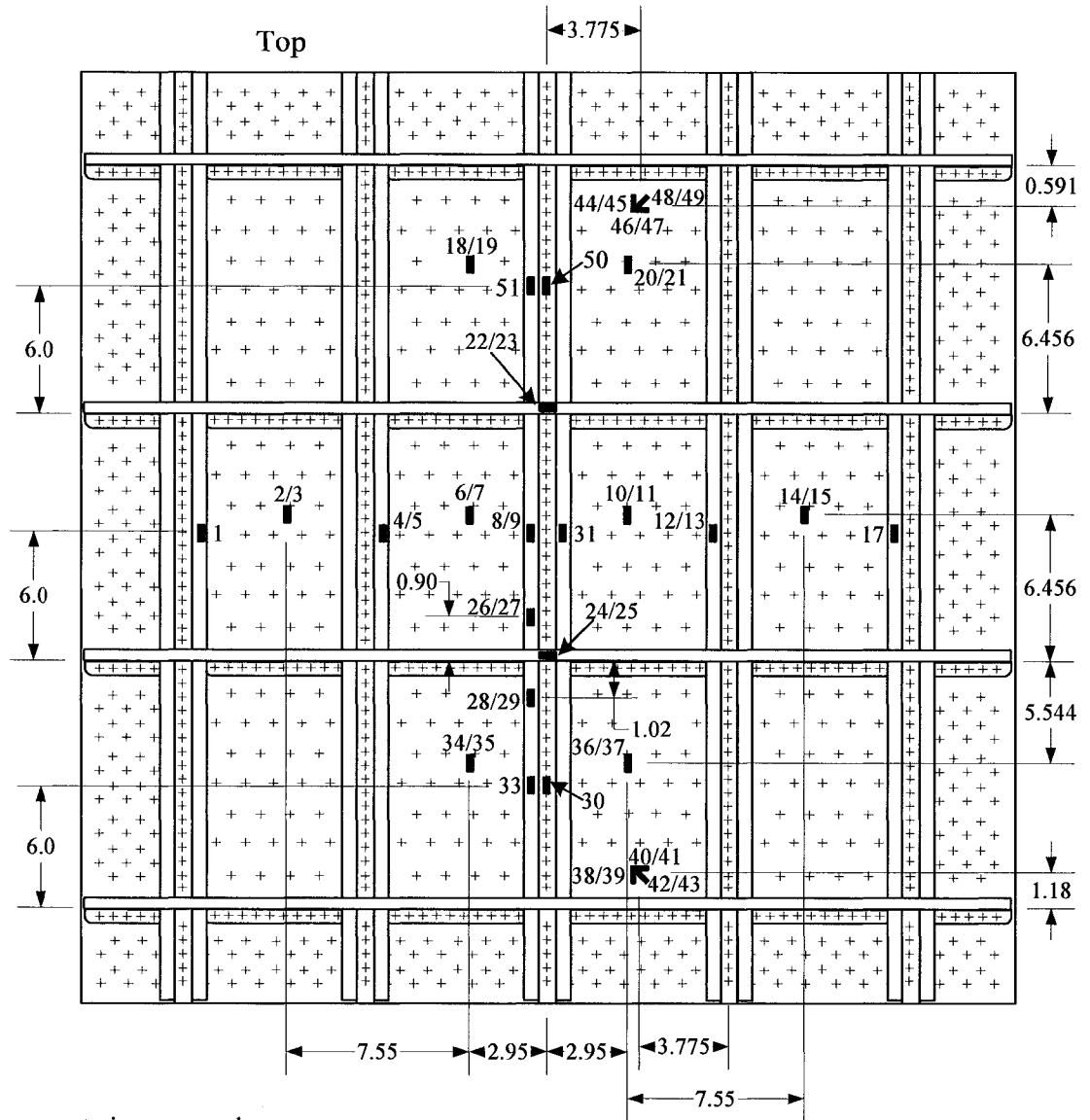


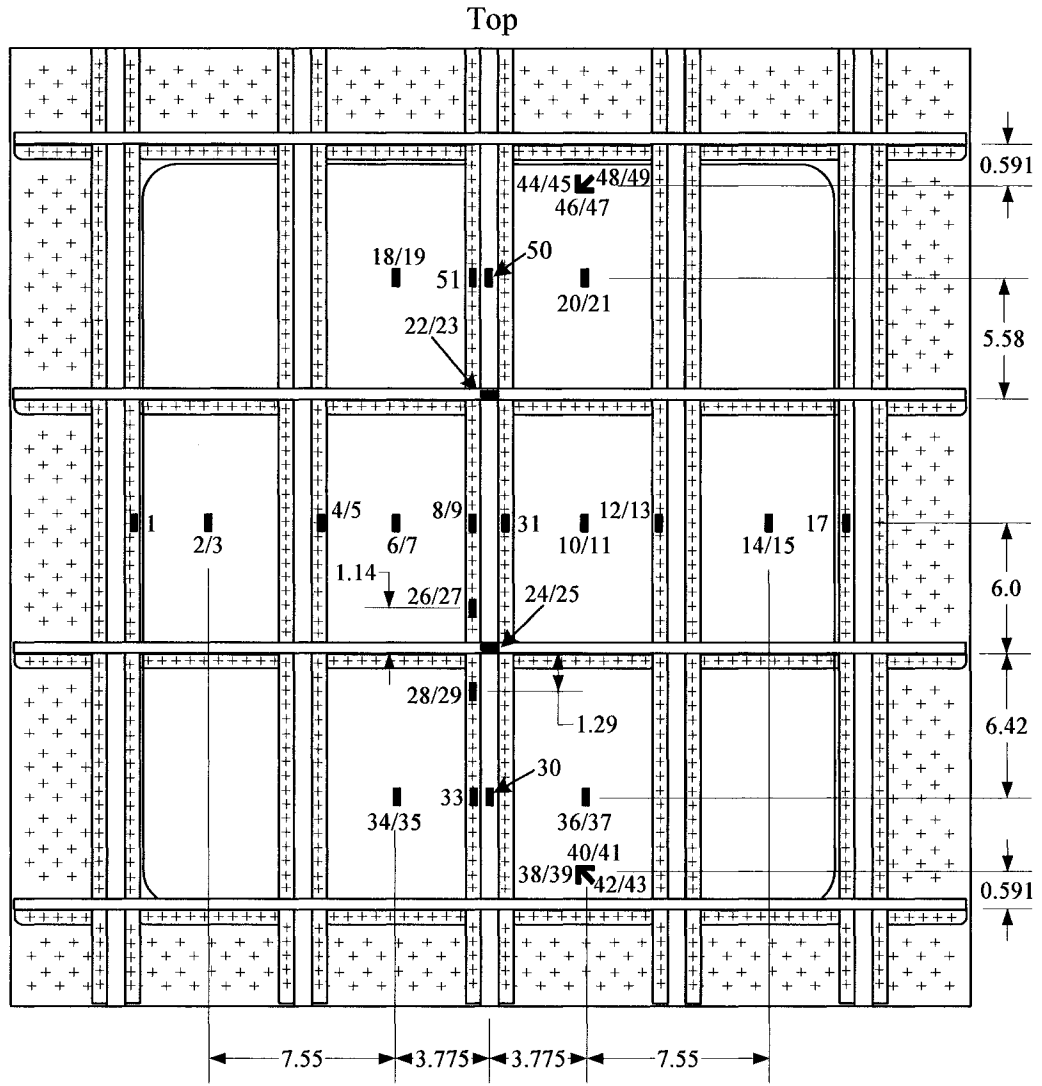
Figure 13. Strain gage locations for panel configurations 614 and 615



strain gage numbers:
 odd numbers = interior surface (stringer side)
 even numbers = exterior surface



Figure 14. Strain gage locations for panel configuration 616



strain gage numbers:
 odd numbers = interior surface (stringer side)
 even numbers = exterior surface

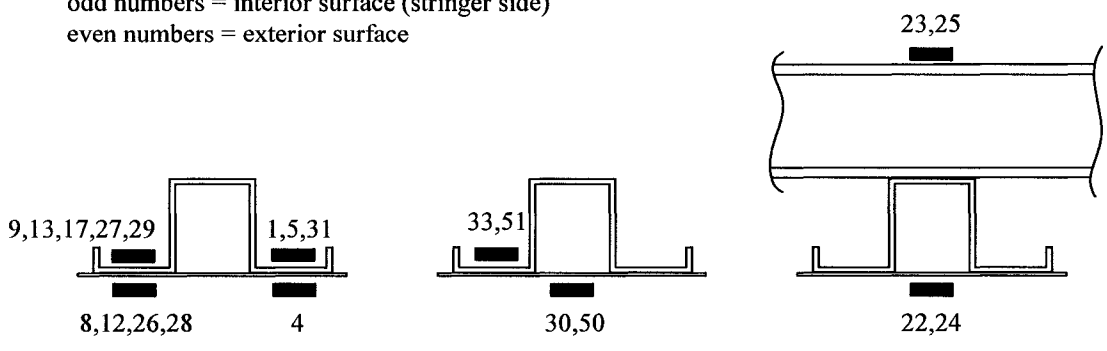


Figure 15. Strain gage locations for panel configuration 617

The out-of-plane displacement was measured at two points on the exterior of the panel. These displacement gages can be seen in the test set up shown in Figure 11. The exact location of the displacement gages is indicated in Figure 16. The displacement gages are positioned directly to the right or left of strain gages 22 and 24. Load versus end shortening was measured by two Linear Voltage differential transducers or LVDTs mounted on stands placed on the loading platen on the exterior side of the panel. The LVDTs were situated vertically along the centerline of the panel. Displacement measurements were taken continuously during the tests.

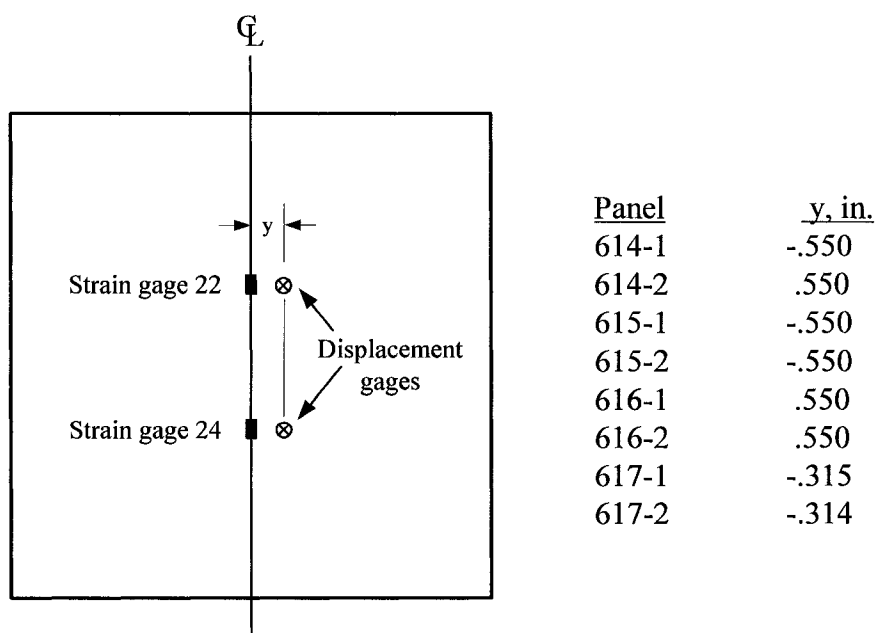


Figure 16. Out-of-plane displacement gage locations viewed from exterior side of panel

Photographs were taken with digital cameras throughout the test. From these photographs buckling and failure modes for each panel were captured. Videotaping of each test was also done.

3.4 Test Results

3.4.1 General

Strain-gage readings were recorded for all panel tests and are included in Appendix B. A numbering system for the panel skin bays, stringers, and frames is given in Figure 17 as a reference guide for identifying local events that occur during the test.

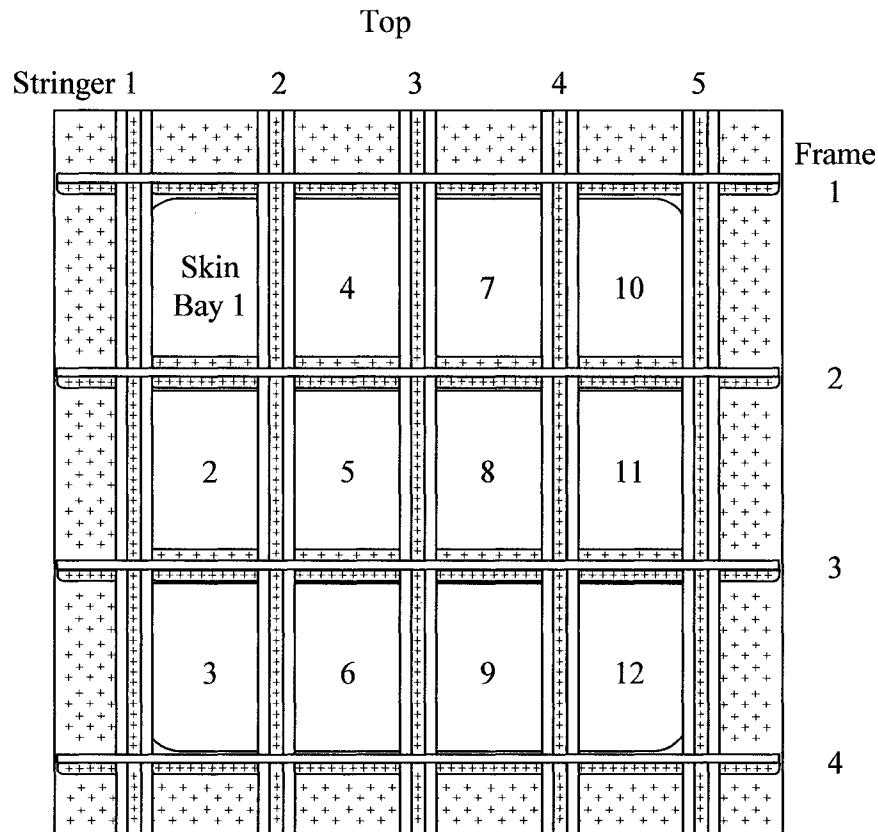


Figure 17. Test panel reference numbering system for identifying panel locations

3.4.2 Panels 614-1 and 614-2

Panels 614-1 and 614-2 have an 0.04-inch-thick skin, 0.025-inch-thick open hat stringers, 0.032-inch-thick doublers under the frames, and gussets at the edges of the panels as described in Section 3.1. The presence of the doublers under the frames effectively

reduces the length of the skin-bay sections. Strain-gage readings for both panels are included in Appendix B. Gages 30, 33, and 38-51 were not included in the panel 614-1 test. After the test was complete, it was decided that these additional gages would be added to subsequent tests.

The load-end shortening response curve for the 614-1 panel is shown in Figure 18. Because these data were recorded by an x-y plotter in real time on paper, only the clearer of the two test panel data curves was converted to numerical data and replotted. For the 614-1 panel, the load-end shortening response curve was initially flat until the loading head became fully engaged. As the compression load increased, evidence of initial buckling is exhibited in the load-end shortening response curve by an abrupt decrease in load. Strain-gage data indicated local skin-bay buckling continued to occur sequentially as load increased. Buckling did not occur initially in the center skin bays (bays 5 or 8). This is most likely due to imperfection in the outer skin bays. All of the skin bays buckled prior to panel failure for both the 614-1 and 614-2 panels.

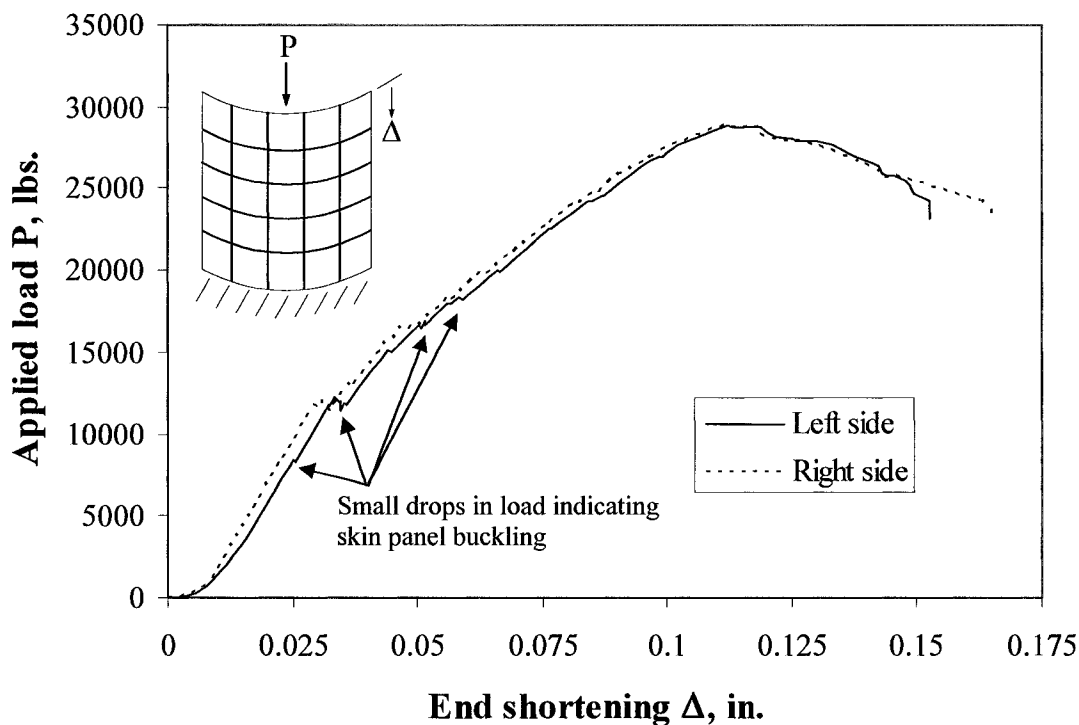


Figure 18. Load end-shortening response curve for panel 614-1

The dips in the load end-shortening response curve occur as each skin-bay buckles as the load increases. The number of displacement gages is insufficient to tell the order of skin-bay buckling. However, skin bay buckling can be seen in the back-to-back strain-gage data for skin bays 2,4,5,7,8, and 11 as shown in Figure 19. Prior to buckling the back-to-back strain gages indicate the same surface strain on both surfaces. When these gages indicate different values, a local event has occurred and is believed to be associated with a local skin-bay buckling. The triangular symbol on the skin-bay strain gage plots indicates the load at which buckling was observed visually for that panel during the test.

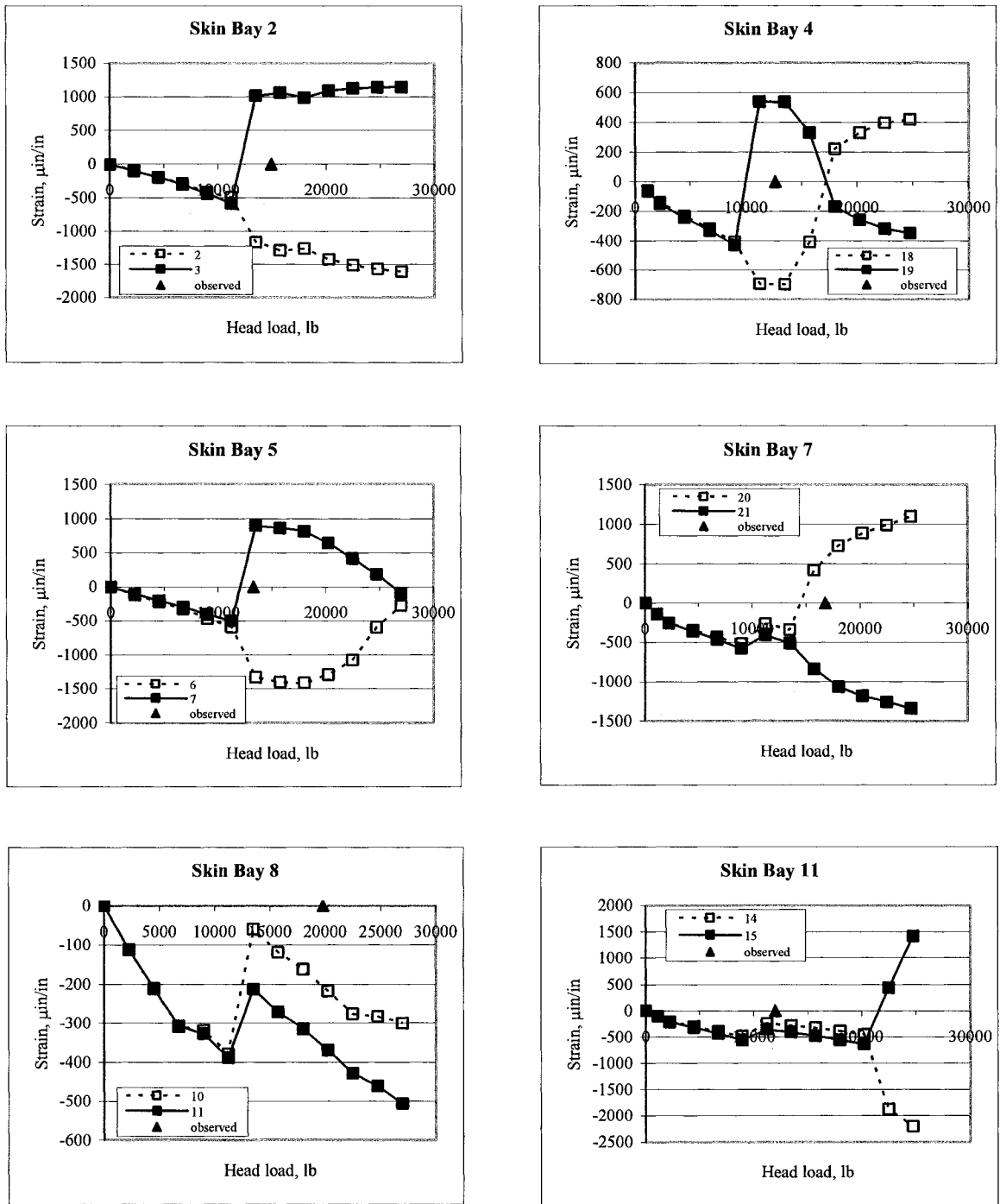


Figure 19. Back-to-back strain gage-data for panel 614-1 skin bays

The sequence of skin-bay buckling and the corresponding load as observed visually during the test are listed in Table 6. However there is some amount of uncertainty as to the exact load a particular skin bay buckles, which is evident by comparing the load value when the strain values deviate from one another and the load value for the visual observation.

Panel 614-1		Panel 614-2	
Buckling load, lb.	Skin bay	Buckling load, lb.	Skin bay
8318	9	7868	1
11690	3	9442	2
12005	11	10229	7
12185	1	10454	9
12657	4	10903	6
13264	5	11241	5
14927	2	11465	4,8,11
15872	12	17760	3,10,12
16771	7		
18434	10		
19783	6,8		
Failure load		Failure load	
28821		28551	

Table 6. Buckling loads of skin bays for panels 614-1 and 614-2 based on visual observations

During increased load application, it was noted that the buckle shape changed in some of the skin bays, but the details were not recorded. The strain-gage readings for skin bay 4 indicate an initial buckling load for that bay between 8,992 lbs and 11,240 lbs, compared to a visually observed load of 12,657 lbs. Strain readings indicated a subsequent mode change occurred between 15,736 lbs and 17,985 lbs. The initial skin-bay buckling loads recorded visually occurred close to or slightly after the values indicated by the strain-

gage data except for skin bay 8. Both strain-gage readings indicate compression for the duration of the test indicating a shallow buckling of the panel which would be hard to observe visually.

The failure load for panel 614-1 was 28,821 lbs. Failure load is defined as the maximum load sustained without any significant load reduction event. Failure may occur as a gradual loss of load-carrying capability as indicated in Figure 18 or as in a sudden collapse. Panel 614-1 failed in the lower area of the panel halfway between frames 3 and 4 across the skin bays 3, 6, 9, and 12. The failure mode was *stringer crippling* and overall buckling of the skin areas along with inter-rivet buckling (i.e., local buckling between rivets). A sharp wrinkle is visible between the skin/stringer rivets as indicated in Figure 20. No rivet failure or rivet pull through was observed.

The failure load for panel 614-2 was 28,551 lbs. The failure mode for panel 614-2 was the same as for panel 614-1 except the failure occurred at the top of the panel between frames 1 and 2 across skin bays 1, 4, 7, and 10. The exterior and interior sides of panel 614-2 are shown in Figures 21 and 22, respectively, after panel failure has occurred.

The failure location coincided with the location of the first skin bay buckling for both the 614-1 and 614-2 panels. After the skin bays buckled, the load redistributed to the adjacent stringers. As the load increased, the buckle depth of these skin bays grew larger and triggered the crippling failure of the stringers.

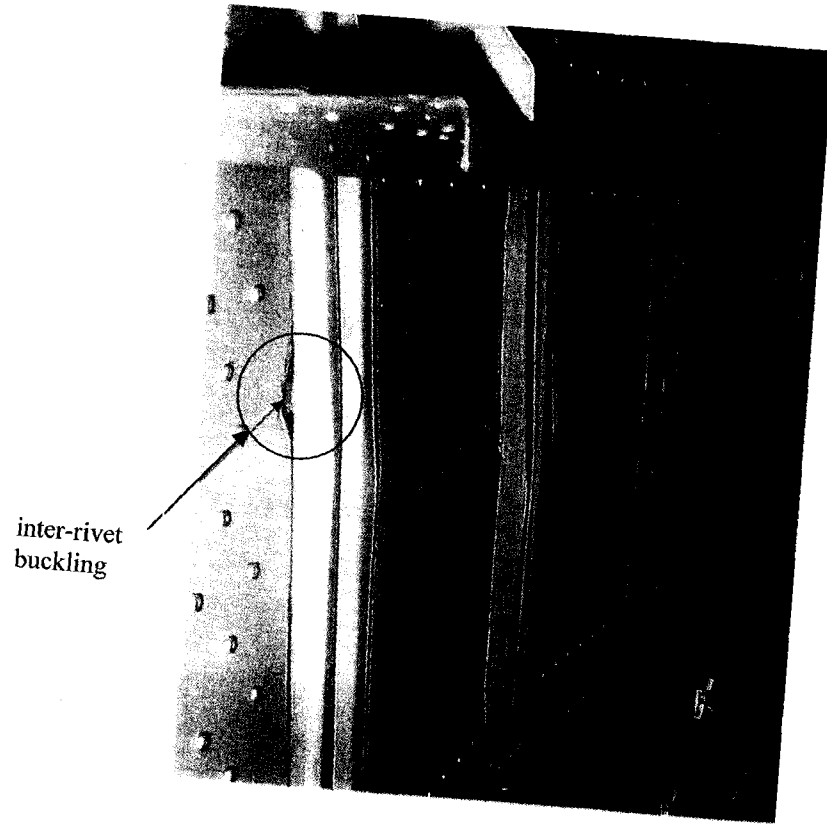


Figure 20. Panel 614-1 failure mode

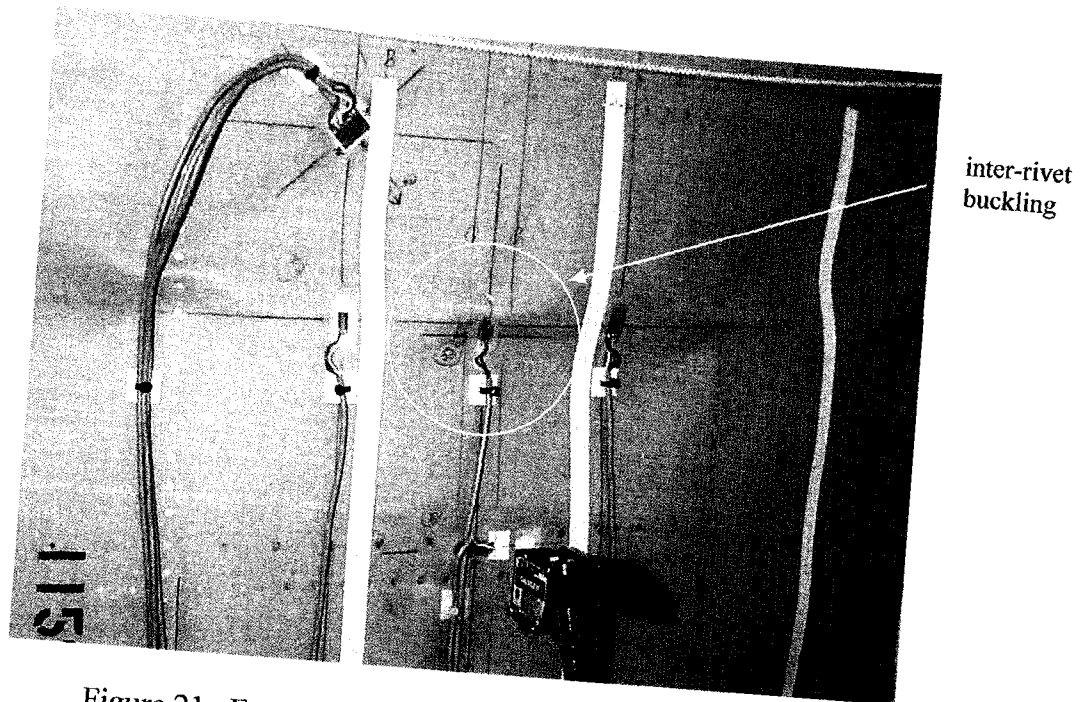


Figure 21. Exterior view of failed section of panel 614-2

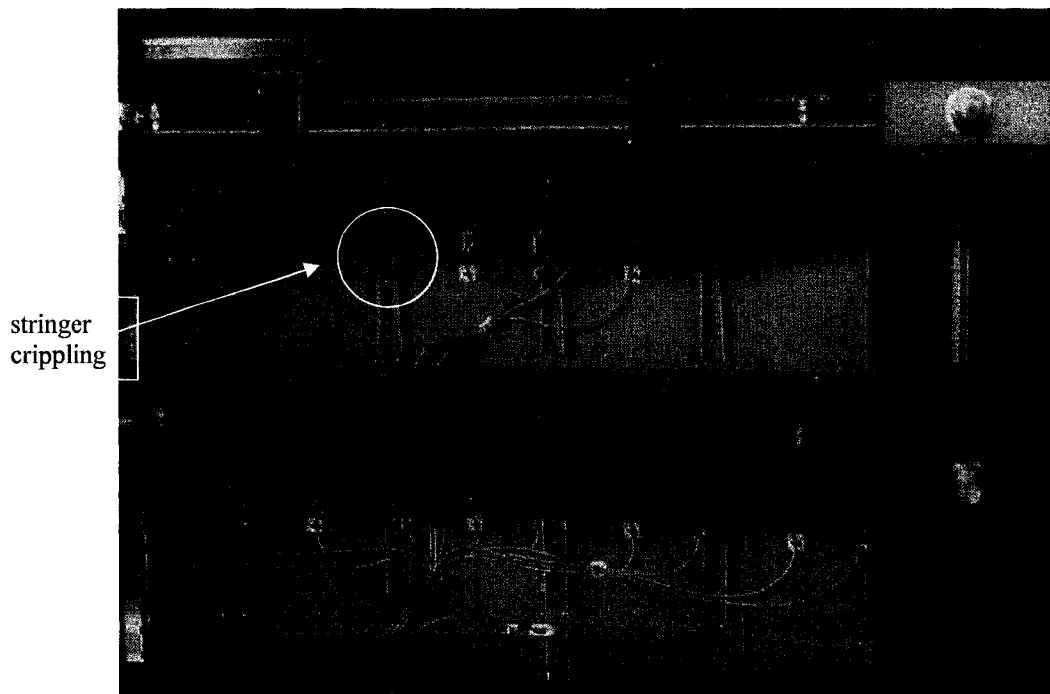


Figure 22. Interior view of failed section of panel 614-2

3.4.3 Panels 615-1 and 615-2

Panels 615-1 and 615-2 have an 0.04-inch-thick skin, 0.025-inch-thick open hat stringers, 0.032-inch-thick doublers under the frames and stringers, and gussets at the edges of the panels as described in Section 3.1. The 615 panels differ from the 614 panels in that the 615 panels have doublers under the stringers as well as the frames. Having doublers under both frames and stringers effectively reduces the skin-only portion of each skin-bay section. Strain-gage readings for both panels are included in Appendix B. All of the skin bays buckled prior to panel failure for both the 615-1 and 615-2 panels. However, there was no stringer buckling prior to failure. The load end-shortening response curve for the 615-2 panel is shown in Figure 23.

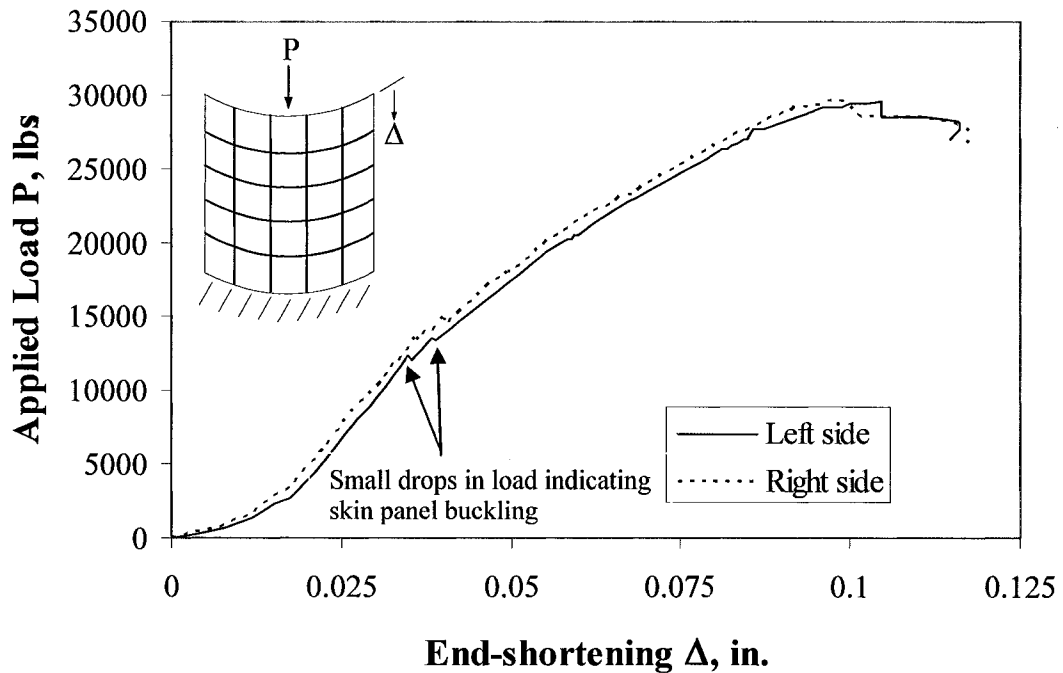


Figure 23. Load end-shortening response curve for panel 615-2

As with the 614 panels, the load-end shortening response curve was initially flat until the loading head became fully engaged. The dips in the curve occur as the skin buckles in each of the panel sections. Skin panel section buckling can be seen in the back-to-back strain-gage data for skin bays 2, 4, 5, 6, 7, 8, 9, and 11 shown in Figure 24. Solid triangular symbols indicate the value at which skin buckling was observed visually during the test. In some cases, the exact load level at which buckling occurred in a skin bay was not recorded. Instead skin-bay buckling was only recorded as occurring at some time above a certain load level. For these cases, open triangular symbols indicate the value above which skin-bay buckling was recorded to occur.

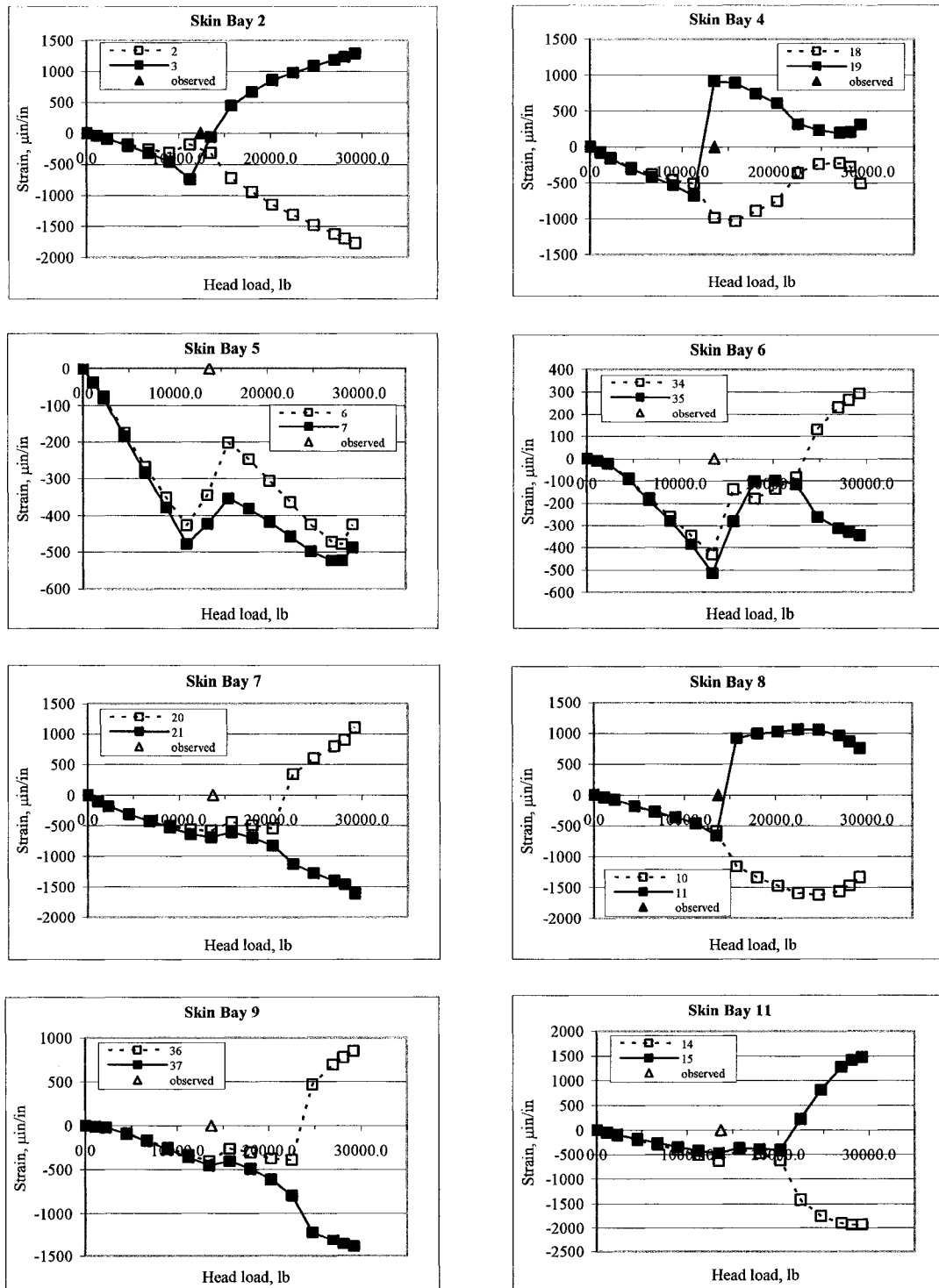


Figure 24. Strain-gage data for 615-2 panel skin bays

The sequence of skin-bay buckling and the corresponding load when observed visually during the test are listed in Table 7.

Panel 615-1		Panel 615-2	
Buckling load, lb.	Skin bay	Buckling load, lb.	Skin bay
13039	1,3,10-12	12365	2
14275	8	13489	4
15737	2,4-7,9	13713	8
		13713<load<29563	1,3,5-7,9-12
Failure load		Failure load	
29787		29563	

Table 7. Buckling loads of skin bays for panels 615-1 and 615-2 based on visual observations

For some panels, skin-bay buckling load levels were not recorded as in the case of Panel 615-2. After the 13,713 load level, the test report (Simmons, 2000) only noted that all additional bays buckled prior to failure. The buckling loads that were observed and recorded agreed well with strain-gage data for panel 615-2. A buckling mode change for skin bay 2 is indicated by strain-gage data shown in Figure 24.

The failure load for panel 615-1 was 29,787 lbs. Panel 615-1 failed by *stringer crippling* between frames 3 and 4. Prior to failure, buckling of the skin occurred across the entire width of the panel between frames 3 and 4, and sharp buckles developed in the skin, triggering the crippling failure of the stringers. As with the 614 panels, failure occurred in the bays where the skin-bay buckling was first observed. The exterior of the failed 615-1 panel is shown in Figure 25, and the interior view is shown in Figure 26.

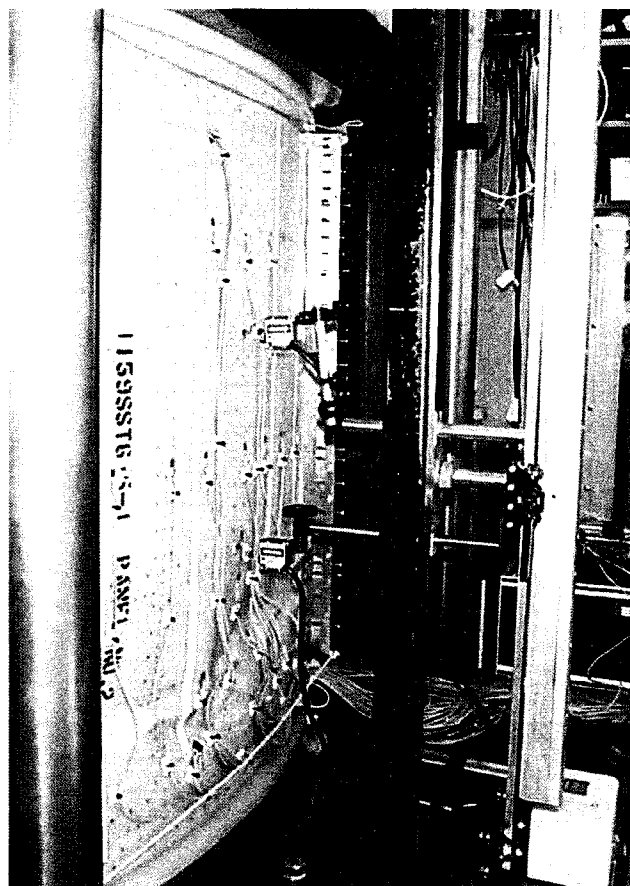


Figure 25. Exterior view of failed section of panel 615-1

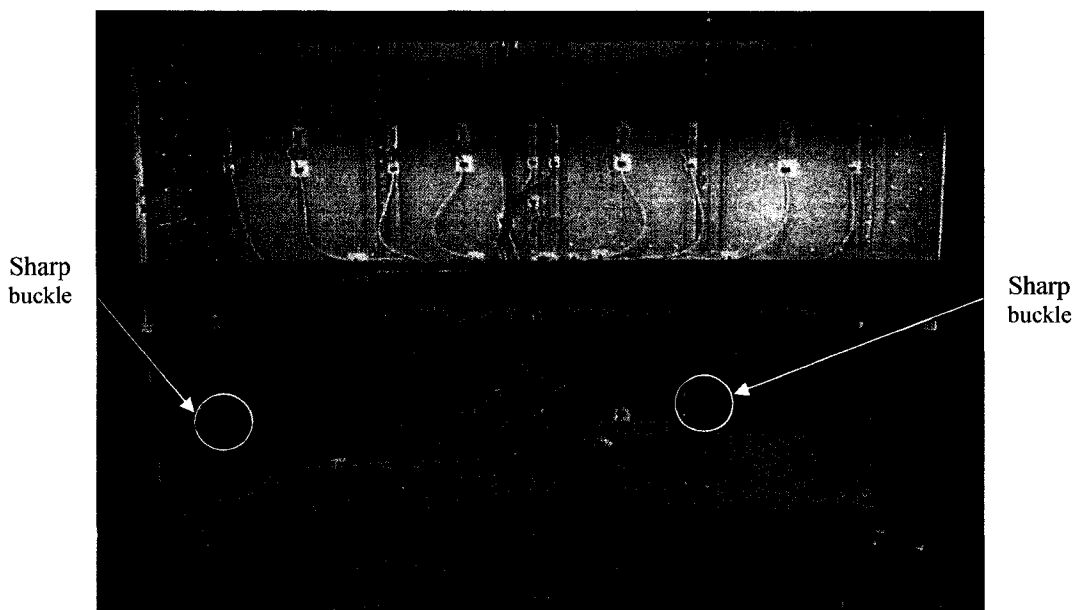


Figure 26. Interior view of failed section of panel 615-1

The failure load for panel 615-2 was 29,563 lbs. Panel 615-2 experienced the same failure mode as panel 615-1 except that the failure occurred between frames 1 and 2, and only stringers 3, 4, and 5 crippled. Failure did not occur between the frames where skin-bay buckling was first observed, but did occur in the area where the second observation of skin-bay buckling was made. Strain-gage data for stringer 3 between frames 1 and 2 are shown in Figure 27. The strain gages show a sharp divergence in strain just prior to the stringer crippling failure.

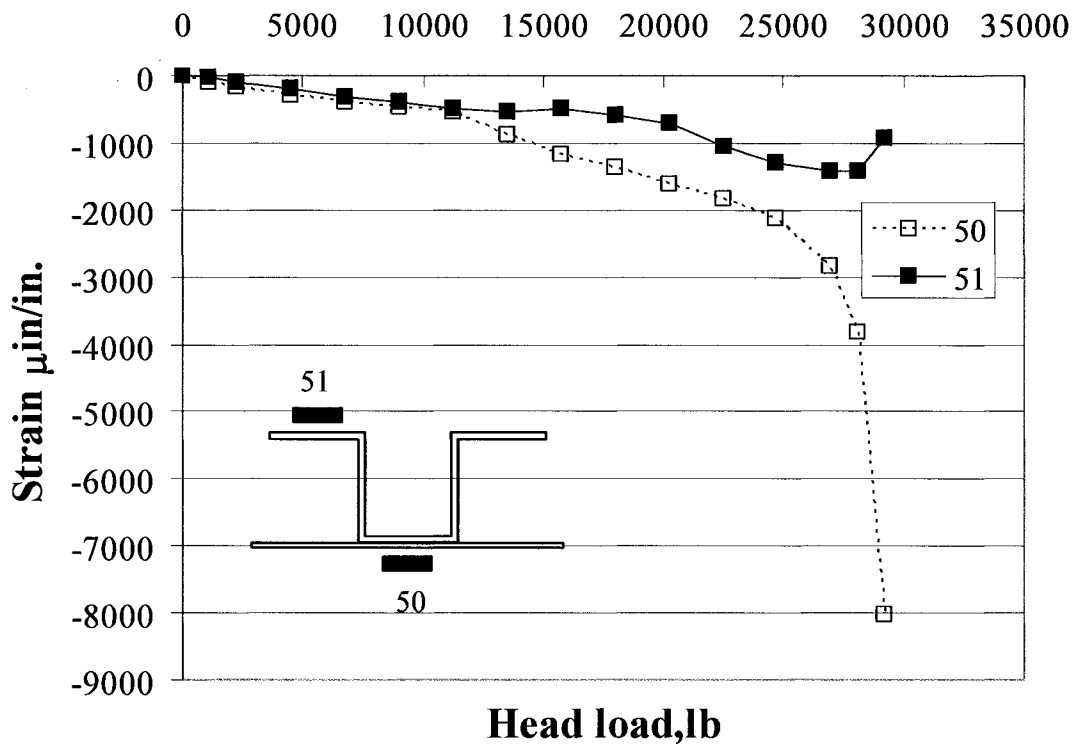


Figure 27. Stringer strain-gage data for panel 615-2

The failure modes for the 615 panels were the same as the 614 panels except that no inter-rivet buckling occurred for the 615 panels. The extra stiffness gained by the

addition of the doublers under the stringers for the 615 panels prevented the inter-rivet buckling from occurring. No rivet failure or rivet pull through was evident in either test.

3.4.4 Panels 616-1 and 616-2

Panels 616-1 and 616-2 have an 0.04-inch-thick skin, 0.063-inch-thick open hat stringers, an 0.032-inch-thick doubler over the entire skin, and gussets at the edges of the panels as described in Section 3.1. The 616 panels differ from the 614 and 615 panels in that the 616 panels effectively have a thicker skin (skin plus doubler) and thicker stringers.

Strain-gage readings for both panels are included in Appendix B. Gages 1-5 were not included in the 616 panel tests because the panel response was expected to be symmetric about the vertical centerline of the panel. All of the skin bays buckled prior to panel failure for both the 616-1 and 616-2 panels. The load end-shortening response curve for the 616-2 panel is shown in Figure 28. Initial buckling and panel failure occur at load levels nearly three times the same values observed for the previous panels. (Compare Figure 28 with Figure 18 for the 614 panel and Figure 23 for the 615 panel.)

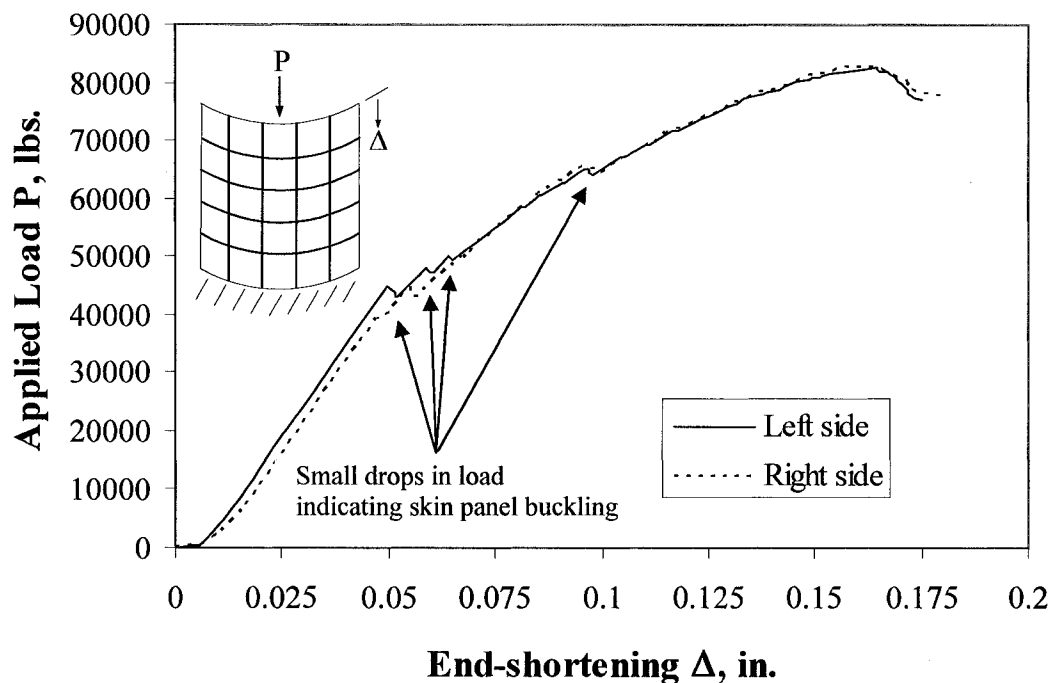


Figure 28. Load end-shortening response curve for panel 616-2

As with the 614 and 615 panels, the load-end shortening response curve was initially flat until the loading head became fully engaged. Skin panel section buckling can be seen in the back-to-back strain-gage data for skin bays 4, 5, 6, 7, 8, 9, and 11 shown in Figure 29. Solid triangular symbols indicate the value at which skin buckling was observed visually during the test. Open triangular symbols indicate the load level above which buckling was noted to occur by the test engineer during the test.

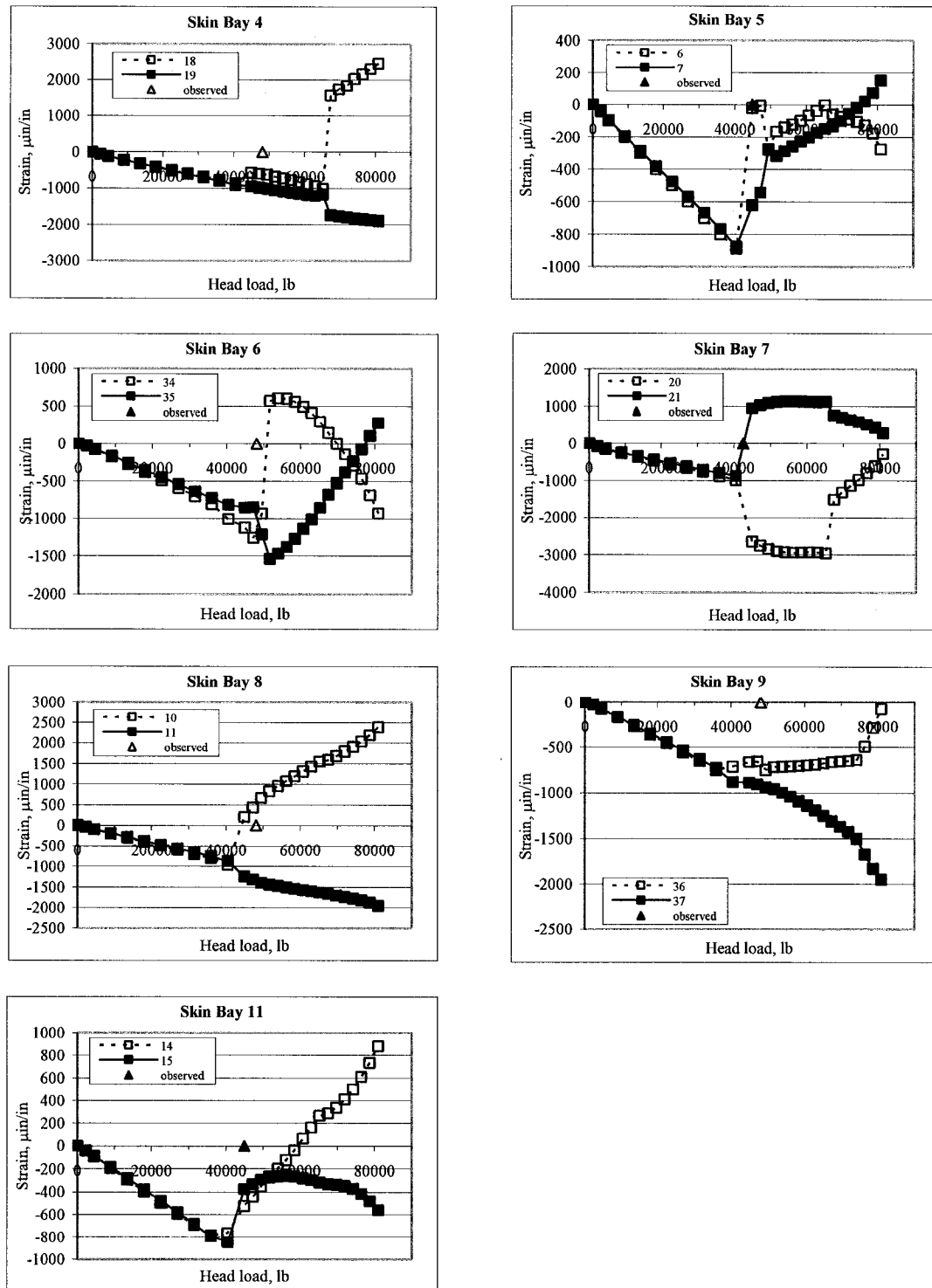


Figure 29. Strain-gage data for 616-2 panel skin bays

The sequence of skin buckling and the corresponding buckling load observed visually during the test are listed in Table 8.

Panel 616-1		Panel 616-2	
Buckling load, lb.	Skin bay	Buckling load, lb.	Skin bay
31473	8,11	39342	3
37094	4,5,7	42489	7,10
37094<load<78684	1-3,6,9,10,12	44962	5,11
		48109	12
		48109<load<82730	1,2,4,6,8,9
Failure load		Failure load	
78684		82730	

Table 8. Buckling loads of skin bays for panels 616-1 and 616-2 based on visual observations

For some panels, skin-bay buckling load levels were not recorded as was seen for Panel 615-2. At some high load level (37,094 lbs for panel 616-1 and 48,109 lbs for panel 616-2), the test report (Simmons, 2000) only noted that all additional bays buckled prior to failure. Visually observed skin buckling is in good agreement with the buckling loads derived from the strain-gage data. Mode shape changes are detected by the strain-gage data for skin bays 4, 5, 6, and possibly 7.

The failure load for panel 616-1 was 78,684 lbs. Panel 616-1 failed in the middle of the panel halfway between frames 2 and 3. The failure mode was *Euler-column buckling* of the stringers. Stringers 1 and 5 buckled outward in the skin direction and stringers 2, 3, and 4 buckled inward in the stringer direction. The failure occurred in the middle of the panel due to the fact that Euler-column buckling loads are dependent on the boundary

conditions at the ends of the column or stringer. The amount of end-fixity provided to the stringers by the center frames was less than the fixity provided to the stringers by the frames adjacent to the fixed ends of the panel. Therefore, the Euler-column buckling load level for the center stringers was less than for the top and bottom stringers. The exterior and interior sides of panel 616-1 are shown in Figures 30 and 31, respectively, after panel failure has occurred. No rivet failure or rivet pull through was evident.

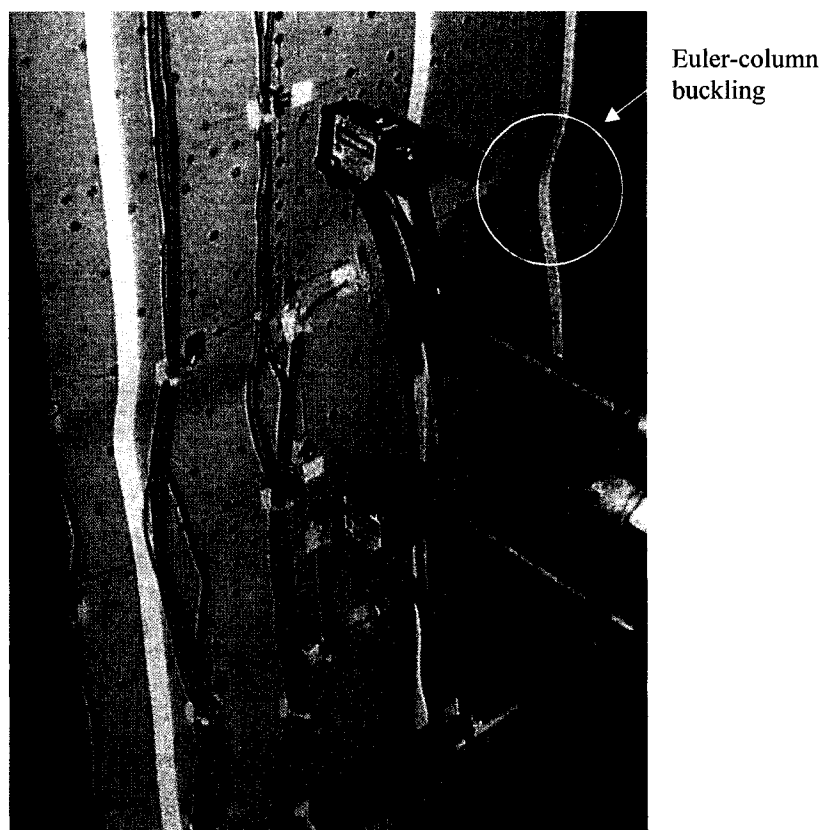


Figure 30. Exterior view of failed section of panel 616-1

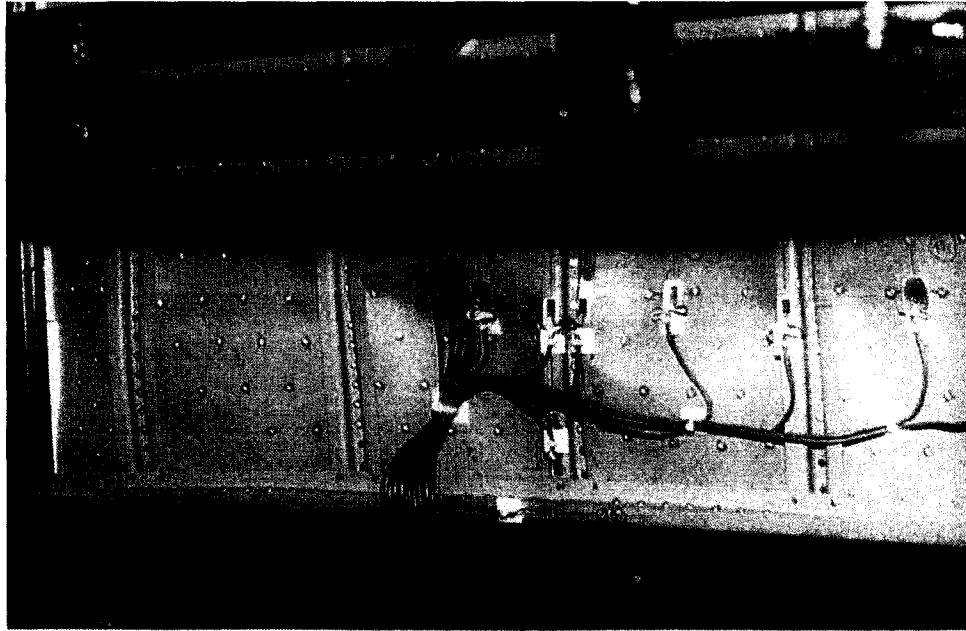


Figure 31. Interior view of failed section of panel 616-1

The failure load for panel 616-2 was 82,730 lbs. The failure mode for panel 616-2 was the same as for panel 616-1, Euler-column buckling of the center stringers, with stringers 1 and 5 buckled outward in the skin direction and stringers 2, 3, and 4 buckled inward in the stringer direction. Strain-gage data for stringer 3 are shown in Figure 32. The gages clearly show stringer 3 initially bowing outward in the skin direction until shortly before failure where the stringer flange bows inward in the stringer direction.

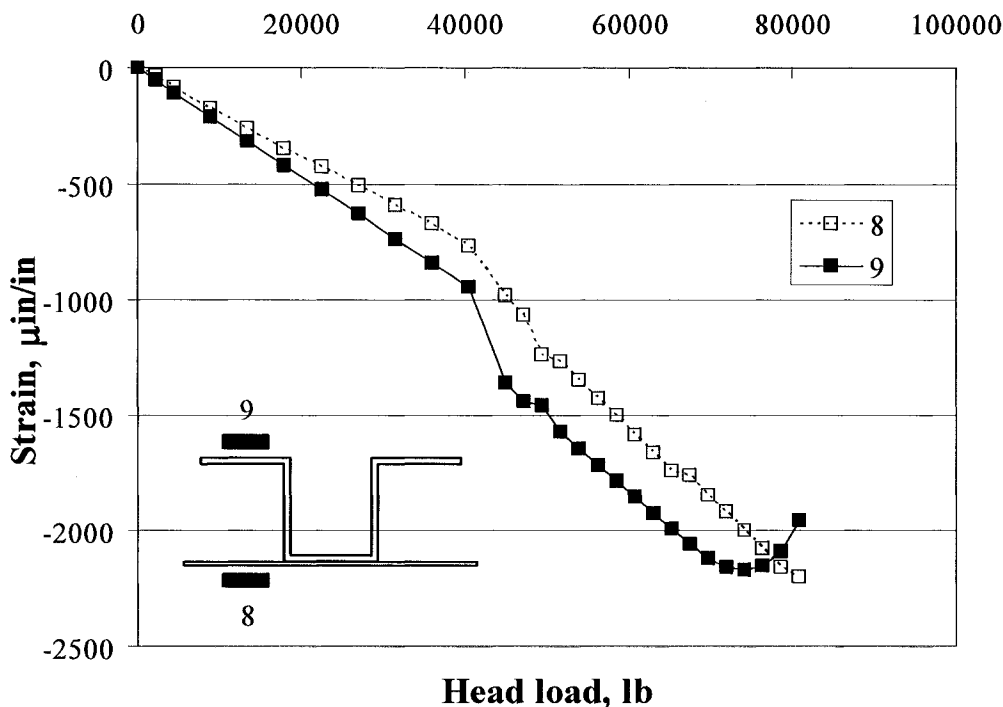


Figure 32. Stringer 3 strain-gage data for panel 616-2

3.4.5 Panels 617-1 and 617-2

Panels 617-1 and 617-2 have an 0.063-inch-thick skin, 0.025-inch-thick inverted hat stringers, no doublers, and gussets at every frame/stringer intersection as described in Section 3.1. Even though this panel has no doublers, the flanges of the inverted hat stringers effectively decrease the stiffener spacing compared to the previous panels.

Also, the gussets provide extra support to the stringers at the stringer/frame intersections effectively reducing the column length of the stringers for Euler-column buckling.

Strain-gage readings for both panels are included in Appendix B. All of the skin bays buckled prior to panel failure for both the 617-1 and 617-2 panels. The load end-shortening response curve for the 617-1 panel is shown in Figure 33.

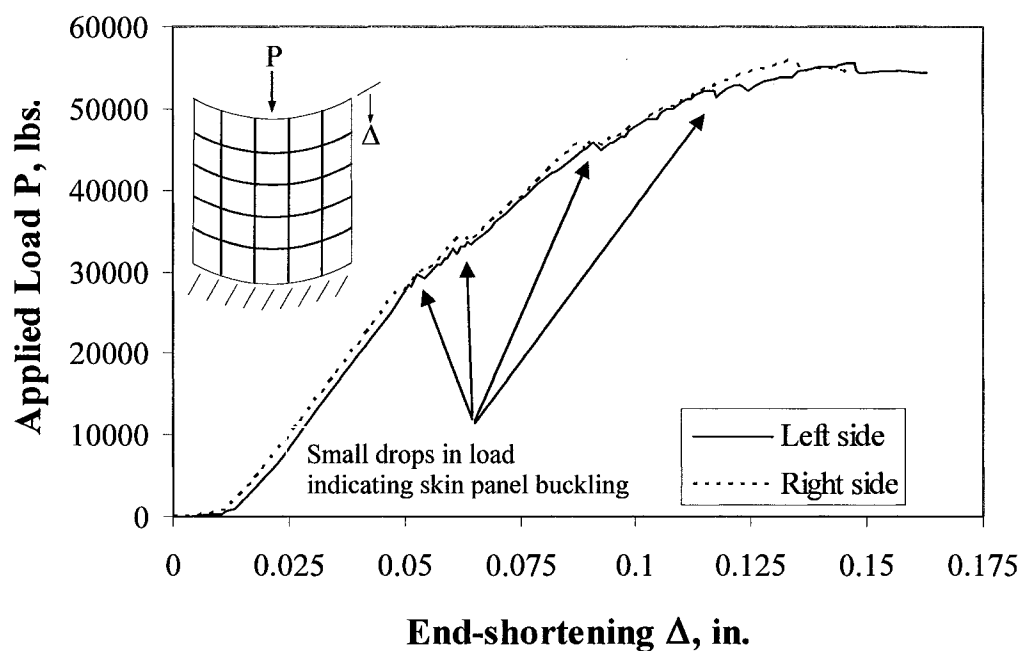


Figure 33. Load end-shortening response curve for panel 617-1

As with the previous panels, the load-end shortening response curve was initially flat until the loading head became fully engaged. Skin panel section buckling can be seen in the back-to-back strain-gage data for skin bays 2, 4, 5, 6, 7, 8, 9, and 11 shown in Figure 34. Solid triangular symbols indicate the value at which skin buckling was observed visually during the test.

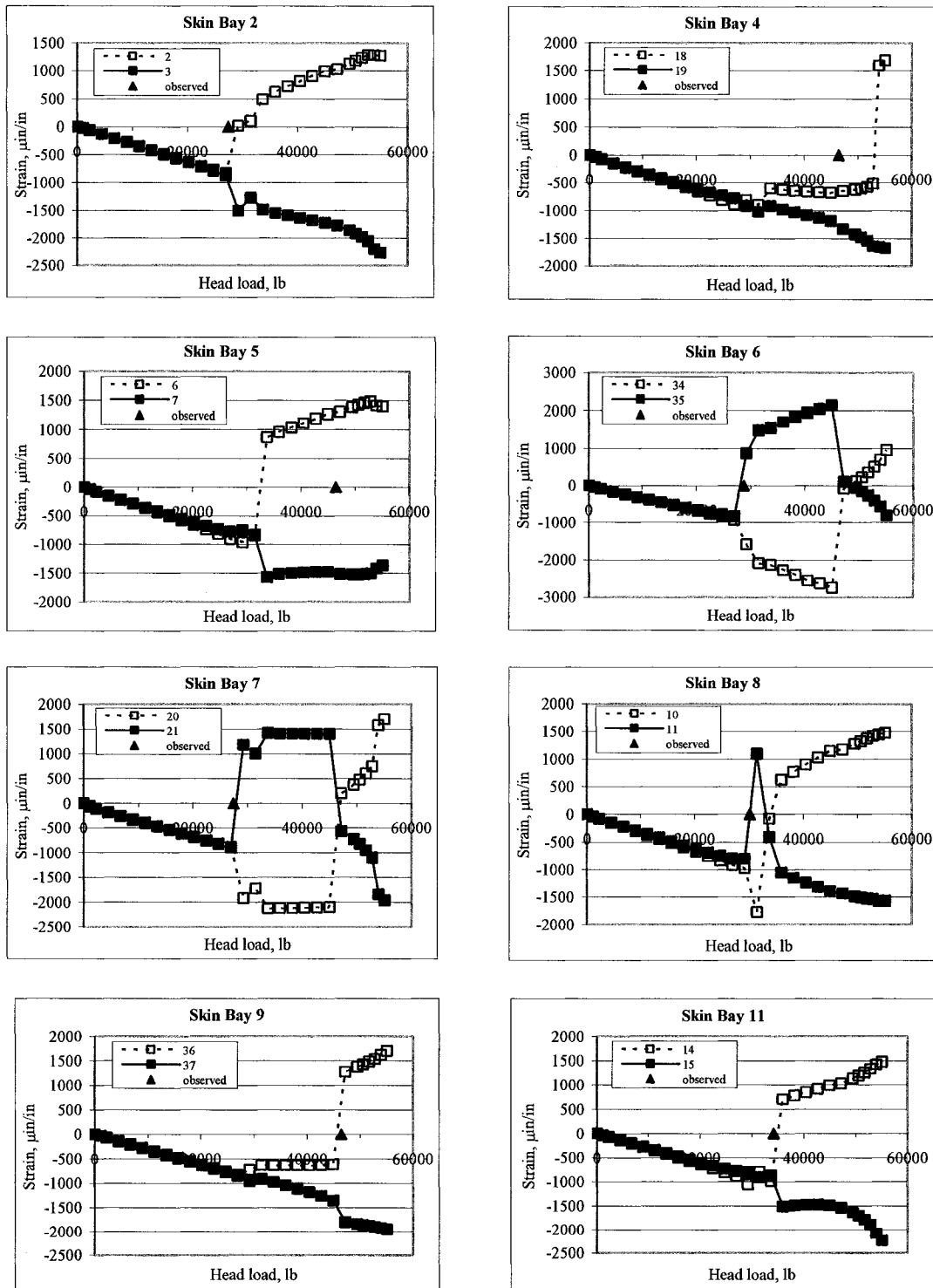


Figure 34. Strain-gage data for 617-1 panel skin bays

The sequence of skin buckling and the corresponding buckling load are listed in Table 9.

Panel 617-1		Panel 617-2	
Buckling load, lb.	Skin bay	Buckling load, lb.	Skin bay
27427	2,7	28326	3,12
28776	6	28776	9
30125	8	29113	5
33497	3	30574	7,10
34171	11	42826	11
45636	1	42826<load<54764	1,2,4,6,8
46435	4,5,9,10,12		
Failure load		Failure load	
55640		54764	

Table 9. Buckling loads of skin bays for panels 617-1 and 617-2 based on visual observations

As with previous panels, some skin-bay buckling load levels were not recorded as was the case for panel 617-2. The test report (Simmons, 2000) only stated that all additional bays buckled between 42,826 lbs and 54,764 lbs. The strain-gage data are in good agreement with the observed buckling loads except for skin bays 4 and 5, which both buckled much sooner based on strain-gage data than was seen visually. Skin buckling mode changes were detected from the strain-gage data in skin bays 6, 7, and 8.

The failure load for panel 617-1 was 55,640 lbs. Panel 617-1 failed in the middle of the panel halfway between frames 2 and 3. The failure mode was *stringer crippling* of stringers 1, 2, and 5, which buckled outward in the skin direction, and *Euler-column buckling* of stringers 3, and 4, which buckled inward in the stringer direction. The crippled stringers failed in the top of the hat-section. Crippled stringers 1 and 2 bounded

the bay where skin-bay buckling was first observed and showed crippling of both small lips of the riveted flanges of the inverted hat stringer. Strain-gage data for the riveted flanges for stringers 3, 4, and 5 shown in Figure 35 indicate buckling of the attach flanges between 29,000 lb and 33,700 lb.

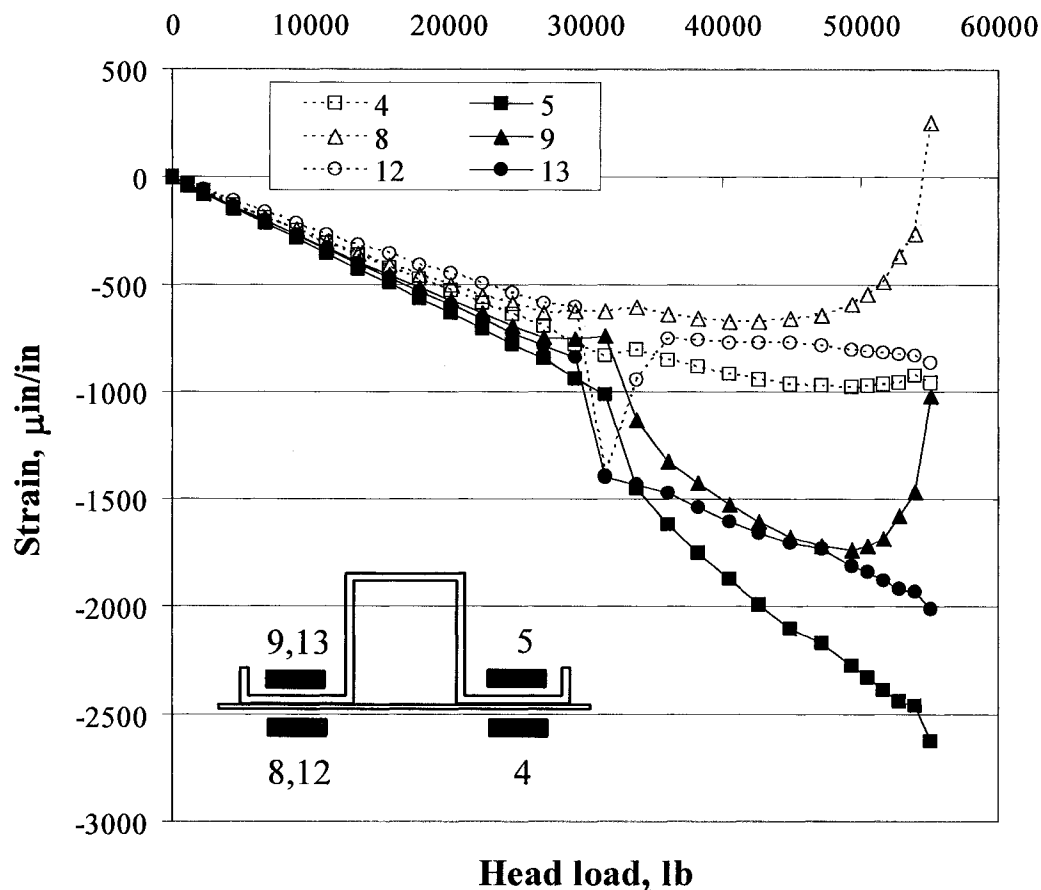


Figure 35. Stringer attach flange strain-gage data for panel 617-1

The failure load for panel 617-2 was 54,764 lbs. The failure mode for panel 617-2 was the same as panel 617-1 except that only one stringer showed crippling of both small lips of the riveted flanges. The exterior and interior sides of panel 617-1 are shown in Figures 36 and 37, respectively, after panel failure has occurred. Stringers 3, 4, and 5 on the

interior of panel 617-1 after failure are shown in Figure 37. Stringers 2, 3, and 4 on the interior of panel 617-2 after failure are shown in Figure 38. No rivet failure or rivet pull through was evident in either test.

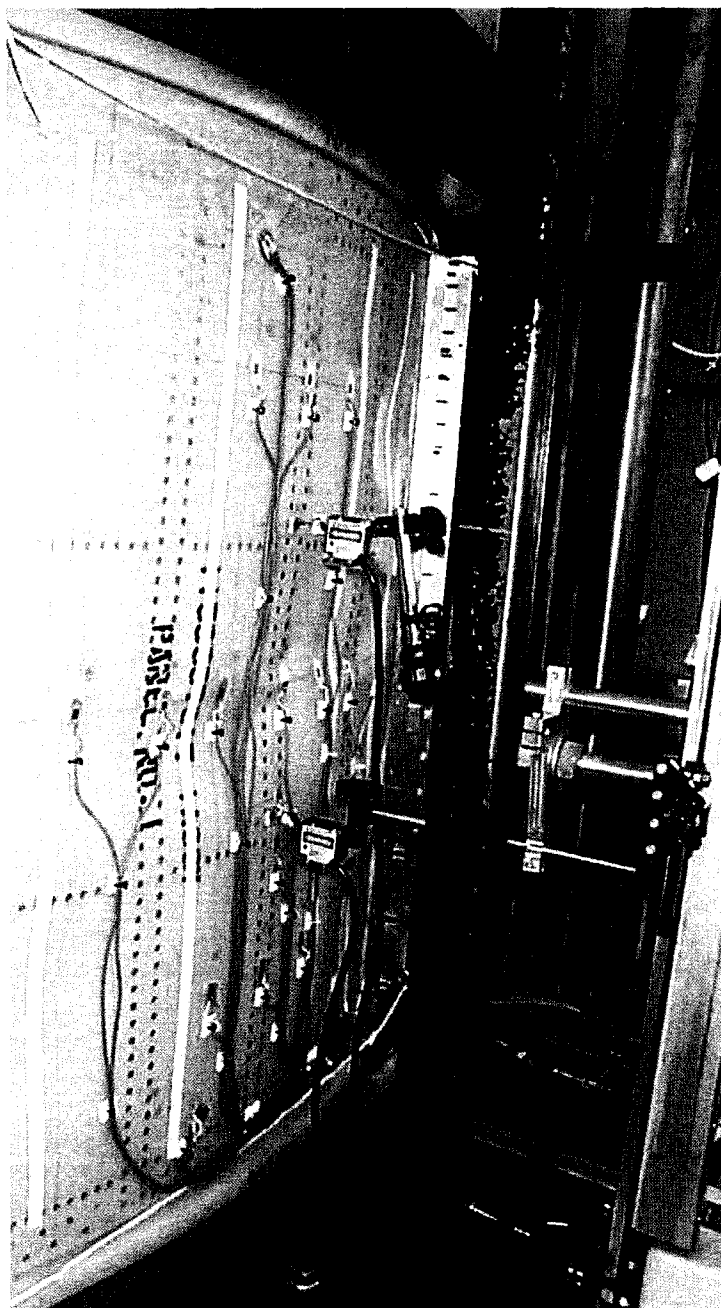


Figure 36. Exterior view of failed section of panel 617-1

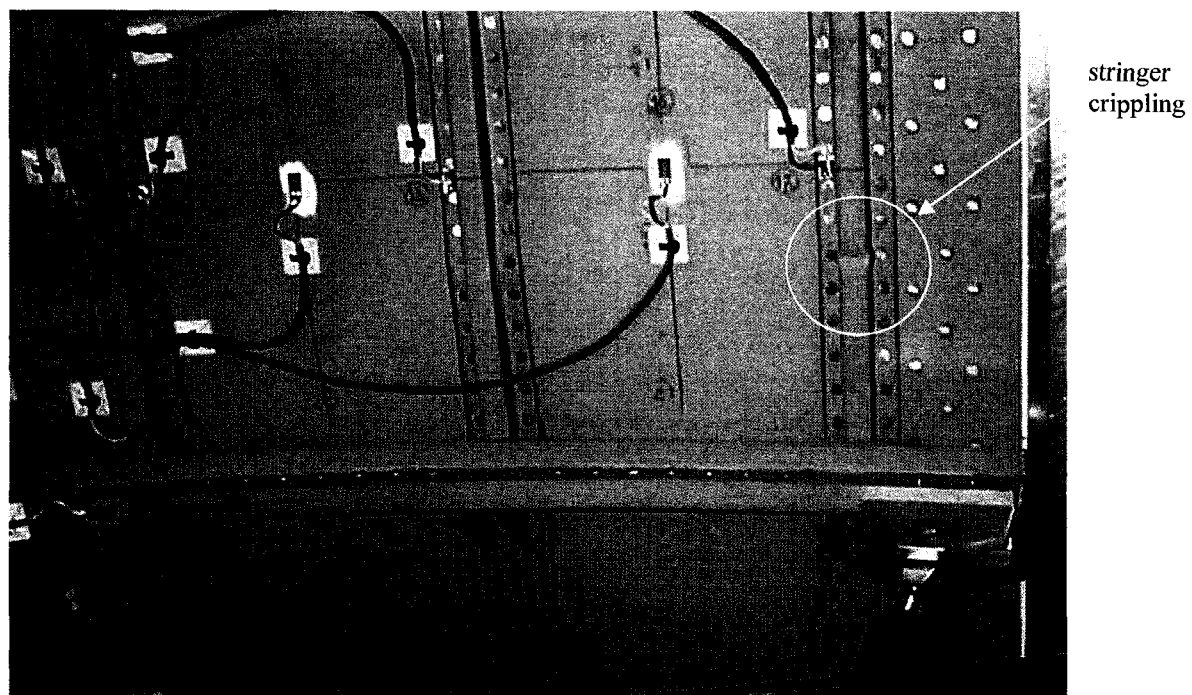


Figure 37. Interior view of failed section of panel 617-1

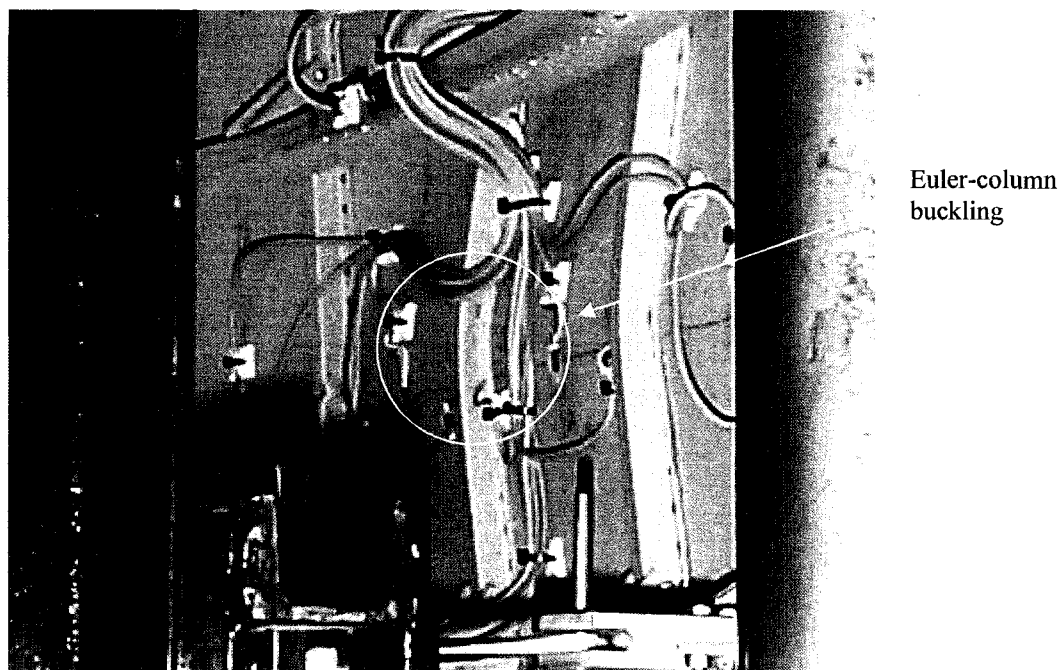


Figure 38. Interior view of failed section of panel 617-2

3.5 Test Results Summary

A summary of the test buckling and failure loads and failure modes is shown in Table 10. The cross-sectional area of a single skin-bay midway between two frames is also shown in Table 10. This area includes the stringer area plus the skin and doubler area measured from the centerline of the skin bay on either side of the stringer. For this set of panels, the failure load increases as the skin-bay cross-sectional area increases. The two panel configurations having the smallest cross-sectional area (614 and 615) fail due to stringer crippling, and the panel with the largest skin-bay cross-sectional area (616) fails due to Euler-column buckling. The panel in the middle (617) experiences both stringer crippling and Euler-column failures. Stringer crippling failures are most likely to occur in the bay where skin-bay buckling first occurs, while Euler-column failures always occur in the center of the panel where the end fixity provided by the frame is the least. All of the panels have significant postbuckling strength, and none experience any rivet failures or fastener pullout.

Panel #	Skin thickness, in. ²	Stringer thickness, in. ²	Single skin-bay cross-sectional area, in. ²	Buckling load, lbs.	Failure load, lbs.	Failure mode
614-1 614-2	0.040	0.025	0.383	8318 7868	28821 28551	stringer crippling, inter-rivet buckling
615-1 615-2	0.040	0.025	0.445	13039 12365	29787 29563	stringer crippling
616-1 616-2	0.040	0.063	0.709	31473 39342	78684 82730	Euler-column buckling of stringers
617-1 617-2	0.063	0.025	0.556	27427 28326	55640 54764	Euler-column buckling of stringers, stringer crippling

Table 10. Test panel failure summary

Although the 615 panels that include a waffle doubler have a cross-sectional area 16% greater than the 614 panels, they do not exhibit a significant increase in failure load. The waffle doubler does however support the skin bay and delays the onset of buckling in the panel. The load-end shortening response curves shown in Figure 39 summarize the behavior of all the panel configurations.

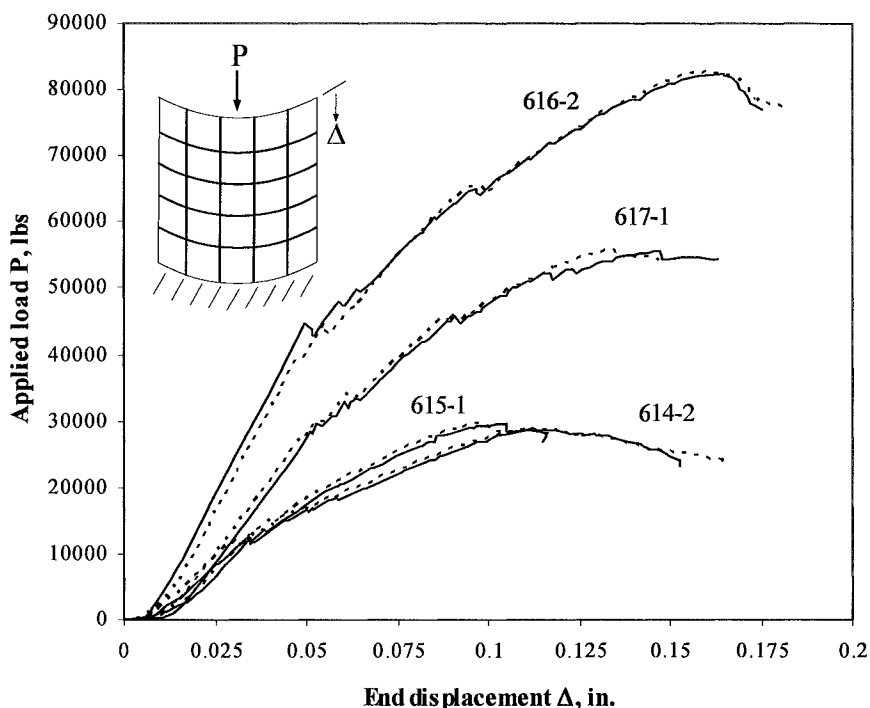


Figure 39. Load-end shortening response curves for all test panels

The 616 panel which has the thickest skin bay (.04 skin + .032 doubler) has the greatest initial stiffness and experiences initial panel buckling at a load higher than the failure load of the thinner 614 and 615 panels. The thicker stringer (.063 in. instead of .025 in.) does not locally buckle or cripple. The failure load for the 616 panel is pure Euler-column buckling. The 617 panel has a thicker skin than the 614 and 615 panels and thus

has a higher initial panel buckling load. The inverted hat stringers have more stability than the open hat stringers of the 614 and 615 panels. This results in the 617 panel failing in Euler-column buckling of the center stringers. The 617 panel failure load is almost twice that of the 614 and 615 panels that both fail due to stringer crippling. Therefore, in areas of high compression loads, the most desirable panel configuration is one with either a thick open hat stringer or a thinner inverted hat stringer. Both offer greater stability.

SECTION 4

BASELINE NUMERICAL STUDIES

An extensive assessment of the failure prediction capability of three stiffened-panel analysis tools is presented. The three analysis tools, PAGE, PANDA2, and STAGS, are used to analyze a generic panel configuration (i.e., stiffened panels between two frames), subject to a compression load. The panel configuration is similar to panels 617-1 and 617-2 discussed in Section 3.4.5. The 617 configuration is chosen because it has inverted hat stringers, and therefore meets the requirements to be analyzed with PANDA2. The panel response is studied using both a single-stiffener repeating section with symmetric boundary conditions for all tools and a larger three-stiffener repeating section for PANDA2 and STAGS – PAGE only considers a single-stiffener repeating section. The analytical comparison of the three tools identifies both global and local failure modes, determines the critical mode type for the panel, and assesses the accuracy and adequacy of each tool in determining the failure mode based on a comparison with test results from the Panel 617 configuration.

The remainder of this section is organized as follows. First, the geometry and boundary conditions of the panel configurations studied are defined. Second, the analysis results for the single-stiffener case are presented for the PAGE analysis tool. Third, the PANDA2 results for both the single-stiffener case and the multi-stiffener case are discussed. Then the STAGS results for both the single-stiffener case and the multi-

stiffener case are discussed. Finally, a summary of all results are presented and compared to the test results for Panels 617-1 and 617-2.

4.1 Geometry, Boundary Conditions, and Loads

The repeating element of the stiffened panel has a length of 12 in. (segment between two frames), a 47-in. radius, and an arc length of 7.55 in. The skin is made of .063-in.-thick 2024-T3 clad aluminum, and the stiffener is made from .025-in.-thick 7075-T6 clad aluminum. The stiffener is modeled as either continuously attached to the skin as is the case for a bonded stiffener, or attached to the skin at discrete points as in a mechanically fastened connection. The 617-1 and 617-2 test panels have mechanically-fastened stiffeners. The single-stiffener repeating panel and the larger multiple-stiffener panel with labeled dimensions are shown in Figure 40.

The boundary conditions for the panel section depend on the analysis tool. For the PAGE analysis tool, the boundary conditions depend upon the failure mode being analyzed. For the PANDA2 analysis tool, simply supported boundary conditions along all four sides of the panel are assumed. For the STAGS finite element analysis tool, the panel is defined to have essentially symmetry boundary conditions on all four sides. In addition, the out-of-plane displacement is restrained on the transverse edges to simulate the restraint of the frames. The longitudinal displacement is restrained on the bottom edge of the panel, and the longitudinal displacement along the top edge of the panel is uniformly applied (i.e., uniform end shortening). The boundary conditions for the STAGS analysis models are shown in Figure 40.

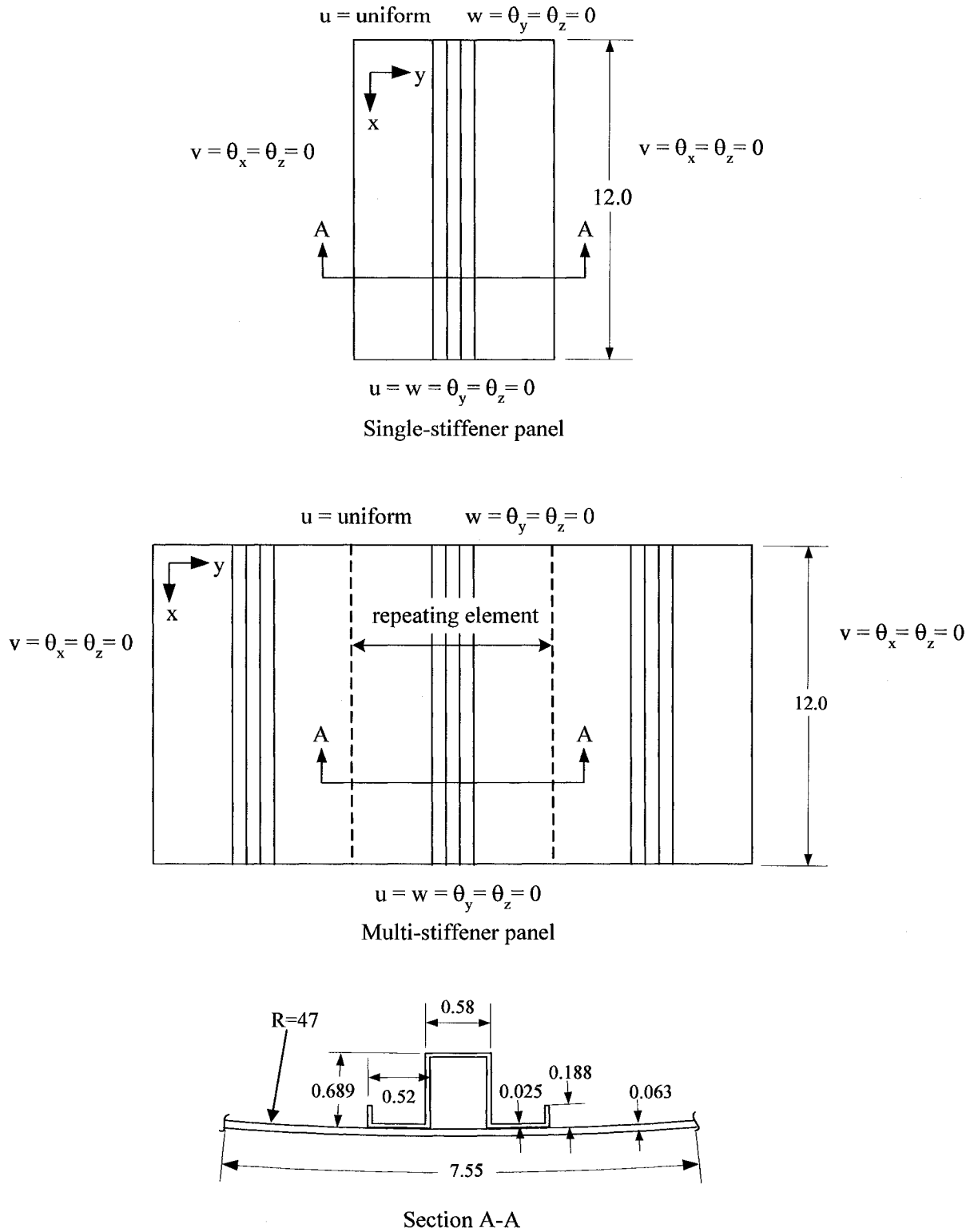


Figure 40. Analysis panel configurations (all units are in inches)

The loading in each case is uniform end shortening. To compare the calculated buckling and failure loads for the analysis models considered with the observed test loads from Section 3, it is assumed that each of the five repeating elements of the panel (see Figure 17) carries an equal share of the total load. Hence, the single-stiffener panel models should have a failure load of 11,128 lbs. or one fifth the failure load for the complete panel (see Table 10).

4.2 PAGE Results

PAGE failure predictions are based on closed-form equations that apply only to curved hat-stiffened panels. Special limitations on the panel geometry are recommended in order to keep the design conservative. The single-stiffener panel model fits the PAGE analysis and design requirements. However, for a conservative design, certain criteria

need to be observed as discussed in Appendix A. One criteria is that $\frac{t_{stiffener}}{t_{skin} + t_{doubler}} \geq 0.5$.

The current test panel configuration does not satisfy this geometric criterion in that

$$\frac{t_{stiffener}}{t_{skin} + t_{doubler}} = \frac{.025}{.063} = 0.397. \text{ Since PAGE is being used as an analysis tool in this case}$$

rather than a design tool, the actual test panel section geometry is used. The accuracy of the PAGE failure predictions is evaluated with this conservative design criterion ignored.

The PAGE analysis of the single-stiffener panel section predicts that the skin will buckle at a load of 5,917 lbs, redistributing the load to the stringer. It predicts that the panel section will ultimately fail due to Euler-column buckling of the stiffener at 7,677 lbs. The Euler-column buckling load is determined using an analysis that accounts for

exceeding the proportional limit of the stiffener material. The overall compressive stress-strain relationship of the stiffener material is represented using the modified Ramberg-Osgood equation (Ramberg and Osgood, 1943). The next closest failure mode is skin wrinkling that occurs at 9,212 lbs. Skin wrinkling occurs when local buckles in the skin run across the stiffeners and extend into adjacent skin bays, distorting the attachment flanges. The distortion of the stiffener flange leads to the ultimate failure of the panel. Fastener failure and the effects of fastened connections are not included in the PAGE analysis.

4.3 PANDA2 Results

PANDA2 includes specific stiffener configurations for stiffened panel analysis. The stiffener on the 617 panel configuration includes 0.188-inch-high lips on the flanges of the stiffener (see Figures 40 and 41(a)). These lips are not included in the PANDA2 closed-hat stiffener configuration. Therefore, three different configurations shown in Figure 41 are analyzed using the PANDA2 analysis tool. For the first configuration, the lips are simply not included in the analysis (see Figure 41(b)). For this case, the attach flange will not have the benefit of the extra stiffness that the lip provides. This approach should therefore give the most conservative answer. For the other two configurations, the attach flanges are modified such that the total area of the actual stringer is preserved. In one case the flanges are elongated by length of lip (see Figure 41(c)), and in the other, the flanges are thickened to include area of lips (see Figure 41(d)). For either case, the overall height of the stiffener is constant.

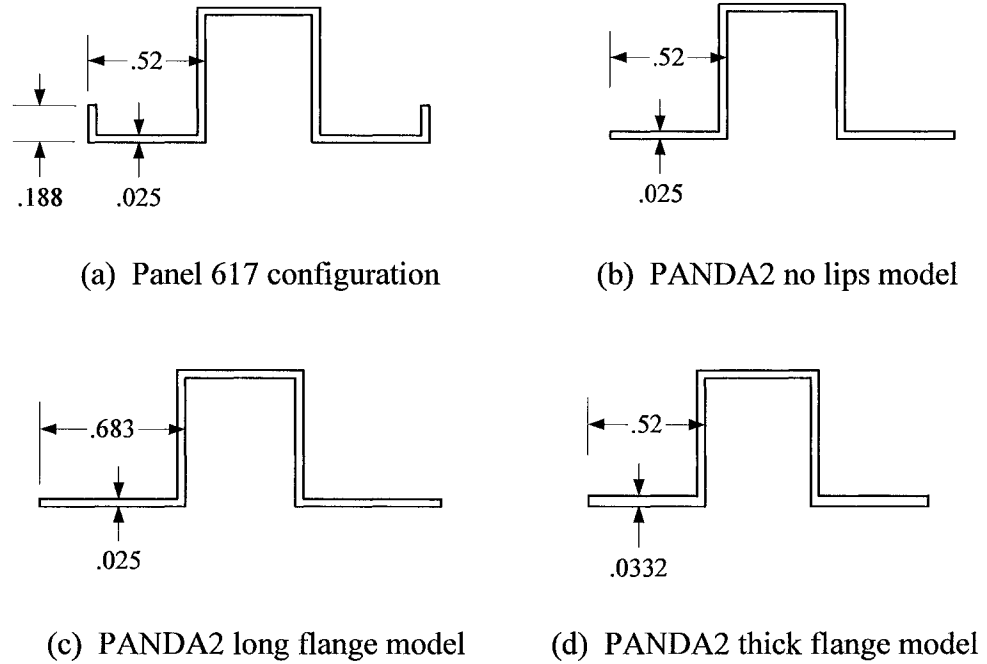


Figure 41. Stiffener configurations for PANDA2 analysis

Analyzing a single-stiffener panel section is not recommended in PANDA2, but for comparison purposes, the single-stiffener panel section is analyzed. The lowest buckling loads for the skin and stringer for all three lip approximations are shown in Table 11. The stringer configuration with the lips removed has the lowest skin and hat-buckling loads. When the lips are accounted for by either lengthening or thickening the attach flanges, the buckling loads increase approximately 4-9%.

Failure load, lbs			Failure mode
no lips	long flange	thick flange	
9052	9468	9468	Local skin buckling
11710	11793	12707	Hat buckling

Table 11. PANDA2 buckling predictions for a single-stiffener panel section

Following PANDA2 user guidelines, a three-stiffener section panel is analyzed using the same three stringer configurations shown in Figure 41. The results of this analysis are shown in Table 12.

Failure load, lbs			Failure mode
no lips	long flange	thick flange	
3006	3148	3131	Local skin buckling
8986	9019	9028	Hat buckling

Table 12. PANDA2 buckling predictions for a three-stiffener panel section

As expected, the buckling loads for the stringers without any lips are lower than the buckling loads for cases with the area of the lips included on the attached flanges. As with the single-stiffener panel configuration, there is very little difference in buckling loads between the two methods of incorporating the lips into the stringer configuration. The local skin buckling values are much less for the three-stiffener analyses than the single-stiffener analyses because of the assumed edge restraints in PANDA2. The vertical edges of a PANDA2 panel are assumed to be simply-supported, therefore a single-stiffener analysis unreasonably constrains the panel in the center of a skin bay. For the single-stiffener analyses, the skin buckles in four axial half-waves versus two

axial half waves for the three-stiffener analyses. The failure loads for the three-stiffener analyses are approximately 25% less than the failure loads for the single-stiffener analyses. Although the deformed shape at failure load of the stiffener is the same for both the single- and three-stiffener analyses, the magnitude of the deflections are larger for the three-stiffener analyses resulting in lower failure loads.

4.4 STAGS Results for Single-Stiffener Repeating Section

STAGS results are presented for four different modeling approaches. First, the smeared-stiffener approach is studied wherein the stiffness of the hat stiffeners is “smeared” over some portion of the panel skin. Second, the discrete-stiffener approach is studied wherein the stiffener is treated as a discrete beam with stiffness “lumped” along a longitudinal line. Third, the branched-plate approach is studied where each leg of the stiffener is modeled using shell elements. In one case, the stiffeners are assumed to be consistently and uniformly bonded to the panel skin. In another case, the stiffener attachment fasteners are explicitly included in the model.

The baseline finite element discretization for the panel skin for each stiffener modeling approach is the same. The panel skin has seventy-two 4-node quadrilateral elements along the panel length, sixteen 4-node quadrilateral elements from the panel edge to the attachment flange and twelve 4-node quadrilateral elements across the stiffener region. A total of 3,168 quadrilateral elements and 3,285 nodes are used in the baseline model of the panel skin. In the smeared-stiffener approach, the size of the computational problem is defined by the number of nodes and elements in the panel skin model. The same is

true for the discrete-stiffener approach. However, in the branched-shell approach, each segment of the hat stringer is modeled using 4-node quadrilateral elements. For the bonded- and fastened-stiffener models, the total number of 4-node quadrilateral elements is 4,896, and the total number of nodes is 5,548. For the fastened-stiffener model, an additional 46 fastener elements are included, as well as contact elements between the skin and stiffener.

For each modeling approach, finite element discretization studies are performed to assess the ability of the mesh to capture the response of the panel adequately. Linear eigenvalue analyses are conducted for each level of mesh refinement. In all cases, a doubling of the baseline mesh refinement selected for this study does not change the linear buckling mode shapes, and results in less than a 0.3% change in the predicted linear buckling loads of the panels. Thus the baseline mesh refinement selected for these studies is deemed adequate and computationally efficient for predicting the nonlinear behavior of the single-stiffener panels. For these nonlinear analyses, buckling is said to occur when there is a drop in the load as indicated in the load versus end-shortening response curve, and there is one negative root in the stiffness matrix, in addition to the negative roots associated with each Lagrange constraint in the finite element model. After initial buckling, the load will eventually begin to increase again, and the stiffness matrix will no longer contain negative roots associated with the panel's nonlinear response. When the load decreases to zero, and a negative root is present in the stiffness matrix, failure is said to have occurred. In some cases, the load does not drop all the way to zero but instead reaches a point where a converged nonlinear solution cannot be found. If additional

negative roots still exists in the stiffness matrix at this point, failure is also assumed to occur.

4.4.1 Smearred Stiffener Properties

Using a smeared-stiffener-property option in STAGS, a single-stiffener repeating section model loaded in compression is analyzed to determine the predicted maximum load achieved before failure of the panel. Using the smeared-stiffener option, only elastic material response is permitted by STAGS. The stiffener cross-sectional properties, spacing, and eccentricity are taken into account in the analysis. The model discretization is shown in Figure 42. The model consists of 3,168 E410 4-node, C^1 quadrilateral shell elements, 3,285 nodes, and 19,710 active degrees of freedom. The center strip of the model, where the stiffener is located, has a mesh density consistent with the subsequent models. The computational cost of this finite element analysis model is driven by the finite element discretization of the panel skin. Because of the smeared-stiffener approximations, only global panel behavior, similar to an orthotropic plate, can be determined – local details of the stiffener are “smeared” over the panel surface.

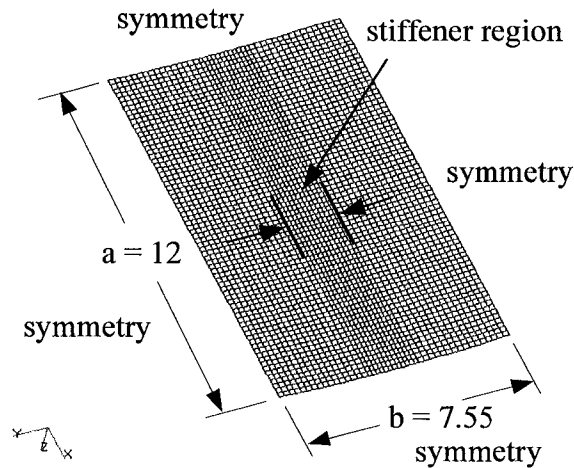


Figure 42. Smeared-stiffener finite element model

For the first smeared analysis approach, the stiffener properties are smeared over the width of the entire single-stiffener section. The calculated linear eigenvalue for buckling is 19,732 lbs. The mode shapes corresponding to this eigenvalue and the next 3 modes are shown in Figure 43. All four modes have one half wave in the axial direction, which is symmetric about the centerline of the section. The first mode has one full wave in the circumferential direction that is symmetric about the centerline of the section. Modes 2 and 3 have one half wave and three half waves, respectively, in the circumferential direction that are antisymmetric about the center of the section. Mode 4 has two full waves in the circumferential direction that are symmetric about the section centerline.

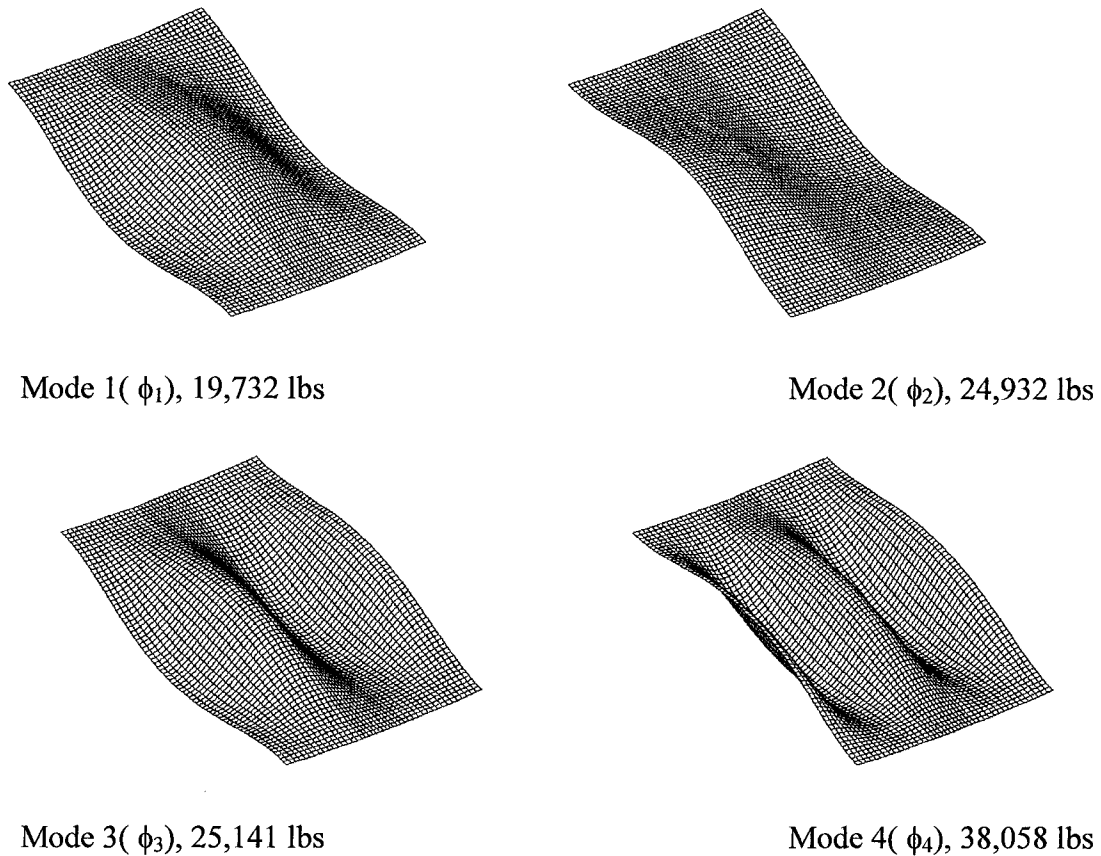


Figure 43. Linear eigenmodes and buckling loads for smeared-stiffener model

Using a nonlinear analysis, the maximum load achieved before failure of the section under uniform compressive load and without any initial geometric imperfections is predicted to be 49,087 lbs – over twice the initial buckling load obtained from a linear eigenvalue analysis. This result indicates that the panel should have significant postbuckling capability. The elastic nonlinear response for the case without imperfections is a smooth behavior typical of Euler-column collapse as shown in Figure 44. The predicted failure shape of the single-stiffener repeating section without the geometric imperfection is shown in Figure 45(a).

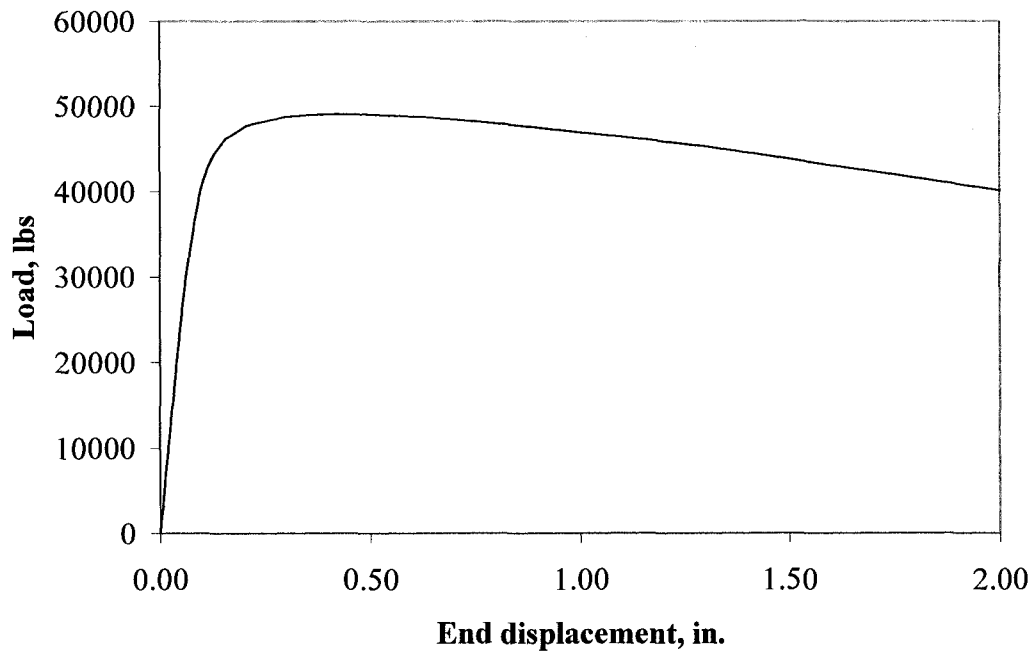


Figure 44. Load-shortening curve for perfect single-stiffener repeating section model with smeared-stiffener properties

The nonlinear analysis is repeated with an initial geometric imperfection defined by a linear combination of the first four linear eigenmodes (those shown in Figure 43). The equation for the geometric imperfection is as follows:

$$\{w_0\} = 0.5t_s\{\phi_1\} + 0.25t_s\{\phi_2\} + 0.125t_s\{\phi_3\} + 0.125t_s\{\phi_4\} \quad (1)$$

where:

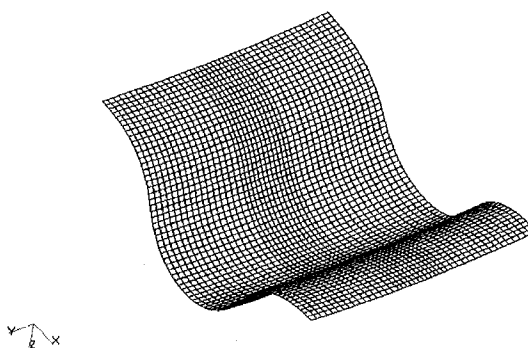
$\{w_0\}$ = initial geometric surface imperfection

t_s = skin thickness

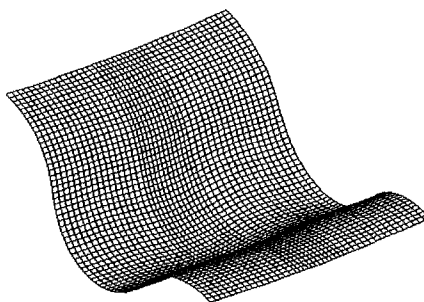
$\{\phi_i\}$ = mode shape corresponding to the i^{th} eigenvalue

Note that STAGS normalizes the eigenvectors by their maximum component (i.e., largest component is +/- 1). For these four modes, the largest component is associated with an out-of-plane displacement degree of freedom, and hence each mode contributes to the

imperfection definition such that the maximum surface imperfection is at most equal to the panel thickness. The predicted maximum load for the imperfect single-stiffener repeating section model is 48,786 lbs which is only slightly less than the maximum load of the perfect panel. The predicted deformed shape of the section at failure with exaggerated displacement is shown in Figure 45(b). The failure mode of the panel does not change due to the addition of the initial geometric imperfection.



(a) without imperfection



(b) with imperfection

Figure 45. Failure shapes from nonlinear analyses for smeared-stiffener section with and without geometric imperfection

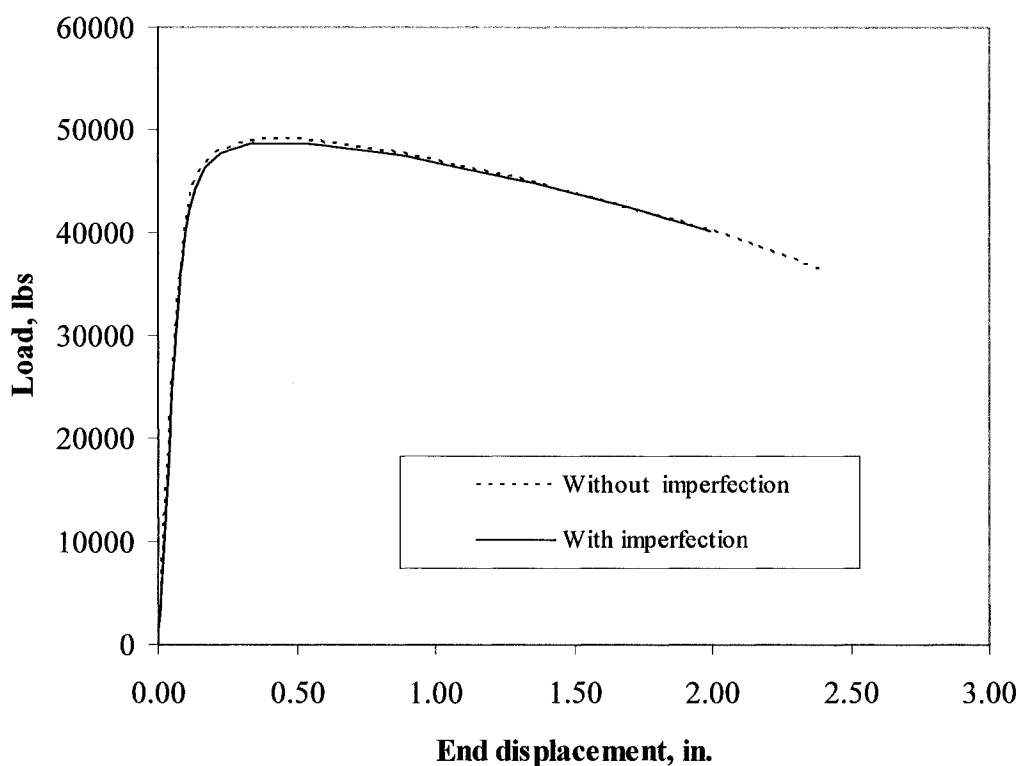


Figure 46. Load-shortening curves for single-stiffener repeating section model with globally-smearred stiffener properties

The load-shortening curves for the perfect and imperfect sections are shown in Figure 46. The imperfect panel collapses in an Euler-column-type failure similar to the section without the imperfection and reaches a maximum load only slightly lower than the panel without imperfections.

The buckling and maximum loads of the smeared-section analysis seem unreasonably high, because a smeared-modeling approach is more appropriate for stiffeners with less attachment to the panel skin (i.e., effective width issue). Therefore, to better account for this approximation, the analyses are repeated with the stiffener properties smeared only over the stiffener region of the section shown in Figure 42.

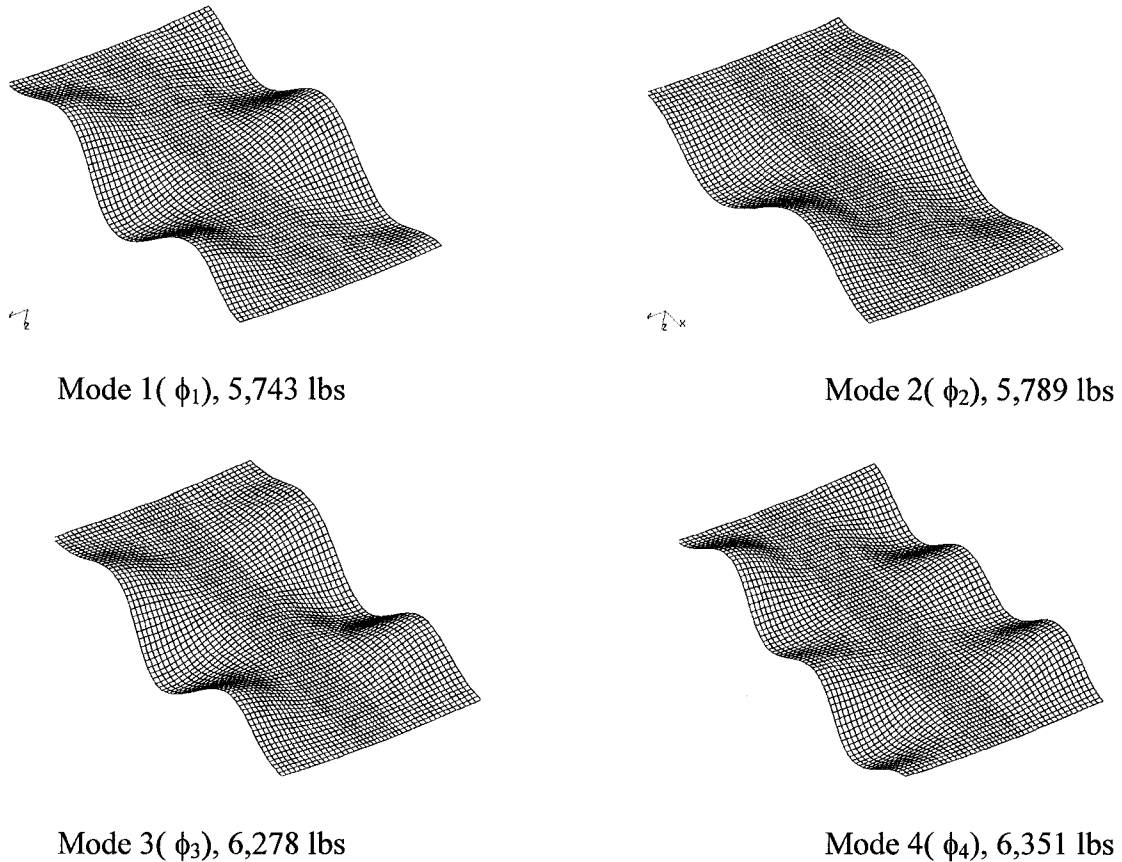


Figure 47. Linear eigenmodes and buckling loads for smeared-stiffener model where stiffener properties are smeared locally over stiffener region

The calculated linear eigenvalue for buckling is 5,743 lbs. This value is more in line with the test panel buckling load. The mode shapes corresponding to the first four modes are shown in Figure 47. The mode shapes for the locally stiffened section show deformations in the skin areas while the stiffener region remains relatively undeformed. This result gives a better approximation for the actual stiffness distribution across the panel. Using a nonlinear analysis, a load of 6,284 lbs is reached. At this point, a nonlinear eigenvalue analysis is performed, and the mode shapes obtained are shown in Figure 48.

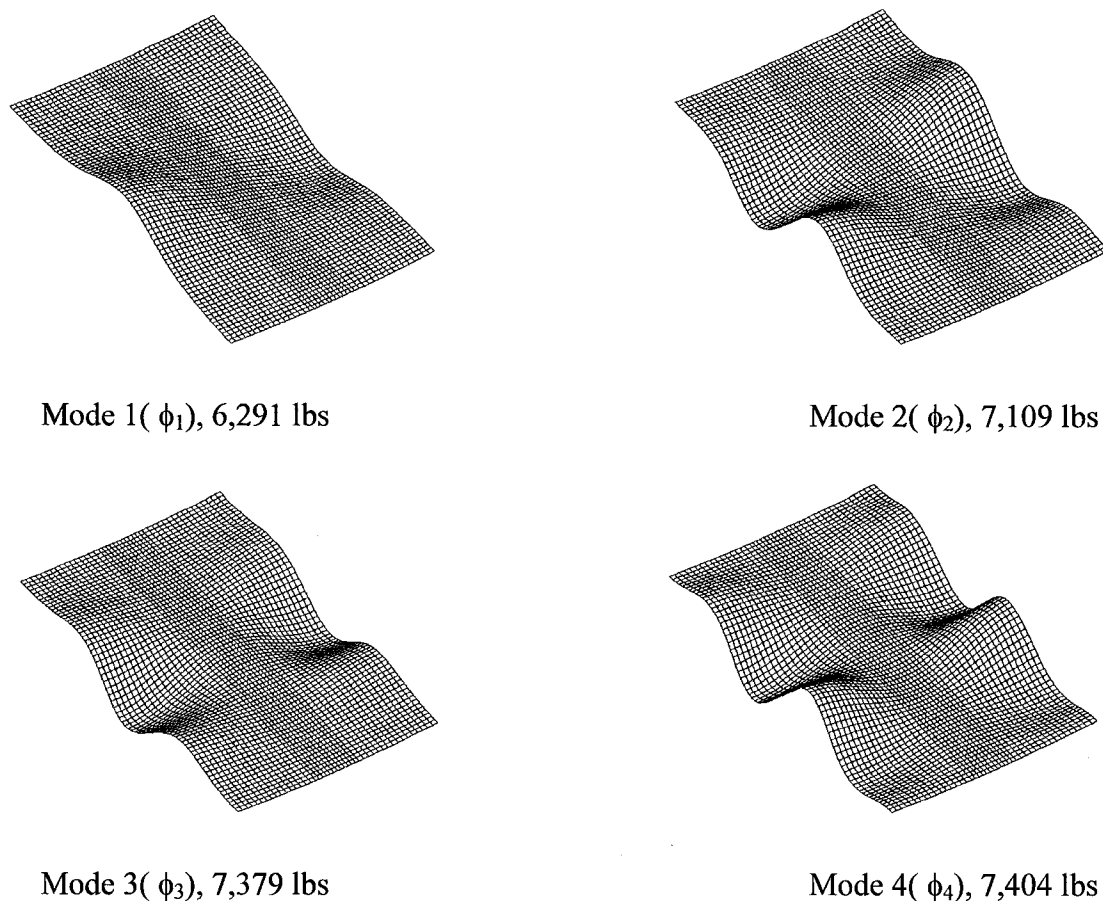


Figure 48. First four eigenmodes and buckling loads for the locally smeared-stiffener section calculated from a nonlinear equilibrium state

In order to push the finite element analysis beyond the skin buckling limit point, the single-stiffener repeating section models assumed to have an initial geometric imperfection formed by a linear combination of the first four eigenmodes (shown in Figure 48) calculated from the nonlinear equilibrium state at 6,284 lbs. The equation for this imperfection is the same as for the section with the stiffener smeared globally (Eqn. 1). The elastic nonlinear analysis is repeated from zero load with this imperfection, and a maximum load of 27,392 lbs is obtained.

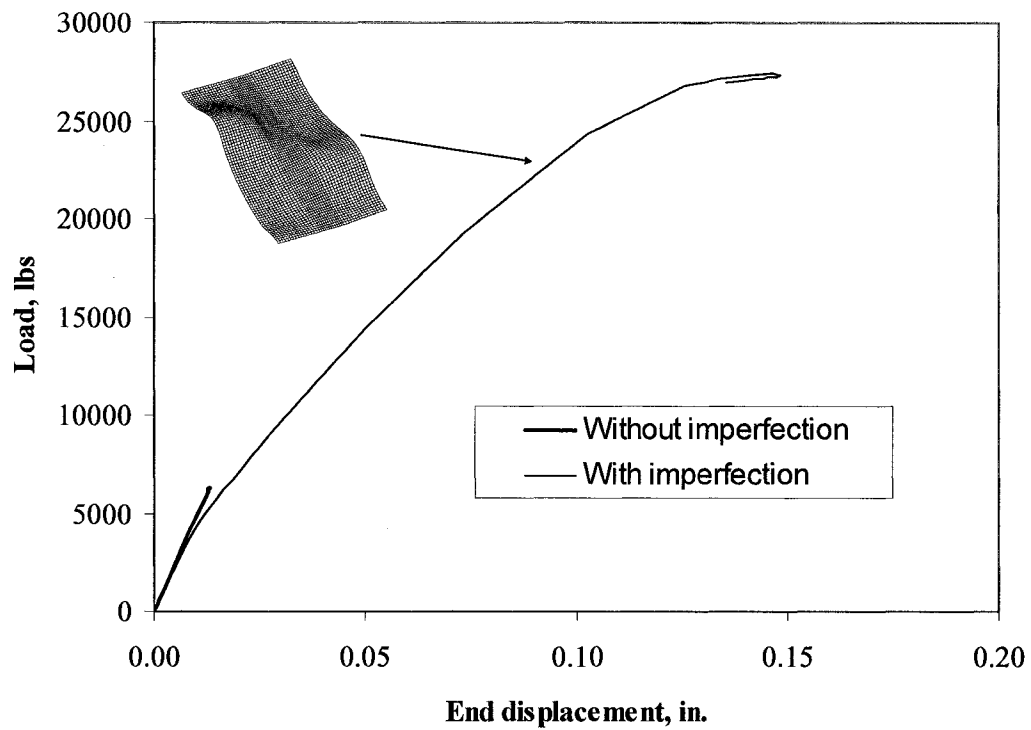


Figure 49. Load-shortening curves for single-stiffener repeating section model with locally smeared-stiffener properties

The load-shortening curve and deformed shape along the imperfect section load path are shown in Figure 49. Notice that at the maximum load level, the total end-shortening for the locally-smeared-stiffener approach is approximately 0.15 in., as compared to 0.54 in. for the globally-smeared approach. In addition, the maximum load for the locally-smeared-stiffener analysis is almost half that of the globally-smeared approach. These results indicate the sensitivity of the nonlinear response for these hat-stiffened panels to modeling assumptions. Apparently the smeared stiffener approach is unconservative for this stiffener configuration.

4.4.2 Discrete Stiffener

The next level of finite element modeling consists of the skin section and a continuously attached beam stiffener with cross-sectional properties equivalent to the actual stiffener cross-sectional geometry. This model is shown in Figure 50. The model consists of 3,168 STAGS E410 4-node, C^1 quadrilateral shell elements, 72 STAGS 210 2-node C^1 beam elements, 3,285 nodes, and 19,710 active degrees of freedom. Notice that the discrete beam model and the smeared-stiffener model have the same computational size in terms of number of active degrees of freedom. The center strip of the model where the stiffener is located has a mesh density consistent with the other finite element models used in the single-stiffener repeating section analyses. The hat stiffener is modeled as a discrete beam located at the center of the section and offset in the z -direction where z is normal to the section surface. In STAGS, the rectangular subelement option is used to define the stiffener properties so that plasticity can be included. The stiffener is defined using seven rectangular subelements as shown in Figure 51. Stress output can be obtained at the corners of each subelement.

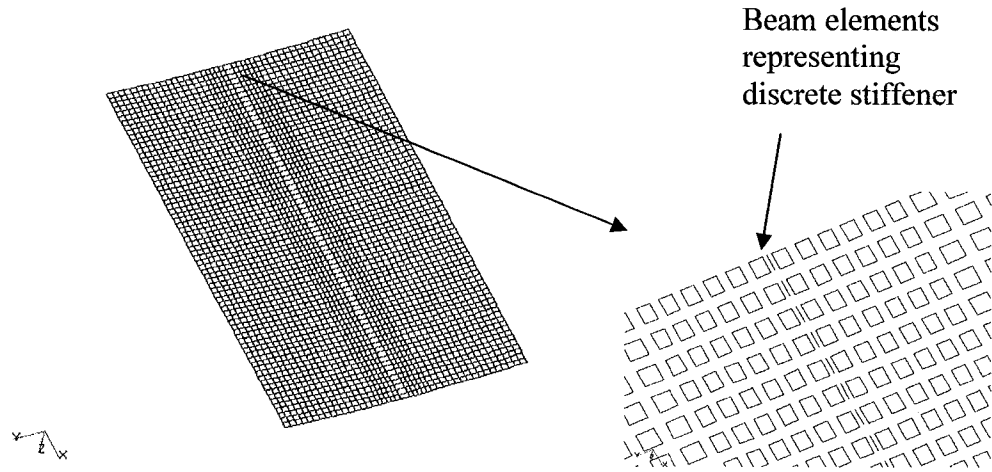


Figure 50. Discrete stiffener finite element model

However, the location of the discrete beam on the section is along a single longitudinal line in the section center. The local influence of the inverted hat stiffener flanges on the skin response is ignored.

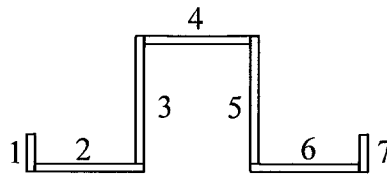


Figure 51. STAGS rectangular subelement stiffener definition

The single-stiffener repeating section model with a discrete-beam stiffener predicts buckling and maximum load values significantly lower than the smeared-stiffener approach. The first buckling mode is skin buckling, and therefore the single-stiffener repeating section with the stiffener properties smeared into the skin has a higher buckling load. The linear buckling load for the discrete-beam model of the single-stiffener repeating section is predicted to be 4,788 lbs – approximately one tenth of the load

predicted by using the globally-smearred-stiffener modeling approach, but within 17% of the load predicted by the locally-smearred-stiffener modeling approach. The highest value achieved with an elastic nonlinear analysis without imperfections is 5,590 lbs. At 5,590 lbs, an eigenvalue analysis is performed and the nearest eigenvalue is determined to be 5,597 lbs. The mode shape corresponding to the first four eigenvalues calculated from the nonlinear stress state are shown in Figure 52. All of the eigenmodes are skin buckling modes. Because the hat stiffener is modeled as a discrete beam, it acts like a node line in the buckling modes (i.e., a line with zero out-of-plane displacements).

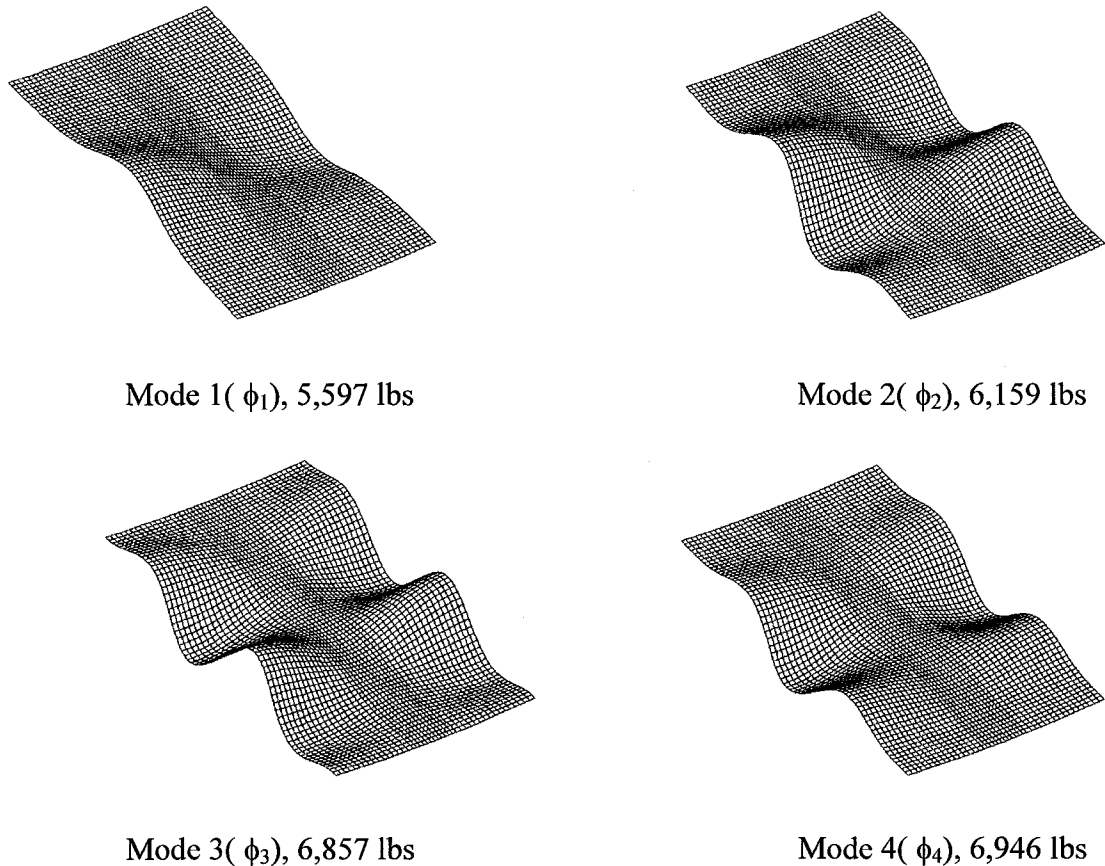


Figure 52. First four eigenmodes and buckling loads for the discrete beam model calculated from a nonlinear equilibrium state

In order to push the finite element analysis beyond the skin buckling limit point, the single-stiffener repeating section is assumed to have an initial geometric imperfection defined by a linear combination of the first four eigenmodes (shown in Figure 52) calculated from the maximum nonlinear load value of 5,590 lbs. Eqn. (1) is used to determine this imperfection using the same approach as used for the smeared approach. The elastic nonlinear analysis is repeated from zero load with this imperfection and a maximum load of 24,209 lbs is obtained. The load-shortening curve and deformed shapes along the load path are shown in Figure 53. Initially there is skin deformation (shape 1 in Figure 53), and at 22,395 lbs there is a load drop where the skin deflection pattern changes (shape 2 in Figure 53). Load continues to increase until a maximum load of 24,209 lbs is reached. At this load level the stiffener deforms out-of-plane and the panel is unable to carry additional load, as shown by the large increase in end-shortening with no increase in load level.

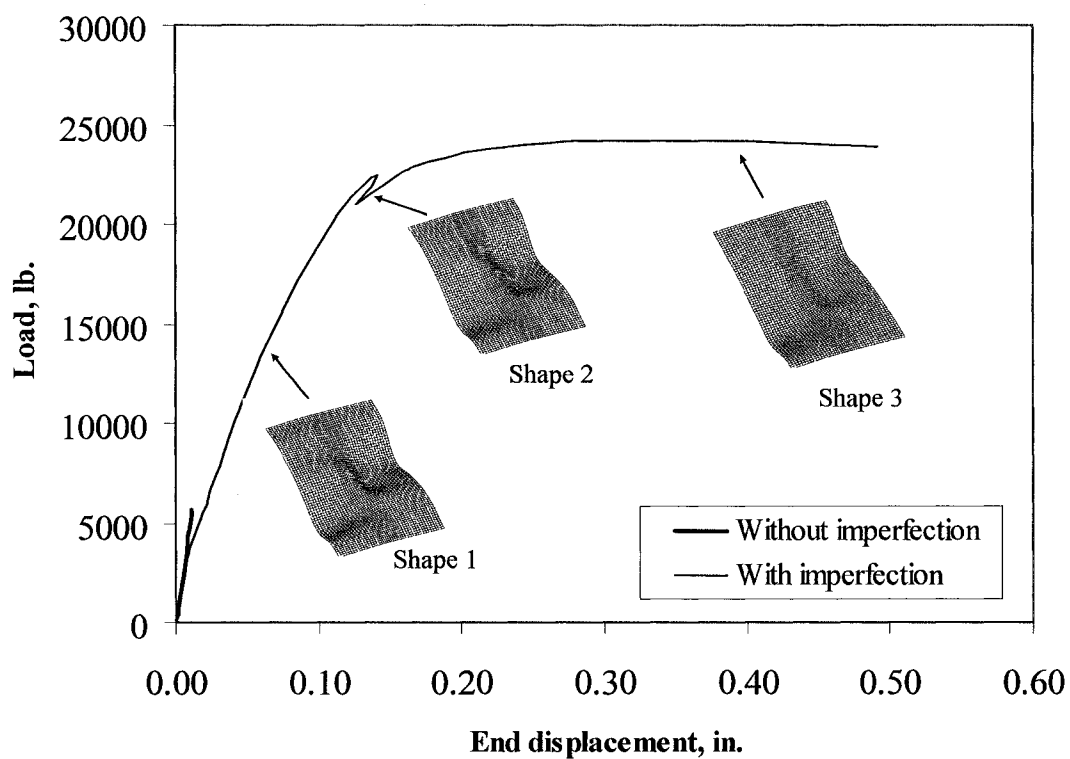


Figure 53. Load-shortening curve for single-stiffener repeating section model with discrete beam stiffener

If the same analysis is performed with elasto-plastic material properties applied to both the stringer and skin, the maximum load achieved before failure is predicted to be 10,599 lbs. The load-shortening curve with deformed shapes is shown in Figure 54 for both the elastic and elasto-plastic analyses.

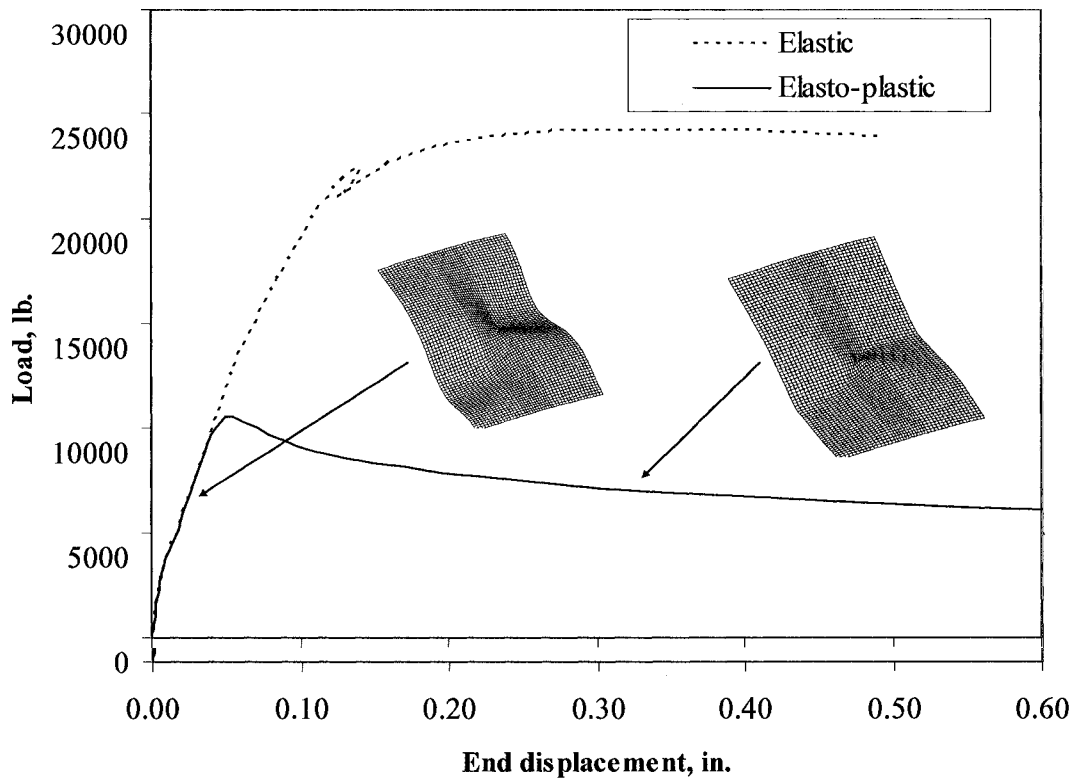


Figure 54. Load-shortening curve for single-stiffener repeating section model with discrete beam stiffener for elastic and elasto-plastic materials

The skin material begins to experience plastic deformation adjacent to the beam location at a load of 6,689 lbs and an end shortening of .025 in. The hat-stiffener begins to deform plastically at a load of 10,123 lbs and an end shortening of .0544 in. The area of the beam cross-section experiencing the plastic deformation is the attached flange of the closed-hat and the small lip extending from this flange. These areas are defined as subelements 1, 2, 6 and 7 in Figure 51. The area of the section where plastic deformation is most severe is shown in Figure 55. Failures of the section occur on either side of the stiffener and lead to a stiffener deformation that causes failure of the section. Failure of

the section is assumed to occur because as the load level decreases, the end-shortening of the section continues to increase at an increasing rate.

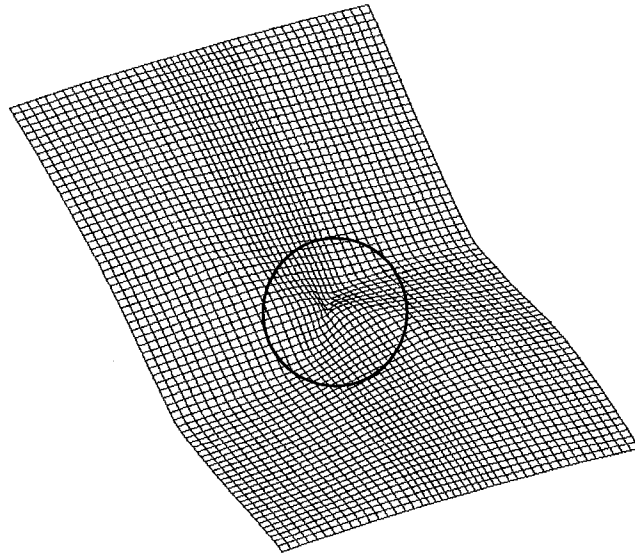


Figure 55. Plastic deformation of section with discrete beam stiffener

Again the modeling assumption based on the discrete stiffener approach leads to a computationally efficient model; however, it lacks sufficient resolution to capture the local stiffener distribution due to the hat-section flanges. Alternate modeling strategies could be employed by treating the lips as discrete beams, the attached flanges as a step increase in the skin thickness and the hat section as two independent and unconnected L-shaped discrete beams. This approach was not examined.

4.4.3 Branched-Shell Bonded-Stiffener

The next level of finite element modeling for the single-stiffener repeating section consists of the skin panel with a branched shell closed-hat stiffener that is continuously

connected to the skin (bonded-stiffener). The stiffener geometry is modeled explicitly, and LaGrange constraints are used to connect the stiffener flanges to the skin. Partial compatibility constraints available in STAGS are used to attach these branch plate segments of the skin and the stiffener attachment flange. All translations and rotations are constrained to be equal between each skin node and its corresponding stiffener node. The finite element mesh for this model is shown in Figure 56. The model consists of 4,896 STAGS E410 4-node, C^1 quadrilateral shell elements, 5,548 nodes, 1,168 constraints, and 33,288 active degrees of freedom.

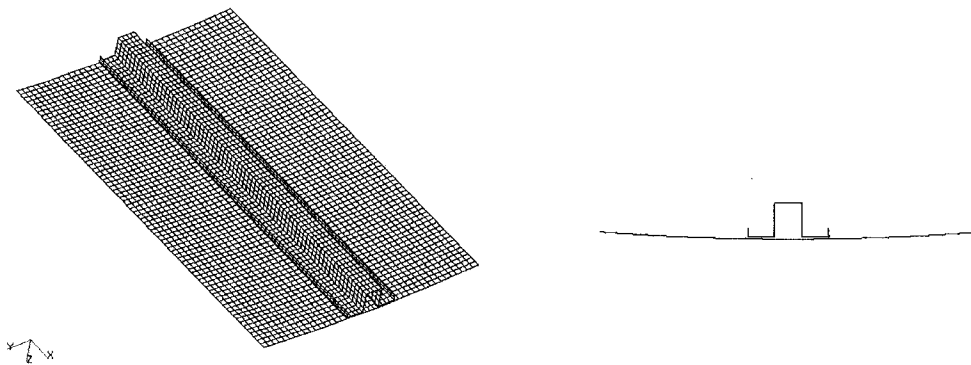


Figure 56. STAGS branched-shell bonded stiffener model

The linear buckling load is predicted to be 5,506 lbs and is within 100 lbs of the linear buckling load predicted by the discrete beam model. This buckling load corresponds to a skin buckling mode. The highest load value achieved with an elastic nonlinear analysis is 6,000 lbs. At 6,000 lbs, an eigenvalue analysis using this nonlinear stress state is performed, and the nearest eigenvalue is found to be at 6,137 lbs. The first four eigenmodes calculated from the 6,000-lb nonlinear stress state are shown in Figure 57.

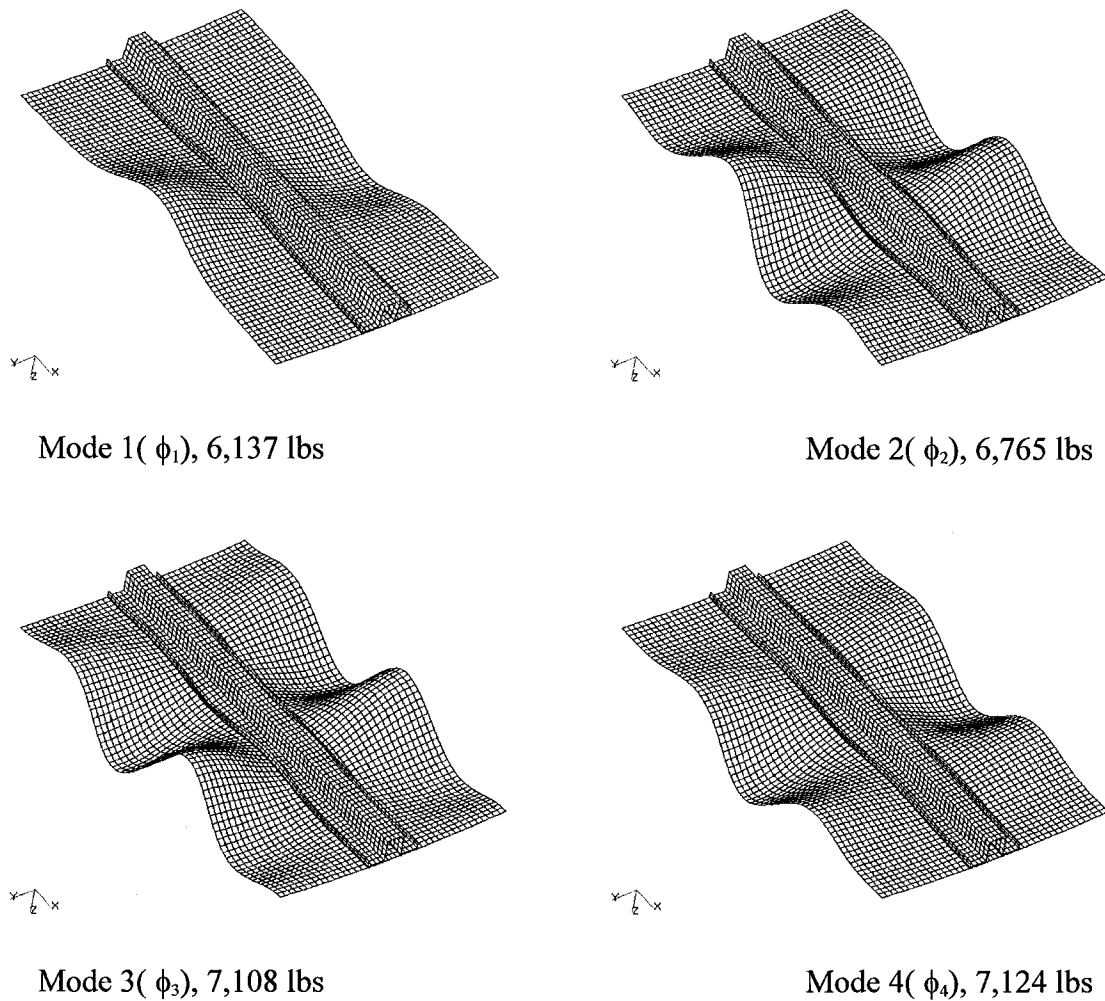
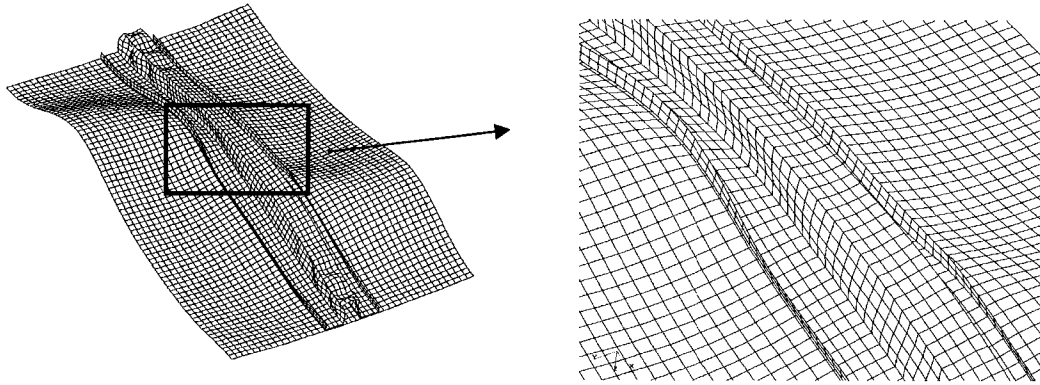


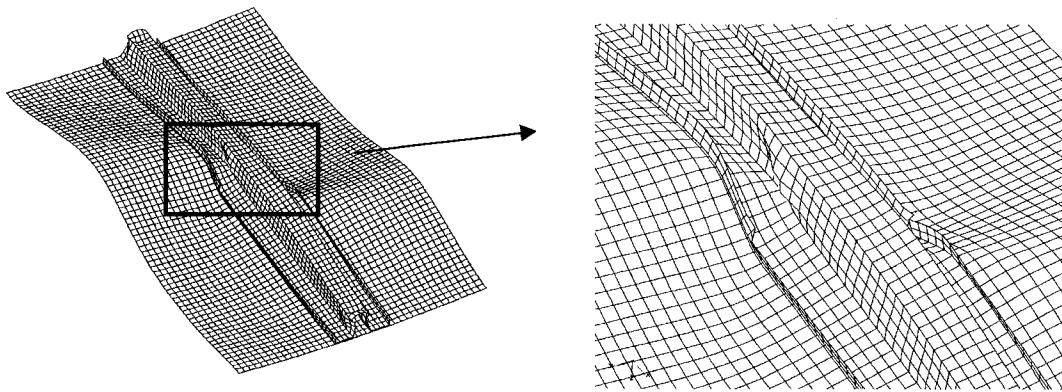
Figure 57. First four eigenmodes and buckling loads for the bonded-stiffener model calculated from a nonlinear equilibrium state

The nonlinear analysis is repeated with an initial geometric imperfection formed as a linear combination of the first four eigenmodes (shown in Figure 57) calculated from the stress state at the maximum nonlinear load value of 6,000 lbs. The equation for this imperfection, Eqn. (1), is the same as for the smeared and discrete beam approaches. First, an elastic nonlinear analysis is performed with this imperfection, and a maximum load of 18,893 lbs is obtained. Then the same analysis is repeated with material

nonlinearity enabled (elasto-plastic response permitted). Plastic deformation begins to occur at a load of 7,053 lbs, corresponding to an end shortening of .022 in, and the final maximum load is predicted to be 11,835 lbs. The deformed shapes corresponding to the failure load from the elastic and elasto-plastic failure analyses are shown in Figure 58. For the elastic nonlinear analyses, some local buckling of the stringer appears towards the edges of the panel. However, this deformation mode is a result of the symmetry assumptions of the repeating section, and these edges of the model are in the center of the skin bay. Furthermore, the deformation pattern corresponding to the failure load appears to be a global Euler-column buckling mode as shown in Figure 58(a). In the case of the elasto-plastic nonlinear analysis, the overall failure of the panel is caused by a localized stiffener crippling failure as indicated in Figure 58(b). In the elasto-plastic analysis, yielding begins in the lips of the hat stiffener (stiffener segments 1 and 7 shown in Figure 51) just above the center of the section. The yielding of the lips causes a redistribution of load resulting from a stiffener loss of stiffness that eventually causes yielding to occur at the top of the hat section thus leading to the panel failure. The elasto-plastic failure shape is shown in Figure 58(b).



(a) Failure shape from elastic analysis



(b) Failure shape from elasto-plastic analysis

Figure 58. Deformed shapes at the failure load for the bonded-stiffener model (exaggerated displacements)

A load-shortening curve of the three runs - elastic, elastic with imperfection, and plastic with imperfection - is shown in Figure 59. The local yielding of the stiffener results in a greatly reduced maximum load of the section.

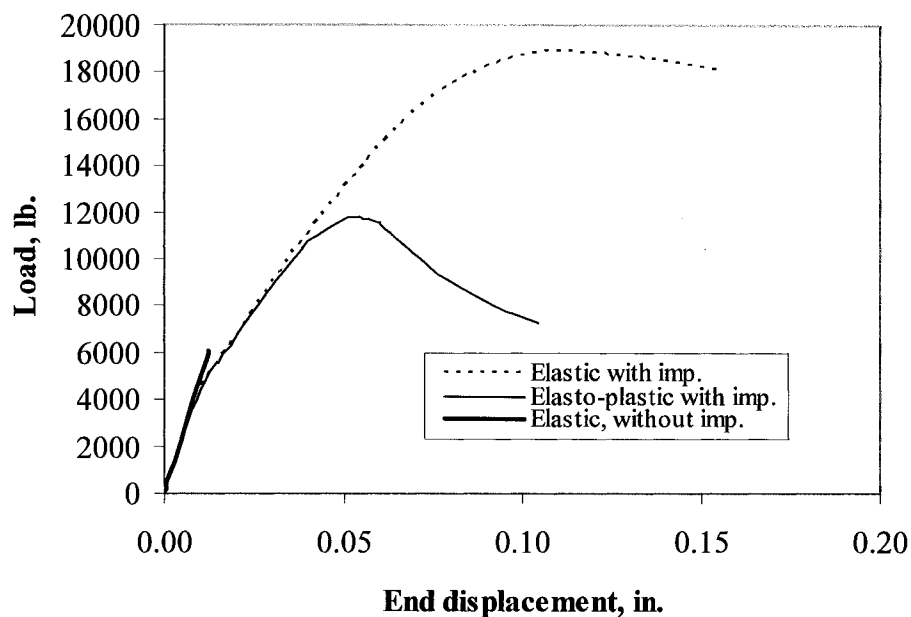


Figure 59. Load-shortening curve for single-stiffener repeating section of branched-shell bonded-stiffener model

4.4.4 Branched-Shell Riveted Stiffener

The last level of refinement added to the STAGS model consists of modeling the riveted attachment of the hat stiffener flanges to the skin. This model, referred to as the riveted-stiffener model, is exactly the same as the bonded-stiffener model except that the flanges of the hat stiffener are attached to the skin using E120 rigid link elements. The rigid-link elements are used to model 46 fasteners, 23 in a row down the center of each attachment flange of the hat stiffener. The fasteners are spaced 0.5 in. apart in the axial direction which corresponds to a rivet at every third node along the length of the stiffener. Contact between the flange and skin is modeled with STAGS contact elements. The contact capability is only active for the nonlinear analyses. This riveted-stiffener model of the single-stiffener repeating section predicts buckling and maximum loads slightly lower than the bonded-stiffener model. The linear buckling load is predicted to be 5,273 lbs.

The highest load value achieved with an elastic nonlinear analysis is 5,787 lbs. At 5,787 lbs, an eigenvalue analysis based on this nonlinear stress state is performed, and the nearest eigenvalue is found to be at 5,814 lbs. The mode shape corresponding to this eigenvalue, shown as mode 1 in Figure 60, is the same skin buckling mode as predicted by the bonded-stiffener analysis shown in Figure 57. The elastic nonlinear analysis is repeated with an initial geometric imperfection defined by a linear combination of the first four eigenmodes (shown in Figure 60) calculated from the stress state at the maximum nonlinear load value of 5,787 lbs.

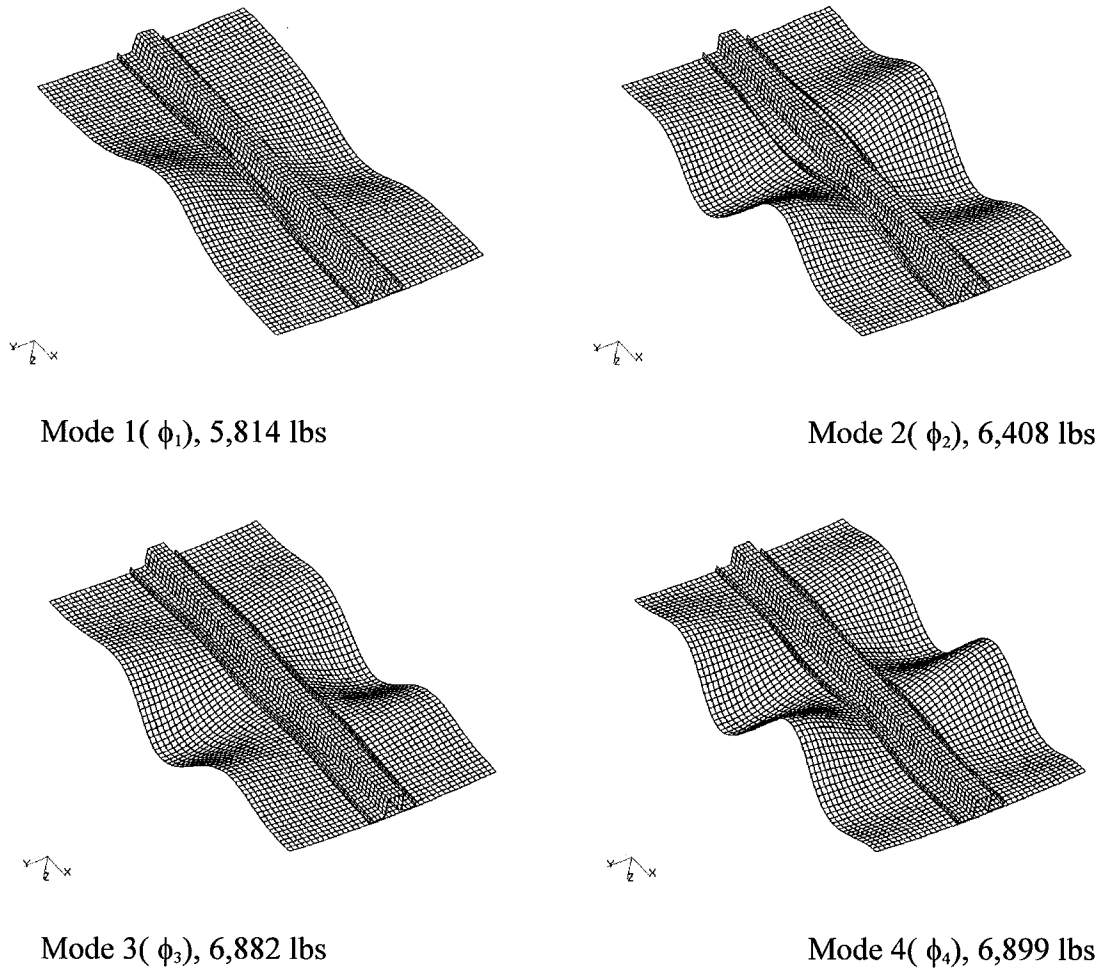
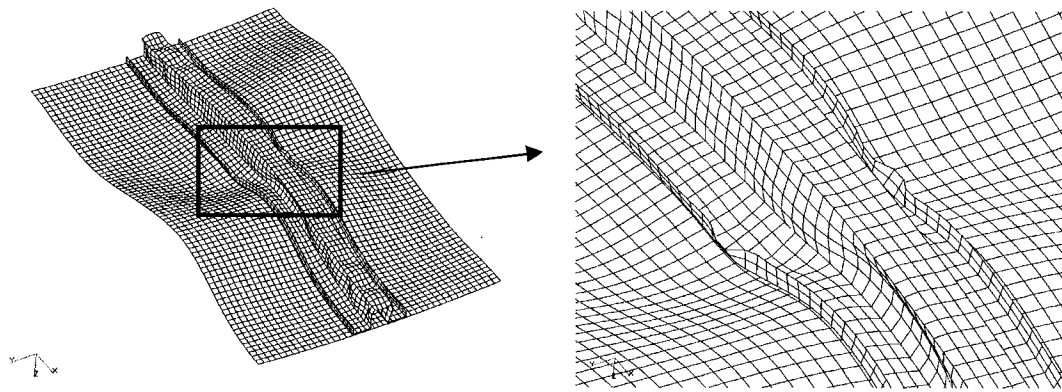
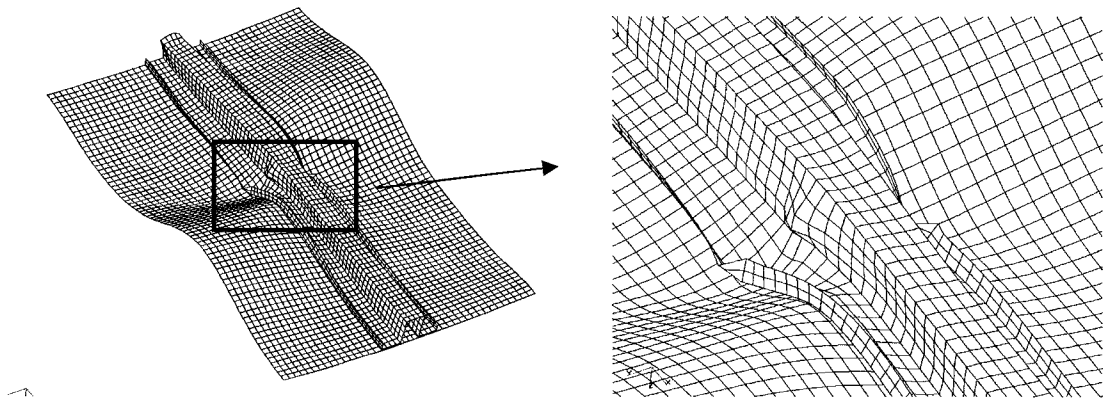


Figure 60. First four eigenmodes and buckling loads for the riveted-stiffener model calculated from a nonlinear equilibrium state

The equation for this imperfection, Eqn. (1), is the same as for the smeared and discrete beam approaches. The elastic nonlinear analysis is repeated with this imperfection and a maximum load of 17,256 lbs is predicted. When the same analysis is performed with material nonlinearity, plastic deformation begins to occur at a load of 6,325 lbs corresponding to an end shortening of .02 in, and the maximum load is predicted to be 10,350 lbs. The elastic and elasto-plastic failure shapes are shown in Figure 61.



(a) Failure shape from elastic analysis



(b) Failure shape from elasto-plastic analysis

Figure 61. Deformed shapes at failure loads for the riveted-stiffener model

The deformed shape at failure load for the elastic nonlinear analyses appears to be a local stiffener buckling mode whereas the elasto-plastic nonlinear analysis leads to a localized stiffener crippling failure. Unlike the elastic bonded-stiffener model, the elastic riveted-stiffener model shows buckling of the stiffener lips at the center of the panel due to the flexibility of the stiffener flanges between rivets. Deformation of the stiffener lips is evident in the elasto-plastic analysis. Yielding begins in the lips of the hat stiffener eventually leading to yielding at the top of the hat section similar to the response

observed with the bonded-stiffener model. A load-shortening curve for each of the three analyses (elastic, elastic with imperfection, and elasto-plastic with imperfection) is shown in Figure 62.

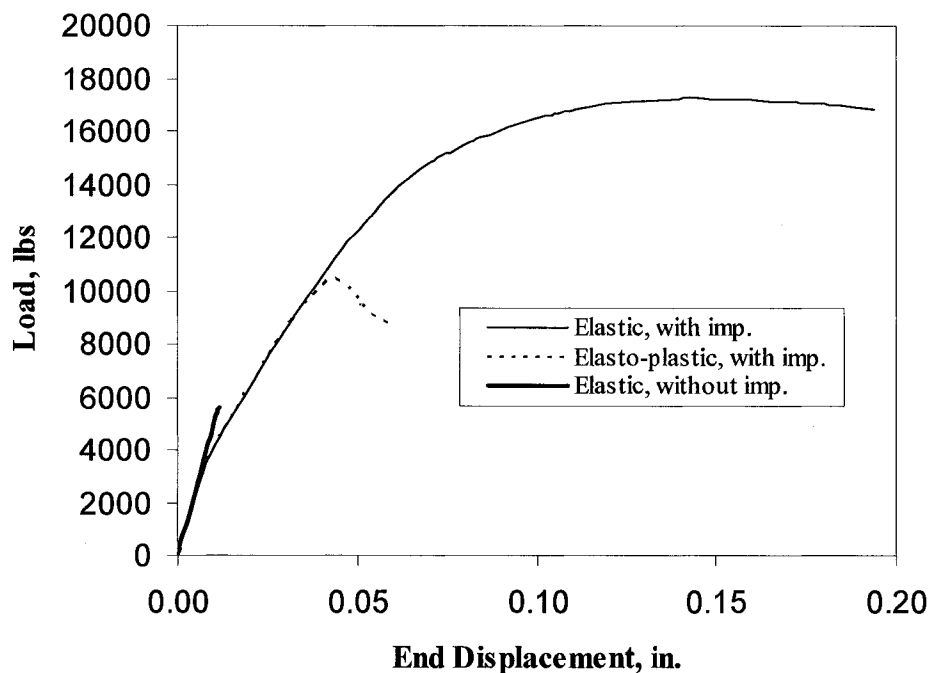


Figure 62. Load-shortening curve for single-stiffener repeating section of branched-shell riveted-stiffener model

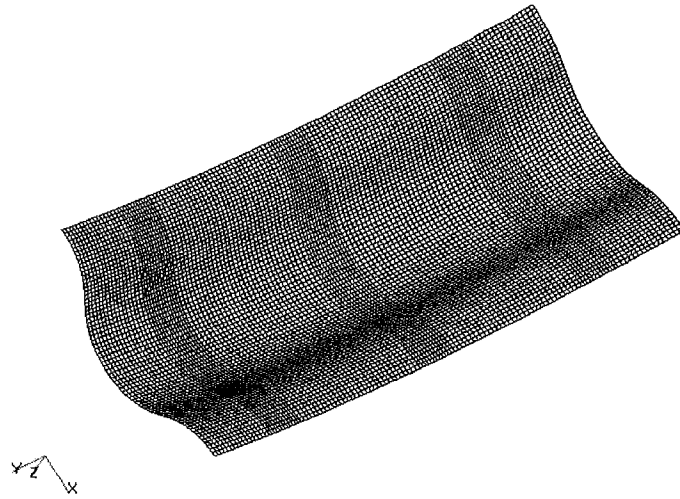
4.5 STAGS Results for Three Repeating Elements

The single-stiffener repeating section model with symmetric boundary conditions cannot capture every possible failure mode for a large stiffened panel. There may be asymmetric skin panel buckle modes that exist. Therefore, a three-stiffener repeating section model is created from each of the previous single-stiffener models to determine if any buckling or deformed shape at failure loads are missed by the simplified models. The three-stiffener model will consist of three repeating elements from Figure 40 joined together

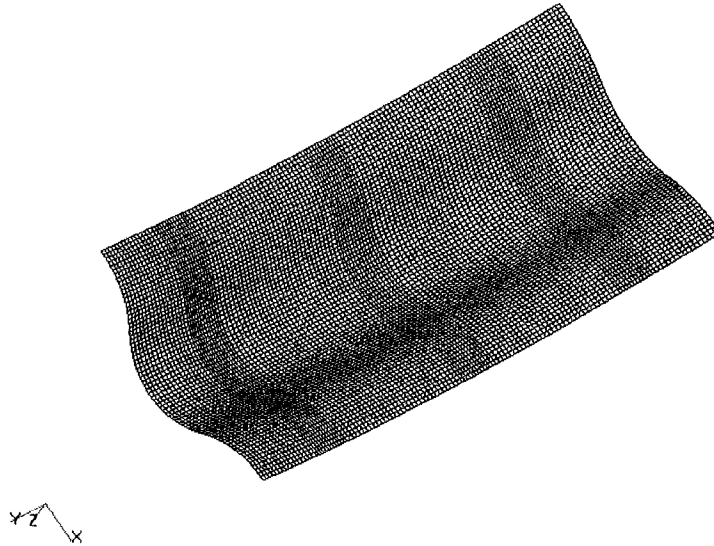
circumferentially. When comparisons are made between the single-stiffener and three-stiffener models, the maximum load of the three-stiffener model will be divided by three.

4.5.1 Smearred-Stiffener Properties

The three-stiffener repeating section is first analyzed for the case where the stiffener properties are smeared over the entire model. The three-stiffener repeating section analysis produces results that match exactly the single-stiffener model buckling and failure modes for globally smeared stiffeners. For comparison purposes, the same imperfection shape is used for the three-stiffener repeating section model as for the single-stiffener model. Therefore, the eigenmodes used to compose the initial imperfection are not the lowest four modes for the three-stiffener repeating section, but are the three-stiffener repeating section modes (Modes 1, 6, 7, & 12) that are identical to the lowest four modes from the single-stiffener repeating section model. Mode 1 for both the single- and three-stiffener models is symmetric and consists of one axial half-wave and 2 circumferential half-waves per stiffener section (i.e., 2 half-waves for the single-stiffener model and 6 half-waves for the three-stiffener model). Modes 2 thru 5 of the three-stiffener model have one axial half-wave and 5, 7, 4, and 8 circumferential half-waves, respectively. Because the number of circumferential half-waves cannot be evenly distributed among each of the three stiffener sections, these mode shapes cannot be captured by the single-stiffener repeating section model. The deformed shapes of the three-stiffener repeating section models for the predicted maximum loads obtained from the elastic nonlinear analysis with and without initial geometric surface imperfections are shown in Figure 63.



(a) Elastic failure shape without imperfection



(b) Elastic failure shape including geometric imperfection

Figure 63. Elastic three-stiffener repeating section model failure shape for globally smeared-stiffener approach

The three-stiffener repeating section is also analyzed with the stiffener properties smeared locally as is done for the single-stiffener case (see Section 4.4.1). The linear

buckling analysis gives the same result for both the single- and three-stiffener repeating section models as does the nonlinear elastic analysis. The assumed imperfection shape used for the three-stiffener repeating section is the same imperfection assumed for the single-stiffener repeating section analysis. Modes 1, 3, 7, and 8 from the three-stiffener eigenvalue analysis match the first four modes of the single-stiffener eigenvalue analysis and are used to form the imperfection for the three-stiffener model. The maximum load value (factored by three to compare to the single-stiffener model) reached by the three-stiffener repeating section before failure is 27,392 lbs, exactly the same as the single-stiffener model. These results indicate that no additional failure modes were detected by the extension of the single-stiffener model to the single-stiffener model for the smeared-stiffener approach. The load-shortening curve for the nonlinear analysis of the single- and three-stiffener repeating section models with both globally and locally smeared stiffener properties is shown in Figure 64.

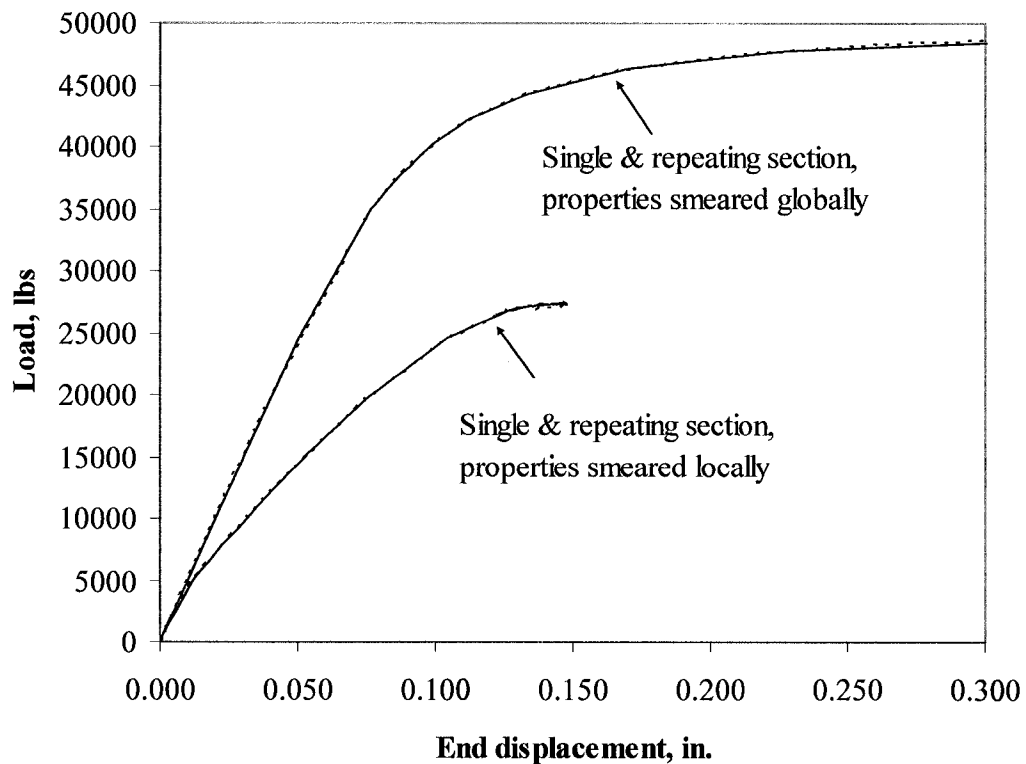


Figure 64. Load-shortening curves for elastic single- and three-stiffener repeating section models with locally and globally smeared stiffener properties

The deformed shape at the failure load for the locally-smeared stiffness approach is shown in Figure 65. Failure occurs when the center stiffener area deforms sufficiently out of plane and can no longer support the compression load. The maximum out-of-plane deflection of the stiffener section of the model reaches 0.387 inches, approximately 6 times the panel skin thickness, before the panel fails.

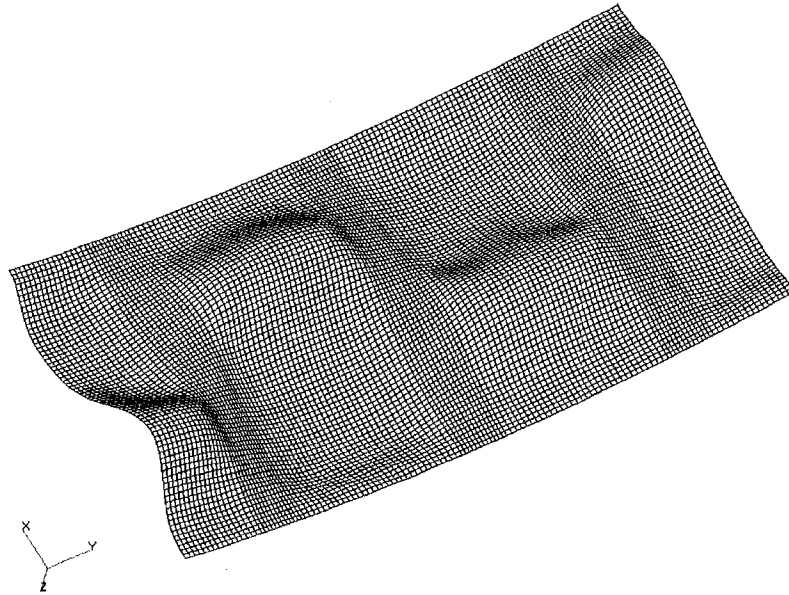


Figure 65. Elastic three-stiffener repeating section model failure shape for locally smeared-stiffener approach

4.5.2 Discrete Stiffeners

The discrete-stiffener three-stiffener repeating section model analysis produces results that are nearly identical to the single discrete-stiffener repeating section model buckling and failure modes (see Section 4.4.2). As with the smeared-stiffener models, geometric imperfections used in the three-stiffener analysis were matched to those used in the single-stiffener analysis. Modes 1, 3, 7, and 8 from the three-stiffener eigenvalue analysis are used to define the surface imperfection. The load-shortening plots for both the single- and three-stiffener repeating section models with imperfections are shown in Figure 66.

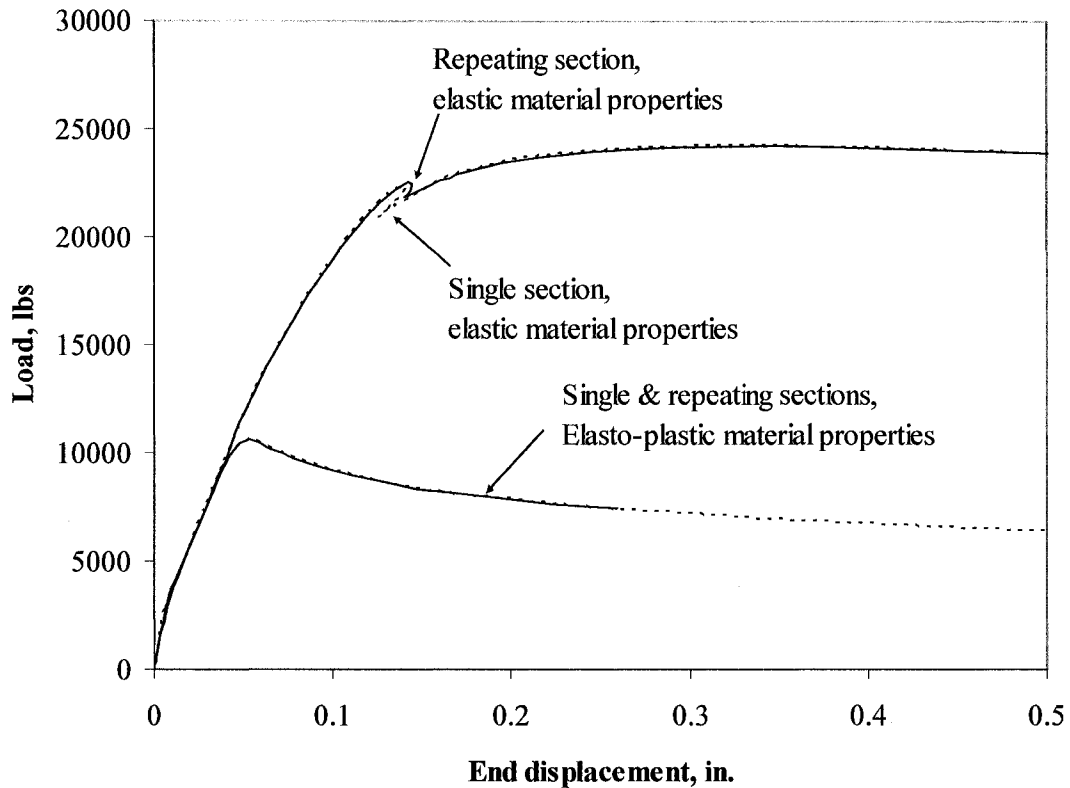
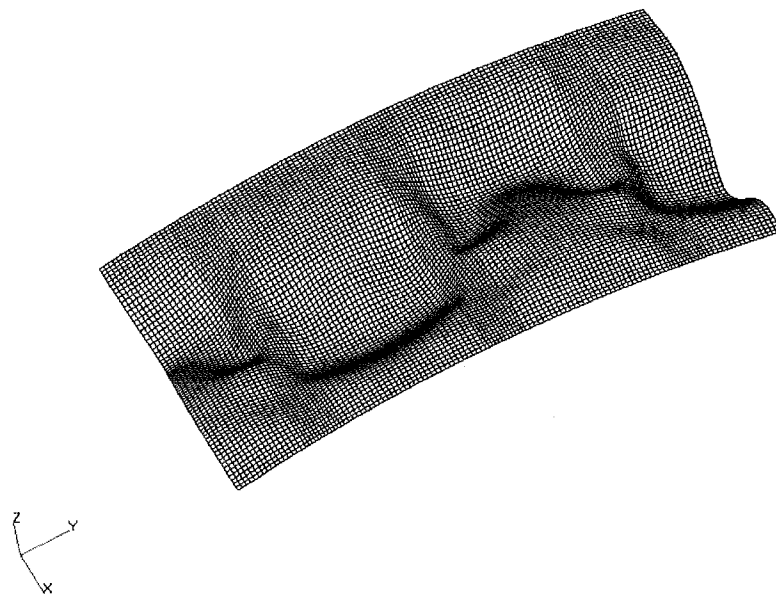
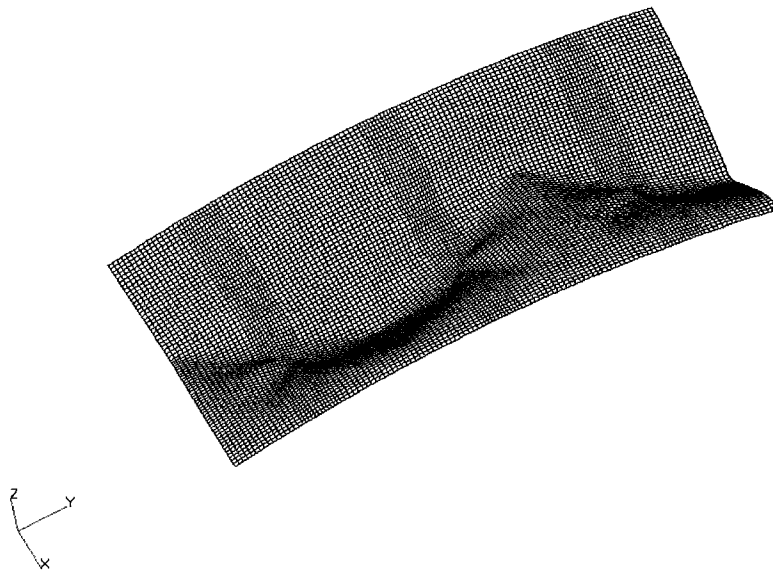


Figure 66. Load-shortening curves for single- and three-stiffener repeating section models with discrete stiffeners and initial imperfections

For the elastic analyses, the three-stiffener repeating section model has a slightly higher initial buckling load than the single-stiffener model, but the maximum load that the panels achieve is the same. The average single-stiffener section buckling load and maximum load obtained from the three-stiffener model are 22,501 lbs and 24,190 lbs, respectively. The single-stiffener repeating section model initially buckles at 22,395 lbs and fails at 24,209 lbs. The difference in initial buckling loads between the two models is due to the solution step size taken during the nonlinear solution sequence. The deformed shapes for the elastic analysis after initial buckling and after the maximum load is reached are shown in Figure 67.



a) Initial buckling mode shape



b) Deformed shape at failure load

Figure 67. Elastic three-stiffener repeating section buckling and failure shapes for discrete-stiffener approach

The initial buckling and failure deformed shapes of the center section of the three-stiffener model are identical to the single-stiffener deformed shapes (refer to Figure 53).

When material nonlinearity is included in the analyses, the maximum load levels reached before failure are 10,599 lbs for the single-stiffener repeating section model and 10,618 lbs for a single-stiffener section of the three-stiffener model. As with the elastic analysis, the failure modes of the two models are identical (refer to Figure 54). The elasto-plastic failure mode for the three-stiffener repeating section model is shown in Figure 68.

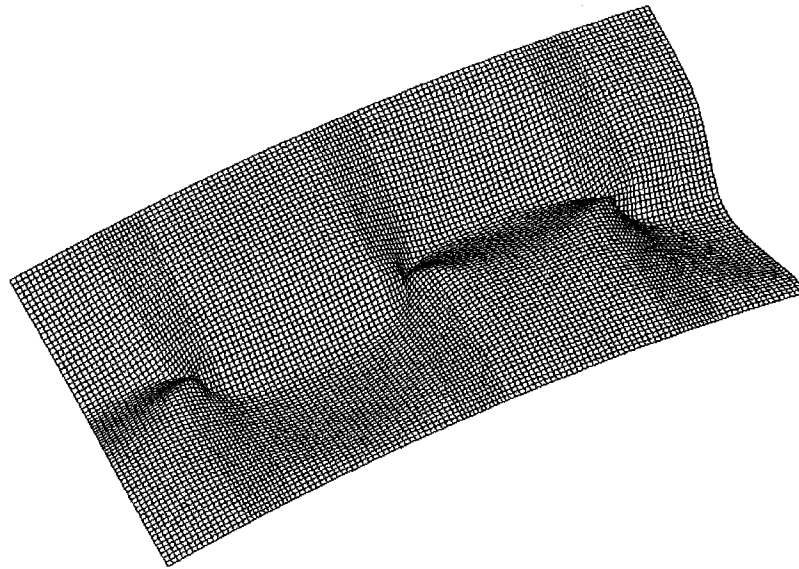


Figure 68. Elasto-plastic three-stiffener repeating section model failure shape for discrete-stiffener approach

4.5.3 Branched-Shell Bonded Stiffeners

The bonded-stiffener branched-shell three-stiffener repeating section model analysis produces results that are the same as the corresponding single-stiffener model buckling and failure modes(see Section 4.4.3). Geometric imperfections used in the three-stiffener analysis were matched to those used in the single-stiffener analysis. Modes 1, 3, 7, and 8 from the three-stiffener eigenvalue analysis are used to define the surface imperfection.

The load-shortening plots for both the single- and three-stiffener models with imperfections are shown in Figure 69.

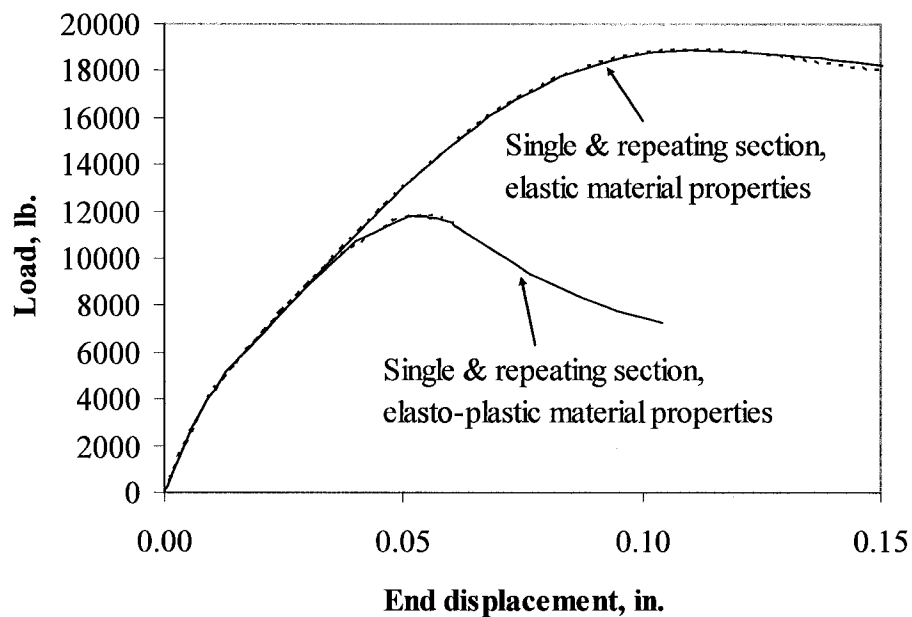
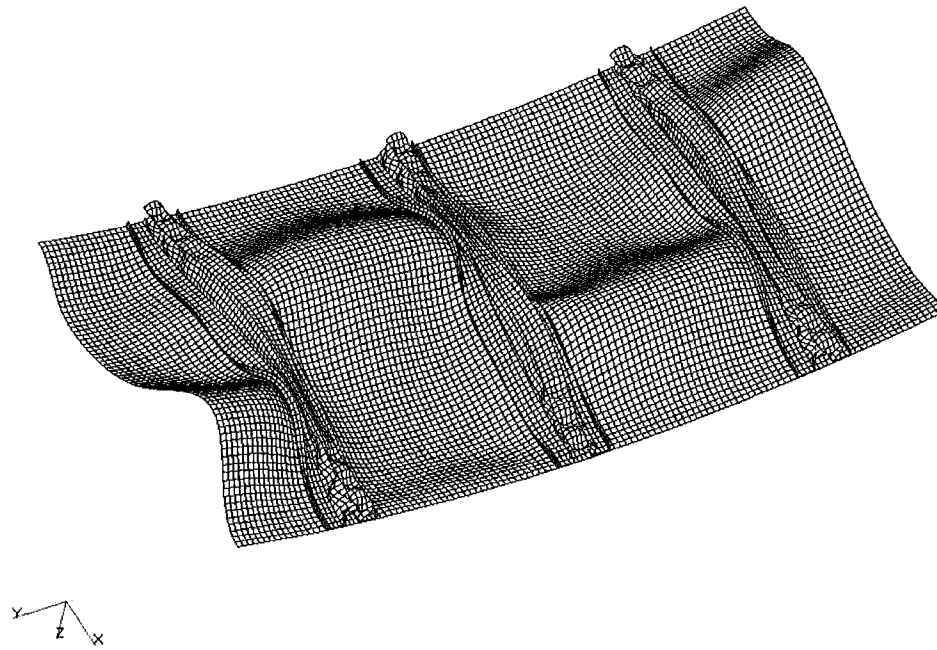
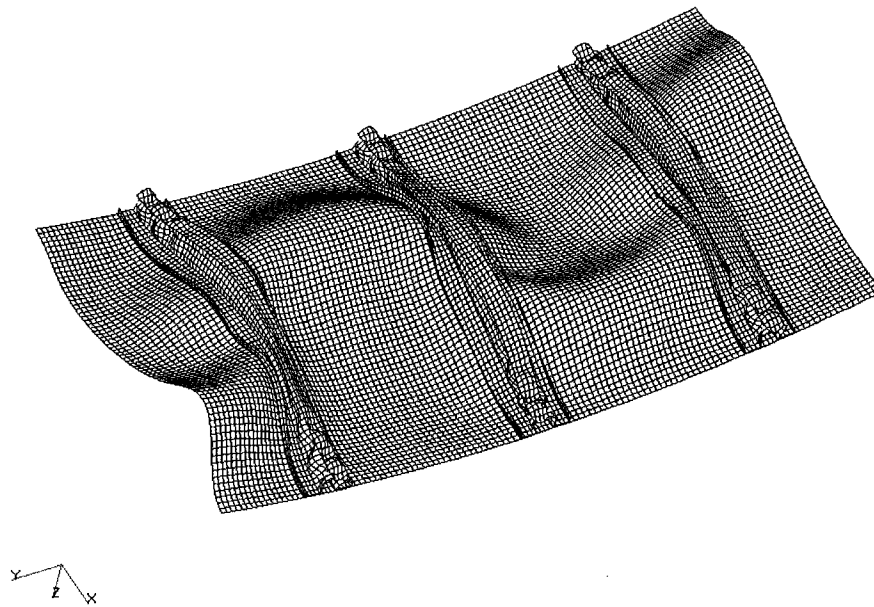


Figure 69. Load-shortening curves for single- and three-stiffener repeating section models (bonded-stiffener branched-shell) with initial imperfections

For the elastic analyses, the single-stiffener model reaches a maximum load of 18,893 lbs, and the average single-section maximum load obtained from the three-stiffener model is 18,895 lbs. The deformed shapes prior to failure and at failure for the elastic analysis of the three-stiffener repeating section model are shown in Figure 70.



(a) Deformed shape at maximum load



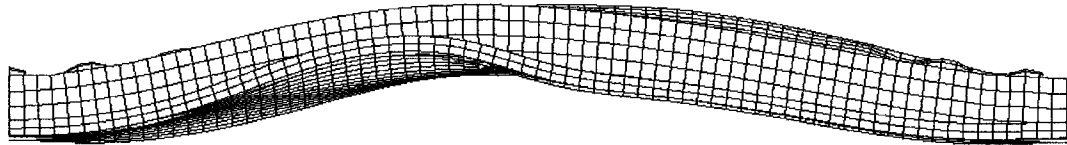
(b) Deformed shape at failure load

Figure 70. Elastic three-stiffener repeating section model failure shape for bonded-stiffener branched-shell approach

The deformed shapes of the center stringer prior to and after failure are shown in Figure 71.



(a) Deformed shape of center hat-stiffener at maximum load



(b) Deformed shape of center hat-stiffener after load decline

Figure 71. Center hat-stiffener deformed shapes for elastic bonded-stiffener branched-shell approach

The mode of failure for the elastic analysis of the three-stiffener repeating section appears to be column buckling of the center hat-stiffener similar to the single-stiffener model stringer local buckling failure mode shown in Figure 58(a).

When material nonlinearity is included in the analyses, the maximum load levels reached are 11,835 lbs for the single-stiffener model and 11,826 lbs for the average single-stiffener section maximum load obtained from the three-stiffener repeating section

model. For the elasto-plastic case, the failure modes for the two models are similar. In the case of both the three-stiffener and the single-stiffener repeating section models, the failure starts in the lips of the hat section as shown in Figure 58(b). The predicted failure mode is a crippling failure of the center of the hat section of the stiffener for both models. The elasto-plastic failure mode for the repeating panel section is shown in Figure 72.

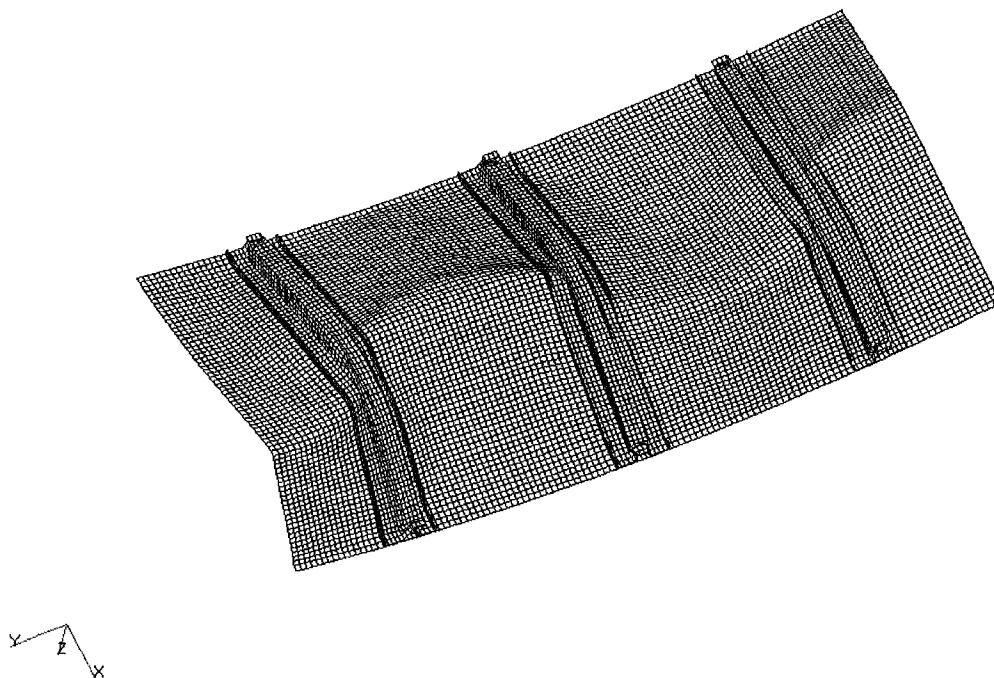


Figure 72. Elasto-plastic three-stiffener repeating section model failure shape for bonded-stiffener branched-shell approach

4.5.4 Branched-Shell Riveted-Stiffeners

The riveted-stiffener branched-shell three-stiffener model analysis produces results that are nearly identical to the single-stiffener model results (see Section 4.4.4) for the elastic case and the elasto-plastic case. Geometric imperfections used in the three-stiffener analysis were matched to those used in the single-stiffener analysis. Modes 1, 3, 7, and 8

from the three-stiffener eigenvalue analysis are used to define the surface imperfection. The load-shortening plots for both the single- and three-stiffener repeating section models with imperfections are shown in Figure 73. The single-stiffener results are shown by solid lines and the three-stiffener repeating section results by dashed lines (almost hidden behind solid lines).

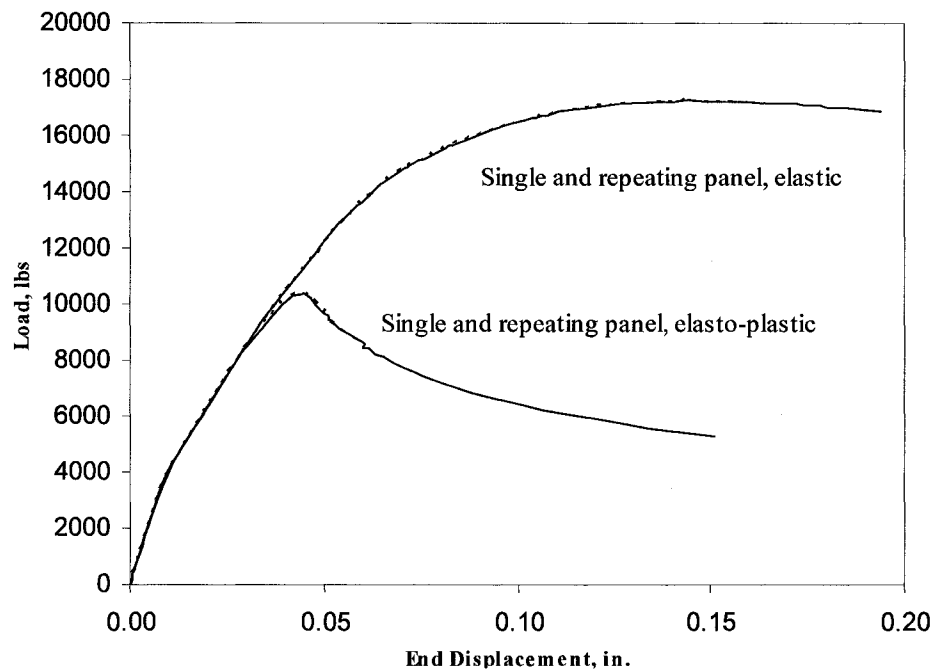


Figure 73. Load-shortening curves for single- and three-stiffener repeating section models (riveted-stiffener branched-shell) with initial imperfections

For the elastic analyses, the single-stiffener repeating section model reaches a maximum load of 17,255 lbs, and the average single-section maximum load obtained from the three-stiffener model is 17,255 lbs. The deformed shape of the three-stiffener repeating section model at the maximum load value indicates a local buckling failure of the stiffeners and is shown in Figure 74.

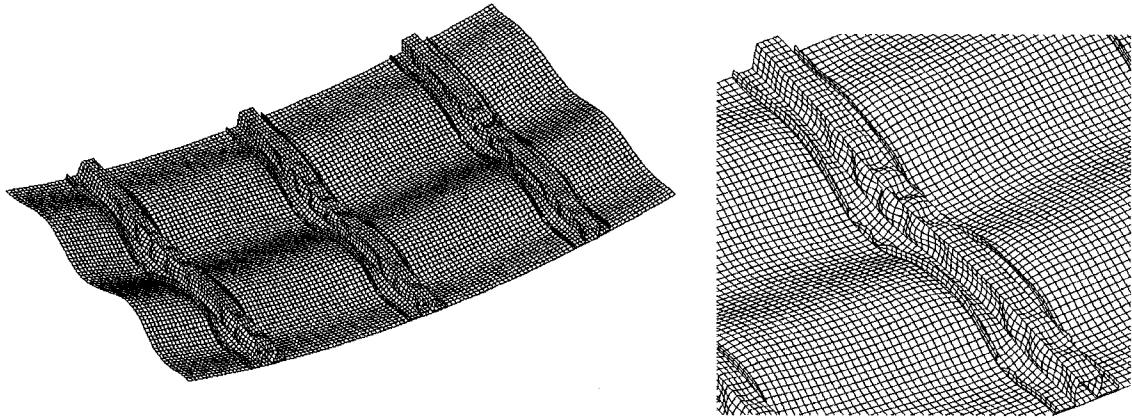


Figure 74. Elastic three-stiffener repeating section model failure shape for riveted-stiffener branched-shell approach

When material nonlinearity is included in the analyses, the maximum load levels reached are 10,350 lbs for the single-stiffener model, and 10,370 lbs for the average single-section maximum load obtained from the three-stiffener model. For the elasto-plastic case, the failure modes for the two models are similar. For both the single-stiffener and three-stiffener repeating section models, the failure starts in the lips of the hat section as shown in Figure 75 and Figure 61(b). The end result is a crippling failure of the center top section of the hat stiffener for both models. The elasto-plastic failure mode for the three-stiffener model is shown in Figure 75.

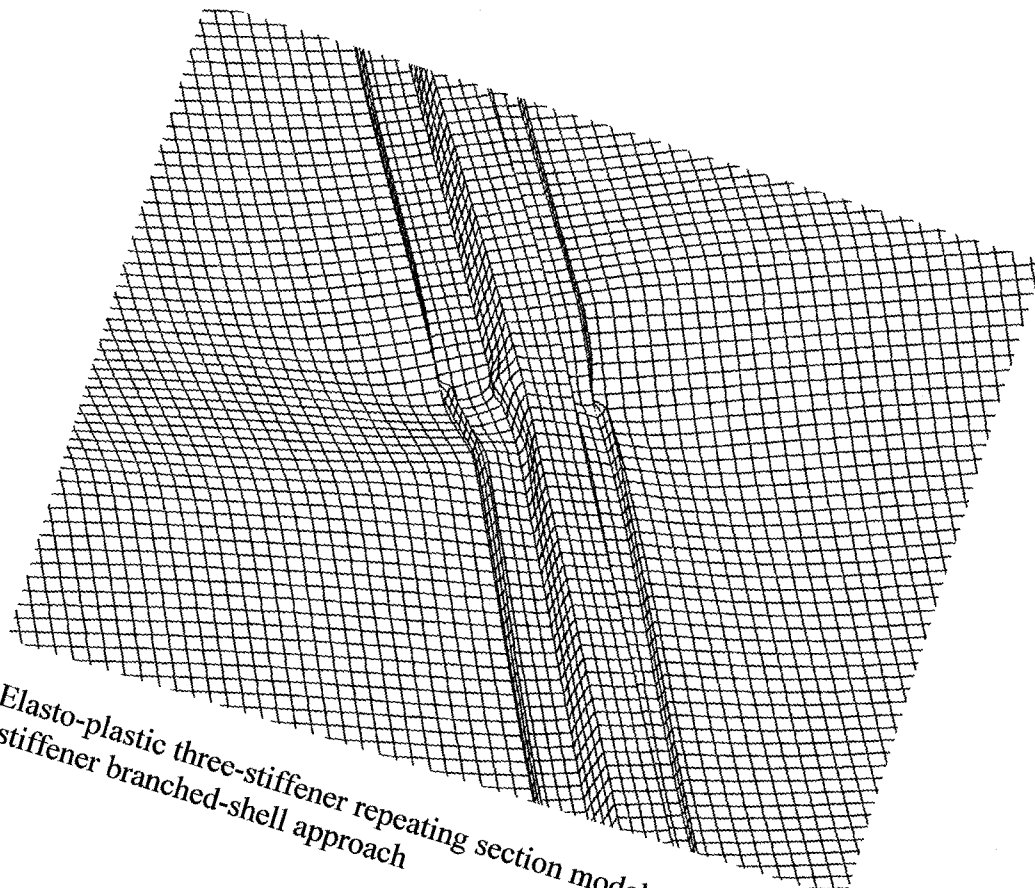
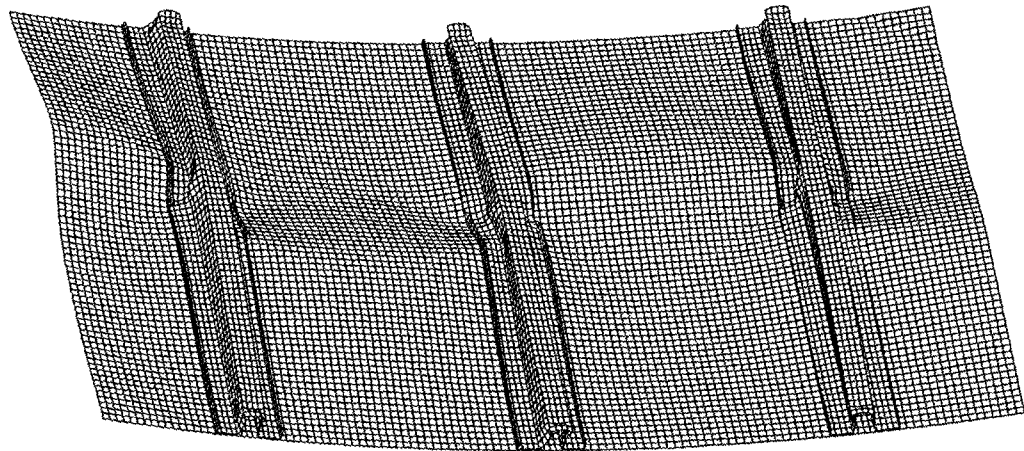


Figure 75. Elasto-plastic three-stiffener repeating section model failure shape for riveted-stiffener branched-shell approach

Reproduced with permission of the copyright owner. Further reproduction prohibited without permission.

4.6 Summary

Baseline analysis models studies for test panel configuration 617 subjected to compression loading are studied. From testing, the average initial skin buckling load of the two 617 panels is 27,877 lbs, and the average failure load is 55,202 lbs. Panel 617 consists of five stringer bays, therefore the buckling and failure loads of a single-panel section are assumed to be 5,575 lbs and 11,040 lbs, respectively (i.e., total load averaged over five bays). Failure of the 617 test panel occurs across the center of the panel between frames 2 and 3. The failure is caused by simultaneous Euler-column buckling of stringers 2 and 3 and crippling of the stringers 1, 2, and 5 (See Section 3.4.5). The stiffener section between frames 2 and 3 that includes stringer 3 is most representative of the baseline analysis models.

The PAGE analysis predicts a reasonable buckling load of 5,917 lbs which is 6% higher than the initial buckling load observed during the test. PAGE predicts that the ultimate failure of the panel is caused by column buckling at 7,677 lbs, which is significantly less than the average test failure load value of 11,040 lbs.

The PANDA2 analysis predicts local skin buckling loads from 9,019 lbs to 9,468 lbs using the single-section model. This buckling load is quite a bit higher than the test-averaged observed skin buckling value, and the increased load may be attributed to overly stiff boundary conditions. The PANDA2 analysis of the three-stiffener panel section predicts skin buckling loads from 3,006 lbs to 3,131 lbs. The increase in panel width relaxes the boundary conditions in the center section of the panel thereby resulting

in a decrease in panel buckling load to a value below the test-averaged observed buckling load of 5,575 lbs. For the single-section model, PANDA2 predicts failure occurrence of the panel due to hat buckling at approximately 12,070 lbs (average of three stiffener approximations), a value higher than the actual failure load of the test panel. PANDA2 is not recommended for analyzing a single-section model because PANDA2 assumes the model to be large enough that the boundary conditions at the edges of the panel do not affect the behavior of the section of the panel being analyzed. The predicted failure load of the three-stiffener panel section is 9,011 lbs, a value lower than the test section failure load. Comparing the PANDA2 failure predictions to STAGS and PAGE shows that the predicted failure value for the three-stiffener panel model is less than the elasto-plastic failure loads obtained from the finite element analyses, but higher than the PAGE failure prediction.

A summary of the eigenvalue and maximum loads for the eight STAGS models is shown in Table 13. The maximum load value reached before failure for the three-stiffener section models are divided by three to get an average single-stiffener section maximum load and thus provide an equal comparison to the single-stiffener section models.

Stiffener	Model	Linear eigenvalue (lbs)	Nonlinear Elastic Failure Load (lbs)	Nonlinear Elasto-plastic Failure Load (lbs)
Smearred globally	single	19732	48786	Not available
	repeating	19732	48786	Not available
Smearred locally	single	5743	27392	Not available
	repeating	5743	27392	Not available
Discrete	single	4788	24209	10599
	repeating	4788	24190	10618
Bonded	single	5506	18893	11835
	repeating	5506	18895	11826
Riveted	single	5253	17256	10350
	repeating	5253	17255	10370

Table 13. STAGS baseline panel model results summary

All linear eigenvalues correspond to the lowest skin buckling modes. The smeared-stiffener model with the stiffness smeared globally grossly over-predicts the buckling and maximum loads. Because the stiffeners are smeared and the panel is homogenous, there is no difference between the single- and three-stiffener repeating section models. When the stiffener properties are smeared only over the stiffener region, the failure predictions for the repeating section models greatly improve. The other stiffener models do a better job of predicting the linear buckling load as well, because the skin is the actual thickness. The other models over-predict the failure load if elastic material properties are used, but are very close to the failure load of the test panel if elasto-plastic material response is permitted. The skin buckling loads are higher for the bonded-stiffener panel than for the riveted-stiffener panel because the skin panel is essentially wider for the riveted-stiffener panel because the skin-to-stiffener connection occurs at the fastener line instead of at the edge of the stiffener attachment flange. Similarly, stiffener failure occurs sooner in the

riveted-stiffener panel because the stiffener attachment flanges are not supported over the entire width of the stiffener attachment flanges.

The load-shortening curves for the STAGS elastic single- and three-stiffener repeating section models are shown in Figures 76 and 77, respectively. The test failure load along with the PAGE and PANDA2 skin and column buckling loads are also shown in the figures. The results for the single-stiffener model are essentially identical to the three-stiffener model indicating that the assumption of symmetric boundary conditions in the center of the skin bays in the single-stiffener model was correct for the 617 panel configuration. All of the elastic models produced failure loads higher than the test-averaged observed panel failure load with the riveted-panel model that failed at 17,255 lbs coming closest to the test-averaged observed panel failure load of 11,040 lbs.

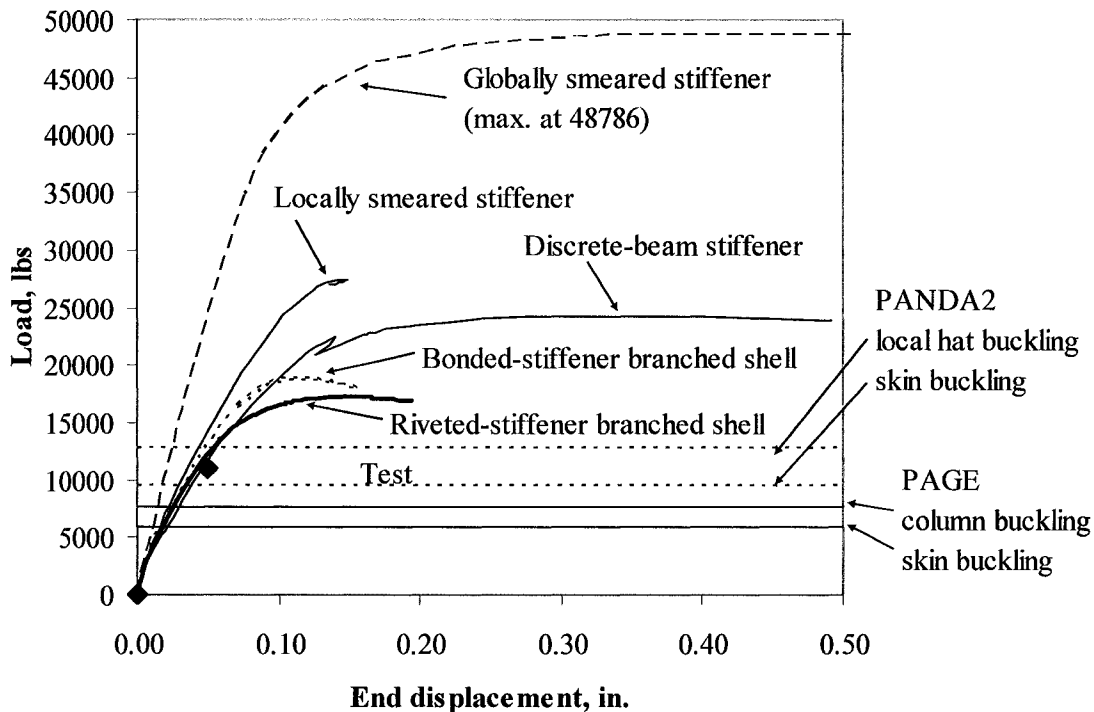


Figure 76. Load-shortening curves for single-stiffener repeating section model with elastic material properties

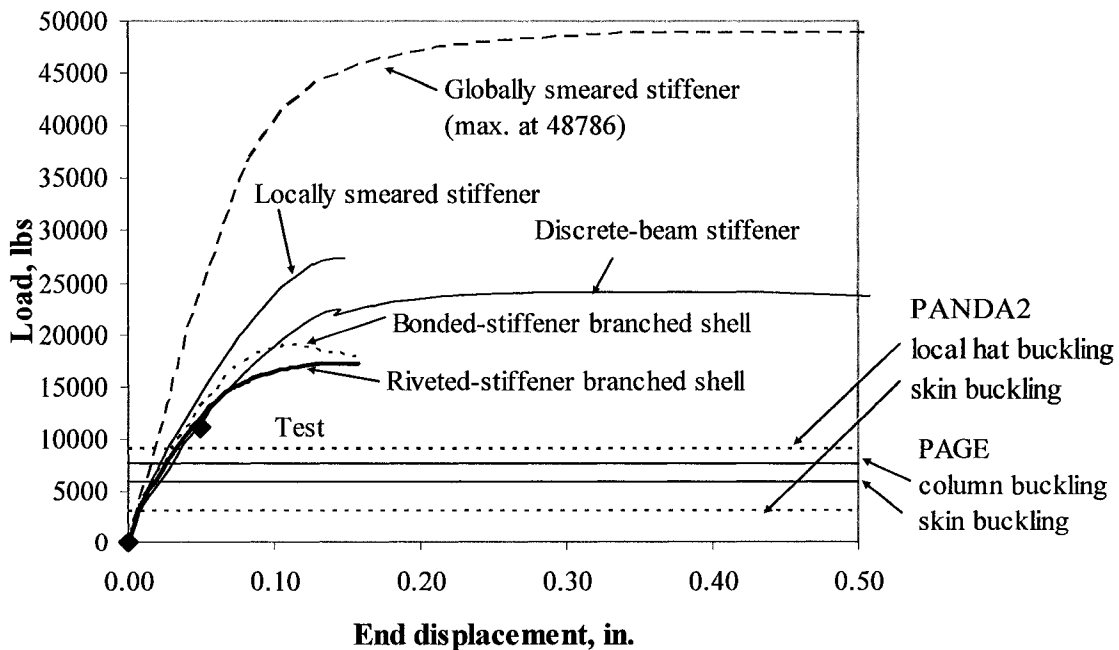


Figure 77. Load-shortening curves for three-stiffener repeating section model with elastic material properties

The load-shortening curves for the elasto-plastic single- and three-stiffener repeating section models are shown in Figures 78 and 79, respectively. Elasto-plastic material properties are not supported for smeared properties in STAGS, so results are only presented for the discrete-stiffener, bonded-stiffener, and riveted-stiffener models. The single- and three-stiffener models show good correlation with the test-averaged observed panel failure load as well as the test end shortening. The bonded-stiffener model predicts a slightly higher failure load than the test-averaged observed failure load as would be expected due to the added support provided by the bonded connection to the stiffener across the full width of the attachment flanges. The riveted-stiffener model under predicts the failure load as does the discrete-stiffener model.

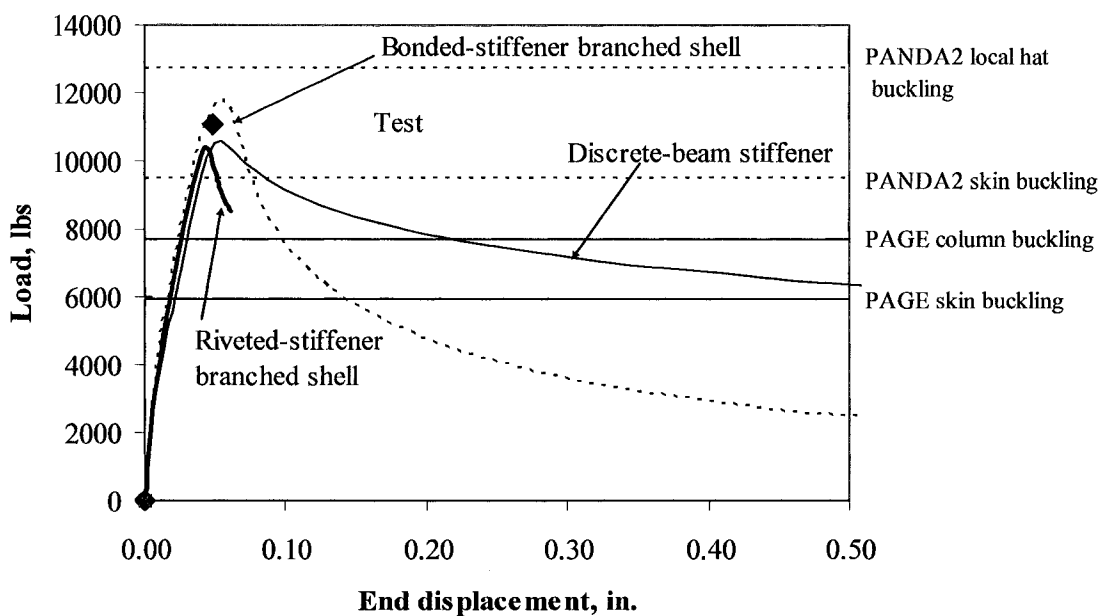


Figure 78. Load-shortening curves for single-stiffener repeating section model with elasto-plastic material properties

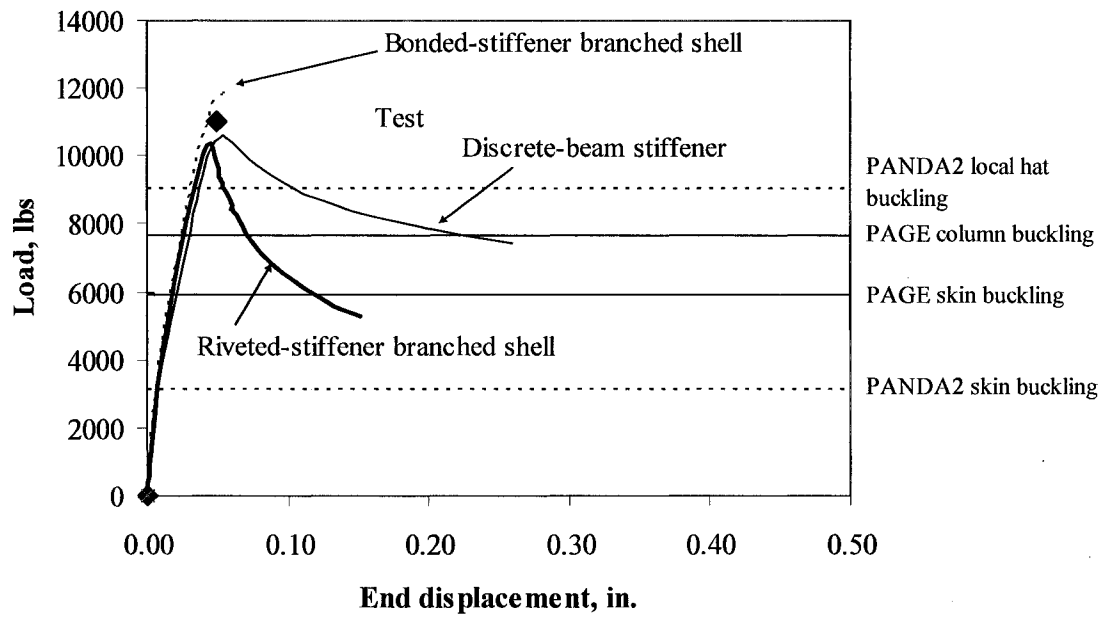


Figure 79. Load-shortening curves for three-stiffener repeating section model with elasto-plastic material properties

SECTION 5

NUMERICAL ANALYSIS OF TEST PANELS

A comparison of the failure prediction capability of the closed-form analysis tool PAGE and the nonlinear finite element tool STAGS is presented in this section for stiffened fuselage panel design. PANDA2 is excluded from this study because it does not have the capability to analyze open-hat stringer cross-sections. STAGS and PAGE, both described in Appendix A, are used to analyze the four stiffened fuselage panels described in detail in Section 3. A brief summary of the four configurations is shown in Table 14. It is important to note that all components (stringers, frames, doublers, gussets) of the test panels were attached to one another with rivets.

	Test Panel Configuration			
	614	615	616	617
Skin thickness (in.)	0.04	0.04	0.04	0.063
Stringer thickness (in.)	0.025	0.025	0.063	0.025
Stringer orientation	open hat	open hat	open hat	inverted hat
Doubler location	under frames	under frames and stringers	over entire skin	none
Gussets	edges only	edges only	edges only	all frame/stringer intersections

Table 14. Test panel configuration summary

The analyses presented in this section will differ from the analyses in Section 4 in that all four panel configurations will be analyzed, and the entire test panel (skins, doublers, stringers, frames, and gussets) will be included in the STAGS analyses. In , only the 617 panel configuration was analyzed, and only the stringer with attached skin and doublers were included in the PAGE and STAGS analyses. The effect of the frames and gussets was approximated by the imposed boundary conditions. The STAGS analysis results

approximated the test results reasonably well (maximum load predicted within 7.5%) as long as elasto-plastic material response was included and the stringer was modeled discretely. PAGE results were conservative in predicting the maximum load by a large margin (30%).

5.1 PAGE Analysis Results

A comparison of the PAGE-predicted panel maximum loads and the actual test panel maximum loads is shown in Table 15. Test results, as noted in the summary table, indicate some degree of conservatism in the predicted panel failure loads obtained from the PAGE analysis tool. In this context, the degree of conservatism, C , is defined by the predicted failure load $P_{predicted}$ being less than the observed test failure load P_{test} by a percentage of the test failure load. That is,

$$C(\%) = \frac{P_{test} - P_{predicted}}{P_{test}} \times 100\%$$

If the value of C is positive, then the prediction is conservative.

Panel Configuration	PAGE		Test		% Conservatism
	Maximum Load, lbs	Failure Mode	Maximum Load, lbs	Failure Mode	
614	21825	Skin Wrinkling	28821	Skin Wrinkling	32
			28551		31
615	23680	Skin Wrinkling	29787	Skin Wrinkling	26
			29563		25
616	81195	Euler Column	78684	Euler Column	-3
			82730		2
617	38520	Euler Column	55640	Euler Column	44
			54764		42

Table 15. Test and PAGE-predicted panel maximum loads

For the 614 and 615 panels, the PAGE-predicted failure mode was skin wrinkling. Skin wrinkling in a stiffened fuselage panel manifests itself as a buckle of the panel skin that also runs across the stringers and deforms the attached flanges of the stringers. At failure, these skin-wrinkling buckles become almost cylindrical in shape, and the deformation of the attached flange is sufficient to cause collapse of the stringers due to crippling. Test results in comparison to the PAGE analysis indicate a 20% to 24% conservatism. This conservatism is a result of the fact that the design allowable wrinkling stresses are based on the conservative assumption that the panel skin behaves as a column on an elastic foundation wherein the stringer acts as the elastic foundation. The spring rate of the stringer (as the elastic foundation) is estimated, and a closed-form equation is evaluated to determine the critical wrinkling stress. Although the critical wrinkling stress is derived from a stability analysis of the panel skin, the failing member is actually the attached flange of the stringer.

Euler-column failure modes were predicted with great accuracy for panels without any local stringer gussets at frame intersections in the interior of the panel (i.e., not including gussets along panel edges). The observed maximum load for the 616 panels was within 5 percent of the maximum load predicted by PAGE. One 616 panel reached a slightly lower maximum load than was predicted by PAGE; however, that particular 616 panel was known to be warped before testing. The test of the warped panel resulted in an observed maximum load 3% lower than the maximum load predicted by PAGE. The second 616 panel was not warped and resulted in an observed maximum load prior to failure 2% higher than the predicted maximum load. The accuracy of these PAGE

predictions is an indication of how well PAGE can predict Euler-column failure loads and is a direct result of the fact that Euler-column failure predictions implemented within PAGE are based on extensive empirical data.

The 617 panels with local stringer gussets at frame intersections were also predicted to fail in an Euler-column failure mode. These panels, however, showed approximately a 30% to 31% conservatism over the PAGE prediction. This degree of conservatism is attributed to the fact that local gussets connect each stringer to a frame member in the actual panels, and the PAGE analysis ignores the presence of gussets. The gussets represent a local change in stiffness and effectively shorten the column length of the stringer in the Euler-column buckling analysis

(i.e., $P_{cr} = \frac{\pi^2 EI}{L_{eff}^2}$). Hence these gussets increase the buckling load of the stringer

significantly (i.e., local change in boundary stiffness results in a shorter effective column length).

5.2 STAGS Analysis Results

Finite element analyses of the four test panel configurations are performed using the STAGS nonlinear finite element tool. For the first set of baseline models, referred to as the unrefined baseline models, the same level of finite element mesh refinement is used for all four panel configurations. The entire test panel is modeled, and all frames, shear clips, stringers, and gussets are modeled explicitly. Constraints are used to connect these components to one another and to the panel skin, however, the modeling approach essentially simulates a bonded connection rather than a discrete rivet connection. All

finite element analyses include geometric (large deformations, large rotations permitted) and material (elasto-plastic response permitted) nonlinearities. A higher level of finite element mesh refinement is incorporated in the finite element models of the 614 and 615 panels to capture the stringer crippling failure modes. These models will be referred to as the refined baseline models.

Smaller single-bay study models, similar to the panels described in , are created for all four panel configurations to assess the effect of riveted versus bonded stringer/skin connections on the ultimate failure response of the panel. These smaller study models have a higher level of finite element refinement than the larger unrefined and refined baseline models and also include modeling of the rivet connections using point constraints. The finite element mesh incorporated in the study models is sufficient for capturing local buckling between rivets as well as crippling failures of the stringer. For each panel configuration two study models are created, one representing a bonded skin-stringer connection and one representing a riveted skin-stringer connection. Based on the change in the failure load between the bonded and riveted study models, adjustment factors are determined to account for local effects.

These adjustment factors are applied to the ultimate failure load of the panels obtained from the baseline finite element models of the entire stiffened panel. That is,

$$(P_{predicted})_{Adjusted} = f_1 f_2 f_3 \dots f_n (P_{predicted})_{BaselineFEM}$$

where each adjustment factor f_i accounts for an uncertainty between the actual test panel and the analysis model of the panel. These adjusted failure loads, $(P_{predicted})_{Adjusted}$, are then compared to the observed test panel failure loads, P_{test} .

5.2.1 STAGS Predictions for Panel 614

The unrefined baseline finite element model of the 614 panel configuration is shown in Figure 80(a). This model consists of 11,840 STAGS E410 4-node, C^1 quadrilateral shell elements, 1,424 STAGS E210 2-node, C^1 beam elements, 19,274 nodes, and 93,888 active degrees of freedom. The frame caps and stringer lips (dimension s4 on Figure 10) are modeled using beam elements. This finite element model grossly over-predicts the failure mode. The failure mode predicted by this analysis model is an Euler-column buckling mode, while a stringer-crippling mode is observed in the test. However, the baseline finite element model was not capable of representing stringer-crippling failure modes. Therefore, a second finite element model, referred to as the refined baseline model, was developed for the 614 panel that included a higher mesh refinement and more detail in the stringer cross-section as shown in Figure 80(b). This finite element model consists of 20,340 STAGS E410 4-node, C^1 quadrilateral shell elements, 664 STAGS E210 2-node, C^1 beam elements, a total of 34,414 nodes, and 163,848 active degrees of freedom. In this finite element model, the stringer lips are modeled using shell elements and hence stringer cross-sectional deformations can be captured.

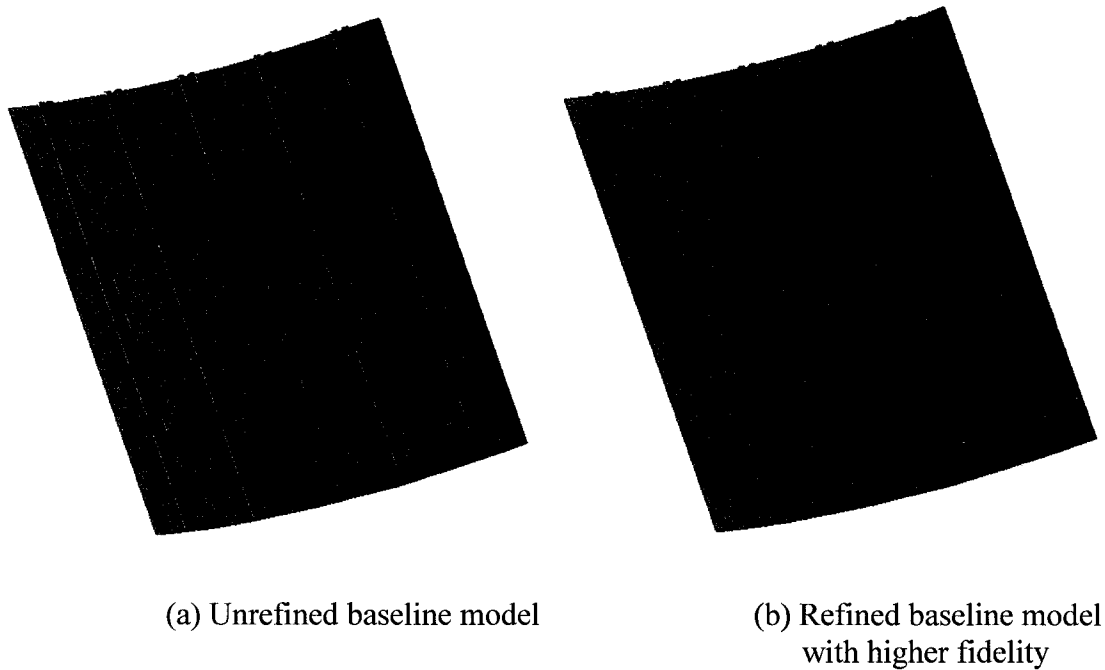


Figure 80. Finite element models for 614 panel configuration

A linear buckling analysis is first performed using STAGS and the finite element model in Figure 80(b). The finite element model is an idealized form of a geometrically perfect fuselage panel. In STAGS, a linear buckling analysis first involves a linear stress analysis of the finite element model subjected to a given system of loads and boundary conditions to determine the prebuckling stress state. This calculation is followed by a linear eigenvalue analysis based on the computed membrane stress state to extract the lowest eigenvalue or buckling load[†]. Each eigenvalue (buckling mode) has a corresponding eigenvector (buckling load factor). The linear finite element analysis predicts the first buckling load to be 13,506 lbs and corresponds to a skin-buckling mode as shown in Figure 81. The buckling mode is predominantly in the lower half of the panel.

[†] A linear eigenvalue analysis is based on the membrane stress state from the predicted linear stress analysis. Bending contributions to the stress state are ignored. To include the complete stress state, an eigenvalue analysis from the nonlinear stress state needs to be performed.

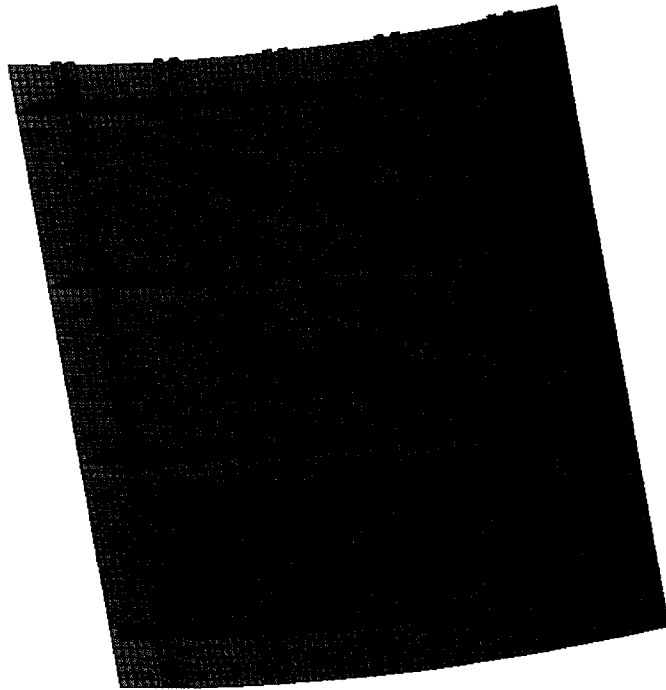


Figure 81. Panel 614 first buckling mode shape

Secondly a nonlinear finite element analysis of the 614 panel configuration is conducted including both geometric and material nonlinearities. The onset of skin buckling is predicted to occur at a load level of 11,305 lbs, which is less than the linear buckling prediction. The eigenvector corresponding to this load value is shown in Figure 82.

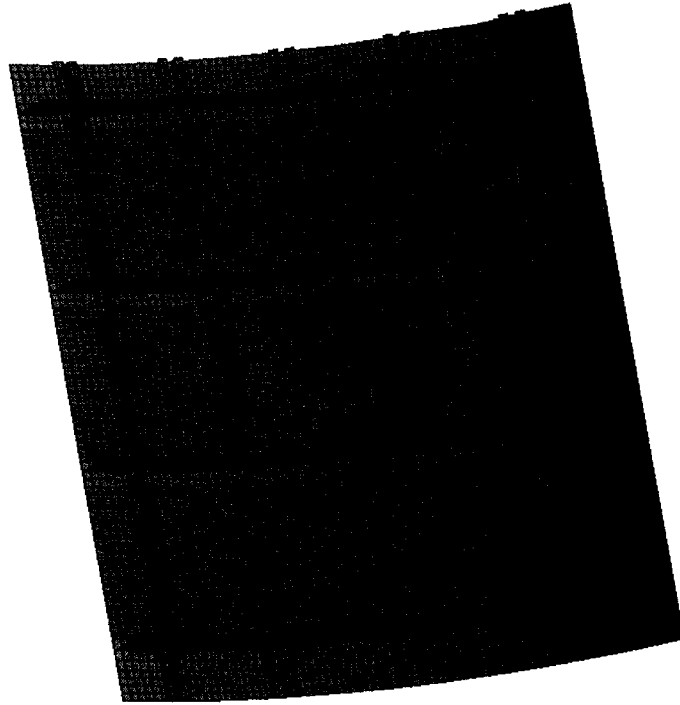


Figure 82. Nonlinear buckling mode shape for 614 panel

Both the linear and nonlinear predicted initial buckling loads are considerably higher than the lowest test panel skin buckling loads of 7,868 lbs and 8,318 lbs. However during the test, sequential skin buckling in other bays of the test panels continues to occur up to a load of 19,783 lbs. The fact that the test panels experience skin buckling prior to the predicted buckling load indicates the presence and influence of significant geometric imperfections in some of the panel skin bays or some eccentricity in the load application. Identifying the various factors that influence the test results and their relative importance to the analysis model is a process that leads to a high-fidelity analysis capability. Recognizing short falls between the analysis model and the test configuration enables a set of adjustment factors to be developed.

The initial load versus end shortening response for the 614 panel without any initial geometric surface imperfections and with imperfections based on the deformation patterns shown in Figures 81 and 82 with a maximum imperfection amplitude of 0.04 in. is shown in Figure 83. There is a 20% reduction in initial buckling load due to the introduction into the panel of either the multi-bay imperfection obtained from the linear eigenanalysis or the single-bay imperfection obtained from the eigenanalysis at the nonlinear equilibrium state. Although the initial buckling loads these two panels are essentially the same, the overall stiffness of the panel with the imperfection from the linear eigenanalysis is less than that of the panel with the imperfection based on the eigenanalysis from the nonlinear equilibrium state. The actual panel imperfections were not measured and may be larger and/or occur in additional skin bays resulting in further reductions in the initial buckling load as witnessed in the initial buckling load values of the test panels, also shown in Figure 83.

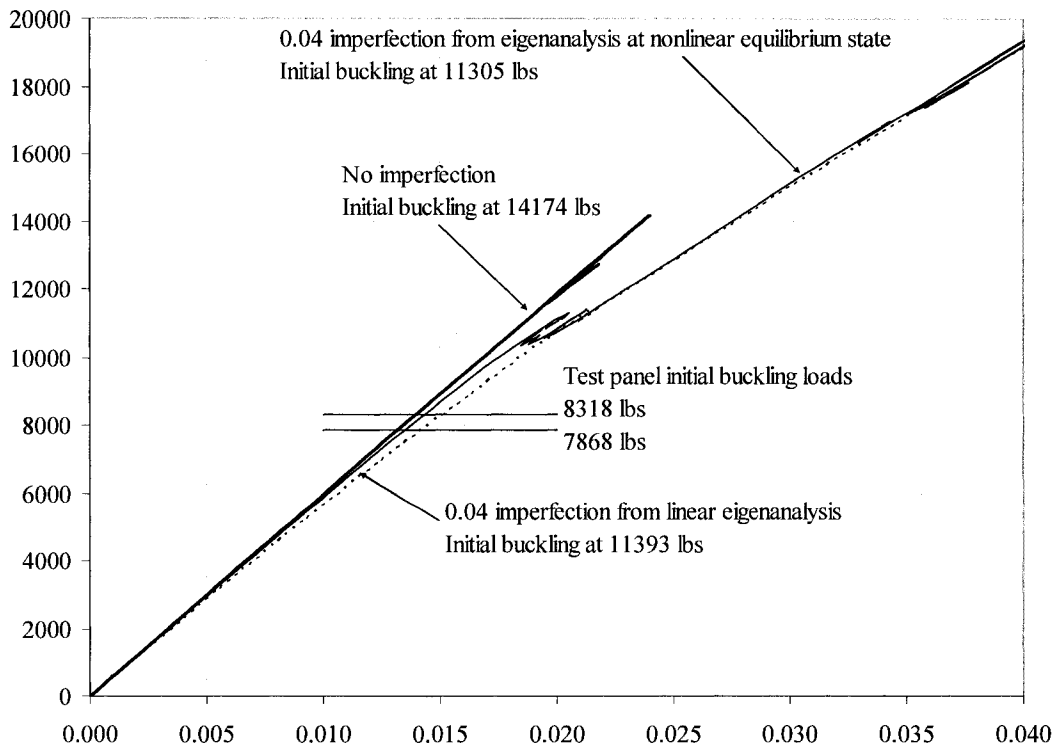
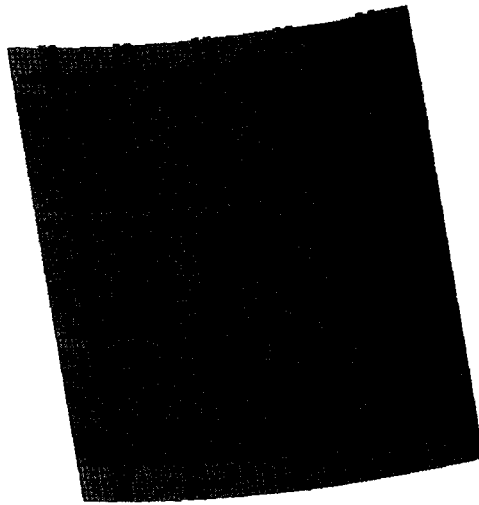


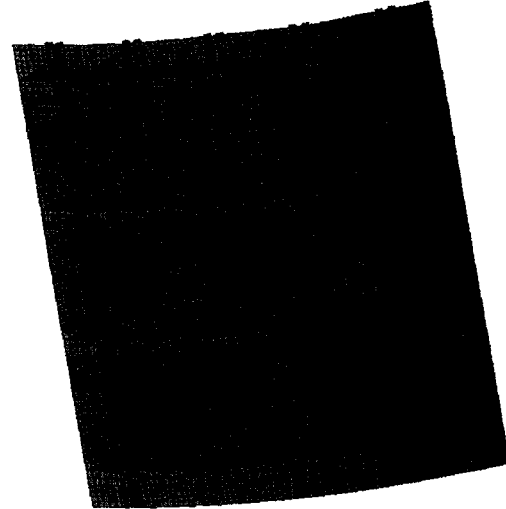
Figure 83. Load vs. end-shortening response for perfect and imperfect 614 panel

In the nonlinear finite element model, initial geometric surface imperfections in both the skin and stringers are derived by using a linear combination of the eigenmodes calculated at various nonlinear equilibrium states. This imperfection shape based on combined eigenmodes is readily defined and enables the STAGS analysis result to be extended beyond limit points in the nonlinear load-deflection response. Each time the STAGS analysis reaches a limit point in the nonlinear solution space where a unique solution cannot be found, the eigenvalues are calculated at that load level. The lowest eigenmode is then combined with the previous eigenmodes (all of the same amplitude) to form a new geometric imperfection to the panel, and the nonlinear analysis is restarted from a zero load level.

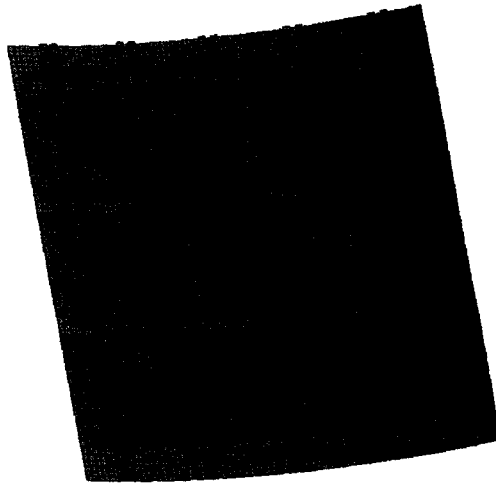
A series of deformed shape plots from four separate model runs is shown in Figure 84 to illustrate the progression of the skin panel buckling as predicted by the finite element model as the applied load increases. The first model run, which does not include surface imperfections, reaches a maximum load level of 11,305 lbs and has the deformed shape shown in Figure 84(a). The lowest eigenmode predicted at that load level is incorporated as an initial imperfection with a maximum amplitude of .04 inches. The second model run reaches a maximum load level of 12,729 lbs and has the deformed shape shown in Figure 84(b). The third model run includes geometric imperfections obtained from the first eigenmode from the eigenanalyses of the first and second model runs. The imperfection amplitudes are both 0.04 inches. The third model reaches a maximum load of 16,432 lbs. The final deformation pattern for the third model is shown in Figure 84(c). The fourth model run includes imperfections, all with a maximum amplitude of 0.04 inches, from the first three model runs. The last change in the deformation pattern of the skin occurs at 17,041 lbs and is shown in Figure 84(d). From this point on the deformation pattern in the skin remains constant with only the magnitude of the displacement changing. The lowest stringer eigenmode is calculated at a nonlinear load level of 39,200 lbs and is added to the skin geometric imperfections using a maximum amplitude of 0.2 inches. This model run reaches a maximum load of 43,471 lbs before buckling of the stringers leads to a collapse of the panel. A study of the effect of stringer imperfection magnitude on panel failure is presented later in Section 5.2.5.



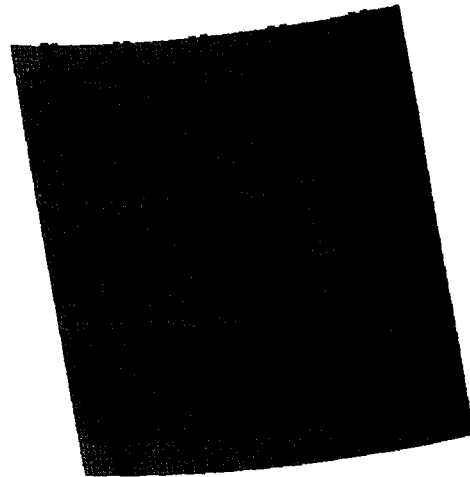
(a) initial run, 11,305 lbs



(b) second run, 12,729 lbs



(c) third run, 16,432 lbs



(d) fourth run, 17,041 lbs

Figure 84. Skin buckling sequence for panel 614 configuration

Skin buckling occurs in the skin panels between the load levels of 11,305 lbs and 17,041 lbs. The predicted panel buckling load range is enveloped by the actual test skin buckling load range of 7,868 lbs to 19,783 lbs. The highest load value achieved by the nonlinear analysis before stringer failure is predicted to occur leading to panel collapse is 43,471

lbs, assuming bonded connections for all skin, stringer, and frame members. This value corresponds to the predicted failure load for the baseline finite element model ($P_{\text{base}}\text{pred}$). The maximum load obtained by the STAGS finite element model is 51 percent higher than the highest test panel failure load of 28,821 lbs. The deformed shape of the panel at the final load step of the elasto-plastic failure analyses is shown in Figure 85. Local stringer crippling shown in Figure 85 is evident and is a contributing factor leading to panel failure as seen in the test panel (Figure 22).

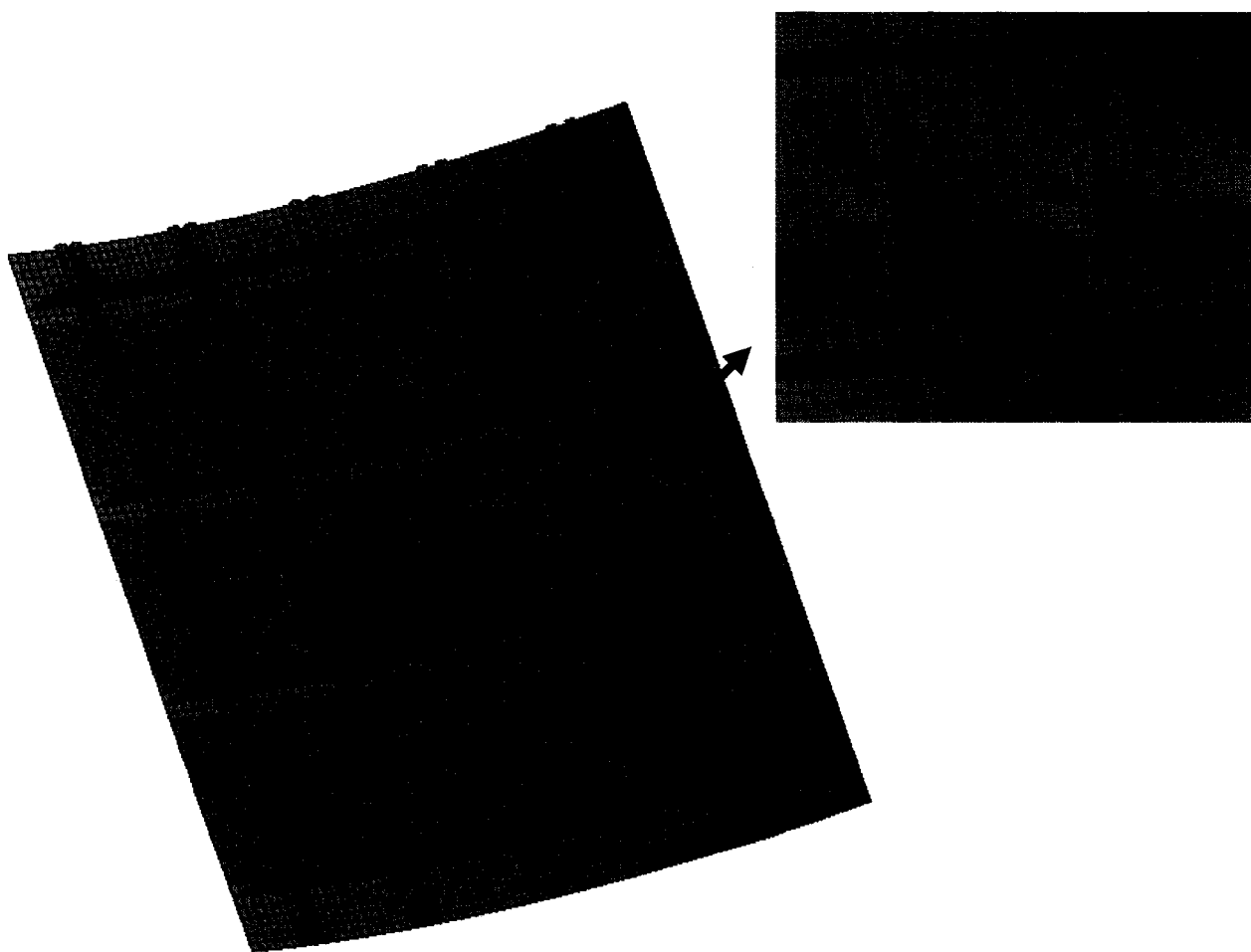


Figure 85. Deformed shape of 614 panel configuration at failure

The unconservative prediction of the failure load may be affected by a variety of factors with a primary factor associated with analyzing the test configuration, i.e., are the analysis assumptions valid? To assess the reduction in failure load for a riveted panel of this configuration (i.e., the test panel) versus a bonded panel of the same construction (i.e., the baseline model), two smaller finite element models are created: one with riveted skin-stringer connections and one with bonded skin-stringer construction. The failed single-bay models are shown in Figure 86. Local buckling that occurs between the rivets cannot be predicted with a bonded-stringer model. A comparison of the deformed shapes at failure for the bonded- and riveted-stringer, single-bay models is shown in Figure 86. Local buckling between the rivets is clearly evident in Figure 86(b). The predicted failure load of the simulated riveted panel, $(P_f)_{rivet}$, is 5,313 lbs, and the predicted failure load of the simulated bonded panel, $(P_f)_{bond}$, is 6,640 lbs. The adjustment factor, f_1 , due to riveted construction versus bonded construction is calculated as follows:

$$f_1 = ((P_f)_{bond} - (P_f)_{rivet}) / (P_f)_{bond} = 0.20$$

This adjustment factor is applied to the predicted failure load, $(P_{base})_{pred}$, as follows:

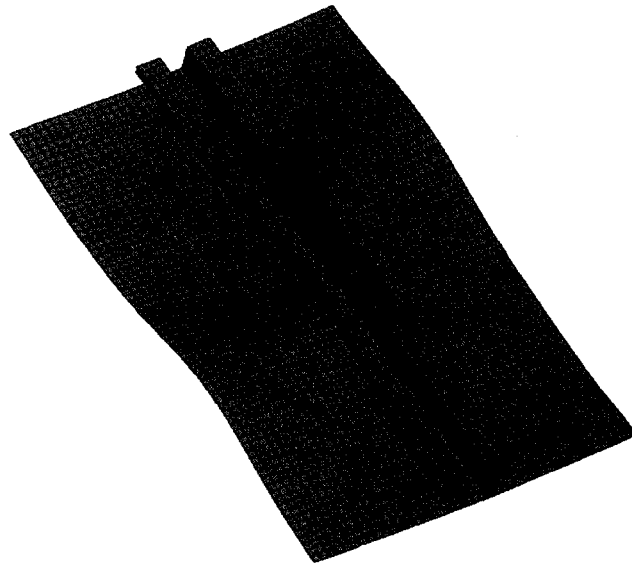
$$(P_{base})_{rev} = (1 - f_1) * (P_{base})_{pred} = \frac{(P_f)_{rivet}}{(P_f)_{bond}} * (P_{base})_{pred} = (1 - 0.2) * 43,471 = 34,777$$

The revised estimated failure load, $(P_{base})_{rev}$, of 34,777 lbs is 21 percent higher than the test panel failure load.

The next issue to be explored is how this adjustment factor, f_1 , varies for different panel constructions. A similar study model approach will be taken for the other three fuselage panel configurations, and the adjustment factor due to riveted versus bonded construction will be compared for all four of the test panel configurations.



(a) Bonded stringer failure, $P_f = 6,640$ lbs



(b) Riveted stringer failure, $P_f = 5,313$ lbs

Figure 86. Single-bay model failures for 614 panel configuration

5.2.2 STAGS Predictions for Panel 615

The 615 panel fails due to stringer crippling, therefore a higher fidelity analysis model similar to the 614 panel model shown in Figure 80(b) is necessary to capture the failure mode observed for the 615 panel configuration. The 614 refined baseline finite element panel model is modified to include the skin doublers under the stringers to create the 615 refined baseline finite element model. As with the 614 panel model, the 615 refined baseline model is assumed to have doublers and stringers bonded to the skin. The 615 panel configuration finite element model consists of 20,340 STAGS E410 4-node, C^1 quadrilateral shell elements, 664 STAGS E210 2-node, C^1 beam elements, a total of 32,446 nodes, and 167,484 active degrees of freedom.

A linear elastic buckling analysis for longitudinal compression loading is performed. The first buckling load of 16,211 lbs, corresponding to a skin-buckling mode is predicted. The predicted buckling load is higher than the lowest test panel skin buckling loads of 13,039 lbs and 12,365 lbs. However, after skin buckling is first observed in the test, skin buckling in other bays of the test panels continues to occur as the load increases up to 15,737 lbs. As with the 614 panels, this observation during testing indicates the presence and influence of generalized imperfections.

A nonlinear finite element analysis of the 615 panel configuration is conducted including both geometric and material nonlinearities. Initial geometric surface imperfections derived from a linear combination of eigenmodes calculated at various nonlinear equilibrium states are included in the finite element model to help push the STAGS

analysis beyond limit points associated with local buckling modes. The highest load value achieved with the nonlinear analysis is 45,621 lb, which is referred to as $(P_{\text{base}})_{\text{pred}}$. The deformed shape of the panel from the elasto-plastic failure analyses at this load is shown in Figure 87. Stringer crippling failures, as seen in the test panel (Figure 26), are evident in the deformed finite element shape from the STAGS nonlinear analysis.

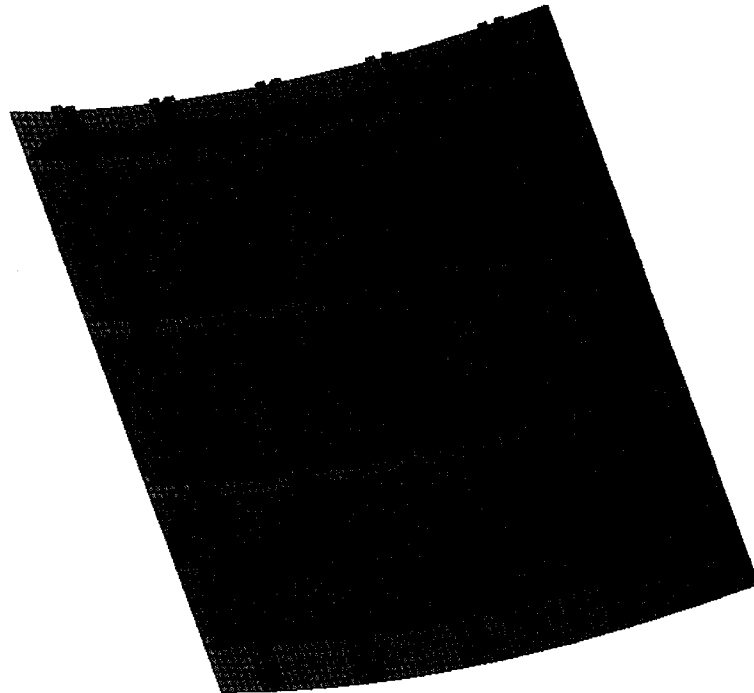


Figure 87. Deformed shape of 615 panel configuration at predicted failure load of 45,621 lb

The maximum load obtained by the finite element model is 53 percent higher than the highest test panel failure load of 29,787 lbs. To assess the reduction in failure load for a riveted panel of this configuration versus a bonded panel of the same construction, two smaller single-bay finite element models are created: one with riveted skin-stringer connections and one with bonded skin-stringer connections. The deformed shapes of the

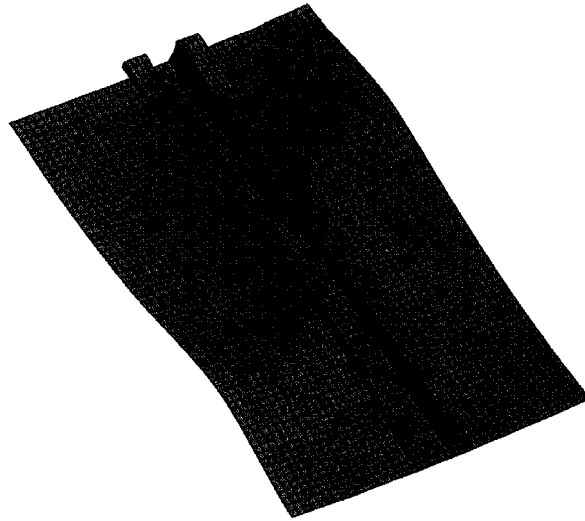
single-bay models at the predicted failure load are shown in Figure 88. The failure load of the riveted panel, $(P_f)_{rivet}$, is 7,500 lbs, and the failure load of the bonded panel, $(P_f)_{bond}$, is 8,924 lbs. The adjustment factor, f_1 , due to riveted construction versus bonded construction for the 615 panel configuration with a doubler under the stringer is calculated as follows:

$$f_1 = ((P_f)_{bond} - (P_f)_{rivet}) / (P_f)_{bond} = 0.16$$

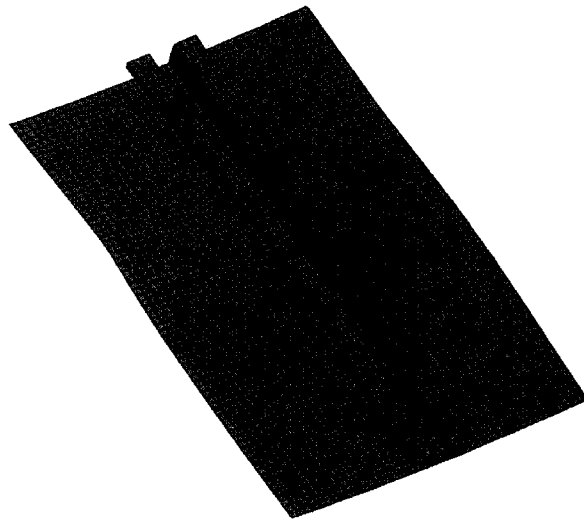
This adjustment factor is applied to the predicted failure load, $(P_{base})_{pred}$, as follows:

$$(P_{base})_{rev} = (1 - f_1) * (P_{base})_{pred} = \frac{(P_f)_{rivet}}{(P_f)_{bond}} * (P_{base})_{pred} = (1 - 0.16) * 45,621 = 38,321$$

The revised estimated failure load, $(P_{base})_{rev}$, of 38,321 lbs is 29 percent higher than the test panel failure load.



(a) Bonded-stringer failure, $P_f = 8,924$ lbs



(b) Riveted-stringer failure, $P_f = 7,500$ lbs

Figure 88. Single-bay model failures for 615 panel configuration

5.2.3 STAGS Predictions for Panel 616

The failure mode for the 616 panel is a global failure of the stringer, therefore the unrefined baseline panel model similar to the 614 model in Figure 80(a) has adequate mesh refinement for modeling the 616 panel configuration. For the unrefined baseline model a bonded construction is assumed. The 616 panel finite element model consists of 11,820 STAGS E410 4-node, C^1 quadrilateral shell elements, 584 STAGS E210 2-node beam elements, 19,274 nodes, and 93,888 active degrees of freedom.

A linear elastic buckling analysis for longitudinal compression loading is performed and predicts an initial buckling load of 45,314 lbs corresponding to a skin buckling mode. The predicted buckling load is again higher than either of the test loads observed for initial buckling during the test (31,473 lbs and 39,342 lbs). In addition, skin buckling in other bays of the test panels continues to develop during the test even after the test load exceeds 48,000 lbs. As with the 614 panels, this progression of local skin-bay buckling indicates the presence of imperfections in the actual panel.

A nonlinear analysis of the 616 panel configuration is conducted including both geometric nonlinearity and material nonlinearity. Initial geometric imperfections in the skin panels, derived from eigenmodes calculated at various nonlinear equilibrium states during the nonlinear analysis, are included in the analysis model to help push the analysis beyond limit points associated with local buckling modes. The highest load value achieved with the nonlinear analysis is 95,188 lb which is 15 percent higher than the highest test panel failure load of 82,730 lbs. The deformed shape of the panel from the

elasto-plastic failure analyses is shown in Figure 89 for the final load step. The Euler-column failures, as seen in the test panel (Figure 31), are visible in the center section of the model shown in Figure 89.

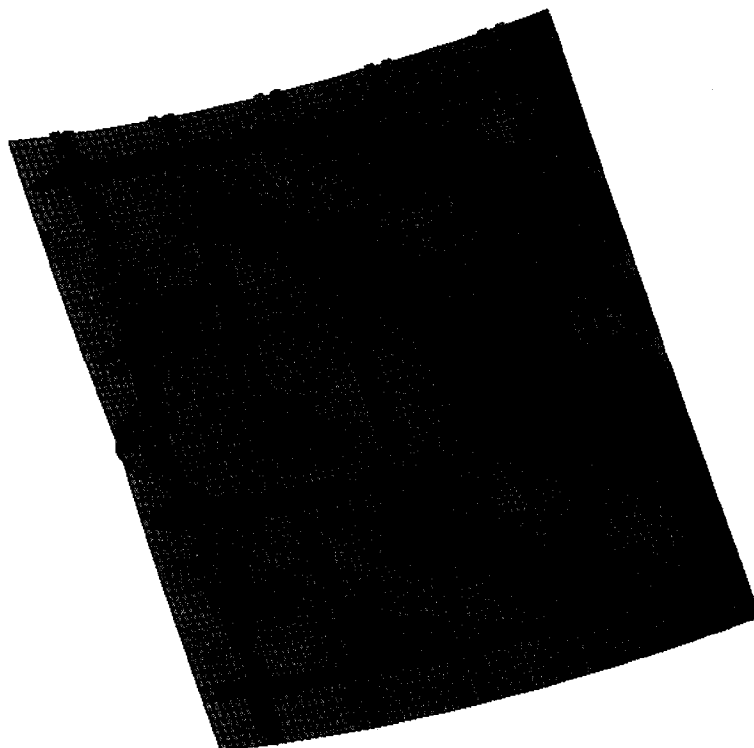


Figure 89. Deformed shape of 616 panel configuration at failure

To assess the reduction in failure load for a riveted panel of this configuration versus a bonded panel of the same construction, two smaller single-bay models are created with and without riveted skin-stringer connections. The deformed shapes of the single-bay models are shown in Figure 90. The predicted failure load of the riveted panel, $(P_f)_{\text{rivet}}$, is 17,438 lbs, and the predicted failure load of the bonded panel, $(P_f)_{\text{bond}}$, is 19,044 lbs. The adjustment factor, f_1 , to account for riveted construction compared to bonded

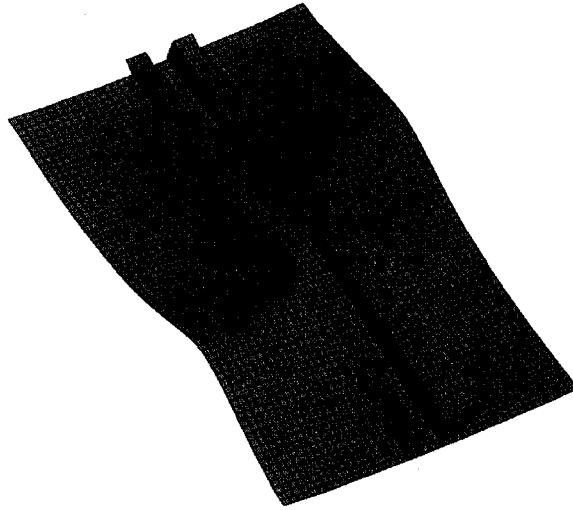
construction for the 616 panel configuration with a doubler under the stringer is calculated as follows:

$$f_1 = ((P_f)_{\text{bond}} - (P_f)_{\text{rivet}}) / (P_f)_{\text{bond}} = 0.084$$

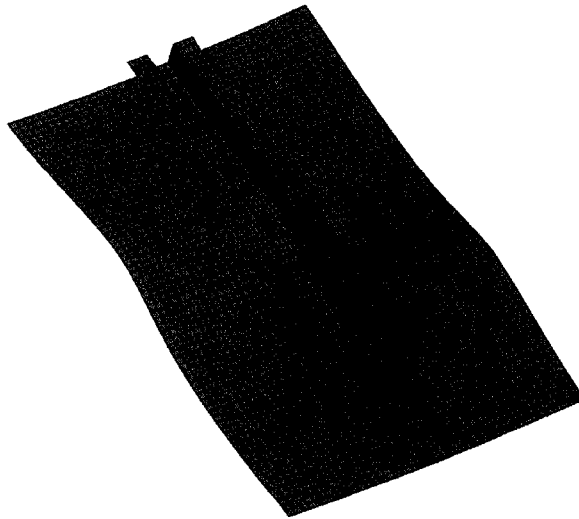
This adjustment factor is applied to the predicted failure load, $(P_{\text{base}})_{\text{pred}}$, as follows:

$$(P_{\text{base}})_{\text{rev}} = (1 - f_1) * (P_{\text{base}})_{\text{pred}} = \frac{(P_f)_{\text{rivet}}}{(P_f)_{\text{bond}}} * (P_{\text{base}})_{\text{pred}} = (1 - 0.084) * 95,188 = 87,192$$

The revised estimated failure load, $(P_{\text{base}})_{\text{rev}}$, of 87,192 lbs is 5 percent higher than the test panel failure load.



(a) Bonded-stringer failure, $P_f = 19,044$ lbs



(b) Riveted-stringer failure, $P_f = 17,438$ lbs

Figure 90. Single-bay model failures for 616 panel configuration

5.2.4 STAGS Predictions for Panel 617

The failure mode for the 617 panel is also a global failure of the stringer, therefore the unrefined baseline model, having a level of mesh refinement similar to the 616 model shown in Figure 89, is used. For the unrefined baseline model a bonded construction is again assumed. Gusset plates are included at each intersection of stringers and frames. The finite element model consists of 10,404 STAGS E410 4-node, C^1 quadrilateral shell elements, 1,424 STAGS E210 2-node beam elements, 17,934 nodes, and 86,568 active degrees of freedom.

First a linear buckling analysis for a longitudinal compression prestress state is performed using the finite element model shown in Figure 91. The linear elastic finite element analysis predicts a buckling load of 29,530 lbs corresponding to a skin buckling mode. This buckling load is slightly higher than the test panel skin buckling loads of 27,427 lbs and 28,326 lbs.

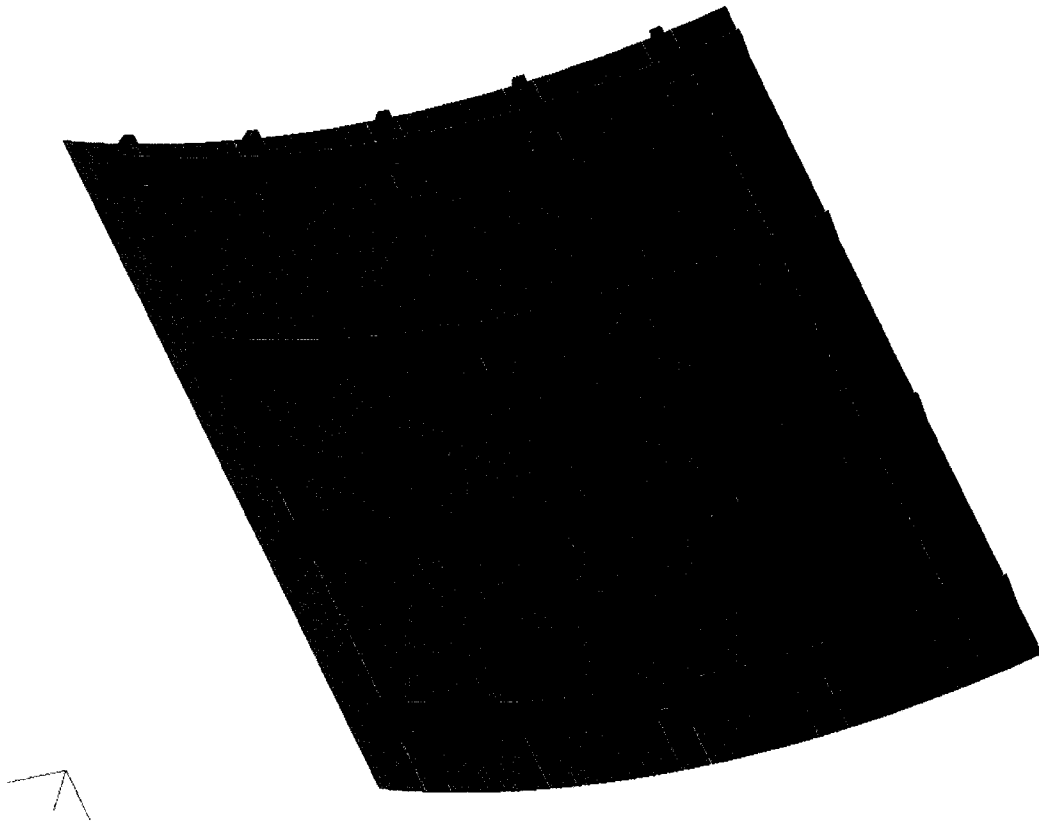


Figure 91. Panel 617 configuration finite element model

Secondly, a nonlinear analysis of the 617 panel configuration is conducted including both geometric nonlinearity and material nonlinearity. Initial geometric imperfections in the skin panels derived from eigenmodes calculated at various nonlinear equilibrium states during the nonlinear analysis are included in the analysis to help push the model beyond limit points associated with local buckling modes. The highest load value achieved with the nonlinear analysis is 59,046 lbs. The deformed shape of the panel from the elastoplastic failure analyses is shown in Figure 92. Euler-column type buckling, as seen in the test panel, is visible in the outer stringers of the center section of the panel. Rolling of the frames is also visible.

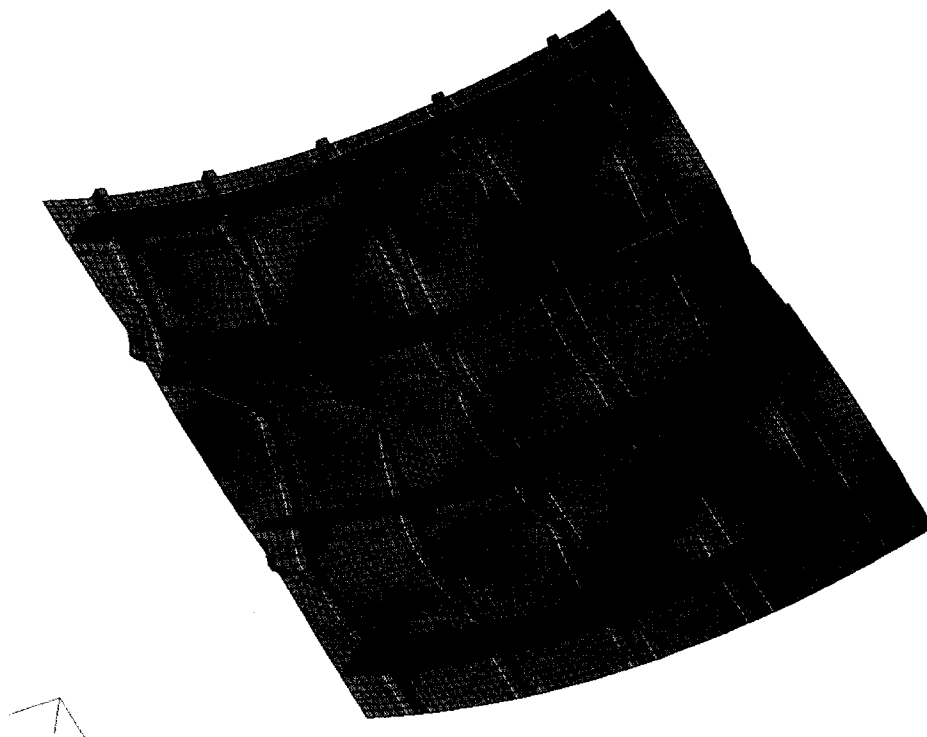


Figure 92. Deformed shape of 617 panel configuration at failure

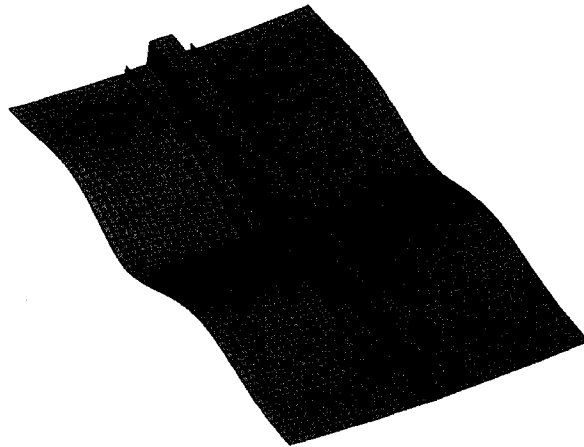
The maximum load obtained by the finite element model is 6.5 percent higher than the highest test panel failure load of 55,460 lbs. To assess the reduction in failure load for a riveted panel of this configuration versus a bonded panel of the same construction, two smaller single-bay models are created with and without riveted skin-stringer connections. The deformed shapes of the single-bay models are shown in Figure 93. The predicted failure load of the riveted panel, $(P_f)_{rivet}$, is 10,350 lbs, and the predicted failure load of the bonded panel, $(P_f)_{bond}$, is 11,835 lbs. The adjustment factor, f_1 , to account for riveted construction compared to bonded construction for the 617 panel configuration with a doubler under the stringer is calculated as follows:

$$f_1 = ((P_f)_{bond} - (P_f)_{rivet}) / (P_f)_{bond} = 0.13$$

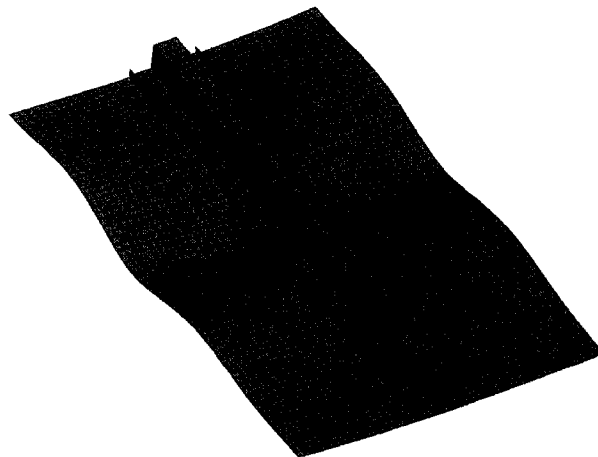
This adjustment factor is applied to the predicted failure load, $(P_{\text{base}})_{\text{pred}}$, as follows:

$$(P_{\text{base}})_{\text{rev}} = (1-f_1) * (P_{\text{base}})_{\text{pred}} = \frac{(P_f)_{\text{rivet}}}{(P_f)_{\text{bond}}} * (P_{\text{base}})_{\text{pred}} = (1-0.13)*59,046 = 51,370$$

The revised estimated failure load, $(P_{\text{base}})_{\text{rev}}$, of 51,370 lbs is 8 percent lower than the test panel failure load.



(a) Bonded-stringer failure $P_f = 11,835$ lbs



(b) Riveted-stringer failure $P_f = 10,350$ lbs

Figure 93. Single-bay model failures for 617 panel configuration

5.2.5 STAGS Analysis Summary

A summary of the STAGS finite element analyses and test results is presented in Table 16. The initial buckling response of the panels is driven by the skin thickness and stringer doubler width. The 614 panel configuration has a 0.04-in.-thick skin and no doubler and has the lowest initial buckling load. The 615 panel configuration has a 0.04-in.-thick skin and a 2.0-in.-wide doubler under all stringers and has the next lowest initial buckling load. Adding the doubler increases the buckling load. The 616 panel configuration, which has a doubler over the entire 0.04-in.-thick skin for a total thickness of 0.072 inches, has the highest skin buckling load. The 617 panel configuration has a uniform 0.063-in.-thick skin instead of any doubler, inverted hat stringers, and gussets. The 617 panel configuration has initial buckling loads between 10 and 30 % of the buckling load values predicted for the 616 panel configuration that has a uniform 0.04-in.-thick skin with an 0.032-in.-thick doubler over all the skin. However, the inverted hat stringer offers less resistance (less stiffness) than the hat stringers on the other configurations. Finite element initial buckling predictions are from linear elastic eigenvalue analyses that assume a perfect shell structure. Initial geometric surface imperfection measurements of the skin panels indicate that for the 0.04-in.-thick skin panels (614, 615, and 616 configurations) the skin surface imperfection magnitude is greater than the skin thickness along the circumferential arclength of the panels. For the panel with the thicker skin (617 configurations), the skin surface imperfections along the arclength of the panel are less than the skin thickness. For this reason, the initial buckling predictions for the 617 panel are more accurate than the predictions obtained for the other panel configurations (i.e., less sensitive to assumed initial geometric surface imperfection

assumptions). However for each panel, a progressive buckling of subsequent skin bays does occur in the range of the predicted buckling load.

Panel Configuration	Buckling Load, lbs			Failure Load, lbs			
	FEM	Test	%diff	FEM	Adjusted FEM	Test	%diff (adjusted)
614	13506	8318	-62	43471	34777	28821	-21
		7868	-72			28551	-22
615	16726	13039	-28	45621	38321	29787	-29
		12365	-35			29563	-30
616	45314	31473	-44	95188	86621	78684	-10
		39342	-15			82730	-5
617	29530	27427	-8	59046	51370	55640	8
		28326	-4			54764	6

Table 16. Test and STAGS buckling and failure loads

The ultimate failure of the panels is driven by the stiffness of the stringers. The 614 and 615 panel configurations both have 0.025-in.-thick open-hat stringers that fail due to stringer crippling. The 616 panel configuration has a 0.063-in.-thick open-hat stringer, and the 617 panel configuration has a 0.025-in.-thick closed-hat stringer. Both the 616 and 617 panel configurations experience Euler-column failures of the stringers.

Therefore, the original less-refined finite element models for these two configurations predict failure with reasonable accuracy when the effect of the riveted connection is taken into consideration. Additionally, stringer imperfections are not required in the finite element analysis to trigger the failure of these panels. However, alternate stiffened fuselage panel designs may require additional analysis fidelity to account for stringer imperfections, skin-thickness variations, or other generalized imperfections.

Because the 614 and 615 panel configurations fail due to local stringer crippling, additional finite element mesh refinement is needed in the finite element models. A

higher mesh density, a greater stringer cross-section modeling fidelity, and the inclusion of stringer imperfections are all necessary to predict the failure of the 614 and 615 panels. Failure predictions for these two panel configurations are the least accurate for the present analysis models, most likely due to imperfections in the stringers that were not quantified before testing.

In order to explore this hypothesis, a stringer-imperfection sensitivity study was performed on the 614 panel configuration. Stringer imperfection refers to the deviation from straightness of the stringer along the length of the stringer and includes waviness of the stringer's web and flanges. Also included in the imposed geometric imperfection is the waviness in the attached skin segments and/or adjacent skin. The panel imperfection shape, shown in Figure 94, is assumed to take the form of the first buckling mode from an eigenvalue analysis performed at a nonlinear stress state just prior to stringer buckling (as shown in Figure 84) in the 614 panel analysis described in Section 5.2.1. The stringer imperfection shape shown in Figure 94 illustrates the rolling of stringers between frames especially for the outer stringers. Also visible is the opening up and bowing inward of the stringer cross-section, mainly for the interior stringers. This imperfection shape is dominated by the stringer participation with minimal participation of the panel skin or frames. The maximum magnitude of the stringer imperfection is varied from 0.05 in. to 0.2 in. The imperfection magnitude ranges from 8 to 34% of the distance between stringer upright flanges (dimension s_3 in Figure 10). This dimension changes as the stringers begin to bow inward or push outward.

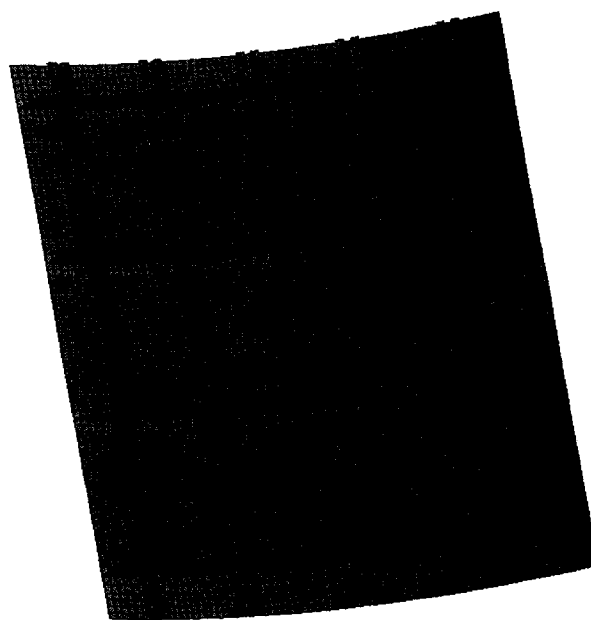


Figure 94. Stringer imperfection shape for 614 panel configuration

The corresponding load-deflection curves obtained from a STAGS nonlinear analysis of the 614-panel configuration, assuming a bonded-stringer attachment with different maximum imperfection amplitudes, are shown in Figure 95. As the magnitude of the imperfection increases, the slope of the load-deflection curve and the maximum load (failure load) carried by the panel both decrease. However, the predicted failure loads still exceed the observed test failure load, which corresponds to an unconservative prediction. Applying the adjustment factor for the 614 panels to relate bonded analysis results to a riveted attachment (without the need for explicit detail modeling) reduces the predicted failure load but it still exceeds the failure load observed in test. A comparison between the test failure load and the baseline and adjusted predicted failure loads associated with different imperfection magnitudes are shown in Figure 96.

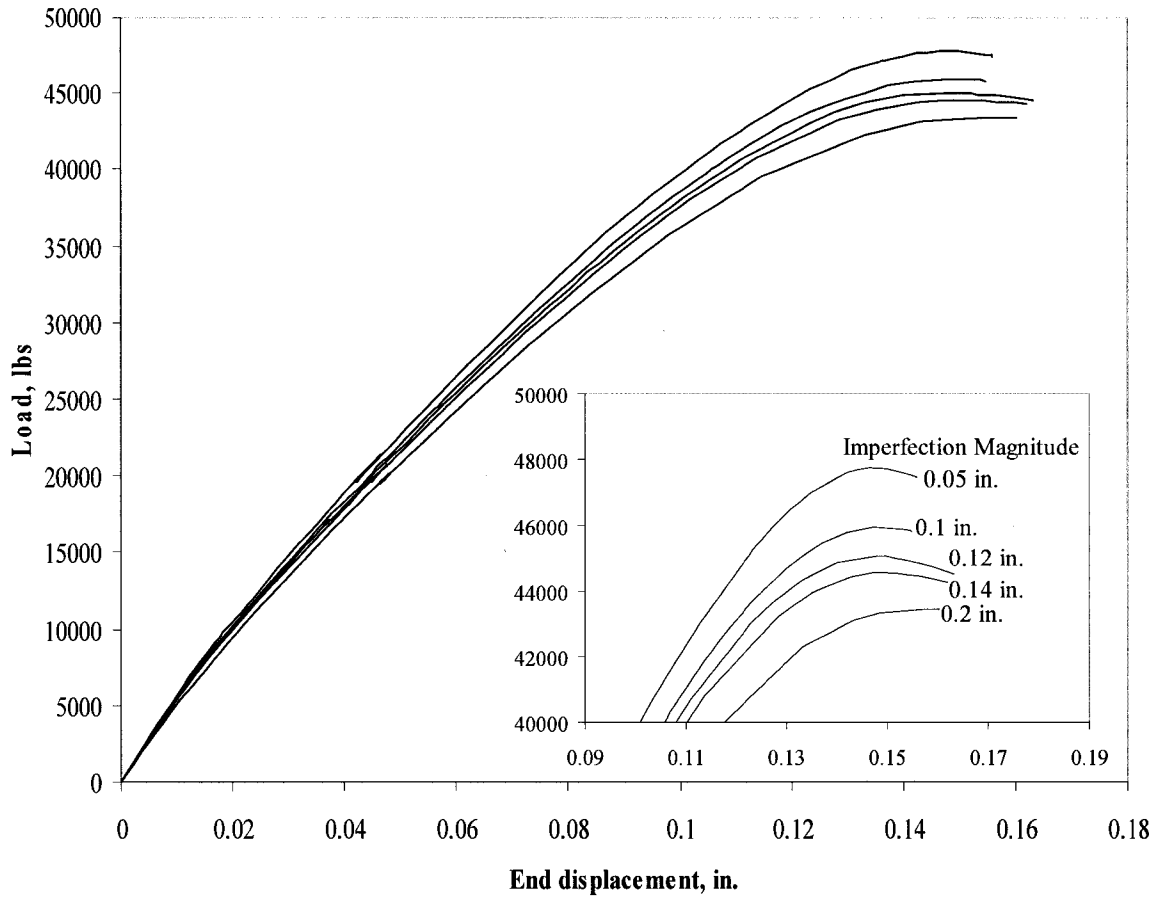


Figure 95. Load-shortening curves for the 614 panel configuration with imperfections

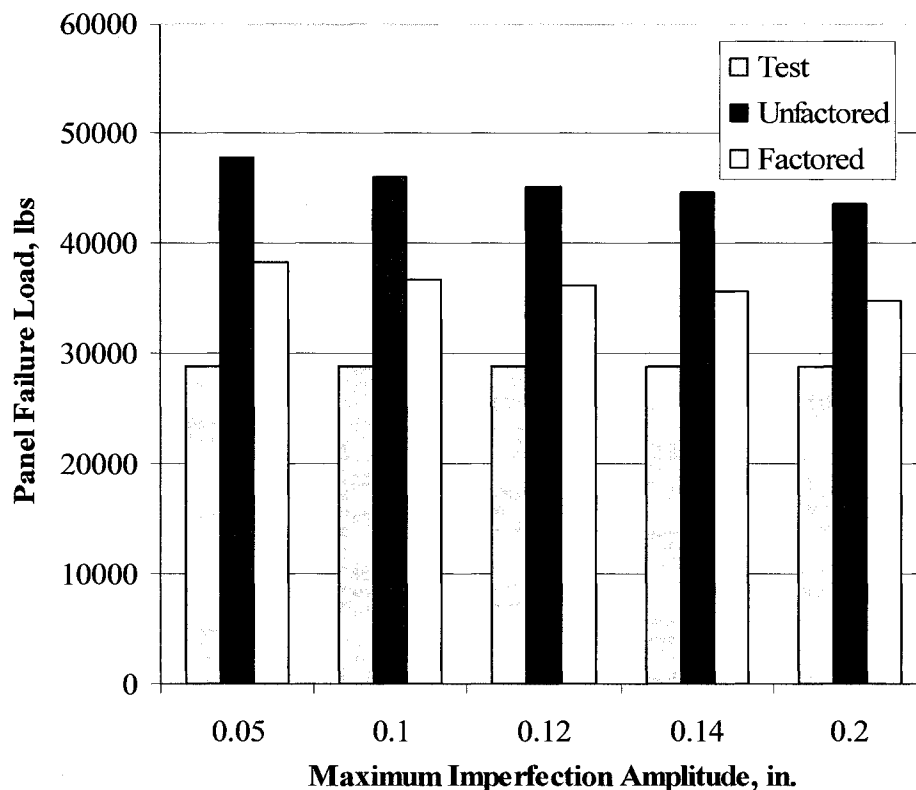


Figure 96. Baseline and adjusted failure loads for the 614 panel configuration

Different finite element modeling approximations were studied for the 614-panel configuration. A complete or full panel model and a single-stringer local model were analyzed. In Section 5.2.1, the baseline finite element models are described, and results are given for the geometric and material nonlinear analyses performed assuming an initial surface imperfection derived from the eigenmodes. Sensitivity to initial surface imperfections was investigated, and the conclusion was that a surface imperfection with a maximum amplitude on the order of the skin thickness in a single skin bay could reduce the initial panel bucking load by 20%. Furthermore, an adjustment factor of 20% on the overall failure load of the panel for riveted versus bonded skin-stringer connections was

determined. Here results from the stringer imperfection study indicate that the change in failure load is approximately a linear relationship to the stringer imperfection amplitude.

5.3 Proposed PAGE Analysis/Design Improvements

The two failure modes predicted by PAGE for the test panels are Euler-column buckling failure of the stringer and skin wrinkling leading to catastrophic local buckling of the stringer. This section will propose improvements to the PAGE analysis to account for errors in the predicted failure load for these two failure modes.

5.3.1 Euler-Column Failure Mode

Euler-column failures are well understood and predictions from both PAGE and STAGS are in good agreement with the test results except for the PAGE results for the 617 panel configuration. The reason for the discrepancy for the 617 panel is due to the local gussets connecting the stringers to the frames. These gussets effectively shorten the column length of the stringer and increase the Euler-column failure load. To remedy this problem, additional input needs to be provided to PAGE for gusseted panels. This input can either be in the form of a column length adjustment factor supplied by the user, or the gusset geometry from which PAGE will calculate an adjustment factor.

One method of generating an effective column length based on gusset and stringer geometry using finite element models is proposed. This method will use simple finite element analyses to create curves relating stringer area, stringer spacing, gusset thickness, and gusset attachment length to an effective column length for the stringer to be used in

the Euler-column failure calculation. Several finite element models having the same stringer geometry, but varying gusset geometries will be used to calculate the failure loads of the stringer. The stringer will be modeled with beam elements and the gussets will be modeled with triangular elements. The stringer will be simply supported on one end and a compression load will be applied to the opposite end. The gusset will be attached to the stringer at the simply-supported end and will also be simply supported along the bottom edge of the gusset as shown in Figure 97.

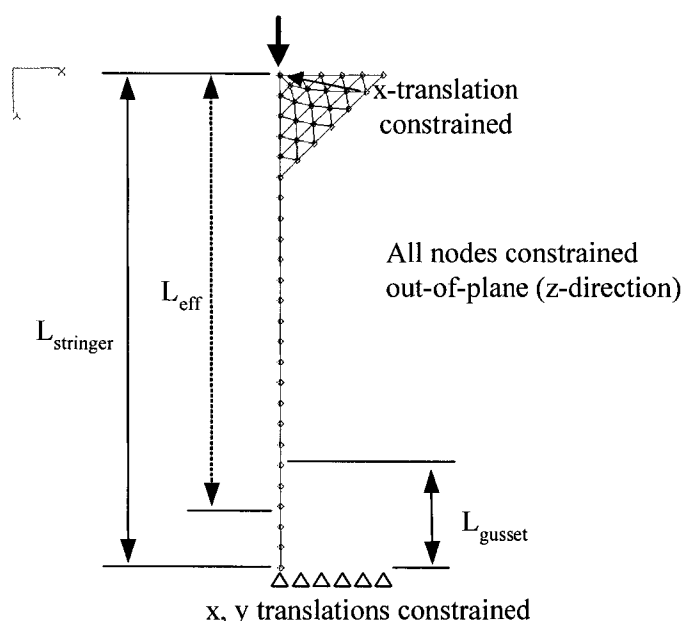


Figure 97. Finite element model of stringer with attached gusset

Four gusset lengths were modeled: 1 in., 1.5 in., 2.0 in., and 2.5 in. The simply-supported edge of the gusset was modeled to have the same length as the edge attached to the stringer. For each of the four gusset lengths, five gusset thicknesses were modeled: 0.01 in., 0.02 in., 0.03 in., 0.04 in., and 0.05 in. The stringer was modeled to have the same geometry as in the 617 test panel configuration, as well as the 12 inch stringer spacing. A geometrically nonlinear analysis is performed to determine the Euler-column

failure load of the stringer. Results for the 20 finite element analysis runs are shown in Table 17. An effective stringer length, L_{eff} (see Figure 97), is calculated for each configuration such that the stringer failure load, P_{cr} , is calculated by $P_{\text{cr}} = \pi^2 EI / L_{\text{eff}}^2$

where:

$$E = 10.5 \times 10^6 \text{ psi}$$

$$I = 0.009 \text{ in}^4$$

The calculated Euler-column failure load, P_{Euler} , for the stringer without a gusset is 6,477 lbs and is confirmed by finite element analysis of the stringer without a gusset. The ratio of the failure load of the stringer with a gusset to the Euler-column failure load of the stringer without a gusset, $P_{\text{cr}}/P_{\text{Euler}}$, is also shown in Table 17.

L_{gusset} , in.	t_{gusset} , in.	P_{cr} , lbs	$P_{\text{cr}}/P_{\text{Euler}}$	L_{eff} , in.
1	0.01	8407	1.30	10.53
1	0.02	9687	1.50	9.81
1	0.03	10564	1.63	9.40
1	0.04	11187	1.73	9.13
1	0.05	11648	1.80	8.95
1.5	0.01	10020	1.55	9.65
1.5	0.02	11661	1.80	8.94
1.5	0.03	12539	1.94	8.62
1.5	0.04	13076	2.02	8.45
1.5	0.05	13437	2.07	8.33
2	0.01	11591	1.79	8.97
2	0.02	13263	2.05	8.39
2	0.03	14037	2.17	8.15
2	0.04	14489	2.24	8.02
2	0.05	14794	2.28	7.94
2	0.1	15559	2.40	7.74
2.5	0.01	12979	2.00	8.48
2.5	0.02	14616	2.26	7.99
2.5	0.03	15347	2.37	7.80
2.5	0.04	15788	2.44	7.69
2.5	0.05	16097	2.49	7.61
2.5	0.1	16939	2.62	7.42

Table 17. Results for gusseted-stringer models

The effective length of the stringer for Euler-column failure calculations should be directly proportional to the stringer area, A_{str} , and stringer length, L_{str} , and inversely proportional to the gusset thickness, t_{gusset} and gusset length, L_{gusset} ; therefore, L_{eff} is plotted as a function of the quantity, $A_{\text{str}} L_{\text{str}} / t_{\text{gusset}} L_{\text{gusset}}$ in Figure 98. For the 617 panel configuration, $A_{\text{str}} = 0.1925 \text{ in}^2$, and $L_{\text{str}} = 12 \text{ in}$.

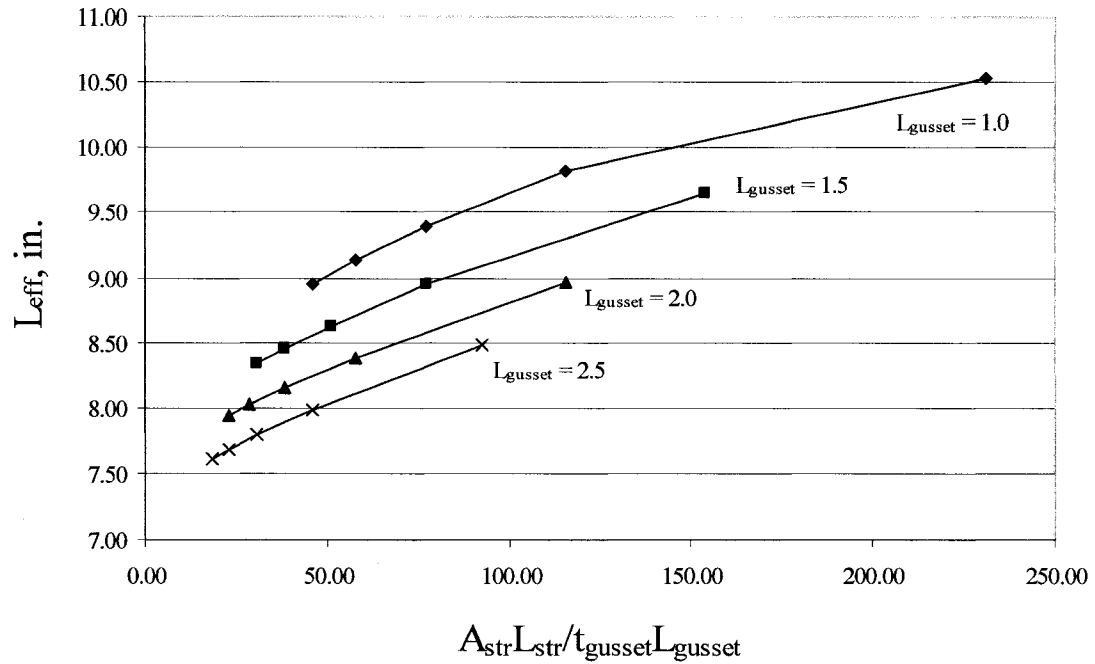


Figure 98. Effective stringer length for Euler-column failure calculations as a function of stringer and gusset geometry

A second order polynomial curve fit can be performed on each of the 4 curves representing different gusset lengths in Figure 98. The general formula for the equation is, $L_{eff} = ax^2 + bx + c$, where $x = A_{str} L_{str} / t_{gusset} L_{gusset}$ and the coefficients a, b, and c are listed in Table 18 for each of the four gusset lengths.

L_{eff}	a	b	c
1.0	-3.41E-05	0.0180	8.202
1.5	-3.34E-05	0.0168	7.846
2.0	-2.99E-05	0.0153	7.606
2.5	-4.12E-05	0.0162	7.331

Table 18. Second order polynomial coefficients

Each of the coefficients a, b, and c can be similarly related to L_{eff} using third and second order polynomial curve fits. The general formulas for the equations are:

$$a = 1.7464 L_{\text{eff}}^3 - 6.6828 L_{\text{eff}}^2 + 8.2584 L_{\text{eff}} + 0.088$$

$$b = 0.0022 L_{\text{eff}}^3 - 0.0083 L_{\text{eff}}^2 + 0.0079 L_{\text{eff}} + 0.0161$$

$$c = 0.0585 L_{\text{eff}}^2 - 0.8188 L_{\text{eff}} + 8.9571$$

Using the polynomial equations with the coefficients in Tables 18 and listed above, the effective length for Euler-column failure equations can be calculated for a given gusset and stringer geometry. A comparison of the stringer failure loads calculated by the finite element analyses to those calculated with the polynomial equations is shown in Table 19.

L _{gusset} , in.	t _{gusset} , in.	FEM	Equations		P _{cr}
		P _{cr} , lbs	L _{eff} , in.	P _{cr} , lbs	%diff
1	0.01	8407	10.53	8415	0.09
1	0.02	9687	9.81	9685	-0.02
1	0.03	10564	9.37	10612	0.46
1	0.04	11187	9.12	11219	0.28
1	0.05	11648	8.95	11639	-0.07
1.5	0.01	10020	9.65	10018	-0.02
1.5	0.02	11661	8.95	11642	-0.16
1.5	0.03	12539	8.63	12521	-0.14
1.5	0.04	13076	8.45	13048	-0.21
1.5	0.05	13437	8.34	13398	-0.29
2	0.01	11591	8.93	11703	0.96
2	0.02	13263	8.37	13321	0.43
2	0.03	14037	8.12	14130	0.66
2	0.04	14489	7.99	14601	0.77
2	0.05	14794	7.91	14908	0.76
2	0.1	15559	7.74	15582	0.15
2.5	0.01	12979	8.44	13094	0.88
2.5	0.02	14616	7.99	14607	-0.06
2.5	0.03	15347	7.78	15402	0.35
2.5	0.04	15788	7.67	15869	0.51
2.5	0.05	16097	7.59	16175	0.48
2.5	0.1	16939	7.44	16850	-0.53

Table 19. Comparison of failure loads calculated by finite element analysis and derived polynomial equations

The derived equations can be used to predict the Euler-column failure value for the 617 panel configuration. The length of the gusset connection to the stringer (frame attach rivet to last gusset rivet) is 1.5 inches, and the gusset thickness is 0.032 in. The stringer area not including any attached skin is 0.1925 in², and the stringer spacing is 12 in. Using these values, $A_{str} L_{str} / t_{gusset} L_{gusset} = 48.13$. Substituting this value into the polynomial equations gives a value of 8.59 in. for the effective length, resulting in an Euler-column failure prediction of 12,647 lbs. The original PAGE failure prediction was 7,704 lbs per stringer bay, and the average test failure load per bay was 11,040 lbs. In

reality some amount of effective skin is working with the stringer in the Euler-column failure equation. If we include 2 in. of the .063-in.-thick skin in the stringer area calculation ($A_{str} = 0.391 \text{ in.}^2$), the predicted Euler-column failure load is 11,074 lbs which is very close to the actual failure load. A conservative amount of skin needs to be included in the stringer area calculation so that the PAGE predicted failure load will always be less than the actual failure load of the panel. The results presented in the section represent a method for adjusting the predicted Euler-column failure loads for gusseted-panels, however, additional finite element analyses need to be performed to represent a wider variety of panel configurations before this method can be incorporated into PAGE.

5.3.2 Skin Wrinkling Failure Mode

The other failure load observed in the test panels is skin wrinkling leading to a catastrophic local failure of the stringer. PAGE skin-wrinkling failure predictions are conservative by 20-24% using the stringer area only. This amount of conservatism results in a significant increase in structural weight in the preliminary design phase and should be addressed. A study was performed using the single bay STAGS models for the 614, 615, and 616 panel configurations to see if any trends were noticeable for the different fidelity models as described in Section 4.4. The goal is to establish a factor based on the study models that would improve the PAGE failure estimates for the skin-wrinkling failure modes (panels 614 & 615) without significantly changing the results of the more accurate Euler-column failure predictions (panel 616). A summary of the results are shown in Table 20.

Failure mode	614		615		616	
	Skin wrinkling		Skin wrinkling		Euler column-SS	
	Failure Load	% diff	Failure Load	% diff	Failure Load	% diff
TEST (avg)	5737		5935		16141	
PAGE	4365	-24	4736	-20	16239	1
STAGS-Single						
Smearred elastic	33245	479	37993	540	59958	271
Discrete elastic	25275	341	29887	404	51404	218
Discrete elas/plas	7888	37	10982	85	17730	10
Bonded elastic	11939	108	13734	131	39620	145
Bonded elas/plas	6640	16	8924	50	19044	18
Riveted elastic	9311	62	12331	108	35329	119
Riveted elas/plas	5313	-7	7500	26	17438	8

Table 20. Panel 614, 615, and 616 study model results

The results summarized in Table 20 show a possible link between three different levels of finite element modeling fidelity in the STAGS models and the level of conservatism in the PAGE predictions. Using ratios of the discrete, bonded, and riveted elastic/plastic failure predictions, a factor can be developed that is close to the level of conservatism in the PAGE predictions. The factor incorporates an average of two effects: (1) the effect of cross-sectional deformation represented by discrete vs. branched shell model results and (2) the effect of the attachment modeling assumptions represented by bonded vs. riveted model results. The equation applying the factor to the PAGE failure load is as follows:

$$0.5 * \left(\frac{\text{Discrete Elas/plas}}{\text{Bonded Elas/plas}} + \frac{\text{Bonded Elas/plas}}{\text{Riveted Elas/plas}} \right) \times \text{PAGE prediction} = \text{Revised prediction}$$

Applying this equation to the 614, 615, and 616 panel configuration PAGE predictions gives:

$$\text{Panel 614: } 0.5 * \left(\frac{7888}{6640} + \frac{6640}{5313} \right) (4365) = (1.22) * 4365 = 5320 \text{ lb.} \quad (-7\% \text{ error})$$

$$\text{Panel 615: } 0.5 * \left(\frac{10982}{8924} + \frac{8924}{7500} \right) (4736) = (1.21) * 4736 = 5732 \text{ lb.} \quad (-3\% \text{ error})$$

$$\text{Panel 616: } 0.5 * \left(\frac{17730}{19044} + \frac{19044}{17438} \right) (16239) = (1.01) * 16239 = 16427 \text{ lb.} \quad (+2\% \text{ error})$$

Using this factoring approach, the 614 and 615 panel failure predictions remain conservative and show a higher level of accuracy than the unfactored PAGE results when compared to the test panel failure loads. The factored failure load for the 616 panel is slightly unconservative, however, the factored failure load of 16,427 lbs is lower than the failure load of the second 616 test panel. The factored failure load is higher than the first 616 test panel failure load, but the first 616 test panel was noted to be warped before the test. Therefore, this factoring approach for the PAGE program results in reasonable test panel failure predictions. A simplified approach to factoring the PAGE predictions would be to simply factor all skin-wrinkling failure loads by a factor of 1.2 and leave the Euler-column failure predictions unchanged unless gussets were included as discussed in Section 5.3.1. Additional tests that included more panel geometries would be necessary to verify this factoring approach.

5.4 Analysis Summary

A summary of the test panel failure loads as predicted by STAGS, PAGE, and a modified PAGE is shown in Table 21. The STAGS panel predictions are from the full panel finite element models. The modified PAGE results reflect a proposed factor of 1.2 to be applied to all skin wrinkling failures and a calculated factor to be applied to all Euler-column buckling failures where gussets are present. Therefore, failure predictions for

panels 614 and 615 include a 1.2 factor because the original PAGE failure mode for these two configurations is skin wrinkling. The PAGE-predicted failure mode for the 616 and 617 panels is Euler-column buckling, therefore the 616 failure prediction is unchanged and the 617 failure prediction is factored due to the presence of the gussets on the 617 panel. The modified PAGE results show a significant decrease in the degree of conservatism in the predicted failure loads which will translate into a significant reduction in weight.

Panel Configuration	Test	STAGS		PAGE		PAGE (modified)	
	Maximum Load, lbs	Maximum Load, lbs	% error	Maximum Load, lbs	% error	Maximum Load, lbs	% error
614	28821	34777	-20.7	21825	24.3	26190	9.1
	28551		-21.8		23.6		8.3
615	29787	38321	-28.7	23680	20.5	28416	4.6
	29563		-29.6		19.9		3.9
616	78684	86621	-10.1	81195	-3.2	81195	-3.2
	82730		-4.7		1.9		1.9
617	55640	51370	7.7	38520	30.8	55370	0.5
	54764		6.2		29.7		-1.1

Table 21. Summary of STAGS and PAGE failure predictions

SECTION 6

CONCLUSIONS AND RECOMMENDATIONS

6.1 Conclusions

Analytical design tools based on closed-form solutions are very efficient for analyzing stiffened-panel failure loads, but are limited in scope and generally lead to overly conservative estimates. The closed-form design tool PAGE that was investigated does not include fasteners, is limited to hat-section stringers, and does not include any stiffener gusset supports that are present in the production Gulfstream aircraft. The accuracy of the PAGE predictions also varies with failure mode type. PAGE Euler-column failure predictions are accurate if gussets are not present. However, when gussets are present, PAGE has been shown to under-predict the failure load by as much as 30%. PAGE has also been shown to under-predict skin-wrinkling failures by as much as 26%. An alternate closed-form design tool, PANDA2, that was studied only includes capabilities for a select number of stringer cross-sections but does not include the open-hat stringers. PANDA2 failure predictions for the panel with closed-hat stiffeners under-predicted the failure load by 18%. In summary, the analytical tools based on closed-form solutions lead to safe fuselage panel designs, but do not produce the lightest-weight designs.

The finite element modeling study presented in Section 4 showed that the accuracy of the failure predictions was very sensitive to the modeling assumptions. For example, a smeared-stiffener modeling approach produced more accurate results if the stringer area was smeared only over the local stiffener area rather than over the entire panel. However

local stiffener failure modes were lost in this modeling approach. Modeling the stiffener as an attached beam produced even more accurate results compared to the smeared-stiffener approach. However, detailed interaction of attachment flanges and inclusion of cross-sectional deformations are ignored. An increase in the model complexity to include branched-shell stiffeners further increased the accuracy of the failure predictions, as did modeling mechanical fasteners in the stiffener-skin connection. In order to obtain accurate failure predictions, all panel components needed to be modeled as branched-shells, and geometric and material nonlinearities had to be included. In addition, an adjustment factor was required for the finite element results when the actual stiffener was attached by rivets and the finite element model represented the connection as bonded. Large panel finite element models of the four Gulfstream test panels described in Section 5 indicated that unknown geometric imperfections in the stiffened panels reduced the failure load, resulting in unconservative failure predictions. Even if the appropriate detail is included in the finite element model, an over-prediction of the failure load may occur, thus leading to an unconservative design.

6.2 Recommendations

The analysis approach that is best able to meet the goal of a safe and lightweight stiffened-panel design is one that is based on closed-form solutions and adjusted for known design details that change the failure load of the panel. It is recommended that the Gulfstream analysis tool, PAGE, be adjusted for two failure modes. The Euler-column buckling prediction should be adjusted to account for gusseted stiffeners by providing a column-length reduction factor as discussed in Section 5.4.1. In addition, the skin-

wrinkling failure load should be adjusted by a factor to remove excessive conservatism as discussed in Section 5.4.2. The proposed factoring approach was based on the small-panel finite element study presented in Section 4. The appropriate factor should be developed based on additional finite element modeling and small-panel testing that is specific to the Gulfstream fuselage design.

REFERENCES

1. Anderson, M. S., Stroud, W. J., Durling, B. J., and Hennessy, K. W., "PASCO: Structural Panel Analysis and Sizing Code, User's Manual", NASA TM-80182, November 1981.
2. Arnold, R. R., and Parekh, J. C., "Buckling, Postbuckling, and Failure of Stiffened Panels Under Shear and Compression," *Journal of Aircraft*, Vol. 24, No. 11, November 1987, pp. 803-811.
3. Arnold, R. R., Yoo, S. Y., and Mayers, J., "Buckling, Postbuckling and Crippling of Shallow Curved Composite Plates with Edge Stiffeners," AIAA Paper 85-0769, 1985.
4. Anonymous, *The NASTRAN User's Manual*, NASA-SP-222, 1970.
5. Anonymous, *ABAQUS/Standard User's Manual*, Vol. I & II (ver. 5.4), Hibbit, Karlsson & Sorensen, Inc., Pawtucket, Rhode Island, 1994.
6. Baruch, M., and Singer, J., "Effect of Eccentricity of Stiffeners on the General Instability of Stiffened Cylindrical Shells Under Hydrostatic Pressure," *Journal of Mechanical Engineering Science*, Vol. 5, No. 1, 1963, pp. 23-27.
7. Batdorf, S. B., Schildcrout, M., and Stein, M., "Critical Shear Stress of Long Plates with Transverse Curvature," NACA TN 1346, June 1947.
8. Batdorf, S. B., Schildcrout, M., and Stein, M., "Critical Combinations of Shear and Longitudinal Direct Stress for Long Plates with Transverse Curvature," NACA TN 1347, June 1947.
9. Biggers, S. B., and Dickson, J. N., "POSTOP: Postbuckled Open-Stiffener Optimum Panels – User's Manual", NASA CR-172260, N84-18682, January 1984.
10. Brogan, F. A., Rankin, C. C., and Cabiness, H. D., "STAGS User Manual," Lockheed Martin Missiles and Space Co., Rept. LMSC P032594, Palo Alto, CA, June 1994.
11. Bruhn, E. F., "Analysis and Design of Flight Vehicle Structures," Jacobs and Associates, Indianapolis, IN, June 1973.
12. Bunce, F. E., "The Analysis of Curved Stiffened Sheet Subject to In-Plane Shear and Compressive Loads," SAR-78-4, November 1978.

13. Bushnell, D., "BOSOR4: Program for Stress, Buckling, and Vibration of Complex Shells of Revolution," Structural Mechanics Software Series – Vol. 1, University Press of Virginia, Charlottesville, 1977, pp. 11-131.
14. Bushnell, D., "PANDA2 – Program for Minimum Weight Design of Stiffened, Composite, Locally Buckled Panels," Computers and Structures, Vol. 25, No. 4, 1987, pp. 469-605.
15. Bushnell, D., "Theoretical Basis of the PANDA Computer Program for Preliminary Design of Stiffened Panels Under Combined In-plane Loads," Computers and Structures, Vol. 27, No. 4, 1987, pp. 541-563.
16. Bushnell, D., Jiang, H., Knight, N. F. Jr., "Additional Buckling Solutions in PANDA2," AIAA Paper 99-1233, Proceedings of the AIAA 40th Structures, Structural Dynamics, and Materials Conference, April 1999, pp. 302-345.
17. Bushnell, D., and Rankin, C., "Optimization of Perfect and Imperfect Ring and Stringer Stiffened Cylindrical Shells with PANDA2 and Evaluation of the Optimum Designs with STAGS," AIAA Paper 2002-1408, Proceedings of the AIAA 43th Structures, Structural Dynamics, and Materials Conference, April 2002, pp. 1-51.
18. Collier, C., Yarrington, P., and Pickenheim, M., "The HyperSizing Method for Structures," NAFEMS World Congress '99 on Effective Engineering Analysis, Newport, Rhode Island, April 25-28, 1999, p.853.
19. Collier, C., Yarrington, P., and Van West, B., "Composite, Grid-Stiffened panel Design for Post Buckling Using Hypersizer," AIAA Paper AIAA-2002-1222, 2002.
20. Dickson, J. N., Biggers, S. B., "POSTOP: Postbuckled Open-STiffener Optimum Panels – Theory and Capability," NASA CR 172259, January, 1984.
21. Domb, M. M., "Nonlinear Buckling Predictions of Curved Panels Under Combined Compression and Shear Loading," International Council of the Aeronautical Sciences, Toronto, Canada, September 2002.
22. Donnell, L., H., "A New Theory for the Buckling of Thin Cylinders Under Axial Compression and Bending," ASME Transactions, Vol. 56, No. 11, November 1934, pp. 795-806.
23. Gerard, G., and Becker, H., "Handbook of Structural Stability, Part 1 – Buckling of Flat Plates, NACA TN 3781, 1957.
24. Grumman Structures Manual, Internal Company Document, 1982.

25. Jaunky, N., and Knight, N. F., Jr., "An Assessment of Shell Theories for Buckling of Circular Cylindrical Laminated Composite Panels Loaded in Axial Compression," *International Journal of Solids and Structures*, Vol. 36, 1999, pp. 3799-3820.
26. Johnston, G. S., "Stringer Panel Analysis Methods," 1985.
27. Knight, N. F., Jr., Starnes, J. H., Jr., "Developments in Cylindrical Shell Stability Analysis," AIAA Paper 97-1076, Proceedings of the AIAA 38th Structures, Structural Dynamics, and Materials Conference, April 1997, pp. 1933-1947.
28. Knight, N. F., Jr., Rankin, C. C., and Brogan, F. B., "STAGS Computational Procedure for Progressive Failure Analysis of Laminated Composite Structures," *Int'd J. for Nonlinear Mechanics*, Vol. 37, No. 4-5, June/July 2002, pp. 833-849.
29. Knight, N. F., Jr., and Rankin, C. C., "STAGS Example Problem Manual", NASA CR 2006-214281, March 2006.
30. Koiter, W. T., "Het Schuifplooiveld by Grote Overshrijdingen van de Knikspanning," National Luchtvaart, Laboratorium, Report X295, November 1946.
31. Kromm, A., "The Limit of Stability of a Curved Plate Strip Under Shear and Axial Stresses", translated from German, NACA TM 898, June 1939.
32. Lamberti, L., Venkataraman, S., Haftka, R. T., and Johnson, T. F., "Preliminary Design Optimization of Stiffened Panels Using Approximate Analysis Models," *International Journal of Numerical Methods in Engineering*, Vol. 57, July 2003, pp. 1351-1380.
33. Leggett, D. M. A., "The Elastic Stability of a Long and Lightly Bent Rectangular Plate Under Uniform Shear," *Proceedings of the Royal Society of London, Ser. A*, Vol. 162, No. 908, September 1, 1937, pp. 62-83.
34. Loendorf, D. D., Sobieszczanski, J., and Stroud, J., "A Computer-Aided Design Study of All-Metal and Composite Stiffened Metal Fuselage Structures," AIAA Paper 73-373, Proceedings of the AIAA 14th Structures, Structural Dynamics, and Materials Conference, March 1973.
35. Melcon, M. A., and Ensrud, A. F., "Analysis of Stiffened Curved Panels Under Shear and Compression," *Journal of the Aeronautical Sciences*, February 1953, pp. 111-126.
36. Minnetyan, L., Rivers, J. M., Murthy, P. L. N., and Chamis, C.C., "Structural Durability of Stiffened Composite Shells," AIAA Paper 92-2244, Proceedings of the AIAA 33rd Structures, Structural Dynamics, and Materials Conference, April 1992, pp. 2879-2886.

37. Piurkowski, B., "PAGE (Panel Analysis – Gulfstream Example) Computer Programs for Analysis of Hat-Stiffened Panels," GAC-SM-21, Dec. 1992.
38. Ramberg, Walter, and Osgood, William, "Description of Stress-Strain Curves by Three Parameters", NASA-TN 902, July 1943.
39. Rice, R. C., Jackson, J. L, Bakuckas, J., Thompson, S., "Metallic Materials Properties Development and Standardization", DOT/FAA/AR-MMPDS-01, January 2003.
40. Rose, C. A., Moore, D. F., Knight, N. F., Jr., Rankin, C. C., "Finite Element Modeling of the Buckling Response of Sandwich Panels," AIAA Paper 2002-1517, Proceedings of the AIAA 43rd Structures, Structural Dynamics, and Materials Conference, April 2002.
41. Schildcrout, M. and Stein, M., "Critical Combinations of Shear and Direct Axial Stress for Curved Rectangular Panels," NACA TN 1928, August 1949.
42. Shafer, B.W., "Thin-walled Column Design Considering Local, Distortional, and Euler Buckling," Annual Technical Session and Meeting, Structural Stability Research Council, Ft. Lauderdale, FL., 2001.
43. Simmons, F., "Gulfstream V JAA Fuselage Panel Test Results Report", Gulfstream Report No. GV-GER-1432, December 2000.
44. Starnes, J. H., Jr., Hilburger, M., Nemeth, M. P., "The Effects of Initial Imperfections on the Buckling of Composite Cylindrical Shells," Composite Structures: Theory and Practice, ASTM STP 1383, 2000, pp. 529-550.
45. Stroud, J., Agranoff, N., Anderson, M. S., "Minimum-Mass design of Filamentary Composite Panels Under Combined Loads: Design Procedure Based on a Rigorous Buckling Analysis," NASA TN D-8417, July 1977.
46. Stroud, W., and Anderson, Melvin S., "PASCO: Structural Analysis and Sizing Code – Capability and Analytical Foundations," NASA TM 80181, January 1980.
47. Vanderplaats, G. N., "CONMIN, a FORTRAN program for constrained function minimization: user's manual", NASA TM X-62282, August 1973.
48. Viswanathan, A. V., Tamekuni, M., and Baker, L. L., "Elastic Stability of Laminated, Flat and Curved Long Rectangular Plates Subjected to Combined Inplane Loads," NASA CR-2330, June 1974.
49. von Karman, T. and Tsien, H.-S., "The Buckling of Thin Cylindrical Shells Under Axial Compression," Journal of the Aeronautical Sciences, Vol. 8, No. 8, June 1941, pp. 303-312.

50. Weller, T., and Singer, J., "Experimental Studies on Buckling of 7075-T6 Aluminum Alloy Integrally Stringer-Stiffened Shells," Air Force Office of Scientific Research, October 1971.
51. Whitney, J. M., "Buckling of Anisotropic Laminated Cylindrical Plates," AIAA Journal, Vol. 22, No. 11, November 1984, pp. 1641-1645.
52. Williams, F. W. and Anderson, M. S., "Incorporation of Lagrange Multipliers into an Algorithm for Finding Exact Natural Frequencies or Critical Buckling Loads," International Journal of Mechanical Sciences, Vol. 25, No. 8, 1993, pp. 579-584.
53. Williams, F. W. and Anderson, M. S., "User's Guide to VIPASA (Vibration and Instability of Plate Assemblies Including Shear and Anisotropy)", Department of Civil Eng., Univ. of Birmingham, 1973.
54. Wittrick, W. H., and Williams, F. W., "Buckling and Vibration of Anisotropic or Isotropic Plate Assemblies Under Combined Loadings," Int. J. Mech. Sci., Vol. 16, 1974, pp. 209-239.
55. Yang, T. Y., and Kunoo, K., "Buckling of Cylindrical Shells with Smeared-Out and Discrete Orthogonal Stiffeners," AIAA Journal, Vol. 15, No. 12, December 1977, pp. 1704-1711.
56. Yoo, S. Y., "On Maximum Strength of Plates Under Axial Compression – Effects of Curvature and Edge-Stiffener Extensional and Torsional Rigidity," Ph.D. Dissertation, Stanford University, Stanford, CA, 1977.
57. Young, W. C., "Roark's Formulas for Stress and Strain", McGraw Hill, Sixth edition, 1989.
58. Zhang, Y. and Matthews, F. L., "Initial Buckling of Curved Panels of Generally Layered Composite Materials," Composite Structures, Vol. 1, June 1983, pp. 3-30.
59. Zhang, Y. and Matthews, F. L., "Postbuckling Behavior of Anisotropic Laminated Plates Under Pure Shear and Shear Combined with Compressive Loading," AIAA Journal, Vol. 22, No. 2, February 1984, pp. 281-286.

APPENDIX A

REVIEW OF SELECTED STIFFENED FUSELAGE PANEL

ANALYSIS TOOLS

A.1 PASCO (Panel Analysis and Sizing COde)

PASCO (Anderson et al., 1981; Stroud and Anderson, 1980) is a structural sizing code that couples the optimization code CONMIN (Vanderplaats, 1973) with the plate analysis code VIPASA (Williams and Anderson, 1973; Wittrick and Williams, 1974). VIPASA calculates the buckling load of prismatic stiffened panels modeled as a series of linked plates assuming linear elastic material behavior. PASCO assumes a trigonometric series solution along the panel length and discretizes along the panel width.

A.1.1 Geometric Limitations

PASCO is designed to analyze uniaxially stiffened flat panel segments (i.e., prismatic structures). The stiffeners are in the longitudinal direction only. The panel cross section is composed of an arbitrary assemblage of thin, flat, rectangular plate elements that are connected together along their longitudinal edges. The panel can include a bow-type imperfection. Curved panels can be modeled using a series of flat plate elements (i.e., facet approximation). Boundary conditions (free, simple support, clamped, and symmetry) can only be prescribed along the longitudinal edges of panel. The other edges are assumed to be simple support.

A.1.2 Material Limitations

PASCO includes capabilities for metallic and composite material properties. Each panel section must be composed of a balanced symmetric laminate of any number of layers of orthotropic material. Only linear elastic material properties are included. Elasto-plastic material response is not included.

A.1.3 Loading Capability

PASCO loading conditions include inplane loads (N_x , N_y , N_{xy}), normal pressure, temperature, and bending moment about the transverse axis (M_x). Full N_y loading is carried by the skin alone (none is carried by the stiffeners). The stress distribution is assumed to be uniform along the panel length.

A.1.4 Failure Modes

PASCO is designed to be a sizing tool for buckling-critical uniaxially stiffened panels. PASCO does not predict failure, but it does allow the user to pick design requirements to be applied to the panel including initial buckling, material strength, stiffness, and vibration frequency. The user is responsible for evaluating the PASCO results to determine if the panel has buckled or has exceeded its material strength.

A.1.5 Theoretical Approach

The buckling displacement for each plate element is assumed to be:

$$w(x,y) = f_1(y) \cos \frac{\pi x}{\lambda} - f_2(y) \sin \frac{\pi x}{\lambda}$$

where λ is the longitudinal buckle half wavelength, x is the longitudinal coordinate direction, y is the transverse coordinate direction, and $w(x,y)$ is the out-of-plane deflection. The basic formulation is described by Wittrick and Williams (1974). Similar expressions are assumed for the inplane displacements, $u(x,y)$ and $v(x,y)$. These assumed displacements provide an exact solution to the governing equations based on the Kirchhoff-Love hypothesis applied to each plate element. The functions $f_1(y)$ and $f_2(y)$ are selected to impose the desired boundary conditions on the lateral edges of the panel.

An eigenvalue analysis is performed for several values of λ to determine the lowest buckling load and associated mode shape for each λ .

For anisotropic laminates and shear loading conditions, the buckling mode shape node lines are skewed. For these cases, the predicted buckling load from PASC0 can be quite conservative as the buckling wavelength approaches the length of the panel. An alternate analysis is available for analyzing these conditions. This alternate analysis uses a smeared stiffener approach, and the panel is rotated 90-degrees so that the boundary conditions can be modeled accurately on the edges normal to the stiffeners.

A.1.6 Computational Efficiency

Geometric and material limitations are imposed, and several simplifying assumptions are made in order to minimize the VIPASA plate analysis run time. These limitations maximize the computational efficiency of the PASC0 structural sizing code thereby providing a very efficient rapid design tool for preliminary design of stiffened panels.

A.1.7 Code Availability

The PASC0 program was developed in 1981 and adapted to the Macintosh computer in 1991. The Macintosh version of PASC0, MacPASC0, was released in 1992.

MacPASC0 includes an interactive, graphic preprocessor that simplifies the specification of panel geometry and reduces user input errors, thus making the modeling and analysis of panel designs more efficient. MacPASC0 is available for purchase through the Open Channel Foundation[†].

[†]www.openchannelfoundation.org

A.2 POSTOP (Postbuckled Open-STiffener Optimum Panels)

POSTOP (Biggers and Dickson, 1984; Dickson and Biggers, 1984) is another stiffened panel sizing code for open-section stiffeners and elastic material properties. In addition to initial buckling load calculations, stiffened panel failure modes in the postbuckled response regime are included.

A.2.1 Geometric Limitations

The stiffener shapes included in POSTOP are open-section stiffeners that can be created from a basic I-shaped cross-section such as blade-, T-, J-, I-, and Z-shaped stiffeners.

The panel geometry is assumed to be repetitive over several bays in the longitudinal and transverse directions. The ends of the panel are assumed to be simply supported. The panels are assumed to be flat, but an initial bow eccentricity can be included.

A.2.2 Material Limitations

POSTOP includes capabilities for metallic and composite material properties. It is assumed that all plate elements have a sufficient number of plies so that bending-twisting coupling stiffness effects of the plate elements can be neglected, and the plates may be treated as specially orthotropic. Only linear elastic material properties are included.

Elasto-plastic material response is not included

A.2.3 Loading Capability

POSTOP loading conditions include inplane loads (N_x , N_y , N_{xy}), normal pressure, and temperature. Full N_y loading is carried by the skin alone (none is carried by the stiffeners). Load eccentricity is included.

A.2.4 Failure Modes

The failure modes considered are skin buckling, Euler-column buckling of the stiffener, maximum stiffener strain, maximum strain of composite fibers, stiffener local buckling, stiffener rolling, and stiffener torsional/flexural buckling. Skin-stiffener separation is an additional analysis step in the postbuckled configuration (Dickson and Biggers, 1984).

A.2.5 Theoretical Approach

The prebuckling analysis assumes the skin to be unbuckled, and the longitudinal strain and curvature of the panel are calculated accordingly. If the applied loads cause buckling of the skin, a postbuckled plate analysis based on the Koiter (1946) approach is performed, and an iterative procedure is used to calculate the correct strain and curvature of the panel. The stiffener rotational restraint of the skin is re-evaluated during the iterative procedure to account for load redistribution between the skin and stiffener. At each level, the following checks are made on the skin and stiffeners:

- 1) Euler-column buckling load of stiffener is calculated and compared to applied loading.
- 2) Tension and compression strain limitations specified by the user are applied at the ply level to skin membrane strains only. However, membrane strains

caused by eccentricities, pressure, and skin buckling are accounted for in addition to the mechanical inplane loads. Thermal strains and local bending strains due to pressure loading and postbuckling are not included.

- 3) Maximum stiffener strength based on either maximum strain criterion or the Tsai-Hill criterion is applied to the critical element of the stiffener, where the critical element is the free flange of T-, J-, I-, and Z-shaped stiffeners or the free edge of a blade stiffener. Local bending and twisting strains in the stiffener elements due to postbuckling deformations of the skin are neglected.
- 4) Stiffener local buckling analyses are performed for half wavelengths from $\lambda=L$ to $\lambda=L/N_{\max}$, where L is panel length, and N_{\max} is the maximum number of half-wavelengths specified by the user. Skin rotational stiffness and stiffener web/skin junction rotational stiffness are calculated using closed-form equations. The critical local buckling load is assumed to occur when the stiffener web/skin junction rotational stiffness equals the skin rotational stiffness.
- 5) Rolling of stiffeners, using an assumed displacement field for the stiffener deformation in the rolling mode, is predicted by minimizing the total potential energy to determine the critical load factor for wavelengths ranging from the panel length to the stiffener spacing.
- 6) The torsional/flexural buckling mode of stiffeners is assumed to be periodic along the width direction with one period including one or more stringers. Displacement in x-direction (u) is a cosine function and displacements in y-direction (v) and normal direction (w) are sine functions. Stability equations

are obtained by considering the equilibrium of forces and moments acting on a small element of the stiffener. An eigenvalue problem is formulated with the lowest eigenvalue corresponding to the stiffener buckling load.

- 7) Skin/Stiffener Interface Loads – To promote computational efficiency, the goal is to prevent this mode of failure from being critical as opposed to predicting the separation load. Interface stress analysis provides a closed-form solution assuming linear elastic material behavior and small deflections. Margins of safety are obtained with the Tsai-Hill criterion for a three-dimensional stress state.

A.2.6 Computational Efficiency

POSTOP is a good preliminary design tool with postbuckling capability that has good computational efficiency. It provides estimates of postbuckled strength and evaluates several stiffener failure modes during the computations. However, like PASCO, several simplifying assumptions associated with geometry and boundary conditions limit its general use.

A.2.7 Code Availability

POSTOP was originally developed by Lockheed-Georgia under contract to NASA Langley Research Center in the 1980s, and it is no longer available.

A.3 PAGE (Panel Analysis – Gulfstream Example)

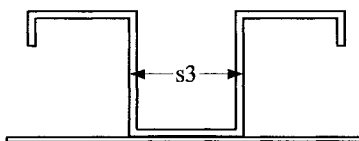
PAGE (Piurkowski, 1992) is an analysis and sizing code designed specifically to analyze curved hat-section stiffened panels for aerospace applications. PAGE includes postbuckling behavior, but only for elastic material properties. Failure modes in PAGE are related to various buckling modes and to stiffener strength. The failure modes are determined using industry-accepted, closed-form equations (Batdorf et al., 1947a & b; Gerard and Becker, 1957; Grumman, 1982) and are described briefly in Section A.3.4. Special limitations are applied to the stiffeners so that the analysis produces conservative predictions.

A.3.1 Geometric Limitations

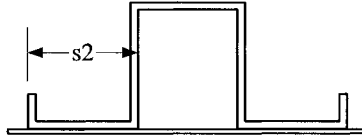
The PAGE analysis applies to curved fuselage panels with hat-stringers. Several constraints are imposed on the stiffened panel geometry to insure a conservative prediction of the failure modes considered and their range of applicability. The frame spacing must be greater than the stringer spacing. The frames can have any cross-section, but the stringers must be open or closed hat sections that obey the following rules:

$$\frac{t_{\text{stringer}}}{t_{\text{skin}} + t_{\text{doubler}}} \geq 0.5$$

For an open hat stringer: $10 \leq s_3/t_{\text{stringer}} \leq 22$ where s_3 =width of hat section attached to skin



For a closed hat stringer: $10 \leq s_2/t_{\text{stringer}} \leq 22$ where s_2 = width of one flange attached to skin



The minimum moment of inertia of a stringer stiffener required for the stringer to act as an effective simple support bounding the two skin bays is determined by:

$$I_{\text{stringer}} \geq \frac{(t_{\text{skin}} + t_{\text{doubler}})^3 b (E_c)_{\text{web}}}{12(1 - \mu^2)(E_c)_{\text{stringer}}} [30(L/b)^2 - 10(1 + L/b)]$$

where:

b = stringer spacing

L = frame spacing

μ = average Poisson's ratio of skin and doubler $(\frac{\mu_{\text{skin}} + \mu_{\text{doubler}}}{2})$

$(E_c)_{\text{st}}$ = compressive Young's modulus of stringer

$(E_c)_{\text{web}}$ = effective compressive Young's modulus of skin and

doubler defined as: $\frac{t_{\text{skin}} (E_c)_{\text{skin}} + t_{\text{doubler}} (E_c)_{\text{doubler}}}{t_{\text{skin}} + t_{\text{doubler}}}$

Mechanically fastened stringers are subject to the following constraints:

$$(\text{rivet pitch})/(\text{stringer spacing}) < 0.5$$

$$(\text{rivet pitch})/(\text{rivet diameter}) \leq 8.0$$

A.3.2 Material Limitations

PAGE only considers isotropic material properties. No capability for orthotropic materials or laminated composite structures is currently provided. Inelastic material behavior is included only in failure analyses of the stringer stiffeners; however, all skin and frame failure analyses assume linear elastic material behavior.

A.3.3 Loading Capability

The available loading conditions for PAGE are: compression applied parallel to the direction of the stringers, inplane shear, and combined compression and inplane shear.

A.3.4 Failure Modes

Failure modes are included for the stiffeners and the skin. The skin failure modes are: skin crippling, skin wrinkling (short-wavelength buckles), and web ultimate compression strength. The stiffener failure modes are stringer local elastic and plastic buckling, stringer crippling, Euler-column buckling of stringer, forced crippling of stringer, and forced crippling of frame.

A.3.5 Theoretical Approach

The failure load calculations for panels loaded in compression are different from those calculations for panels loaded in combined compression and inplane shear. The failure models for compression loading only are as follows:

- 1) Stiffener Local Elastic and Plastic Buckling (with no lips on flanges): Closed-form equations (Purkowsky, 1992) are used to calculate the elastic

compressive buckling stress of each individual flat plate element of the stiffener. Edges of a plate element in a corner are modeled first as simply supported and then as clamped. Any edges not in a corner are treated as free. The buckling stress of the cross-section is determined by summing the minimum buckling load of each section and dividing by the total cross-sectional area of the stiffener. The minimum buckling stress of a plate element is either its simply supported buckling stress or the lowest clamped buckling stress of all the plate elements, whichever is smaller. As the local elastic buckling stress, $F_{cr \text{ elastic}}$, approaches the proportional limit of the material, the reduced bending stiffness of the material causes the section to buckle at a stress, F_{cr} , below the theoretical local elastic buckling stress such that:

$$F_{cr} = \eta F_{cr \text{ elastic}}$$

The reduction factor, η , is computed using the approach given by Gerard and Becker (1957) as follows:

$$\eta = \left[\frac{E_s}{E_c} \right] \left[\frac{1 - \nu_e^2}{1 - \nu^2} \right] \left\{ 0.50 + 0.25 \left[1 + \frac{3E_T}{E_s} \right]^{\frac{1}{2}} \right\}$$

where:

ν = inelastic Poisson's ratio, $\nu_p - (\nu_p - \nu_e)E_s/E$

ν_e = elastic Poisson's ratio

ν_p = plastic Poisson's ratio

E = Young's modulus

E_C = Compressive Young's modulus

E_S = Secant modulus, σ/ε

E_T = Tangent modulus, $d\sigma/d\varepsilon$

σ = normal stress

ε = normal strain

- 2) Stiffener Local Elastic and Plastic Buckling (with lips on flanges): The lips provide stability to the free edges of the stiffener. The same procedure for the stiffener cross-section without lips, just described, is used for the analysis of this failure mode except that the buckling stress is increased using a factor derived from the lip geometry.
- 3) Skin Crippling: The curves and closed-form equations presented by Batdorf, Schildcrout, and Stein (1947b) for long plates with transverse curvature in axial compression are used to calculate the initial elastic buckling stress for the skin. The initial elastic buckling stress of the sheet, F_{crel} , is calculated by:

$$F_{crel} = K_c E_c \left(\frac{t}{b} \right)^2$$

where:

K_c = elastic buckling coefficient (Batdorf et al., 1947b)

E_c = Compressive Young's modulus

t = skin thickness

b = stiffener spacing

If F_{crel} is greater than or equal to 80 % of the reference stress, $F_{0.7}$, the allowable crippling stress, F_{cc} , is equal to F_{crel} . However, if F_{crel} is less than 80% of the reference stress, then the crippling stress is defined by the following equation:

$$F_{\text{cc}} = 0.89 \sqrt{F_{\text{crel}} F_{0.7}}$$

The reference stress, $F_{0.7}$, is defined by:

$$F_{0.7} = F_{\text{cy}} \left(214.3 \frac{F_{\text{cy}}}{E_C} \right)^{1/(n-1)}$$

where

F_{cy} = compressive yield stress of the material

n = Ramberg-Osgood shape factor (Ramberg and Osgood, 1943)

- 4) Stiffener Crippling: Derived using the local plastic and elastic buckling stresses obtained in failure models 1 and 2 and the graph from the Grumman Structures Manual (1982) shown in Figure A1.

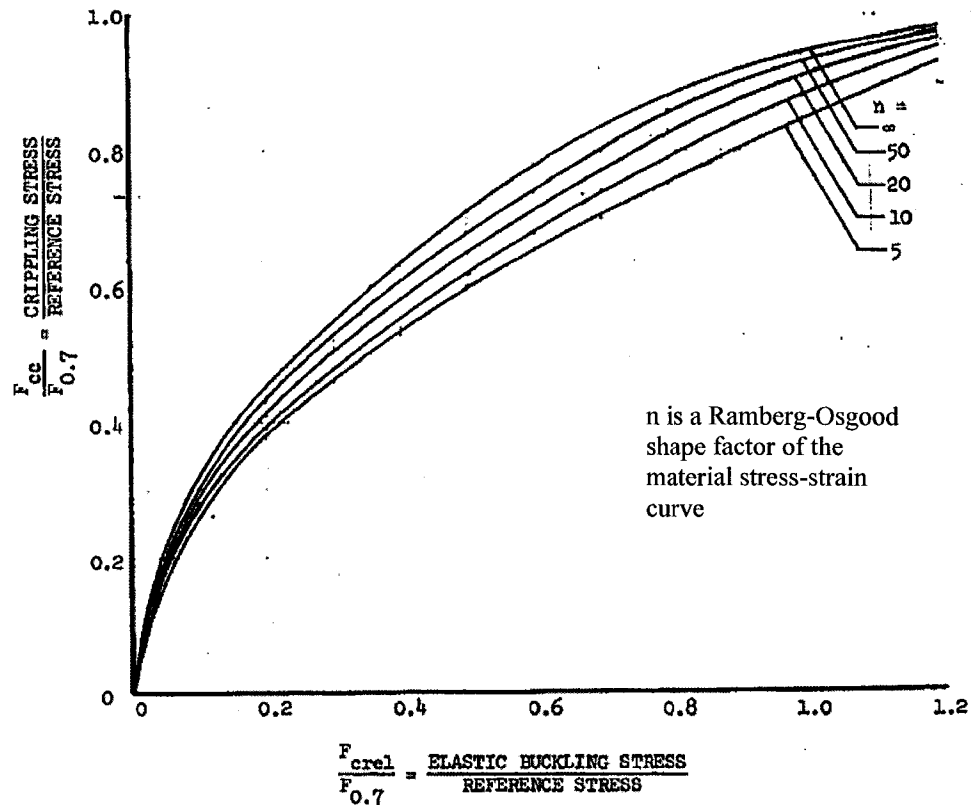


Fig. A1: Nondimensional curves for stiffener crippling (Grumman, 1982)

- 5) Euler-column Buckling of the Stiffener: A modified Euler-column buckling analysis is performed taking into account that the effect of exceeding the proportional limit of the material. The modified Euler-column buckling equation is as follows:

$$F_{Euler} = \frac{\pi^2 (E_{tan})_{st} (I_{eff})_{st}}{L^2 (A_{eff})_{st}}$$

where A_{eff} and I_{eff} are the area and moment of inertia of the effective section which includes the stiffener and the effective portion of the skin and doubler, L is the frame spacing, and E_{tan} is defined as follows:

$$E_{\tan} = \frac{E_c}{1 + \frac{3n}{7} \left(\frac{F}{F_{0.7}} \right)^{n-1}}$$

where F is the applied stress, and $F_{0.7}$ is the reference stress given by the equation:

$$F_{0.7} = F_{cy} \left(214.3 \frac{F_{cy}}{E_c} \right)^{\frac{1}{n-1}}$$

where E_c is the compressive Young's modulus, F_{cy} is the compressive yield stress, and n is the Ramberg-Osgood shape factor (Ramberg and Osgood, 1943) for the material.

- 6) **Skin Wrinkling:** This failure mode is where buckles in the skin run across the stiffeners and distort the attached flanges of the stiffeners. At failure, the buckles become quasi-cylindrical in shape and the distortion of the attached flange is sufficient to cause crippling of the stiffener. The skin-wrinkling stress is derived from a stability analysis of the skin, but the failing member is the attached flange of the stiffener. The allowable skin wrinkling stress is based on the skin acting as a column on an elastic foundation where the stiffener acts as the elastic foundation. The spring rate of the stiffener (i.e., the elastic foundation) is estimated, based on the stiffener geometry and orientation, and a closed-form equation is used to determine the wrinkling stress. An iterative procedure is used to determine the stiffener stress corresponding to the critical wrinkling stress of the skin.

- 7) **Forced Crippling of the Stiffener:** In the wrinkling mode, the lateral loads that force the attached stiffener flange to conform to the buckle shape will impose a lateral deflection on the flange. This deflection will cause a transverse bending stress in the flange. If this bending stress combined with the stiffener axial stress exceeds the compressive yield stress for the stiffener material, forced crippling of the stiffener is said to occur.

For combined compression and inplane shear, the total load on the stiffener consists of the applied compression load plus the load induced by the diagonal tension from the shear loading. The failure models for combined compression and inplane shear loads are as follows:

- 1) **Web Compression:** The web equivalent uniaxial (octahedral) stress calculated at three critical points in the structure and checked against the material allowable yield and ultimate stresses.
- 2) **Euler-column Buckling of the Stiffener:** The procedure is the same as for the compression-loading-only case. The only difference is that the effective area and moment of inertia are different because the frames are included. An effective frame spacing is used instead of the actual value.
- 3) **Stiffener Local Elastic and Plastic Buckling (with or without lips on flanges):** Allowables are the same as calculated for compression-only-loading. The load calculation also includes the additional stiffener bending moment induced by diagonal tension.

- 4) Stiffener Crippling: Allowables are the same as calculated for compression-only-loading. The load calculation also includes the additional stiffener bending moment induced by diagonal tension.
- 5) Skin Wrinkling: This is a modified version of the procedure used for compression only loading. The modification deals with the calculation of the stiffener effective width.
- 6) Forced Crippling of the Stiffener: This is a modified version of the procedure used for compression only loading. The modification deals with the calculation of the running load along the attached flange of the stiffener.
- 7) Forced Crippling of the Frame: The clip attaching the frame to the skin and doubler is subject to a running inplane load along an effective width. This running load, which arises from the buckled deformation of the underlying skin and doubler, will cause a transverse bending stress to exist in the attached flange of the clip. A compressive stress also exists in the clip due to the diagonal tension effects. The resultant stress due to this combined bending and compression in the attached clip flange cannot exceed the compressive yield stress for the clip material.

A.3.6 Computational Efficiency

PAGE is a preliminary design tool created for specific geometry and loading conditions, resulting in high computational efficiency. It is specialized to one main configuration (hat stringers) and accounts for known failure modes in a conservative manner.

A.3.7 Code Availability

The input to PAGE is in the form of a simple easy-to-use spreadsheet. PAGE is a proprietary analysis code of Gulfstream Aerospace Corporation.

A.4 PANDA2

PANDA2 (Bushnell, 1987a & b) is a panel analysis and sizing code for elastic-plastic isotropic materials, elastic composite materials, and sandwich structures. PANDA2 includes initial buckling load calculations, as well as postbuckling failure load calculations. PANDA2 has also demonstrated an analysis link to STAGS for detailed finite element analysis of the final optimized design (Bushnell and Rankin, 2002).

A.4.1 Geometric Limitations

PANDA2 is used for the analysis of flat or cylindrical panels with ring and stringer stiffeners. The stiffener shape can be a blade-, T-, J-, I-, and Z-shaped, closed-hat, or corrugated shape. PANDA2 can be used to analyze a complete cylinder, but is best suited for panel sections. PANDA2 accounts for imperfections. The boundary conditions can be specified as simply supported along straight edges and as simply supported or clamped along curved edges. The clamped boundary condition is simulated by using a shorter panel of length equal to $L/\sqrt{3.85}$ with simply supported edges.

A.4.2 Material Limitations

PANDA2 includes capabilities for isotropic and composite materials. Plasticity is allowed for isotropic materials or materials with stiffness in one coordinate direction only (i.e., a smeared stiffener segment). It also includes capabilities for sandwich panels.

A.4.3 Loading Capability

The loading includes inplane loads (N_x , N_y , N_{xy} where the axial load can vary linearly across panel width), normal pressure, edge moments, temperature, and combined loads.

A.4.4 Failure Modes

PANDA2 predicts more than twenty failure modes. These failure modes include:

- general buckling (both stringers and rings participate)
- inter-ring buckling (buckling between adjacent ring stiffeners in which stringers participate, but the lines of intersection of ring web roots with the panel skin do not translate)
- local skin buckling (buckling between adjacent stringers and rings)
- crippling
- rolling of stiffeners
- maximum tensile or compressive stress along fibers
- maximum tensile or compressive stress normal to the fibers in each lamina
- maximum inplane shear stress in each lamina.

A.4.5 Theoretical Approach

PANDA2 utilizes different analytical approaches for calculating failure loads depending on panel geometry and loading conditions. The various failure models are as follows:

- 1) Closed-form equations are used for general, local and panel buckling, crippling of stiffener parts, and rolling of stiffeners with and without participation of panel skin. Failure modes for sandwich panels are also evaluated (face sheet wrinkling, buckling over the diameter of a single cell of a honeycomb core, and core crimping). Buckling loads are calculated using simple assumed displacement equations appropriate for each different type of buckling (Bushnell, 1987b). Buckling formulas are derived from minimum potential energy theory and Donnell's equations with '*a posteriori*' application of a reduction factor for panels in which the axial half-wavelength of the buckling pattern is longer than the panel radius of curvature.
- 2) Discretized single skin-stringer model (Bushnell, 1987a, Fig. 1) used for local buckling, local postbuckling, and wide column buckling of the panel region between rings. The model includes the cross-section of a stiffener plus the skin width equal to the spacing between stiffeners. Symmetry conditions are applied at the left and right edges of the skin. The deflection in the axial direction is assumed to be harmonic [$\sin(nx)$ or $\cos(nx)$]. The discretized model is analyzed with a finite difference energy method. This model includes local postbuckling growth and modification of the local skin buckling mode as predicted by a modified form of a theory formulated by

Koiter (1946). This method works well when there are at least three or four equally spaced stringers in the panel.

- 3) Discretized model of entire width of panel with the stiffeners treated as smeared. This model is used when the axial load varies across the width of the panel and when there is applied normal pressure.
- 4) Local buckling between adjacent stringers and rings of a cylindrical or flat panel obtained from a Ritz model in which the buckling modal displacement components, u , v , w , are expanded in double trigonometric series. The local region is assumed to be simply supported on all four edges (Bushnell, 1987a).
- 5) General buckling of a cylindrical panel in which stringers and rings are treated as discrete beams with undeformable cross sections. Again, the general buckling modal displacement components, u , v , w , are expanded in double trigonometric series. The edges of the domain (a 3-bay by 3-bay subdomain of the entire panel) are assumed to be simply supported and to have discrete stiffeners of half the user-specified modulus. (Bushnell, 1987a)
- 6) A discretized single module model for a cylindrical panel in which the ring segment and panel skin (with smeared stringers) is modeled. The rings can be blades, Ts, Js, or Zs. Solution methods are those used in BOSOR4 (Bushnell, 1977) and include a finite difference method, Fourier superposition in the circumferential variable, Newton method of solution of nonlinear axisymmetric problem, inverse power iteration with spectral shifts for eigenvalue extraction, Lagrange multipliers for constraint conditions, and thin shell theory (Bushnell, 1987a, Bushnell et al., 1999).

A.4.6 Computational Efficiency

PANDA2 is a preliminary design tool with high computational efficiency. It performs multiple levels of analysis including closed-form solutions and BOSOR4 solutions. In addition, PANDA2 can create an input file for the STAGS finite element analysis code.

A.4.7 Code Availability

PANDA2 runs on UNIX computer systems. The user inputs the analysis parameters via an interactive question-and-answer format. PANDA2 is available from Dr. David Bushnell for a donation to Stanford University.

A.5 STAGS (STructural Analysis of General Shells)

STAGS (Brogan et al., 1994; Knight and Rankin, 2006) is a finite element program for the analysis of general shell-type structures. STAGS includes elasto-plastic material properties as well as progressive failure analysis for laminated composite structures. Postbuckling shell analyses are its forte. Other finite element codes such as NASTRAN, ABAQUS, and ANSYS have similar capabilities. However, STAGS was developed primarily for thin-shell structures and the types of analysis problems they pose.

A.5.1 Geometric Limitations

Shells are modeled using faceted approximations through the assembly of flat shell elements with or without stiffeners. Stiffeners may be modeled using either beam or shell elements. A smeared stiffener option is also provided. The availability of numerous wall fabrication and stiffener-cross-section options, combined with a variety of

material models, permits great flexibility in modeling a wide spectrum of construction types. STAGS also includes fastener elements as well as a contact capability between adjacent surfaces. Geometric imperfections are readily included in the finite element model, and other generalized imperfections can also be incorporated through user-written subroutines. While STAGS is primarily a shell analysis code, three-dimensional solid elements and sandwich elements are available for high-fidelity local analyses.

A.5.2 Material Limitations

STAGS has fully anisotropic, nonlinear material properties. Isotropic and orthotropic materials are permitted. Two plasticity models, including isotropic strain-hardening model and the White-Besseling theory, are available. Easily-defined standard wall types include corrugation-stiffened and laminated composite, including up to 100 layers of lamina with arbitrary orientations. Additional generality is provided by the option for direct input of stiffnesses relating force and moment stress resultants to surface strains and changes in curvatures. Stiffener cross sections may be built-up from subelements described either by explicit geometry or by geometric properties. Smearred stiffeners are also an option. In addition, STAGS has progressive failure analysis capability for laminated composite materials (Knight et al., 2002).

A.5.3 Loading Capability

Mechanical loads include point forces, line loads, surface traction, and "live" pressure, which remains normal to the surface throughout large deformations. Thermal loading is defined by accommodating arbitrary definition of temperature throughout the structure.

Standard boundary condition types, such as simple support, (anti)symmetry, and clamped, may be defined automatically along edges. In addition, various constraint relations, including multi-point constraints, single-point constraints, and Lagrange constraints, are available. Multi-point constraints may be linear or nonlinear, while Lagrange constraints are defined by linear constraint equations.

A.5.4 Failure Modes

STAGS predicts initial buckling loads, postbuckling response, and collapse loads. Material yielding and fastener failure are also included. Progressive failure analyses can be performed to determine damage initiation sites and monitor damage propagation for laminated composite structures. Crack-growth models for isotropic materials based on the crack-tip-opening-angle (CTOA) criterion and the use of load relaxation to re-establish equilibrium as the crack grows are provided.

A.5.5 Theoretical Approach

STAGS is a finite element code designed specifically for the analysis of shell structures, but it has evolved over the years to include solid elements as well as sandwich elements (Knight and Rankin, 2005). STAGS forte is the analysis of complex, nonlinear systems that depend upon post-buckling strength and require analysis well into the post-buckled regime. Solution control is quite sophisticated ranging from simple load/displacement control to the advanced Riks arc-length parameter technique that enables traversal of limit points into the post-buckling regime. Equivalence transformation methods are available to obtain solutions during mode jumping behavior that may occur in bifurcation

and post-buckling response. The hybrid transient static solution approach is also available. Load-relaxation procedure is available to re-establish equilibrium in a rigorous manner when changing solution approaches or when geometric changes occur (e.g., crack growth).

The shell element library includes a 3-node triangle, 4-node and 9-node quadrilaterals, and transition quadrilateral elements for mesh refinement. A 2-node Timoshenko beam is available for modeling shell stiffeners. Smearred stiffeners are also included. The solid element library includes 8-node, 18-node, 20-node, and 27-node brick elements. A nonlinear spring, called a "mount element", permits definition of general force-displacement relations. Rigid links may be used to connect the spring, thereby providing rotational as well as translational stiffness. Special elements include a hyperelastic fastener and a moving-plane boundary, which remains planar throughout arbitrarily large deformations. An 8-node sandwich element is also available in STAGS (Ref. 36). The sandwich element consists of two face sheets modeled with shell elements and separated by a lightweight core.

A.5.6 Computational Efficiency

STAGS is very efficient; however, the computational cost depends on the finite element model size and complexity of the structural response. Linear eigenvalue analyses for initial buckling calculations are generally very fast. Nonlinear analyses that progress into the postbuckling range can be very computationally expensive and require several restarts to predict the complete response curve.

A.5.7 Code Availability

STAGS has been developed over several decades by researchers at Lockheed Palo Alto Research Laboratory under government sponsorship. NASA Langley Research Center has been the primary sponsor. Requests for STAGS can be directed to the Structural Mechanics and Concepts Branch, NASA Langley Research Center.

A.6 Hypersizer

Hypersizer (Collier et al., 1999 and 2002) is an analysis and sizing code designed for efficient optimization of stiffened panels. Hypersizer is not a finite element code, but it can import finite element loads from several commercial finite element codes to be used in its analyses. Hypersizer predicts the onset of local buckling as well as the final postbuckling load and includes nonlinear material properties.

A.6.1 Geometric Limitations

Hypersizer supports unstiffened, stiffened, and sandwich panels. The stiffener shapes can be blade, hat, tee, angle, I, J, C, and Z. The stiffener layout can be isogrid, orthogrid, Xgrid, Ygrid, and bigrid rib stiffened panels.

A.6.2 Material Limitations

Hypersizer can be used to analyze metals, fiber-reinforced composite materials, and sandwich construction. Elasto-plastic nonlinear material effects are included for metallic materials.

A.6.3 Loading Capability

Loading capabilities include out-of-plane pressure, through-the-thickness temperature gradients, applied edge loads, applied edge moments and shears, enforced displacements, and combined loading.

A.6.4 Failure Modes

Hypersizer applies several different failure criteria including Tsai-Hill, Tsai-Wu, Tsai-Hahn, Hoffman, maximum strain, maximum stress, bond line maximum stress and strain, cylindrical panel buckling, cross-section crippling, Johnson-Euler interaction, local buckling, and bolt bearing. For sandwich construction, face sheet wrinkling and dimpling, and core shear and crushing failure modes are predicted.

A.6.5 Theoretical Approach

The Hypersizer analytical approach consists of four key characteristics:

- 1) A panel and beam formulation consistent with, and coupled to finite element analysis
- 2) Extensive list of physics-based strength and stiffness failure analyses
- 3) 'Design-to' loads using statistical analyses
- 4) Global to local zooming analyses

Closed-form solutions and analytical methods are coupled with finite element analyses (FEA). The Ritz energy method is used for buckling calculations. The effective-width approach is used to predict local postbuckling behavior of a span, where a span can be a stiffener flange, a stiffener web, or a skin bay. Hypersizer uses an approach where the

effective width varies with stress level – the higher the stress level, the smaller the effective width. At a specified load level (combined N_x , N_y , and N_{xy}), using an orthotropic mode shape minimization, Hypersizer calculates the exact width that would cause the span to initiate bifurcation buckling. This width is used as the effective width for calculating new stiffness matrices.

Hypersizer will automatically import internal loads from a STAGS finite element analysis, perform analysis and optimization, and then update the finite element model stiffness properties to reflect the iterated design.

A.6.6 Computational Efficiency

Hypersizer is very efficient computationally due to its ability to calculate failure modes based on finite-element-generated results or user-defined loads. Failure load calculations from user-defined loads and boundary conditions are very efficient. However, the efficiency is reduced somewhat if finite-element-generated loads are used, the stiffness calculation is updated, and the finite element model rerun.

A.6.7 Code Availability

Hypersizer is a Windows-based program presented in a convenient spreadsheet format. Hypersizer includes an interactive graphics capability to provide for visual inspection of the input variables as well as viewing of the analytical results. Hypersizer[‡] is commercially available from Collier Research Corporation in Hampton, Virginia.

[‡]www.hypersizer.com

APPENDIX B

STRAIN GAGE DATA FOR FUSELAGE PANEL TESTS

B.1 Test Panel 614-01

Gage No.	Strain, $\mu\text{in/in}$												
	1	2	3	4	5	6	7	8	9	10	11	12	13
Head load, lb													
0	-1	-1	-1	0	0	0	0	0	0	0	0	0	0
2248.1	-64	-99	-101	-111	-94	-117	-108	-115	-115	-113	-112	-115	-106
4496.2	-156	-195	-200	-211	-186	-224	-204	-217	-218	-212	-211	-223	-208
6744.3	-251	-290	-301	-310	-282	-327	-294	-315	-318	-309	-307	-324	-304
8992.4	-367	-415	-439	-376	-364	-470	-406	-378	-392	-319	-327	-444	-416
11240.5	-478	-498	-587	-461	-474	-595	-500	-458	-501	-378	-388	-555	-521
13488.6	-635	-1165	1018	-684	-785	-1327	896	-755	-796	-60	-213	-1447	-396
15736.7	-598	-1291	1063	-871	-891	-1402	863	-982	-855	-119	-271	-1659	-370
17984.8	-613	-1265	990	-1050	-1032	-1410	819	-1103	-976	-163	-315	-1720	-411
20232.9	-681	-1426	1093	-1177	-1236	-1290	642	-1326	-1081	-218	-369	-1737	-477
22481	-715	-1515	1130	-1356	-1415	-1072	418	-1510	-1185	-277	-428	-1723	-615
24729.1	-748	-1570	1143	-1544	-1610	-596	182	-1709	-1369	-283	-461	-1505	-957
26977.2	-777	-1611	1149	-1714	-1810	-272	-89	-1896	-1500	-300	-506	-1120	-1205

Gage No.	Strain, $\mu\text{in/in}$												
	14	15	17	18	19	20	21	22	23	24	25	26	27
Head load, lb													
0	0	0	0	0	0	0	0	0	0	0	0	0	0
2248.1	-105	-108	-73	-61	-65	-143	-144	28	0	2	4	-105	-133
4496.2	-209	-217	-171	-141	-149	-253	-259	37	-8	10	2	-194	-238
6744.3	-304	-320	-265	-233	-243	-348	-363	40	-14	16	0	-277	-339
8992.4	-399	-434	-369	-317	-331	-435	-464	40	-26	93	-4	-331	-447
11240.5	-484	-556	-471	-407	-428	-517	-578	49	-35	91	-2	-394	-595
13488.6	-244	-351	-654	-697	540	-264	-407	82	-22	20	33	-636	-903
15736.7	-287	-412	-851	-700	538	-341	-512	-87	-22	-45	45	-759	-1113
17984.8	-329	-482	-1121	-407	330	417	-837	-45	-75	90	4	-896	-1343
20232.9	-388	-560	-1478	220	-169	723	-1067	-155	-50	48	-7	-1000	-1648
22481	-451	-631	-1807	328	-258	883	-1183	-333	-56	-18	-11	-1115	-1946
24729.1	-1879	440	-2292	396	-318	992	-1260	-473	-44	-93	-5	-1266	-2301
26977.2	-2209	1416	-2786	418	-347	1100	-1344	-683	-48	-186	0	-1401	-2653

Test Panel 614-01

Gage No.	Strain, min/in		
	28	29	31
Head load, lb			
0	0	0	-1
2248.1	-116	-127	-101
4496.2	-208	-232	-200
6744.3	-293	-333	-301
8992.4	-370	-506	-439
11240.5	-443	-673	-587
13488.6	-598	-987	1018
15736.7	-686	-1213	1063
17984.8	-646	-1368	990
20232.9	-615	-1629	1093
22481	-537	-1875	1130
24729.1	-390	-2127	1143
26977.2	-195	-2402	1149

B.2 Test Panel 614-02

Gage No.	Strain, $\mu\text{in/in}$												
	1	2	3	4	5	6	7	8	9	10	11	12	13
Head load, lb													
0	-1	0	0	0	0	0	0	0	0	0	0	0	0
1124.1	-25	-32	-33	-38	-35	-40	-39	-46	-53	-50	-52	-55	-70
2248.1	-60	-77	-79	-91	-78	-93	-92	-102	-106	-106	-109	-109	-126
4496.2	-150	-176	-181	-200	-176	-200	-195	-211	-211	-215	-223	-216	-238
6744.3	-245	-276	-285	-305	-278	-301	-292	-317	-317	-320	-336	-316	-348
8992.4	-349	-376	-389	-411	-388	-400	-387	-423	-429	-428	-461	-409	-471
11240.5	-532	-1014	940	-625	-634	-321	-372	-506	-524	-447	-696	-496	-621
13488.6	-513	-1142	988	-789	-696	-84	-231	-1340	-769	-1139	870	-1078	-388
15736.7	-534	-1234	1043	-946	-820	-137	-279	-1481	-848	-1192	842	-1253	-407
17984.8	-546	-1399	1155	-1084	-995	-194	-328	-1567	-943	-1179	775	-1397	-484
20232.9	-562	-1548	1234	-1259	-1174	-261	-380	-1624	-1060	-1110	664	-1528	-603
22481	-523	-1710	1351	-1434	-1402	-325	-425	-1610	-1174	-906	445	-1615	-778
24729.1	-518	-1808	1409	-1613	-1643	-274	-421	-1615	-1457	-226	222	-1780	-1619
26977.2	-529	-1864	1441	-1708	-1910	-296	-437	-1585	-1592	-112	100	-2285	-1699
28101.25	-603	-1894	1459	-1628	-2195	-272	-373	-1463	-1893	-72	-116	-2195	-2009

Gage No.	Strain, $\mu\text{in/in}$												
	14	15	17	18	19	20	21	22	23	24	25	26	27
Head load, lb													
0	0	0	0	0	0	0	0	0	0	0	0	0	0
1124.1	-60	-64	-59	-33	-38	-118	-121	-8	2	2	4	-28	-47
2248.1	-109	-116	-110	-89	-95	-203	-210	-1	8	6	4	-70	-96
4496.2	-202	-216	-204	-198	-205	-332	-351	4	16	16	3	-158	-198
6744.3	-284	-310	-304	-307	-317	-420	-458	0	16	26	1	-244	-299
8992	-341	-385	-414	-414	-443	-483	-565	-18	4	39	0	-331	-405
11240.5	-372	-447	-565	-418	-562	29	-113	72	-30	173	-4	-392	-582
13488.6	-301	-426	-761	-261	278	621	-868	27	-6	91	23	-633	-794
15736.7	-362	-484	-958	-166	206	685	-870	-104	1	-6	32	-764	-982
17984.8	-431	-549	-1223	426	-310	721	-810	-205	6	54	16	-868	-1184
20232.9	-511	-606	-1526	522	-384	778	-826	-392	-8	-16	20	-983	-1440
22481	-617	-627	-1865	598	-448	840	-860	-625	-30	-130	21	-1125	-1729
24729.1	-2097	1908	-2131	647	-494	893	-912	-740	2	-211	9	-1334	-2116
26977.2	-2281	2062	-2442	618	-515	1011	-1055	-1015	-10	-337	13	-1486	-2468
28101.25	-2292	2025	-2907	440	-469	1826	-2048	-1141	-71	-191	-48	-1440	-2602

Test Panel 614-02

Gage No.	Strain, $\mu\text{in/in}$		
	28	29	31
Head load, lb			
0	0	0	0
1124.1	-25	-42	-54
2248.1	-67	-93	-107
4496.2	-158	-202	-213
6744.3	-249	-314	-318
8992.4	-339	-431	-433
11240.5	-466	-680	-534
13488.6	-554	-899	-322
15736.7	-626	-1084	-320
17984.8	-639	-1270	-356
20232.9	-639	-1493	-440
22481	-595	-1731	-573
24729.1	-456	-1958	-925
26977.2	-256	-2243	-1163
28101.25	-195	-2313	-1640

B.3 Test Panel 615-01

Gage No.	Strain, $\mu\text{in/in}$												
	1	2	3	4	5	6	7	8	9	10	11	12	13
Head load, lb													
0	-2	-1	-1	-1	-1	0	0	-1	-1	-1	0	0	0
1124.05	-12	-28	-29	-38	-42	-55	-55	-59	-59	-68	-67	-60	-64
2248.1	-34	-63	-63	-77	-82	-105	-106	-110	-104	-122	-121	-108	-109
4496.2	-112	-152	-149	-154	-168	-196	-198	-195	-195	-216	-213	-193	-201
6744.3	-207	-245	-242	-233	-261	-286	-291	-279	-289	-309	-304	-277	-295
8992.4	-303	-334	-338	-310	-355	-376	-384	-362	-383	-403	-392	-360	-389
11240.5	-402	-415	-441	-388	-450	-468	-480	-446	-481	-500	-479	-442	-484
13488.6	-511	-439	-525	-476	-547	-572	-603	-543	-617	-675	-585	-524	-598
15736.7	-652	-1020	744	-479	-672	-301	-440	-574	-790	-1455	1113	-1461	-548
17984.8	-690	-1086	784	-574	-783	-293	-436	-736	-823	-1635	1182	-1854	-468
20232.9	-751	-1208	865	-686	-910	-339	-476	-889	-892	-1784	1241	-2127	-426
22481	-809	-1334	948	-789	-1065	-386	-515	-1040	-989	-1904	1293	-2276	-451
24729.1	-865	-1461	1030	-898	-1237	-438	-553	-1194	-1095	-1987	1323	-2330	-485
26977.2	-908	-1595	1116	-1010	-1429	-494	-589	-1362	-1197	-2032	1331	-2289	-525
26977.2	-932	-1617	1131	-1006	-1486	-506	-596	-1364	-1208	-2044	1342	-2235	-587
29225.3	-987	-1734	1200	-1082	-1742	-527	-598	-1435	-1448	-2108	1360	-2191	-773

Gage No.	Strain, $\mu\text{in/in}$												
	14	15	17	18	19	20	21	22	23	24	25	26	27
Head load, lb													
0	-1	-1	-1	0	-1	0	0	0	0	0	0	0	-1
1124.05	-54	-56	-31	-56	-60	-74	-78	13	31	2	34	-59	-58
2248.1	-101	-103	-64	-106	-113	-128	-134	28	47	11	49	-109	-103
4496.2	-193	-200	-147	-195	-211	-215	-228	54	49	31	51	-196	-193
6744	-282	-299	-237	-283	-310	-300	-323	80	41	53	46	-282	-287
8992.4	-366	-400	-328	-367	-412	-383	-419	105	33	73	40	-367	-381
11240.5	-443	-511	-420	-447	-521	-464	-521	129	25	93	31	-455	-479
13488.6	-428	-485	-498	-518	-672	-481	-592	158	9	102	13	-557	-616
15736.7	-377	-431	-651	-367	46	-399	-512	198	18	187	13	-710	-797
17984.8	-470	-467	-817	-560	318	-468	-551	108	25	125	19	-825	-1006
20232.9	-642	-446	-1011	-428	211	-270	-526	48	8	75	16	-940	-1234
22481	-1591	615	-1150	-282	97	-55	-682	-4	-22	40	15	-1069	-1479
24729.1	-1881	1211	-1359	-192	41	188	-882	-82	-57	-13	5	-1205	-1739
26977.2	-2063	1575	-1621	-153	21	413	-1073	-206	-93	-62	-7	-1362	-2012
26977.2	-2010	1493	-1706	-171	19	456	-1095	-244	-139	90	-46	-1373	-2020
29225.3	-2090	1631	-2066	-229	45	656	-1212	-439	-213	55	-67	-1367	-2444

Test Panel 615-01

Gage No.	Strain, $\mu\text{in/in}$												
	28	29	30	31	33	34	35	36	37	38	39	40	41
Head load, lb													
0	0	-1	0	-1	-1	0	0	0	0	-1	0	-1	0
1124.05	-59	-65	-66	-59	-43	-50	-55	-79	-81	-68	-123	48	23
2248	-106	-115	-117	-104	-90	-100	-108	-133	-137	-106	-201	79	39
4496.2	-188	-211	-206	-193	-180	-186	-205	-225	-235	-166	-343	137	66
6744.3	-268	-309	-294	-286	-272	-271	-305	-312	-333	-215	-491	200	94
8992.4	-347	-407	-382	-378	-363	-349	-410	-395	-433	-250	-648	270	123
11240.5	-427	-510	-472	-474	-458	-417	-531	-472	-540	-268	-826	352	157
13488.6	-519	-637	-594	-608	-559	-374	-777	-495	-630	-288	-1044	454	178
15736.7	-639	-918	-823	-462	-544	-1139	981	-380	-546	-310	-1193	544	195
17984.8	-763	-1191	-1044	-363	-538	-1199	1020	-444	-630	-233	-1521	725	259
20232.9	-874	-1440	-1279	-332	-698	-897	762	-62	-1035	772	-2404	838	248
22481	-969	-1686	-1484	-344	-928	-455	379	371	-1328	1271	-2488	436	274
24729.1	-1047	-1931	-1611	-392	-1088	-247	194	574	-1451	1472	-2472	219	268
26977.2	-1104	-2197	-1634	-467	-1254	-110	58	700	-1516	1526	-2297	1	175
26977.2	-1058	-2247	-1498	-476	-1525	6	-40	847	-1515	1011	-1380	-232	-409
29225.3	-1017	-2608	703	-743	-1327	68	-168	1096	-1674	985	-1249	-414	-272

Gage No.	Strain, $\mu\text{in/in}$									
	42	43	44	45	46	47	48	49	50	51
Head load, lb										
0	0	0	0	0	0	0	0	-1	0	0
1124.05	-18	-61	-87	-87	24	21	-38	-36	-70	-58
2248.1	-25	-97	-147	-146	42	39	-57	-53	-126	-115
4496.2	-29	-162	-239	-242	70	63	-91	-86	-219	-210
6744.3	-23	-230	-330	-337	98	85	-123	-121	-312	-306
8992.4	-4	-300	-420	-434	126	106	-154	-157	-405	-399
11240.5	35	-381	-513	-533	155	127	-186	-194	-499	-494
13488.6	164	-519	-690	-587	159	124	-217	-221	-611	-589
15736.7	127	-630	-981	-503	108	101	-418	-246	-842	-745
17984.8	282	-833	-1393	-230	-62	126	-739	-107	-1058	-841
20232.9	1277	-1724	-402	-243	-579	-62	-635	19	-1321	-1048
22481	1364	-1600	68	-558	-488	-475	-370	-153	-1588	-1271
24729.1	1249	-1429	308	-741	-416	-566	-214	-255	-1895	-1447
26977.2	925	-1129	423	-809	-373	-551	-145	-258	-2302	-1593
26977.2	72	-495	436	-816	-371	-540	-137	-251	-2365	-1615
29225.3	-120	-329	524	-858	-426	-475	-147	-196	-3346	-1688

B.4 Test Panel 615-02

Gage No.	Strain, $\mu\text{in/in}$												
	1	2	3	4	5	6	7	8	9	10	11	12	13
Head load, lb													
0.0	-2	-1	-1	0	-1	0	0	0	0	0	0	0	0
1124.1	-16	-45	-48	-23	-36	-37	-39	-36	-62	-42	-40	-35	-51
2248.1	-64	-93	-100	-48	-81	-76	-81	-73	-108	-84	-79	-71	-96
4496.2	-149	-182	-204	-107	-176	-175	-184	-165	-205	-185	-177	-152	-187
6744.3	-241	-263	-319	-161	-271	-267	-283	-252	-299	-282	-273	-231	-278
8992.4	-332	-316	-456	-209	-365	-351	-378	-332	-391	-372	-364	-305	-367
11240.5	-436	-187	-741	-257	-468	-427	-478	-413	-485	-460	-462	-378	-457
13488.6	-606	-319	-69	-280	-558	-344	-423	-455	-564	-587	-656	-472	-584
15736.7	-713	-731	448	-383	-622	-202	-353	-508	-764	-1159	921	-1031	-631
17984.8	-771	-946	672	-464	-713	-247	-382	-688	-794	-1337	994	-1364	-535
20232.9	-795	-1153	859	-545	-835	-306	-419	-882	-829	-1476	1026	-1615	-451
22481.0	-831	-1316	979	-623	-966	-363	-458	-1020	-917	-1592	1062	-1760	-414
24729.1	-870	-1480	1091	-699	-1116	-425	-498	-1139	-1026	-1621	1052	-1733	-461
26977.2	-889	-1628	1188	-762	-1306	-472	-523	-1285	-1151	-1562	963	-1555	-558
28101.3	-896	-1698	1235	-788	-1430	-479	-523	-1361	-1230	-1468	870	-1404	-632
29225.3	-923	-1772	1285	-799	-1619	-425	-488	-1375	-1391	-1333	754	-1240	-747

Gage No.	Strain, $\mu\text{in/in}$												
	14	15	17	18	19	20	21	22	23	24	25	26	27
Head load, lb													
0.0	0	0	0	0	0	0	0	0	0	-1	0	0	0
1124.1	-54	-47	-26	-75	-81	-106	-105	-9	-5	12	-6	-24	-49
2248.1	-106	-93	-73	-154	-163	-183	-182	10	-14	23	-18	-48	-92
4496.2	-204	-178	-152	-288	-308	-317	-319	40	-8	48	-24	-130	-182
6744.3	-302	-262	-236	-382	-420	-418	-431	64	-10	77	-29	-221	-275
8992.4	-403	-344	-323	-460	-530	-500	-531	85	-17	107	-37	-309	-366
11240.5	-511	-419	-409	-511	-680	-571	-642	105	-24	136	-46	-401	-460
13488.6	-631	-475	-502	-984	917	-580	-689	184	-16	164	-56	-474	-568
15736.7	-393	-368	-632	-1033	892	-444	-603	137	-1	322	-39	-712	-789
17984.8	-479	-397	-809	-894	744	-494	-696	14	9	263	-32	-828	-1004
20232.9	-622	-399	-1006	-756	611	-549	-829	-145	9	174	-33	-959	-1241
22481.0	-1423	220	-1161	-366	317	344	-1131	-177	-11	117	-45	-1100	-1439
24729.1	-1755	811	-1366	-242	227	603	-1278	-219	-49	168	-73	-1226	-1656
26977.2	-1898	1278	-1606	-226	189	799	-1403	-378	-80	202	-92	-1365	-1911
28101.3	-1928	1421	-1751	-271	200	901	-1461	-487	-94	211	-100	-1431	-2058
29225.3	-1926	1476	-1948	-509	311	1105	-1611	-717	-117	302	-122	-1455	-2193

Test Panel 615-02

Gage No.	Strain, $\mu\text{in/in}$												
	28	29	30	31	33	34	35	36	37	38	39	40	41
Head load, lb													
0.0	0	0	0	0	0	0	0	0	0	0	0	0	0
1124.1	-17	-40	-10	-62	-26	-11	-10	-9	-9	-2	-2	2	8
2248.1	-33	-75	-19	-109	-55	-23	-22	-19	-20	-5	-5	5	13
4496.2	-97	-162	-79	-206	-135	-88	-92	-84	-89	-47	-80	30	28
6744.3	-172	-256	-161	-301	-229	-176	-185	-167	-176	-103	-191	70	49
8992.4	-244	-350	-244	-394	-323	-261	-280	-250	-267	-160	-316	116	74
11240.5	-318	-447	-330	-491	-420	-346	-384	-335	-363	-213	-455	169	102
13488.6	-387	-557	-413	-614	-522	-430	-514	-403	-455	-258	-604	231	131
15736.7	-550	-861	-577	-604	-756	-137	-283	-260	-404	-363	-736	298	113
17984.8	-633	-1120	-754	-526	-873	-178	-101	-309	-492	-397	-947	407	148
20232.9	-716	-1377	-920	-487	-997	-135	-98	-376	-615	-365	-1241	574	219
22481.0	-790	-1575	-1056	-531	-1112	-83	-114	-392	-797	-137	-1720	821	345
24729.1	-817	-1782	-1171	-617	-1404	131	-262	469	-1220	1087	-1968	-79	56
26977.2	-843	-2019	-1264	-749	-1602	231	-313	690	-1313	1020	-1681	-195	-93
28101.3	-854	-2146	-1295	-854	-1657	265	-328	776	-1356	1014	-1629	-221	-82
29225.3	-842	-2233	-1264	-1107	-1679	292	-343	848	-1388	1011	-1594	-239	-56

Gage No.	Strain, $\mu\text{in/in}$									
	42	43	44	45	46	47	48	49	50	51
Head load, lb										
0.0	0	0	0	0	0	0	0	0	0	0
1124.1	-10	-8	-134	-165	51	32	-26	-52	-89	-25
2248.1	-20	-19	-218	-277	89	64	-38	-78	-163	-88
4496.2	-49	-71	-345	-466	157	117	-55	-131	-290	-207
6744.3	-70	-127	-431	-613	215	154	-70	-188	-384	-306
8992.4	-80	-181	-495	-742	269	185	-73	-242	-465	-394
11240.5	-82	-241	-550	-882	338	220	-62	-304	-546	-484
13488.6	-68	-295	-729	-999	421	253	-162	-426	-869	-548
15736.7	-77	-387	-944	-933	412	290	-171	-420	-1164	-491
17984.8	-35	-491	-1031	-1053	541	379	-104	-517	-1370	-594
20232.9	85	-639	-1055	-1276	759	533	57	-692	-1610	-712
22481.0	383	-908	1041	-1919	-121	-10	459	-958	-1831	-1062
24729.1	575	-973	1051	-1728	-47	-305	326	-633	-2122	-1303
26977.2	312	-721	1122	-1738	-55	-240	312	-581	-2847	-1411
28101.3	279	-676	1174	-1764	-66	-187	294	-564	-3823	-1408
29225.3	253	-625	1268	-1784	-128	-107	218	-537	-8018	-929

B.5 Test Panel 616-01

Gage No.	Strain, $\mu\text{in/in}$												
	6	7	8	9	10	11	12	13	14	15	17	18	19
Head load, lb													
0	-1	-1	0	0	0	0	0	0	0	0	0	0	0
2248	-31	-33	-33	-56	-33	-37	-45	-44	-59	-51	-48	-89	-85
4496	-70	-73	-73	-107	-72	-77	-92	-92	-116	-100	-100	-170	-163
8992	-160	-164	-169	-209	-165	-175	-202	-195	-232	-202	-187	-304	-291
13489	-256	-259	-267	-316	-259	-274	-305	-298	-343	-302	-276	-409	-394
17985	-352	-355	-369	-421	-349	-370	-408	-395	-449	-395	-372	-505	-489
22481	-448	-452	-471	-526	-439	-468	-511	-491	-557	-490	-471	-601	-584
26977	-541	-551	-575	-631	-527	-567	-613	-587	-663	-586	-570	-696	-678
31473	-629	-655	-681	-739	-610	-669	-717	-679	-749	-691	-672	-789	-777
35970	-722	-782	-807	-888	-613	-803	-888	-680	-1054	-134	-754	-845	-899
40466	-694	-922	-855	-1075	-546	-787	-1095	-671	-1186	123	-811	-909	112
44962	697	-879	-1193	-1646	171	-1031	-1232	-1198	-680	-30	-1210	-735	99
47210	716	-768	-1381	-1758	386	-1103	-1308	-1359	-566	-43	-1335	-471	11
49458	729	-693	-1499	-1875	538	-1151	-1381	-1492	-470	-52	-1445	-333	-19
51706	741	-631	-1605	-1992	661	-1190	-1454	-1615	-397	-51	-1551	-242	-28
53954	749	-572	-1712	-2116	783	-1229	-1537	-1748	-337	-42	-1662	-163	-29
56203	711	-502	-1828	-2215	831	-1240	-1603	-1859	-335	-12	-1805	-86	-28
58451	743	-498	-1900	-2358	943	-1294	-1714	-2022	-284	0	-1955	-18	-21
60699	772	-474	-1983	-2497	1046	-1328	-1803	-2168	-213	-5	-2083	47	-16
62947	810	-453	-2062	-2654	1155	-1364	-1906	-2328	-119	-32	-2299	119	-9
65195	842	-433	-2141	-2802	1260	-1397	-2001	-2487	-18	-60	-2462	181	-4
67443	878	-416	-2215	-2951	1361	-1426	-2099	-2650	90	-93	-2623	243	-3
69691	914	-400	-2282	-3102	1461	-1452	-2205	-2813	208	-131	-2785	307	-5
71939	949	-386	-2340	-3265	1561	-1476	-2316	-2992	336	-180	-2972	371	-10
74187	980	-371	-2384	-3435	1657	-1497	-2428	-3179	471	-238	-3173	434	-20
76435	1001	-349	-2410	-3630	1761	-1512	-2543	-3399	627	-313	-3411	507	-45

Test Panel 616-01

Gage No.	Strain, $\mu\text{in/in}$												
	20	21	22	23	24	25	26	27	28	29	30	31	33
Head load, lb													
0	0	0	0	0	0	0	0	0	0	0	0	0	0
2248	-96	-89	-5	-15	-5	-5	-15	-47	-12	-39	-6	-57	-19
4496	-176	-164	8	-32	3	-24	-36	-91	-30	-78	-13	-107	-46
8992	-309	-293	29	-52	36	-48	-112	-185	-106	-169	-67	-210	-134
13489	-414	-397	51	-65	60	-59	-199	-290	-198	-270	-148	-316	-238
17985	-508	-493	71	-79	85	-68	-288	-395	-294	-373	-228	-418	-346
22481	-600	-589	89	-93	108	-78	-378	-499	-392	-477	-296	-520	-456
26977	-693	-685	106	-108	130	-87	-468	-604	-490	-580	-362	-623	-565
31473	-790	-783	122	-123	151	-97	-558	-710	-589	-685	-426	-727	-676
35970	-907	-909	158	-135	172	-109	-648	-823	-695	-791	-500	-852	-784
40466	244	-1331	158	-134	235	-122	-684	-920	-755	-866	-550	-1010	-867
44962	693	-1424	133	-86	265	-94	-888	-1151	-969	-1262	-665	-1514	-1266
47210	805	-1469	-4	-66	140	-96	-990	-1233	-1047	-1408	-701	-1619	-1358
49458	924	-1501	-109	-54	17	-97	-1076	-1315	-1112	-1527	-747	-1735	-1441
51706	1028	-1531	-218	-42	-109	-96	-1159	-1394	-1172	-1641	-793	-1849	-1523
53954	1133	-1560	-341	-29	-260	-97	-1250	-1480	-1235	-1765	-844	-1973	-1615
56203	1236	-1584	-457	-53	-242	-104	-1277	-1614	-1244	-1934	-945	-2052	-1837
58451	1339	-1611	-596	-84	-381	-113	-1404	-1744	-1331	-2128	-1035	-2219	-2053
60699	1440	-1633	-743	-90	-531	-119	-1494	-1857	-1379	-2279	-1091	-2364	-2166
62947	1549	-1652	-923	-91	-706	-140	-1587	-1992	-1426	-2458	-1152	-2527	-2288
65195	1654	-1675	-1107	-88	-898	-144	-1685	-2111	-1469	-2623	-1206	-2681	-2403
67443	1758	-1696	-1305	-84	-1113	-145	-1786	-2228	-1509	-2789	-1253	-2835	-2519
69691	1867	-1720	-1517	-88	-1353	-143	-1889	-2347	-1544	-2958	-1294	-2991	-2634
71939	1991	-1748	-1758	-77	-1615	-141	-1993	-2474	-1572	-3135	-1330	-3156	-2749
74187	2131	-1784	-2022	-61	-1893	-137	-2097	-2603	-1593	-3312	-1360	-3321	-2855
76435	2313	-1835	-2340	-38	-2196	-129	-2199	-2738	-1606	-3490	-1383	-3500	-2949

Test Panel 616-01

Gage No.	Strain, $\mu\text{in/in}$												
	34	35	36	37	38	39	40	41	42	43	44	45	46
Head load, lb													
0	0	0	0	0	0	0	0	-1	0	0	0	0	0
2248	-5	-6	-4	-7	-2	0	3	8	-1	-2	-106	-126	33
4496	-12	-16	-14	-22	-7	-5	6	11	-11	-16	-196	-227	61
8992	-58	-70	-93	-107	-75	-90	34	36	-66	-85	-334	-378	102
13489	-146	-161	-189	-206	-158	-194	67	57	-91	-133	-435	-489	131
17985	-240	-260	-282	-304	-238	-297	99	77	-113	-179	-524	-589	159
22481	-337	-362	-376	-404	-317	-405	133	96	-131	-227	-613	-688	187
26977	-433	-464	-469	-504	-397	-516	170	118	-149	-278	-702	-786	216
31473	-526	-569	-564	-609	-474	-633	210	140	-166	-333	-794	-885	246
35970	-618	-683	-673	-730	-544	-756	252	170	-183	-402	-859	-996	273
40466	-683	-774	-746	-817	-591	-867	292	192	-182	-459	-1037	-818	261
44962	-610	-155	-478	-878	-840	-975	342	142	-318	-526	-1165	-750	311
47210	-679	-60	-478	-914	-890	-1019	355	140	-336	-540	-1236	-752	321
49458	-731	15	-488	-953	-937	-1067	368	138	-356	-561	-1291	-749	327
51706	-764	68	-505	-993	-980	-1116	377	136	-377	-583	-1348	-745	333
53954	-780	106	-529	-1036	-1023	-1164	375	127	-408	-600	-1409	-739	338
56203	-704	161	307	-1149	-341	-92	-508	29	-622	41	-1493	-727	343
58451	-577	187	560	-1240	-169	-76	-504	52	-490	63	-1602	-707	348
60699	-538	205	701	-1289	-94	-63	-507	71	-448	79	-1700	-680	346
62947	-505	228	842	-1337	-40	-40	-510	88	-422	111	-1815	-641	342
65195	-464	242	965	-1381	18	-37	-514	110	-395	124	-1930	-597	335
67443	-418	251	1085	-1422	76	-38	-520	135	-369	136	-2055	-540	323
69691	-367	256	1202	-1462	138	-47	-527	163	-342	141	-2183	-473	308
71939	-312	257	1322	-1502	204	-60	-536	193	-313	147	-2321	-392	288
74187	-258	256	1439	-1542	271	-76	-549	224	-285	152	-2445	-310	265
76435	-202	250	1561	-1584	346	-96	-566	256	-256	161	-2523	-245	246

Test Panel 616-01

Gage No.	Strain, $\mu\text{in/in}$				
	47	48	49	50	51
Head load, lb					
0	0	0	0	0	0
2248	14	1	-21	-88	-57
4496	38	-13	-41	-157	-127
8992	75	-49	-84	-263	-246
13489	96	-83	-124	-341	-351
17985	112	-115	-166	-407	-456
22481	127	-148	-209	-468	-562
26977	141	-182	-251	-530	-669
31473	156	-219	-295	-593	-778
35970	188	-262	-359	-670	-885
40466	-5	-497	-420	-906	-1106
44962	-125	-409	-403	-937	-1283
47210	-147	-451	-421	-975	-1452
49458	-167	-481	-434	-1009	-1560
51706	-185	-512	-446	-1039	-1656
53954	-202	-547	-458	-1068	-1756
56203	-223	-589	-464	-1090	-1841
58451	-242	-642	-462	-1107	-1955
60699	-260	-697	-467	-1110	-2053
62947	-279	-764	-469	-1096	-2159
65195	-296	-832	-468	-1069	-2267
67443	-312	-908	-462	-1016	-2371
69691	-328	-987	-452	-923	-2478
71939	-345	-1075	-436	-774	-2579
74187	-364	-1155	-420	-540	-2666
76435	-381	-1206	-410	-125	-2719

B.6 Test Panel 616-02

Gage No.	Strain, $\mu\text{in/in}$												
	6	7	8	9	10	11	12	13	14	15	17	18	19
Head load, lb													
0	0	0	0	0	0	0	0	0	0	0	0	0	0
2248	-42	-43	-37	-53	-42	-40	-37	-49	-44	-42	-31	-63	-63
4496	-98	-97	-87	-108	-99	-94	-87	-100	-93	-89	-67	-127	-127
8992	-200	-194	-176	-214	-201	-191	-181	-203	-195	-186	-158	-231	-233
13489	-299	-288	-261	-318	-298	-285	-272	-307	-297	-284	-256	-326	-330
17985	-399	-382	-346	-422	-395	-377	-362	-409	-398	-382	-353	-418	-427
22481	-499	-476	-427	-526	-493	-469	-452	-512	-498	-480	-451	-509	-522
26977	-599	-571	-508	-630	-591	-562	-544	-616	-597	-581	-549	-598	-616
31473	-699	-667	-589	-736	-692	-654	-636	-720	-695	-685	-648	-687	-712
35970	-799	-766	-670	-843	-797	-747	-731	-825	-783	-797	-749	-775	-809
40466	-888	-876	-767	-945	-961	-864	-810	-982	-764	-846	-910	-861	-914
44962	-19	-619	-983	-1359	209	-1242	-1049	-1376	-527	-376	-1160	-580	-953
47210	-8	-543	-1069	-1439	435	-1311	-1120	-1517	-446	-332	-1252	-610	-991
49458	-278	-274	-1238	-1459	665	-1393	-1211	-1691	-354	-294	-1335	-636	-1024
51706	-166	-317	-1268	-1576	828	-1436	-1289	-1826	-268	-276	-1458	-685	-1063
53954	-141	-288	-1347	-1649	957	-1475	-1360	-1947	-197	-264	-1549	-732	-1098
56203	-122	-257	-1424	-1718	1076	-1510	-1432	-2066	-125	-260	-1638	-781	-1132
58451	-99	-228	-1502	-1786	1193	-1543	-1506	-2187	-39	-266	-1733	-833	-1162
60699	-66	-201	-1583	-1856	1311	-1572	-1584	-2314	65	-283	-1837	-888	-1188
62947	-38	-174	-1665	-1927	1430	-1604	-1660	-2445	162	-299	-1953	-950	-1207
65195	-3	-149	-1746	-1992	1553	-1632	-1733	-2575	267	-317	-2074	-1030	-1179
67443	-60	-135	-1762	-2060	1593	-1668	-1747	-2710	289	-332	-2291	1561	-1737
69691	-73	-100	-1846	-2119	1690	-1707	-1815	-2836	339	-334	-2431	1735	-1774
71939	-91	-57	-1920	-2156	1799	-1741	-1882	-2959	411	-347	-2585	183	-1802
74187	-104	-18	-2002	-2172	1916	-1778	-1941	-3090	501	-373	-2764	2024	-1830
76435	-127	21	-2082	-2155	2039	-1820	-1979	-3233	610	-420	-2973	2165	-1855
78684	-176	74	-2160	-2090	2195	-1877	-1984	-3366	735	-481	-3220	2307	-1883
80932	-276	152	-2203	-1957	2391	-1958	-1905	-3473	880	-563	-3551	2459	-1899

Test Panel 616-02

Gage No.	Strain, $\mu\text{in/in}$												
	20	21	22	23	24	25	26	27	28	29	30	31	33
Head load, lb													
0	0	0	0	0	0	0	0	0	0	0	0	0	0
2248	-83	-75	16	-24	5	-15	-33	-52	-31	-48	-22	-52	-32
4496	-159	-144	29	-17	17	-16	-83	-104	-80	-99	-56	-108	-82
8992	-273	-251	54	-22	43	-24	-178	-206	-175	-200	-120	-213	-186
13489	-373	-347	77	-32	69	-35	-271	-308	-269	-301	-183	-317	-293
17985	-473	-441	99	-44	93	-46	-363	-409	-363	-402	-244	-420	-400
22481	-571	-533	116	-61	113	-58	-456	-511	-458	-504	-301	-523	-508
26977	-672	-624	132	-80	133	-71	-549	-614	-553	-607	-359	-627	-616
31473	-776	-714	148	-99	152	-84	-642	-718	-649	-710	-415	-733	-726
35970	-885	-802	164	-119	171	-99	-736	-823	-746	-816	-470	-840	-838
40466	-991	-881	172	-137	192	-119	-830	-929	-842	-938	-536	-962	-992
44962	-2646	949	-15	-87	190	-78	-956	-1118	-1027	-1184	-542	-1202	-1168
47210	-2758	1028	-79	-91	144	-66	-1038	-1195	-1098	-1291	-561	-1299	-1259
49458	-2850	1086	-251	-28	69	-70	-1125	-1316	-1214	-1443	-586	-1348	-1473
51706	-2904	1118	-298	-54	22	-102	-1166	-1415	-1256	-1586	-642	-1504	-1746
53954	-2934	1134	-395	-44	-61	-104	-1232	-1517	-1322	-1720	-672	-1596	-1840
56203	-2943	1136	-499	-32	-155	-102	-1295	-1620	-1387	-1858	-708	-1684	-1929
58451	-2938	1128	-616	-18	-267	-101	-1357	-1729	-1456	-2004	-748	-1771	-2015
60699	-2931	1118	-757	-1	-402	-102	-1418	-1849	-1531	-2165	-790	-1861	-2105
62947	-2936	1114	-909	12	-546	-97	-1483	-1974	-1614	-2335	-839	-1950	-2202
65195	-2965	1122	-1096	30	-726	-90	-1543	-2110	-1702	-2523	-894	-2034	-2298
67443	-1515	753	-1112	-51	-801	-165	-1576	-2196	-1745	-2642	-975	-2132	-2303
69691	-1319	691	-1284	-52	-948	-171	-1634	-2327	-1832	-2822	-1045	-2209	-2379
71939	-1142	634	-1495	-54	-1127	-172	-1684	-2466	-1919	-3019	-1113	-2265	-2472
74187	-975	580	-1744	-56	-1316	-173	-1734	-2620	-2016	-3237	-1187	-2303	-2595
76435	-799	517	-2026	-61	-1493	-171	-1784	-2789	-2117	-3480	-1280	-2311	-2744
78684	-610	438	-2326	-62	-1703	-175	-1831	-2989	-2211	-3767	-1376	-2278	-2891
80932	-289	277	-2657	-57	-1954	-196	-1876	-3221	-2292	-4109	-1480	-2187	-3066

Test Panel 616-02

Gage No.	Strain, $\mu\text{in/in}$												
	34	35	36	37	38	39	40	41	42	43	44	45	46
Head load, lb													
0	0	0	0	0	0	0	0	0	0	0	0	0	0
2248.1	-30	-28	-27	-26	-20	-28	11	13	-14	-18	-87	-114	30
4496.2	-79	-74	-75	-73	-58	-77	25	24	-34	-44	-155	-205	55
8992.4	-179	-167	-170	-165	-138	-180	55	44	-65	-88	-247	-335	89
13488.6	-280	-261	-265	-258	-218	-284	86	64	-87	-129	-322	-447	118
17984.8	-384	-355	-361	-350	-297	-389	118	84	-107	-168	-393	-558	149
22481	-489	-449	-458	-444	-376	-498	153	106	-128	-209	-459	-670	182
26977.2	-594	-543	-556	-537	-456	-611	190	129	-148	-253	-519	-787	217
31473.4	-702	-636	-654	-631	-534	-725	230	153	-167	-297	-573	-909	256
35969.6	-814	-729	-749	-727	-613	-843	274	178	-183	-343	-616	-1043	300
40465.8	-1008	-817	-712	-880	-785	-965	336	170	-212	-371	-640	-1183	349
44962	-1123	-853	-660	-886	-828	-1014	364	168	-211	-375	653	-1440	-3
47210.1	-1256	-847	-654	-906	-866	-1051	381	170	-224	-391	677	-1458	-2
49458.2	-933	-1212	-748	-940	-873	-1127	416	191	-218	-398	676	-1467	18
51706.3	569	-1535	-716	-960	-912	-1192	452	213	-387	-463	688	-1495	29
53954.4	607	-1465	-712	-1001	-947	-1245	491	236	-396	-486	680	-1510	52
56202.5	600	-1378	-709	-1044	-978	-1300	533	264	-398	-509	668	-1526	78
58450.6	559	-1266	-703	-1091	-1002	-1359	585	300	-388	-532	650	-1539	107
60698.7	494	-1136	-695	-1141	-1014	-1430	653	349	-361	-557	628	-1550	138
62946.8	411	-1011	-689	-1195	-1011	-1510	733	410	-319	-584	618	-1571	165
65194.9	296	-858	-675	-1251	-976	-1607	835	488	-255	-614	583	-1579	200
67443	144	-680	-662	-1312	-870	-1764	995	603	-125	-650	-357	-1275	496
69691.1	2	-529	-654	-1371	-702	-1947	1174	724	22	-687	-346	-1338	525
71939.2	-141	-381	-650	-1425	-418	-2204	1405	866	227	-724	-304	-1419	558
74187.3	-287	-235	-639	-1501	24	-2557	1700	1037	472	-745	-218	-1530	601
76435.4	-465	-72	-490	-1674	575	-2920	1887	1192	605	-748	-65	-1681	659
78683.5	-686	104	-284	-1829	1055	-3216	1926	1286	692	-822	193	-1891	737
80931.6	-930	280	-74	-1951	1524	-3499	1928	1358	769	-924	687	-2196	845

Test Panel 616-02

Gage No.	Strain, $\mu\text{in/in}$				
	47	48	49	50	51
Head load, lb					
0	0	0	0	0	0
2248.1	30	-24	-27	-60	-62
4496.2	60	-44	-52	-114	-124
8992.4	91	-69	-92	-190	-235
13488.6	112	-90	-132	-256	-340
17984.8	133	-109	-173	-320	-444
22481	157	-124	-215	-377	-548
26977.2	182	-137	-259	-435	-651
31473.4	209	-143	-306	-492	-756
35969.6	241	-140	-357	-548	-862
40465.8	276	-127	-415	-604	-974
44962	534	429	-423	-980	-888
47210.1	530	442	-442	-1056	-914
49458.2	525	448	-447	-1134	-959
51706.3	521	461	-461	-1204	-970
53954.4	515	467	-477	-1272	-997
56202.5	510	471	-492	-1337	-1025
58450.6	504	473	-506	-1398	-1056
60698.7	499	474	-519	-1457	-1093
62946.8	496	479	-535	-1524	-1143
65194.9	474	479	-558	-1596	-1200
67443	132	23	-599	-1549	-1996
69691.1	151	33	-630	-1556	-2117
71939.2	178	61	-997	-1556	-2240
74187.3	218	112	-715	-1544	-2369
76435.4	269	195	-778	-1508	-2510
78683.5	333	326	-869	-1437	-2677
80931.6	408	554	-986	-1201	-2911

B.7 Test Panel 617-01

Gage No.	Strain, $\mu\text{in/in}$												
	1	2	3	4	5	6	7	8	9	10	11	12	13
Head load, lb													
0	-2	-1	-1	-1	-1	0	-1	-1	-1	-1	-1	0	-1
1124	-19	-27	-28	-30	-34	-38	-38	-34	-37	-42	-41	-31	-37
2248	-46	-62	-62	-65	-72	-81	-79	-70	-76	-85	-82	-61	-74
4496	-107	-131	-130	-128	-143	-153	-150	-130	-142	-158	-152	-113	-140
6744	-179	-204	-204	-190	-215	-226	-220	-188	-206	-230	-222	-166	-207
8992	-250	-276	-276	-251	-286	-297	-289	-246	-270	-303	-291	-218	-273
11241	-319	-346	-348	-310	-356	-369	-357	-301	-332	-375	-359	-268	-339
13489	-391	-417	-421	-366	-427	-440	-424	-354	-394	-448	-427	-315	-404
15737	-460	-488	-493	-421	-497	-513	-490	-407	-454	-521	-494	-360	-468
17985	-529	-558	-566	-477	-567	-586	-555	-458	-515	-596	-561	-408	-533
20233	-600	-629	-640	-531	-638	-662	-619	-506	-576	-673	-627	-453	-598
22481	-670	-699	-714	-587	-708	-740	-680	-553	-635	-752	-690	-499	-662
24729	-740	-765	-791	-640	-779	-821	-734	-592	-694	-833	-751	-542	-726
26977	-811	-824	-875	-697	-850	-909	-780	-635	-749	-920	-805	-586	-791
29225	-994	20	-1505	-779	-942	-960	-755	-629	-757	-976	-807	-611	-843
31473	-1153	110	-1271	-833	-1016	-830	-848	-631	-743	-1771	1095	-1394	-1402
33722	-1256	492	-1485	-806	-1452	869	-1569	-611	-1134	-80	-415	-947	-1430
35970	-1380	624	-1546	-856	-1620	960	-1512	-645	-1324	628	-1058	-753	-1473
38218	-1492	726	-1592	-891	-1750	1040	-1497	-664	-1429	770	-1151	-764	-1542
40466	-1604	818	-1634	-924	-1874	1116	-1486	-675	-1524	902	-1238	-773	-1605
42714	-1714	908	-1678	-949	-1989	1190	-1478	-674	-1607	1027	-1320	-776	-1658
44962	-1824	996	-1722	-966	-2103	1265	-1473	-661	-1678	1147	-1396	-778	-1704
47210	-1941	1030	-1775	-972	-2172	1309	-1514	-646	-1716	1173	-1435	-790	-1734
49458	-2051	1128	-1862	-981	-2278	1385	-1519	-595	-1736	1274	-1485	-808	-1810
50582	-2094	1182	-1918	-974	-2332	1421	-1520	-551	-1719	1323	-1507	-815	-1838
51706	-2136	1234	-1984	-971	-2388	1454	-1514	-488	-1682	1373	-1527	-822	-1877
52830	-2164	1287	-2060	-959	-2444	1483	-1501	-367	-1576	142	-1540	-829	-1915
53954	-2109	1282	-2202	-926	-2459	1410	-1418	-266	-1469	1447	-1578	-837	-1933
55078	-2060	1274	-2264	-961	-2625	1398	-1363	256	-1019	1479	-1570	-866	-2011

Test Panel 617-01

Gage No.	Strain, $\mu\text{in/in}$												
	14	15	17	18	19	20	21	22	23	24	25	26	27
Head load, lb													
0	0	-1	0	0	0	0	0	0	0	0	-1	-1	0
1124	-36	-33	-24	-39	-39	-64	-61	14	28	11	41	-34	-36
2248	-71	-67	-51	-80	-78	-115	-109	27	45	25	56	-71	-75
4496	-139	-133	-112	-153	-148	-189	-182	49	53	47	65	-137	-142
6744	-211	-202	-182	-226	-219	-263	-256	72	49	69	63	-202	-209
8992	-282	-271	-251	-297	-287	-334	-327	93	43	91	58	-266	-274
11241	-353	-338	-319	-367	-353	-404	-396	114	38	113	54	-327	-338
13489	-425	-406	-390	-438	-420	-475	-467	135	28	136	46	-387	-403
15737	-496	-472	-458	-508	-484	-545	-537	154	21	158	40	-445	-468
17985	-569	-537	-525	-580	-547	-614	-607	174	15	181	35	-502	-532
20233	-643	-602	-595	-653	-610	-684	-679	194	5	204	27	-556	-597
22481	-719	-664	-662	-727	-669	-752	-751	213	-1	225	22	-610	-661
24729	-797	-722	-730	-803	-724	-818	-825	233	-11	248	14	-664	-725
26977	-878	-774	-798	-880	-775	-881	-894	252	-20	269	7	-714	-793
29225	-1047	-793	-896	-808	-915	-1917	1180	292	-46	285	-11	-728	-792
31473	-792	-910	-953	-894	-1021	-1725	1002	328	-2	260	40	-859	-934
33722	-983	-871	-1045	-598	-916	-2128	1420	415	59	380	60	-802	-845
35970	710	-1510	-1367	-622	-978	-2124	1404	365	76	434	118	-821	-861
38218	784	-1491	-1479	-638	-1028	-2118	1405	347	114	438	144	-842	-892
40466	852	-1480	-1589	-652	-1078	-2112	1405	324	158	440	173	-843	-926
42714	922	-1479	-1696	-664	-1131	-2108	1405	297	207	434	202	-863	-955
44962	997	-1490	-1798	-672	-1186	-2104	1407	264	265	424	229	-885	-982
47210	1033	-1544	-1866	-642	-1333	201	-568	250	336	633	276	-1062	-1159
49458	1136	-1640	-1943	-616	-1425	375	-725	206	416	623	305	-1109	-1221
50582	1197	-1708	-1961	-595	-1482	479	-824	180	464	614	316	-1136	-1248
51706	1261	-1790	-1984	-567	-1544	600	-945	148	527	601	322	-1159	-1280
52830	1335	-1899	-1994	-511	-1640	751	-1100	111	611	581	322	-1181	-1311
53954	1419	-2085	-1988	1599	-1655	1575	-1842	337	546	566	182	-1210	-1342
55078	1474	-2239	-1949	1686	-1673	1702	-1962	298	717	514	131	-1232	-1404

Test Panel 617-01

Gage No.	Strain, $\mu\text{in/in}$												
	28	29	30	31	33	34	35	36	37	38	39	40	41
Head load, lb													
0	0	0	-1	0	0	0	0	0	0	0	0	-1	0
1124	-35	-35	-41	-39	-36	-43	-52	-31	-32	-18	-32	3	-3
2248	-76	-75	-83	-78	-78	-91	-88	-67	-69	-43	-77	15	2
4496	-147	-144	-154	-145	-145	-168	-164	-138	-142	-93	-169	40	13
6744	-218	-212	-224	-211	-211	-242	-238	-209	-215	-144	-262	67	24
8992	-286	-279	-291	-276	-276	-315	-309	-277	-286	-192	-352	94	35
11241	-351	-347	-358	-340	-340	-388	-380	-345	-356	-238	-440	122	47
13489	-415	-416	-425	-403	-403	-461	-451	-413	-426	-284	-529	152	58
15737	-477	-483	-491	-477	-466	-535	-520	-480	-496	-328	-617	183	71
17985	-541	-552	-558	-540	-530	-610	-589	-548	-566	-372	-705	215	84
20233	-598	-620	-625	-604	-594	-687	-657	-617	-636	-417	-795	251	99
22481	-660	-689	-691	-667	-657	-765	-721	-685	-706	-461	-884	290	114
24729	-719	-759	-755	-730	-719	-845	-780	-754	-776	-506	-972	332	132
26977	-781	-830	-818	-792	-782	-930	-827	-822	-844	-553	-1056	378	151
29225	-814	-834	-1009	-835	-1270	-1583	862	-722	-955	-747	-1082	397	118
31473	-914	-1000	-1218	-1546	-1582	-2090	1483	-626	-916	-844	-1155	440	128
33722	-986	-1041	-1273	-1492	-1659	-2136	1548	-632	-976	-890	-1203	486	143
35970	-1097	-1124	-1448	-1413	-1828	-2273	1706	-626	-1039	-946	-1245	520	156
38218	-1160	-1183	-1604	-1435	-1900	-2399	1837	-631	-1108	-1009	-1287	571	177
40466	-1226	-1242	-1758	-1439	-1939	-2560	1949	-633	-1181	-1067	-1321	626	205
42714	-1293	-1304	-1912	-1415	-1988	-2629	2048	-628	-1262	-1120	-1350	685	240
44962	-1367	-1369	-2062	-1371	-2046	-2741	2143	-614	-1353	-1162	-1380	755	287
47210	-1081	-1841	-2161	-1305	-1993	-81	100	1277	-1808	1552	-2509	-380	362
49458	-1094	-1935	-2284	-1154	-1977	122	-65	1376	-1846	1651	-2585	-398	366
50582	-1100	-1981	-1349	-1045	-1953	229	-153	1429	-1866	1704	-2623	-408	368
51706	-1102	-2026	-2402	-881	-1917	358	-268	1484	-1887	1756	-2664	-417	371
52830	-1098	-2066	-2449	-603	-1850	510	-408	1542	-1909	1811	-2709	-425	373
53954	-1082	-2096	-2488	-441	-1728	700	-565	1624	-1932	1891	-2770	-438	366
55078	-1062	-2152	-2497	395	-1538	952	-809	1706	-1959	1972	-2845	-444	369

Test Panel 617-01

Gage No.	Strain, $\mu\text{in/in}$									
	42	43	44	45	46	47	48	49	50	51
Head load, lb										
0	0	0	-1	0	-1	0	0	0	0	0
1124	-2	-15	-56	-101	29	22	-22	-39	-56	-46
2248	-3	-28	-94	-171	49	40	-34	-63	-102	-86
4496	-18	-66	-146	-271	77	62	-49	-98	-176	-154
6744	-32	-105	-196	-371	106	82	-58	-131	-251	-221
8992	-44	-142	-242	-466	132	100	-67	-163	-322	-285
11241	-55	-179	-285	-558	158	118	-76	-195	-392	-348
13489	-63	-215	-330	-647	182	138	-85	-225	-461	-412
15737	-70	-251	-372	-737	207	160	-93	-255	-530	-474
17985	-75	-288	-410	-831	233	182	-98	-288	-599	-537
20233	-79	-324	-445	-931	263	207	-100	-323	-669	-600
22481	-82	-362	-471	-1038	297	232	-96	-362	-736	-662
24729	-83	-399	-488	-1155	334	261	-83	-404	-803	-722
26977	-84	-437	-472	-1303	383	303	-47	-459	-870	-781
29225	-251	-546	112	-1393	320	416	271	-486	-1127	-676
31473	-288	-584	241	-1556	286	437	324	-564	-1116	-757
33722	-268	-591	66	-1357	373	409	286	-439	-1323	-691
35970	-298	-636	-94	-1228	433	387	216	-422	-1544	-778
38218	-304	-667	-146	-1208	463	382	201	-417	-1672	-840
40466	-303	-693	-191	-1195	489	380	189	-415	-1798	-906
42714	-295	-716	-232	-1188	513	379	178	-413	-1923	-975
44962	-271	-738	-272	-1186	539	380	171	-409	-2051	-1046
47210	603	-840	-835	-1007	477	114	99	-287	-1803	-1144
49458	626	-831	-877	-1058	498	115	125	-302	-1891	-1219
50582	635	-819	-899	-1089	511	117	141	-313	-1933	-1256
51706	643	-800	-921	-1127	526	122	160	-324	-1966	-1293
52830	648	-769	-947	-1175	546	130	185	-338	-1987	-1327
53954	640	-692	-883	-1464	620	303	-118	-632	-2129	-988
55078	639	-610	-845	-1603	697	377	-35	-664	-2139	-858

B.8 Test Panel 617-02

Gage No.	Strain, $\mu\text{in/in}$												
	1	2	3	4	5	6	7	8	9	10	11	12	13
Head load, lb													
0	-2	-1	0	0	0	-1	-1	0	0	0	0	0	0
1124	-28	-28	-16	-33	-39	-45	-42	-40	-46	-45	-43	-34	-41
2248	-58	-59	-37	-67	-79	-88	-84	-78	-90	-88	-84	-68	-80
4496	-117	-122	-83	-131	-155	-168	-160	-145	-167	-165	-157	-130	-153
6744	-184	-193	-146	-192	-228	-241	-230	-204	-239	-235	-225	-189	-223
8992	-254	-265	-218	-252	-302	-314	-300	-262	-310	-307	-293	-250	-295
11241	-322	-336	-287	-310	-375	-387	-367	-318	-380	-379	-361	-311	-367
13489	-389	-407	-355	-367	-448	-461	-435	-374	-451	-452	-428	-371	-440
15737	-455	-478	-422	-417	-520	-534	-500	-420	-522	-524	-493	-427	-512
17985	-521	-550	-489	-463	-594	-610	-566	-468	-593	-600	-558	-480	-586
20233	-584	-623	-554	-511	-667	-687	-629	-515	-663	-677	-620	-535	-658
22481	-647	-698	-621	-558	-739	-767	-690	-562	-732	-756	-678	-589	-729
24729	-706	-774	-686	-605	-810	-851	-744	-608	-800	-840	-730	-643	-800
26977	-761	-854	-752	-650	-880	-944	-788	-653	-866	-931	-770	-698	-862
29225	-817	-739	-810	-1226	-1121	-2016	1295	-1226	-1227	-793	-875	-718	-898
31473	-828	-721	-864	-1514	-1285	-2193	1509	-1494	-1404	-743	-866	-724	-921
33722	-861	-763	-929	-1709	-1425	-2289	1624	-1705	-1554	-698	-895	-747	-970
35970	-890	-808	-993	-1882	-1553	-2384	1723	-1892	-1685	-714	-933	-779	-1024
38218	-912	-854	-1054	-2042	-1676	-2476	1810	-2067	-1807	-735	-968	-811	-1076
40466	-929	-902	-1115	-2194	-1796	-2567	1891	-2236	-1926	-756	-1003	-846	-1128
42714	-939	-955	-1181	-2343	-1918	-2663	1971	-2401	-2039	-777	-1039	-885	-1182
44962	-936	-1020	-1248	-2561	-2072	-2828	2092	-2655	-2181	-736	-1135	-824	-1177
47210	-911	-1094	-1308	-2714	-2193	-2922	2163	-2846	-2286	-752	-1188	-867	-1232
49458	-754	-1297	-1360	-2860	-2336	-3013	2232	-3068	-2384	-763	-1246	-896	-1287
50582	2023	-3088	-1501	-3058	-2638	-2822	2228	-3208	-2413	-692	-1221	-953	-1363
51706	2206	-3155	-1547	-3354	-2756	-2943	2328	-3427	-2423	-566	-1098	-1031	-1413
52830	2357	-3249	-1587	-3716	-2931	-3093	2447	-3730	-2489	-559	-1099	-1036	-1427
53954	2568	-3406	-1665	-4268	-3089	-3332	2640	-4130	-2519	-554	-1106	-1022	-1443

Test Panel 617-02

Gage No.	Strain, $\mu\text{in/in}$												
	14	15	17	18	19	20	21	22	23	24	25	26	27
Head load, lb													
0	0	0	0	0	0	0	0	0	0	0	1	0	0
1124	-30	-32	-20	-28	-29	-45	-43	12	42	18	58	-40	-54
2248	-61	-64	-41	-57	-59	-86	-82	23	68	33	86	-78	-103
4496	-123	-127	-88	-117	-120	-153	-146	40	101	59	124	-141	-192
6744	-190	-195	-146	-179	-183	-216	-209	58	106	82	138	-192	-273
8992	-259	-266	-212	-246	-250	-283	-275	77	101	105	138	-243	-353
11241	-327	-340	-282	-314	-318	-352	-343	96	92	129	133	-292	-432
13489	-395	-415	-354	-382	-387	-421	-411	114	84	152	127	-342	-510
15737	-461	-489	-426	-450	-454	-491	-478	133	74	177	118	-387	-587
17985	-528	-564	-497	-520	-523	-562	-545	151	66	200	112	-433	-665
20233	-594	-641	-569	-589	-592	-633	-612	169	56	225	105	-479	-742
22481	-657	-719	-639	-659	-660	-706	-677	186	47	248	98	-525	-818
24729	-715	-800	-708	-727	-728	-780	-739	202	38	271	92	-571	-895
26977	-767	-888	-778	-795	-797	-858	-795	218	29	293	85	-620	-973
29225	-770	-943	-870	-755	-810	-1017	-806	274	10	352	71	-670	-1171
31473	-748	-1102	-977	-549	-870	-1950	1322	297	52	333	54	-699	-1251
33722	-530	-623	-1175	-589	-919	-1947	1375	276	67	293	58	-732	-1355
35970	-830	-82	-1318	-632	-964	-1946	1410	259	88	265	53	-765	-1457
38218	-1174	421	-1456	-677	-1006	-1952	1442	240	110	235	44	-795	-1557
40466	-1546	901	-1591	-721	-1047	-1962	1472	217	135	200	35	-824	-1659
42714	-1932	1349	-1723	-765	-1091	-1958	1488	190	164	157	20	-854	-1765
44962	-1841	1235	-1774	-820	-1248	530	-755	214	332	114	-12	-882	-1852
47210	-1975	1388	-1885	-820	-1337	669	-874	183	391	60	-34	-914	-1952
49458	-2185	1598	-1998	-756	-1493	843	-1036	142	458	-4	-71	-950	-2060
50582	-2365	1750	-2106	1333	-1789	1438	-1605	348	238	55	-95	-998	-2173
51706	-2413	1790	-2278	1381	-1810	1509	-1677	324	151	301	-256	-1157	-2321
52830	-2485	1834	-2343	1439	-1850	1593	-1747	296	188	271	-269	-1191	-2404
53954	-2519	1815	-2385	1493	-1896	1706	-1854	249	292	186	-259	-1217	-2464

Test Panel 617-02

Gage No.	Strain, $\mu\text{in/in}$												
	28	29	30	31	33	34	35	36	37	38	39	40	41
Head load, lb													
0	0	0	0	0	0	0	0	0	0	0	0	0	0
1124	-42	-56	-66	-41	-68	-68	-66	-52	-55	-48	-70	10	-3
2248	-84	-106	-116	-80	-123	-122	-119	-101	-106	-88	-140	29	13
4496	-156	-193	-195	-149	-209	-210	-206	-180	-190	-144	-241	56	35
6744	-220	-270	-264	-212	-285	-287	-282	-249	-264	-192	-328	80	52
8992	-281	-346	-332	-274	-359	-362	-355	-317	-338	-238	-416	104	68
11241	-341	-420	-398	-335	-433	-435	-426	-384	-411	-284	-506	129	84
13489	-401	-495	-465	-397	-507	-508	-496	-450	-485	-329	-599	156	101
15737	-457	-569	-531	-457	-582	-58	-565	-514	-559	-372	-693	185	120
17985	-512	-643	-598	-515	-657	-655	-632	-577	-635	-413	-792	217	139
20233	-566	-719	-664	-574	-733	-731	-698	-639	-713	-452	-897	253	162
22481	-620	-795	-730	-631	-808	-809	-759	-696	-796	-488	-1007	292	186
24729	-674	-871	-794	-688	-82	-895	-811	-743	-886	-517	-1124	337	214
26977	-727	-948	-858	-744	-954	-1000	-839	-763	-997	-532	-1256	391	251
29225	-751	-1043	-1028	-600	-999	-674	-965	-553	-136	367	-1624	189	445
31473	-774	-1095	-1118	-610	-1067	-687	-1007	-523	-58	495	-1732	148	456
33722	-809	-1165	-1239	-650	-1157	-715	-1060	-608	109	576	-1808	129	467
35970	-845	-1238	-1353	-701	-1245	-744	-1114	-614	191	670	-1901	104	476
38218	-878	-1312	-1465	-754	-1330	-767	-1169	-605	254	761	-1992	80	484
40466	-913	-1389	-1579	-812	-1415	-784	-1228	-594	308	845	-2081	60	493
42714	-952	-1470	-1701	-881	-1508	-793	-1294	-574	351	927	-2172	41	501
44962	-962	-159	-1780	-972	-1580	-785	-1368	-477	306	1018	-2268	16	506
47210	-988	-1630	-1895	-1054	-1670	-766	-1453	-417	302	1099	-2361	0	513
49458	-1017	-1738	-2016	-1148	-1768	-700	-1589	-306	246	1196	-2471	-20	520
50582	-1117	-1870	-2161	-1069	-1856	-679	-1597	-217	202	1286	-2541	-43	524
51706	-1157	-2184	-2498	-1059	-2224	1537	-2291	1528	-2015	1702	-3026	-360	414
52830	-1196	-2306	-2624	-1127	-2268	1575	-2328	1753	-2273	1801	-3106	-395	407
53954	-1231	-2427	-2677	-1239	-2312	1592	-2362	1971	-2518	1891	-3189	-419	403

Test Panel 617-02

Gage No.	Strain, $\mu\text{in/in}$									
	42	43	44	45	46	47	48	49	50	51
Head load, lb										
0	0	0	0	0	0	0	0	0	0	0
1124	-3	-21	-39	-56	19	17	-25	-31	-36	-37
2248	-14	-43	-73	-107	35	33	-43	-56	-71	-73
4496	-35	-81	-122	-186	58	52	-65	-93	-133	-139
6744	-51	-115	-169	-262	79	68	-85	-129	-193	-204
8992	-65	-150	-218	-344	103	85	-100	-164	-259	-275
11241	-76	-183	-268	-429	127	102	-112	-198	-325	-346
13489	-84	-217	-317	-515	154	119	-122	-233	-393	-418
15737	-91	-251	-364	-603	182	137	-130	-268	-459	-490
17985	-96	-287	-410	-692	211	155	-137	-305	-526	-562
20233	-97	-326	-454	-785	243	173	-141	-343	-594	-634
22481	-96	-368	-495	-879	277	192	-142	-382	-660	-705
24729	-88	-412	-534	-975	314	212	-141	-423	-726	-775
26977	-68	-462	-571	-1072	355	232	-136	-466	-790	-844
29225	329	-429	-592	-1176	410	269	-102	-487	-822	-862
31473	371	-435	-277	-1008	417	325	97	-402	-1115	-854
33722	404	-462	-274	-1023	431	326	104	-417	-1271	-929
35970	437	-480	-280	-1040	448	327	112	-427	-1408	-1001
38218	468	-493	-288	-1059	466	329	120	-434	-1541	-1070
40466	495	-504	-296	-1077	484	333	127	-440	-1675	-1140
42714	523	-514	-317	-1092	504	334	134	-439	-1812	-1216
44962	543	-513	-801	-974	393	100	50	-362	-1696	-1365
47210	566	-513	-836	-1017	406	99	67	-379	-1781	-1444
49458	590	-511	-874	-1073	425	101	89	-400	-1865	-1526
50582	618	-494	-860	-1249	459	169	-143	-630	-2169	-1558
51706	371	-1032	-865	-1314	490	197	-103	-648	-2207	-1534
52830	364	-1005	-863	-1381	522	231	-58	-669	-2263	-1472
53954	350	-945	-865	-1451	559	270	6	-678	-2307	-1436

VITA

Vicki Britt was born to Glenn and Joyce Owen in Myrtle Beach, South Carolina on September 14, 1965. After a very adventurous life with the United States Air Force, her family eventually settled in Smithfield, North Carolina in 1979. Vicki attended high school at Smithfield-Selma Senior High School and graduated as class valedictorian in 1983. She then went to North Carolina State University where she received a Bachelor's Degree in Aerospace Engineering in 1987 followed by a Master's Degree in Mechanical Engineering in 1990. After completing her Master's Degree, Vicki went to work at NASA Langley Research Center where she was employed doing research on composite materials and nonlinear shell stability problems until 1996. In 1994, Vicki started work on her Doctorate at Old Dominion University. She finished all of her required classwork before she left NASA and went to work as a structural analyst at Gulfstream Aerospace in 1996. She continued working on her research topic while at Gulfstream. Eleven years and three children later, she finished her dissertation in 2007. She received her Doctorate in Aerospace Engineering from the Frank Batten College of Engineering and Technology at Old Dominion University in Norfolk, Virginia in May, 2007.